Adrián Fernández Lodeiro

Gold, Silver and Platinum Nanoparticles: From New Synthetic Routes to Sensing, Catalysis and Bio-Applications

Dissertação para a obtenção do Grau de Doutor em

Química Sustentável

Orientador

Doutor José Luís Capelo Martínez

Professor Associado com Agregação

Faculdade de Ciências e Tecnologia (FCT)

Universidade Nova de Lisboa (UNL), Portugal

Co-Orientadores

Doutora Julia Lorenzo Rivera

Visiting Professor, Universitat Autònoma de Barcelona, UAB, Spain

Doutor Hugo Miguel Baptista Carreira dos Santos

Investigador Auxiliar, FCT Investigator Programme, FCT, UNL, Portugal

Júri

Presidente	Prof. Doutor Manuel Luís De Magalhães Nunes Da Ponte
Vogais	Prof. Doutor Gilberto Paulo Peixoto Igrejas
	Prof. Doutor José Luís Capelo Martínez
	Prof. Doutor Jorge Pérez Juste
	Doutora Elisabete De Jesus Oliveira Marques

FACULDADE DE CIÊNCIAS E TECNOLOGIA
UNIVERSIDADE NOVA DE LISBOA

March - 2019

Adrián Fernández Lodeiro

Gold, Silver and Platinum Nanoparticles: From New Synthetic Routes to Sensing, Catalysis and Bio-Applications

Dissertação para a obtenção do Grau de Doutor em

Química Sustentável (Sustainable Chemistry)

Orientador

Doutor José Luís Capelo Martínez

Professor Associado com Agregação

Faculdade de Ciências e Tecnologia (FCT)

Universidade Nova de Lisboa (UNL), Portugal

Co-Orientadores

Doutora Julia Lorenzo Rivera

Visiting Professor, Universitat Autònoma de Barcelona, UAB, Spain

Doutor Hugo Miguel Baptista Carreira dos Santos

Investigador Auxiliar, FCT Investigator Programme, FCT, UNL, Portugal

Júri

Presidente	Prof. Doutor Manuel Luís De Magalhães Nunes Da Ponte
Vogais	Prof. Doutor Gilberto Paulo Peixoto Igrejas
	Prof. Doutor José Luís Capelo Martínez
	Prof. Doutor Jorge Pérez Juste
	Doutora Elisabete De Jesus Oliveira Marques

FACULDADE DE CIÊNCIAS E TECNOLOGIA
UNIVERSIDADE NOVA DE LISBOA

March - 2019

Gold, Silver and Platinum Nanoparticles: From New Synthetic Routes to Sensing, Catalysis and Bio-Applications

A mis padres,

José Manuel y María Pilar

Acknowledgments

First of all, I want to thanks the “Fundação para a Ciencia e Tecnología” (FCT), as well as the “Faculdade de Ciências e Tecnologia” (FCT), the “Universidade Nova de Lisboa” (UNL), and all the professors responsible for the “Programa Doutoral em Química Sustentável” (PDQS), for the grant number SFRH/BD/52528/2014.

I want to thanks all the people involved in the REQUIMTE-Chemistry Department of the FCT. To the research units, UCIBIO-REQUIMTE first, and to the LAQV-REQUIMTE later, for their support and help during this period.

Thanks to the Analytical Laboratory at the REQUIMTE-Chemistry Department for their support, and specially the help to Dr. Luz Fernandes, Ms. Carla Rodrigues, Mr. Nuno Costa and Ms. Ana Teresa Lopes. Thanks also to laboratory technicians at the 4th floor of the Chemistry Department, Ms. Idalina Martins e Ms. Conceição Luis for their help and kindness.

I want to thanks my supervisor Professor Dr José Luís Capelo Martinez, as well as the co-supervisors, Professor Dr Julia Lorenzo Rivera and Dr Hugo Santos, for giving me the opportunity to do my PhD under their guidance and supervision. Thanks a lot.

I want to thanks the Proteomass Scientific Society for the support during the PhD, in the form of reagents, general funding and for the last year contract.

I want to do a special thanks to all the people (past and present) of the Bioscope group and Proteomass Scientific Society. It has been several years where I have worked with many people. I can say, happy and proud, that I learned something positive from every person with whom I have coincided, and that without you none of this would be possible. I want to give my sincere thanks, extendible to the others members with whom I have coincided during this "adventure", to the heads of the group, the "catalysts" of all the work present here, Professor Jose Luis Capelo Matínez and Professor Carlos Lodeiro Espiño. Without your tireless work and support, none of this would be possible. I would also like to thank very much the support of two persons who have shared with me these years of work, such as Dr Javier Fernández and Ms Jamila Djafari (almost Dr too). Their constant support in the laboratory, when things didn’t go as expected, as well as their help in understanding when they did, leading me to learn more than I could have thought at the beginning of the thesis. Their passion for science is indeed contagious, and with them, the desire to learn and experiment seems endless. I wanted to leave my sincere thanks, once again, to the Bioscope and the Proteomass, for everything.

I want to thank all the collaborators which have contributed in my work, with the characterization techniques as well as bacterial, cellular or catalytic properties.

Dr Benito Rodríguez-González from the University of Vigo, CACTI (Spain) for some of the TEM, HRTEM, EDS, EELS and HAADF-STEM characterizations.

Dr Fernando Novio Vazquez and Dr Daniel Ruiz Molina from the Universitat Autònoma de Barcelona (Spain) for some Raman, SEM and XPS analysis.

Mr David Lopez-Tejedor, Mr Carlos Perez-Rizquez and Dr Jose M. Palomo, from the Consejo Superior de Investigaciones Científicas (Spain), for some of the HRTEM and catalytic analisys.

Mr Carlos Fernández Lodeiro from the University of Vigo (Spain) for some of the TEM images.

Mr Sergi Rodriguez Calado and Dr Julia Lorenzo Rivera, from Universitàt Autónoma de Barcelona, for the cell toxicity experiments.

Dr Elisabete Muchagato Mauricio from the Universidade Lusófona (Portugal) and Dr Maria Paula Duarte from the Universidade Nova de Lisboa (Portugal) for the antibacterial studies.

A modo personal, me gustaría agradecer a mis todos compañeros del programa doctoral en química sostenible. Al inicio, cuando una persona cambia de país e idioma, la transición entre lo conocido y lo nuevo puede llegar a ser ciertamente complicada. Gracias a su recibimiento, comportamiento y amabilidad, puedo decir que me he sentido como en casa desde el principio. Un agradecimiento especial a mis compañeros "lisboetas" del programa doctoral, que más que compañeros, considero amigos. Muito Obrigado rapazes!

Creo que lo que hace especial a un lugar no son sus monumentos, sus comidas ni sus paisajes naturales. Lo que hace especial a un lugar son sus gentes. Y no solo creo, si no que puedo afirmar, que las personas con las que compartí muchos de mis mejores momentos en estos últimos años, tanto fuera como dentro del laboratorio, hacen grande a Portugal. Muchas gracias a todos los "vicentinos", y en especial a mi gran compañero y amigo Eduardo. ¡Por muchos años más!

Quería agradecer a todos mis amigos de Santiago y alrededores que me han dado su apoyo durante este tiempo. Sobre todo a Ángela, que ha sido una parte importante en estos años. Un agradecimiento especial a una gran persona, a mi amigo el Dr. Rodrigo Lamelas, con quien empecé compartiendo estudios en primero de carrera, y acabé compartiendo autoría en artículos científicos.

No serían agradecimientos completos sin dar las gracias a todos mis amigos "estradenses", a la familia que se escoge. Si hay mejores personas en este mundo, no quiero saberlo. Saber que al volver a casa, a pesar del tiempo y la distancia, siempre se puede contar con vosotros, para lo bueno y para lo malo, es lo mejor que se puede desear. Han sido muchos años hasta llegar aquí, pero no sería posible sin vuestros ánimos y apoyo. Vuestra amistad no solo hace bien a la mente, sino también al corazón. Dicen que si una amistad dura más de siete años, es para toda la vida. Con vosotros, toda la vida hasta me parece

poco. Mención especial a Paula y Rubén. Gracias por vuestra visita, pero ¡aún espero la del resto! ¡Muchas gracias a todos!

A Silvia, por todo el cariño y apoyo en este tramo final. Lo importante no es como se empieza, es como se acaba, y no podría haber acabado mejor.

A mi familia perruna. Por el inmenso cariño que dan sin pedir nada a cambio. En ese sentido, son un ejemplo a seguir.

Por último, a mi familia.

Creo que todavía no se han inventado las palabras necesarias que consigan reflejar mi enorme gratitud hacia todos ellos.

A mis abuelos, José, Hermitas, Esther y Avelino. Los abuelos pasan mucha sabiduría a sus nietos, y ellos, tanto directa como indirectamente, son los mejores profesores.

A mis hermanos, Abel, Javier y Carlos. Mira que vivimos cosas juntos, y más que vendrán. Sois los mejores.

A mis cuñadas, Paula, Jamila y Paula. Muchas gracias por ser como sois, vuestro apoyo, cariño y por soportar a mis hermanos. Eso sí que tiene mérito.

A mi sobrina Valentina. No podría encontrar mejor uso de mí tiempo, que el invertido jugando y aprendiendo contigo. ¡No crezcas tan rápido!

A mis tíos, Carlos y Jose. Por todo el apoyo y cariño. Pero sobre todo por sus incontables consejos, sin los cuales nada de esto sería posible. De hecho, recuerdo una conversación con Jose en el año 2005 sobre la importancia de aportar valor a la sociedad mediante nuestro trabajo diario. Ese día, en un Peugeot 205 de color verde, en la IC20 camino del Almada Forum, en ese preciso día, me decanté por la elección de la química como futuro profesional. Y no puedo estar más agradecido. No por ser donde mas dinero se puede ganar, si no por, como bien apuntó mi tio, ser donde la satisfacción personal es mas elevada. No perdáis nunca ese espíritu.

A mis padres, José Manuel y María Pilar, a quienes dedico esta tesis. Si soy lo que soy, es gracias a vosotros. Gracias por todas las enseñanzas, amor y apoyo durante toda mi vida. Sin vosotros, nada de esto, ya no solo a nivel académico, si no a nivel personal, sería posible.

Y parte de las enseñanzas de mi padre vienen en forma de refrán. Paso a dejar aquí una de tantas, que espero que a los lectores también les sirva de inspiración: “A boa vida é cara, hainas mais baratas, pero non son vida”.

En definitiva, a todas aquellas personas que me han ayudado y apoyado durante todos estos años. ¡Muchas gracias!

Experiment is the interpreter of nature. Experiments never deceive. It is our judgment which sometimes deceives itself because it expects results which experiment refuses. We must consult experiment, varying the circumstances, until we have deduced general rules, for experiment alone can furnish reliable rules.

Leonardo Da Vinci

1452-1519

Resumo

As nanopartículas metálicas de ouro, prata e platina surgiram como ferramentas poderosas com uma ampla gama de aplicações em diferentes campos, como biomedicina, catálise e ciências ambientais. A modificação da composição, tamanho e forma do metal das nanopartículas leva a propriedades totalmente diferentes do nanomaterial. Essa versatilidade sintonizável é responsável pela vasta gama de aplicações de nanomateriais que afeta a maneira como vivemos agora e no futuro.

O projeto desta tese de doutorado foi projetado com o objetivo principal de desenvolver novas metodologias nanossintéticas verdes e sustentáveis para obter novas nanopartículas para aplicações biomédicas, químicas e ambientais.

No capítulo dois, descreve-se a síntese química de novas nanopartículas funcionalizadas de ouro e prata, projetadas para obter a detecção a olho nu de um íon metálico tóxico, a saber, o mercúrio, em líquidos aquosos e não aquosos. Tais realizações foram publicadas na revista Chemistry Open of Wiley, e também destacadas como capa da revista (IF 2.938).

Nos capítulos 3 e 4 é descrita a síntese de novas nanopartículas de platina com formas esféricas ou dendríticas como catalisadores. Além disso, as aplicações catalíticas foram avaliadas na redução de p-nitrofenol em meio aquoso. Além disso, nosso sistema mostra a atividade da catecol-oxidase, que permite a oxidação do aminoácido L-3,4-dihidroxifenilalanina, um medicamento para tratar a doença de Parkinson. Os resultados foram publicados no Scientific Reports (IF 4.122) e na Nano Research (IF 7.994), da editorial Springer Nature.

No capítulo cinco é descrita uma nova metodologia para a preparação de nanobastões de ouro recobertos com uma camada de sílica mesoporosa. Os novos sistemas foram conjugados com doxorrubicina e azul-de-metileno e estudados como novos nanocarreadores de drogas. As propriedades foram testadas com sucesso contra células do Adenocarcinoma de Mama Humana (MCF7) e bactérias Gram-negativas e Gram-positivas como novos antibióticos para combater a resistência microbiana. Os resultados são apresentados em um manuscrito sob revisão.

Palavra Chaves

Ouro, Plata, Platina, Nanopartículas e Nanobastões, Catalises, Biomedicina

Abstract

Gold, Silver and Platinum metallic nanoparticles have emerged as powerful tools with a wide array of applications in different fields, such as biomedicine, catalysis, and environmental sciences. The modification of nanoparticles´ metal composition, size, and shape lead to totally different properties of the nanomaterial. This tunable versatility is responsible for the vast array of applications of nanomaterials that affects the way we live now and will in the future.

The project of this PhD thesis was designed with the main objective of developing new green and sustainable Nano-synthetic methodologies to obtain new Nano-particles for biomedical, chemical and environmental applications.

In Chapter two it is described the chemical synthesis of new gold and silver functionalised nanoparticles, engineered to achieve naked-eye detection of a toxic metal ion, namely mercury, in aqueous and non-aqueous liquids. Such achievements were published in the journal Chemistry Open of Wiley, and also highlighted as journal front cover (IF 2.938).

In chapters three and four the synthesis of new platinum nanoparticles with spherical or dendritic shapes to be used as catalysts is described. In addition, the catalytic applications were assessed in the reduction of p-nitrophenol in aqueous media. Moreover, our system shows catechol-oxidase activity, which allows oxidation of amino acid L-3,4-dihydroxyphenylalanine, a drug to treat Parkinson disease. The results were published in the Scientific Reports (IF 4.122), and in the Nano Research (IF 7.994), from Springer Nature editorial.

In chapter five a new methodology for the preparation of gold nanorods covered with a mesoporous silica shell is described. The new systems were conjugated with doxorubicin and methylene blue and studied as new drug nanocarriers. Properties were successfully tested against Human Breast Adenocarcinoma (MCF7) cells and Gram-negative and Gram-positive bacteria as new antibiotics to fight microbial resistance. Results are presented in a manuscript under revision.

Keywords

Gold, Silver, Platinum, Nanoparticles and Nanorods, Catalysis, Biomedicine

Table of Contents

1 Chapter 1. Introduction 1

1.1 Material Chemistry 3

1.2 Classifications of nanoparticles 4

1.2.1 Organic based nanoparticles 4

1.2.1.1 Dendrimers 4

1.2.1.2 Liposomes 5

1.2.1.3 Polymeric nanoparticles 6

1.2.1.4 Carbon based materials 6

1.2.2 Inorganic based nanoparticles 7

1.2.2.1 Metal based 7

1.2.2.2 Silica nanomaterials 8

1.2.2.3 Quantum dots 8

1.2.3 Composites 9

1.3 Metals in colloidal chemistry 10

1.3.1 Platinum 10

1.3.2 Silver 10

1.3.3 Gold 11

1.4 Geneal approaches to nanoparticles synthesis 12

1.4.1 “Top-down” 12

1.4.2 “Bottom-up” 12

1.5 Nucleation, growth and stability of the nanoparticles 12

1.5.1 Nucleation 13

1.5.2 Growth 15

1.5.2.1 Atom-mediated growth 15

1.5.2.2 Nanoparticle-mediated growth 17

1.5.3 Stability 18

1.6 Surface Plasmon 20

1.7 General synthetic methodologies of gold and silver nanoparticles 26
1.7.1 Direct Synthesis 26
1.7.2 Seed mediated synthesis 30
1.8 General synthetic methodologies of Platinum nanoparticles 34
1.9 Silica coating 34
1.10 Sustainable Chemistry 35
1.10.1 Solvents 37
1.10.2 Catalyst 38
1.10.2.1 Homogeneous catalyst 38
1.10.2.2 Heterogeneous catalyst 38
1.10.3 Ultrasounds and Microwaves. 38
1.10.3.1 Ultrasounds 38
1.10.3.2 Microwaves 39
1.10.4 Electrochemistry and Photochemistry 39
1.10.4.1 Electrochemistry 39
1.10.4.2 Photochemistry 39
1.10.5 Analytical methodologies 40
1.10.6 Toxicity 40
1.11 Material Chemistry and Green Chemistry 41
1.11.1 Nanomaterials and Sensing 41
1.11.2 Nanomaterials and Catalysis 42
1.11.2.1 Platinum Composites 42
1.11.2.2 Platinum nanoparticles 43
1.11.3 Nanomaterials and Biomedical Applications 43

2 Chapter 2. Polyamine Ligand-Mediated Self-Assembly of Gold and Silver Nanoparticles into Chainlike Structures in Aqueous Solution: Towards New Nanostructured Chemosensors 45

2.1 Introduction 47
2.2 Experimental Section 48
2.2.1 General Instrumentation 48
2.2.2 Limit of detection 49
2.2.3 Concentration determination 49
2.2.4 Characterization of the assemblies of AgNPs and AuNPs 50
2.2.5 Synthesis 50
2.2.6 Preparation of AgNPs 51
2.2.7 Preparation of AuNPs 52
2.2.8 Chainlike assemblies of AgNPs and AuNPs 52
2.3 Results and Discussion 52
2.3.1 Formation of chainlike structures from AgNPs and AuNPs 52
2.3.2 Formation of chainlike structures from AgNPs 53
2.3.2.1 Spherical shape 53
2.3.2.2 Triangular shape 56
2.3.3 Formation of chainlike structures from AuNPs 56
2.3.4 Interaction of AgNPs@$(L)^{2-}$ and AuNPs@$(L)^{2-}$ with Hg^{2+} 59
2.4 Conclusions 63
3 Chapter 3. Synthesis and Characterization of $PtTe_2$ Multi-Crystallite Nanoparticles using Organotellurium Nanocomposites. 65
3.1 Introduction 67
3.2 Experimental Section 68
3.2.1 Materials 68
3.2.2 Synthesis of organometallic Pt-Te NPs. 68
3.2.2.1 Reverse order of reagent addition (entry R4). 69
3.2.2.2 Synthesis in the presence of CH_2Cl_2/acetonitrile mixture (entry R5). 69
3.2.2.3 Synthesis of multi-crystallite NPs. 69

3.2.3 Fourier transform ion cyclotron resonance mass spectrometry analysis. 70
3.2.4 Transmission electron microscopy analysis. 70
3.2.5 Scanning electron microscopy. 70
3.2.6 X-ray photoelectron spectroscopy. 71
3.2.7 UV/Vis and FT-IR spectroscopy studies. 71
3.2.8 Inductively coupled plasma analysis. 71
3.2.9 Elemental analysis. 71
3.2.10 Thermogravimetric analysis. 71
3.3 Results and Discussion 72
3.3.1 Synthesis and morphological characterization of organometallic Pt-Te NPs. 72
3.3.2 Chemical characterization of organometallic Pt-Te NPs. 78
3.3.3 Metal-ligand interaction during the reaction. 84
3.3.4 Synthesis and characterization of $PtTe_2$ multi-crystallite NPs. 88
3.4 Conclusion 92
4 Chapter 4. Highly Accesible Aqueous Synthesis of Well-Dispersed Dendrimer Type Platinum Nanoparticles and their Catalytic Applications 95
4.1 Introduction 97
4.2 Experimental Section 98
4.2.1 Materials 98
4.2.2 Methods 99
4.2.3 Sodium citrate assisted synthesis 99
4.2.4 Sodium citrate/PVP assisted synthesis 99
4.2.5 Synthesis of Pt D-NPs for catalysis applications 100
4.2.5.1 Samples PtCat-1 and PtCat-2 100
4.2.5.2 Samples PtCat-3 and PtCat-4 100
4.2.6 Characterization of Pt D-NPs 100
4.3 Results and discussion 101

4.3.1 Synthetic process adjustment 102
4.3.2 Synthesis and characterization of samples for catalysis studies 114
4.3.3 Catalytic applications 122
4.3.3.1 Temperature stability 125
4.3.3.2 Substrate concentration 125
4.3.3.3 Application of the Pt D-NPs as an artificial metalloenzyme with catechol oxidase-like activity 126
4.4 Conclusions 129
5 Chapter 5. Synthesis of Gold Nanorods with Mesoporous Silica Shell Containing Doxorubicin and Methylene Blue as Drugs, and their Applications as Anti-Cancer and Antimicrobial Nanotools 131
5.1 Introduction 133
5.2 Experimental Section 135
5.2.1 Materials 135
5.2.2 Synthesis of gold nanorods 135
5.2.3 Silica coating of gold nanorods 135
5.2.3.1 Preparation of AuNRs_RA@Si_{mes} 135
5.2.3.2 Preparation of AuNRs_RB@Si_{mes} 136
5.2.4 Drug Loading 136
5.2.5 Freeze Drying of AuNRs@Si_{mes}-Drug 136
5.2.6 Cell cytotoxicity assay 137
5.2.7 In vitro photothermal assay 137
5.2.8 Antibacterial activity 137
5.2.9 Statistics in bacterial samples 138
5.3 Results and discussion 138
5.3.1 Synthesis of gold nanorods 138
5.4 Synthesis and purification of AuNRs@Si_{mes} 140

5.4.1 The case of AuNRs_RA@Si_{mes} 141
5.4.2 The case of AuNRs_RB@Si_{mes} 144
5.5 Drug loading experiments 145
5.6 Freeze drying experiments of AuNRs@Si_{mes}-Drug 146
5.7 Exploring the application of AuNRs_RA@Si_{mes}-DOX in cell experiments 148
5.8 Exploring the application of AuNRs_RB@Si_{mes}-MB in antibacterial applicattions 150
5.9 Conclusions 152
6 Chapter 6. General Conclusions and Future Work 153
7 Bibliography 159

List of Figures

Figure 1.1: Lycurgus cup in the British museum. 3
Figure 1.2: Illustration of a dendrimer structure. Reprinted from reference 11. 5
Figure 1.3: Representation of liposomes and the functionalization capabilities. Reprinted from reference 12. 5
Figure 1.4: Representation of two polymeric nanoparticles, nanosphere and nanocapsule. Reprinted from reference 13. 6
Figure 1.5: Representation of a) fullerene and b) carbon nanotube. Adapted from reference 15. 7
Figure 1.6: Microscopy images of Gold Nanorods with different sizes. 7
Figure 1.7: Microscopy image of Silica Mesoporous Nanoparticles. Reprinted from reference 20. 8
Figure 1.8: Representation of a colloidal quantum dot made of Pb and S. Adapted from reference 21. 9
Figure 1.9: Microscopy images of Gold Nanorods@Mesoporous Silica nanocomposites. 9
Figure 1.10: The dependence of the cluster free energy, ΔG, on the cluster radius, r_c according to the CNT. Adapted from reference 43. 14
Figure 1.11: The principle of nanoparticle nucleation due to LaMer's mechanism of nucleation derived from CNT. Adapted from reference 43. 16
Figure 1.12: Schematic illustration of the Ostwald ripening with time (t1<t2<t3). Adapted from reference 49. 16
Figure 1.13: Representation of the digestive ripening process. Reprinted from reference 50. 17
Figure 1.14: Representation of coalescence in the synthesis of gold nanoparticles. Adapted from reference 56 18
Figure 1.15: Representation of an oriented attached mechanism. Reprinted from reference 57 18
Figure 1.16: Representation of Van der Waals interactions that can lead to nanoparticle aggregation. Adapted from reference 59. 19
Figure 1.17: Representation of the EDL, composed by the Stern layer and the Diffuse layer. The total thickness of both is called the Debye length. Adapted from reference 59. 19
Figure 1.18: Representation of the Total Interaction Potential (TIP) from the DLVO theory. Adapted from reference 44. 20
Figure 1.19: Representation of nanoparticles covered with a polymer avoiding particle interaction due to steric repulsion. Adapted from reference 59. 20
Figure 1.20: a) Representation of a homogeneous sphere set into an electrostatic field b) illustration of the surface plasmon resonance, with the collective oscillation of the conduction band electrons due to an incident light. 21
Figure 1.21: Representation of scatter, absorption and transmission process in a nanoparticle. 22

Figure 1.22: (A) Real and (B) Imaginary part for Au (black) and Ag (green). Adapted from Reference 60. 23
Figure 1.23: Resonant frequency and extinction cross section of various metallic nanoparticles with 10 nm size in air. For Ag, the extinction cross section was divided by 20. Reprinted from reference 62. .24
Figure 1.24: a) Representation of a gold nanorod with charge accumulation in the surface and b) absorption spectra of gold nanorods with different aspect ratio. Adapted from reference 62. 25
Figure 1.25: Scheme of the citrate oxidation. 27
Figure 1.26: Scheme of the complex of dicarboxy acetone with the gold and formation of the nanoparticles. 27
Figure 1.27: Schematic representation of the growth silver nanoparticles mechanism. Adapted from reference 76. 29
Figure 1.28: Scheme of the net redox reaction for the reduction of Au(III) to Au(0). 31
Figure 1.29: Scheme of reduction of Au(III) to Au(I) by ascorbic acid. 32
Figure 1.30: Scheme of the disproportionation of Au(I) to Au(0) and Au(III). 32
Figure 1.31: Scheme of the direct reduction of Au(I) to Au(0). 32
Figure 1.32: Scheme of the complex oxidation of L-ascorbic acid. 33
Figure 2.1: Transmission electron microscopy (TEM) images of AgNPs@citrate: A) yellow (25 ± 3 nm polidisperse quasispherical particles); B) blue (64 ±10 nm; average lateral dimension of triangular particles). 51
Figure 2.2 Scheme of the synthetic route to compound L. 52
Figure 2.3: UV/Vis absorption spectra of spherical AgNPs@citrate during titration to A) AgNPs@L and B) AgNPs@$(L)^{2-}$. C) Size distribution diagram for AgNPs@$(L)^{2-}$. TEM images of silver nanowire formed from D,E) AgNPs@L and F,G) AgNPs@$(L)^{2-}$. Visual color changes and TEM images obtained H) before and I) after the addition of L^{2-} to an aqueous solution of spherical AgNPs@citrate. 54
Figure 2.4: IR spectra of AgNPs@citrate, compound L and AgNPS@L in 550-4000 cm^{-1} region (x-axis = cm^{-1}, y-axis = intensity). 55
Figure 2.5: A) UV/Vis absorption spectra of triangular citrate@AgNPs during titration to AgNPs@$(L)^{2-}$ and B) size distribution diagram for AgNPs@$(L)^{2-}$. Visual color changes and TEM images obtained C) before and D) after the addition of L^{2-} to an aqueous solution of triangular AgNPs@citrate. 56
Figure 2.6: Absorption spectra and transmission electron microscopy (TEM) images of AuNPs in aqueous solutions. 57
Figure 2.7: A) UV/Vis absorption spectra recorded in real-time (one spectrum per minute) during the self-assembly of AuNPs@citrate by L^{2-} to form AuNPs@$(L)^{2-}$. B) Size distribution diagram for AuNPs@$(L)^{2-}$. Visual color changes and TEM images of C) AuNPs@citrate and D) gold nanowire formed from AuNPs@$(L)^{2-}$. 58
Figure 2.8: A) Spectrophotometric titration of spherical AgNPs@$(L)^{2-}$ with the addition of increasing amounts of $HgCl_2$ in aqueous solution. B) Modification with time in the absorption spectra of

AgNPs@$(L)^{2-}$ with the addition of 6 µL of $HgCl_2$ (1:1 L/M). TEM images of an aqueous solution of spherical AgNPs@$(L)^{2-}$ C) before and D,E) after the addition of $HgCl_2$ (1 equiv, $[HgCl_2]=1.10x10^{-3}$ M). 60

Figure 2.9: A) Modifications with time in the absorption spectra of triangular AgNPs@$(L)^{2-}$ with the addition of $HgCl_2$ (22 µL, 1:1 L/M). B) Size distribution diagram for an aqueous solution of triangular AgNPs@$(L)^{2-}$ after the addition of $HgCl_2$ (1 equiv, $[HgCl_2]=1.10x10^{-3}$ M). TEM images of an aqueous solution of triangular AgNPs@$(L)^{2-}$ C) before and D, E) after the addition of $HgCl_2$ (1 equiv, $[HgCl_2]=1.10x10^{-3}$ M).....61

Figure 2.10: Spectrophotometric (A) and spectrofluorimetric (B) titrations of compound L as a function of added Hg^{2+} in absolute ethanol. The inset shows the normalised fluorescence intensity at 366 nm (B) λ_{exc} = 295 nm; λ_{em}= 366 nm, [L] = $1.00.10^{-5}$ M.....62

Figure 2.11: Normalised fluorescence intensity of receptor L in the absence and presence of one equivalent of different metal ions (Ag^{+}, Cu^{2+}, Zn^{2+}, Cd^{2+}, Hg^{2+}) in absolute ethanol. λ_{exc} = 295 nm; λ_{em}= 366 nm, [L] = $1.00x10^{-5}$ M.....62

Figure 3.1: Low magnification electron transmission microscopy images obtained for R1 (a, b), R2 (c, d) and R3 (e, f).....72

Figure 3.2: Histogram obtained for R2 and R3 samples. (Histogram was obtained counting a minimum of 100 particles per sample). 73

Figure 3.3: Histogram obtained for R2.1 (oxygen absence) and R2.2 (light absence) samples. 73

Figure 3.4: Low magnification TEM images obtained for R2.1 (a, b), R2.2 (c, d). 74

Figure 3.5: Overview X-ray photoelectron spectroscopy of R4 obtaining under N_2 or O_2 atmosphere. 74

Figure 3.6: Histogram obtained for R4 and R5 samples. 75

Figure 3.7: Low magnification SEM images obtained for R4.....75

Figure 3.8: Low magnification TEM (a, b) and SEM (c, d) images obtained for R5. 76

Figure 3.9: (a) Low magnification TEM (**a**,**b**,**d**,**e**) and SEM (**c**,**f**) images of different sizes of organometallic Pt-Te NPs obtained under higher initial reagent concentrations ([Pt(IV)] = 2.10^{-4} M, [Te-Te] = 6.10^{-4} M) (**a**,**b**,**c**) and ([Pt(IV)] = 8.10^{-3} M, [Te–Te] = $2.4.10^{-2}$ M) (**d**,**e**,**f**). 76

Figure 3.10: Low magnification SEM images obtained for R4 in normal condition (a and b) and modifying the reactant sequence addition (c and d). 77

Figure 3.11: Low magnification electron transmission microscopy images obtained for R2 dispersed in absolute ethanol (a, b) and in water (c, d). 77

Figure 3.12: (a) STEM-HAADF image of a group of Pt-Te NPs and Te, Pt, C, O and Cl EDS elemental maps (1–6). (b) HAADF-STEM image: one group of isolated Pt-Te NPs (1) and two close ups (2) showing the complex structure and the nodules composed of high atomic-number elements (3). (c) HRTEM image and diffraction pattern showing the structure and demonstrating the lack of a crystalline structure in the nodules. 78

Figure 3.13: EDS X-ray microanalysis obtained from an individual particle. 79
Figure 3.14: : (a) STEM-HAADF image of an as obtained organometallic Pt-Te NPs. (b) EDS intensity profiles of the PtLα1 signal (a), and O-Kα1, Pt-Lα1 Te-Lα1, and C-Kα1-2 along the white arrow marked in (a). 79
Figure 3.15: X-Ray diffraction pattern of organometallic Pt-Te NPs in different size. 80
Figure 3.16: EEL spectrum in the region of the C K-edge (a) and Te, O edge (b) obtained for organometallic Pt-Te NPs. 80
Figure 3.17: XPS spectrum of organometallic Pt-Te NPs. Binding energy spectrum of Pt 4 f (a), Te $3d_{3/2}$ and $3d_{5/2}$ (b), and C 1 s (c). 81
Figure 3.18: FT-IR spectrum (overview a, different spectra close-ups b, c, d) of organometallic Pt-Te NPs in KBr disk. 82
Figure 3.19: TG/dTG curves obtained for organometallic Pt-Te NPs. 83
Figure 3.20: UV/Vis study of the time depend interaction of Ph_2Te_2 ([L] = 1.10^{-4} M) with addition of 1:1 (a, b) and 1:3 (c, d) equivalents of H_2PtCl_6 in acetonitrile solution. 85
Figure 3.21: (a) FT-ICR MS (+) spectra of the reaction time at (1) 1 min, (2) 20 min. (b) Experimental isotopic mass spectra for the peaks at m/z 616.833 and m/z 853.398 for Pt and 616.830 m/z and 853.393 m/z for previously reported[290] gold reaction. 86
Figure 3.22: Experimental and theoretical isotopic pattern of 1118.674 m/z. This signal can be formed with one Pt(II) metal coordinated with one molecule of Ph_2Te_2 (blue) and one molecule of an derivative of phenyl tellurium oxidised (red) together to Cl atoms (green). 87
Figure 3.23: In panel a the histograms obtained for organometallic nanoparticles (sample R2) before and after the annealed process (1) and the colour solution of organometallic Pt-Te NPs (2) and annealed ($PtTe_2$ multi-crystallite) NPs (3) can be seen. In painel b images of organometallic Pt-Te NPs (1, 2) and the resulting $PtTe_2$ multi-crystallite NPs (3, 4). 89
Figure 3.24: Low magnification electron transmission microscopy images $PtTe_2$ multi-crystallite particles obtained after annealing process of R5. 89
Figure 3.25: TEM (a), and STEM (b) images of $PtTe_2$ multi-crystallite NPs obtained after the annealing process, HRTEM images of isolated NPs showing lattice image fringes (c,d) and electron diffraction pattern obtained from a group of $PtTe_2$ multi-crystallite NPs showing clear diffraction rings; this pattern was indexed on the basis of the $PtTe_2$ crystalline structure (P −3 m 1, SG: 164) (e).....90
Figure 3.26: EDS X-ray microanalysis spectra of the as obtained organometallic Pt-Te NPs and of the annealed ($PtTe_2$ Multi-Crystallite) NPs, note the drop in the relative intensity of the C-Kα1-2 signal in the annealed NPs. 91
Figure 3.27: STEM image of a group of $PtTe_2$ multi-crystallite NPs showing crystalline contrast, brighter areas are due to the presence of small crystallites within the NPs. Numbers display the length of the black lines. 91

Figure 3.28: (a) STEM-HAADF image of a group isolated $PtTe_2$ multi-crystallite particles and Te, Pt EDS elemental maps (1,2) and STEM image of a group of particles. (b) EDS intensity profiles of the PtLα1 and Te-Lα1, signal along the yellow line. (c) STEM image in high resolution of an isolated particle showing crystalline contrast, brighter areas are due to the presence of small crystallites within the particles. Numbers display the length of the red lines. 92
Figure 4.1: (a) UV/Vis kinetic study of the interaction of K_2PtCl_4 ($[Pt^{2+}]$ = 0.5 mM), with the addition of 4 equivalents of $FeSO_4$ in water (inset show an extension to show $[PtCl_4]^{2-}$ absorption band). (b) UV/Vis kinetic study of the interaction of K_2PtCl_4 ($[Pt^{2+}]$ = 0.5 mM) in presence of 2 equivalents of SC with the addition of 2 equivalents of $FeSO_4$. (c) UV/Vis kinetic study of the interaction of K_2PtCl_4 ($[Pt^{2+}]$ = 0.5 mM) in presence of 4 equivalents of SC with the addition of 4 equiv. of $FeSO_4$ at 22 ºC. 102
Figure 4.2: (a) UV/Vis kinetic study of the interaction of K_2PtCl_4 ($[Pt^{2+}]$ = 1 mM) in presence of 2 equivalents of SC with the addition of 2 equivalents of $FeSO_4$. (c) UV/Vis kinetic study of the interaction of K_2PtCl_4 ($[Pt^{2+}]$ = 1 mM) in presence of 4 equivalents of SC and upon addition of 4 equivalents of $FeSO_4$ at 22 ºC. 103
Figure 4.3: UV/Vis kinetic study of the interaction of K_2PtCl_4 ($[Pt^{2+}]$ = 0.25 mM) in presence of 4 equivalents of SC with the addition of 4 equivalents of $FeSO_4$ at 22 ºC. 103
Figure 4.4: (a-c) UV/Vis kinetic study of the interaction of K_2PtCl_4 ($[Pt^{2+}]$ = 0.5 mM, molar ratio Pt/SC/Fe =1/2/2) (a), extension on the y-axis (b) and colour solution at the end of the study. (d-e) UV/Vis kinetic study of the interaction of K_2PtCl_4 ($[Pt^{2+}]$ = 1 mM, molar ratio Pt/SC/Fe =1/4/4) (d, e) and colour of the solution at the end of the study (f). 104
Figure 4.5: UV/Vis kinetic study of the interaction of $FeSO_4$ ($[Fe^{2+}]$ = 2mM) upon addition of 1 equivalent of sodium citrate. 105
Figure 4.6: UV/Vis spectra of supernatant of reaction in Pt/SC/Fe 1/4/4 with [Pt(II)]=1 mM (yellow line) and UV/Vis spectra of solution produced mixing $FeSO_4$ or $Fe_2(SO_4)_3$ in concentrations of 2mM with one equivalent of sodium citrate (denoted as Fe(II)-SC and Fe(III)-SC respectively). Colour solutions of SN (b), Fe(II)-SC (c) and Fe(III)-SC (d). 106
Figure 4.7: Transmission electron microscopy (TEM) images of the sample obtained under the molar ratio Pt /Fe/SC = 1/4/4. 106
Figure 4.8: TEM images of sample obtained under the molar ratio Pt /Fe/SC = 1/4/5. 107
Figure 4.9: (a) Low-resolution TEM images of obtained Pt D-NPs in different Pt/PVP molar ratio: 1/0.25, (b) 1/1 and (c) 1/5 and the corresponding DLS analysis. 108
Figure 4.10: TEM images of sample obtained under the molar ratio Pt /Fe/SC/PVP = 1/4/4/5. 109
Figure 4.11: TEM images of sample obtained under the molar ratio Pt /Fe/SC/PSS = 1/4/4/5..... 109
Figure 4.12: (a-c) Low-resolution TEM images of obtained Pt D-NPs obtained under molar relation Pt/PVP = 1/1 at 60 °C and (d-f) under boiling condition. 110
Figure 4.13: TEM images (a, b and c) and histogram (d) of sample obtained under molar ratio Pt/Fe/SC/PVP = 1/4/4/1 and under boiling condition. 110

Figure 4.14: (a,b) Low-resolution TEM images, (c) colour solution, (d) histogram and (e and f) FT-IR study of sample obtained under Pt/PVP = 1/5. 112
Figure 4.15: FT-IR spectrum obtained for pure PVP (dotted line, Y axis left) and Pt D-NPs (sample obtained under relation Pt/PVP 1/5) (black line, Y axis right) in KBr disk. Complete spectra between 3100-400 cm^{-1} and different spectrum extensions. The table show different peaks detected with their corresponding assignments. Assignments of the signals have been based on previously detailed works on FT-IR analysis of, pure PVP and PVP/Pt nanocrystals [354,355,356]. 113
Figure 4.16: TEM images of Pt/PVP 1/5 (a) and PtCat-1 (b). DLS comparative analysis Pt/PVP 1/5 vs PtCat-1 samples, distribution by number (c) and by volume (d). 115
Figure 4.17: HRTEM images at different magnification of (a) PtCat-1, (c) PtCat-3 and (e) PtCat-4 synthesised with $[K_2PtCl_4]$ 1, 5 and 10 mM respectively. 116
Figure 4.18: HR- TEM images at different magnification (a, b) and histogram (c) obtained for PtCat-1. 116
Figure 4.19: HR- TEM images at different magnification and histogram obtained for PtCat-3 (a-c), PtCat-4 (d-f). 117
Figure 4.20: (a) HRTEM images at higher magnification, (b) representative lattice fringe under higher magnification and (c) determination of the inter-planar distance using plot profile. 118
Figure 4.21: HRTEM images at higher magnification (a), and the corresponding FFT showing spots assigned to Pt (111) (marked as red), Pt (200) (marked as green) and Pt (022) (marked as yellow) (b). c and e shows two crystalline sections (marked with white box in a) and their corresponding FFT (d and f respectively) of sample PtCat-2. 118
Figure 4.22 HRTEM images at higher magnification (a), and the corresponding FFT showing spots assigned to Pt (111) (marked as red), Pt (200) (marked as green) and Pt (022) (marked as yellow) (b). c and d show two crystalline sections (marked with white box in a) and their corresponding FFT (d and f respectively) of sample PtCat-4. 119
Figure 4.23: (a) HRTEM images at higher magnification and (b) the corresponding FFT showing spots assigned to Pt (111) (marked as red), Pt (200) (marked as green) and Pt (022) (marked as yellow). (c) and (e) shows two crystalline sections (marked with white box in a) and their corresponding FFT with the assignment of the bright spots (d and f respectively). 119
Figure 4.24: XRD spectra of PtCat-3 (a) and PtCat-4 (b) showing clearly the peaks at 39.8° corresponding with Pt (111) crystals planes. 120
Figure 4.25: Graphic representation of ζ-potential analysis obtained for PtCat-3 purified only with water (denoted as PtCat-3_Water) or with EDTA and water process (denoted as PtCat-3_EDTA). 120
Figure 4.26: FT-IR spectrum obtained for pure PVP (black line, Y axis left) and PtCat3 (sample purified only with water (blue line, Y axis right) or EDTA and water (red line, Y axis right) (black line, Y axis right) in KBr disk. Complete spectra between 3100-400 cm^{-1} and different spectrum extensions. The table show the different peaks detected. Assignments of the signals is showed in **Figure** 4.15 121

Figure 4.27: Scheme of the reduction of pNP to pAP.....122
Figure 4.28: Time-dependent absorption spectra of the metal-catalysed reduction of 5 mM pNP in the presence of different Pt D-NPs and $NaBH_4$: a) PtCat-1 (60.6 µg Pt); b) PtCat-2 (89 µg Pt); c) PtCat-3 (71.8 µg Pt); D) PtCat-4 (75 µg Pt). 123
Figure 4.29: a) Catalytic activity of Pt D-NPs represented as the ratio of the produced pAP mmol per milligram of added Pt. b) Turnover frequency (TOF; min^{-1}) of Pt D-NPs.....124
Figure 4.30: Thermostability at different T. b) Thermostability of the PtCat-4 in 50 % DMSO. 125
Figure 4.31: pNP concentration versus time using PtCat-3 as catalyst. Time value shown is the required to complete the reduction of substrate. 126
Figure 4.32: (a) Catechol oxidase activity assay of PtCat-4 catalyst and mushroom tyrosinase under 100 mM Na_3PO_4 at pH 8 to 6 or (b) NaOAc at pH 5 to 4 buffer and 1 mM of L-DOPA.....128
Figure 4.33: Catechol oxidase activity assay of the PtCat-4 catalyst and mushroom tyrosinase under 100 mM Na_3PO_4 at pH 7 and concentrations of L-DOPA from 5 to 0.25 mM. Pt amount was 0.02872 mg/mL and tyrosinase was 0.00246 mg/mL 129
Figure 5.1 Normalised extinction spectra (A), representative TEM images (B), histograms and graphic representation of obtained AuNRs (C-E).....139
Figure 5.2 Normalised extinction spectra spectra (A), representative TEM images (B), histograms and graphic representation of AuNRs sample RB obtained (C-E).....140
Figure 5.3: Normalised extinction spectra spectra (A), representative TEM images (B, C and D), histograms and graphic representation of AuNRs_RA@Si_{mes} (E).....141
Figure 5.4: Normalised extinction spectra spectra (A) and (B), and graphic representation of the ζ-potential obtained for AuNRs@Si_{mes} purified with water (red), ammonium nitrate (green) and successive MeOH whased (blue) (C-E). 142
Figure 5.5: FT-IR spectra (a-d) of CTAB (black line), AuNRs@Si_{mes} only purified with water (blue line) and AuNRs@Si_{mes} purified with MeOH and water (red line). The table show the different peaks detected (e). 143
Figure 5.6: Normalised extinction spectra (A), representative TEM images (B, C and D), histograms and graphic representation of AuNRs_RB@Si_{mes} (E). 144
Figure 5.7: Normalised extinction spectra (A and B), with the representation of the initial spectra of the AuNRs (black), the two different molecules (red) and the final spectra of the AuNRs@Si_{mes}-Drug (Blue) 146
Figure 5.8: Normalised extinction spectra of AuNRs_RA@Si_{mes}-DOX after resuspension (a), and representative SEM images (b, c and e).....147
Figure 5.9: Normalised extinction spectra of AuNRs_RB@Si_{mes}-MB after resuspension (a), and representative SEM images (b and c) 147
Figure 5.10: Effect of various concentrations of AuNRs_RA@Si_{mes} without doxorubicin for 72 h on viability of MCF-7 cells as measured by Presto Blue assay.....148

Figure 5.11: Effect of various concentration of AuNRs_RA@Si_{mes}/DOX, in the presence and absence of the laser treatment (LT). Control states for cells without nanoparticles. 149
Figure 5.12: Inactivation of *S. aureus* (left) and *E. coli* (right) using different concentrations of ROD_MB after exposure to red laser. Different letters within the same curve indicate statistically significant differences among Log10 CFU/mL ($p < 0.05$).....152

List of Tables

Table 3-1: Experimental reaction conditions ([Reagent] in n/L and % H_2O in V/V; P= Presence and A= absence).....69
Table 4-1: Oxidation of L-DOPA catalysed by the different PVP/Pt nanodendrimers.....127
Table 5-1: Encapsulation efficiency obtained for AuNRs_RA@Simes and AuNRs_RB@Simes with the different drugs explored.....145
Table 5-2 Antibacterial activity of samples against *E. coli* and *S. aureus*. Different letters within the same column indicate statistically significant differences among samples ($p < 0.05$).....151

List of symbols

α Polarizability

γ Surface Free Energy

ΔG Gibbs' Free Energy

$\mathbf{\Delta G_V}$ Gibb's Free Energy of the Bulk Crystal

ε Metal-Dielectric Function

$\mathbf{\varepsilon_m}$ Dielectric Constant of the Medium

ζ Z-Potential

λ Light Wavelenght

ρ Density

$\mathbf{\sigma_{Ext}}$ Extinction Cross-Section

List of Abbreviations and Acronyms

1D One-Dimensional

$\mathbf{^1O_2}$ Singlet Oxygen

2D Two-Dimensional

AA Ascorbic Acid

AgNPs Silver Nanoparticles

AgNPs@citrate Silver Nanoparticles Capped Citrate

AgNPs@L Silver Nanoparticle Capped Ligan L

AuNPs Gold Nanoparticles

AuNPs@citrate Gold Nanoparticle Capped Citrate

AuNPs@L Gold Nanoparticles Capped Ligand L

AuNPs@Si Gold Nanoparticles Capped Silica

AuNRs Gold Nanorods

AuNRs@CTAB Gold Nanorods Capped CTAB

AuNRs@Si$_{mes}$ Gold Nanorods Capped Mesoporous Silica

AuNRs@Si$_{mes}$-Drugs Gold Nanorods Capped Mesoporous Silica and Drugs

AuNRs_RA@Si$_{mes}$ Reaction A of Gold Nanorods Capped with Mesoporous Silica

AuNRs_RB@Si$_{mes}$ Reaction B of Gold Nanorods Capped with Mesoporous Silica

BCE Before Common Era

C Concentration of the Solute

C(r) Solubility Concentration

C_0 Equilibrium Concentration

C^0 Solubility of an Atom

CFU Colony Forming Unit

C_{min} Minimum Supersaturation Level

CNT Classical Nucleation Theory

CTAB Hexadecyltrimethylammonium bromide

CTAC Cetyltrimethylammonium chloride

DDA Discrete Dipole Approximation

DLS Dynamic Light Scattering

DLVO Derjaguin, Landau, Verwey, Overbeek

DMEM/F-12 Dulbecco's Modified Eagle Medium/Nutrient Mixture F-12

DNA Deoxyribonucleic Acid

DOI Digital Object Identifier

DOX Doxorubicin

dTGA Differential Thermogravimetry Analysis

E Electric Field

E. coli Escherichia Coli

EA Elemental Analysis

EDL Electric Double Layer

EDS Energy Dispersive X-ray Spectrometry

EDTA Ethylenediaminetetracetate

EELS Electron Energy Loss Spectroscopy

ESI Electrospray Ionization

eV Electronvolt

FCC Face Centered Cubic

FDTD Finite Difference Time Domain

FEM Finite Element Method

Fig Figure

FT/IR Fourier Transform Infrared Spectroscopy

FT-ICR Fourier Transform Ion Cyclotron Resonance

HAADF High-Angle Annular Dark Field

HRTEM High Resolution Transmission Electron Microscopy

ICP Inductively Couple Plasma

IF Impact Factor

iIm[ε] Imaginary Part

IUPAC International Union of Pure and Applied Chemistry

K_B Boltzmann Constant

KHz Kilohertz

kV Kilovolts

LOD Limit of Detection

LPS Lypopolysaccharides

LSPR Localised Surface Plasmon Resonance

$LSPR_{long}$ Longitudinal Localised Surface Plasmon Resonance

$LSPR_{trans}$ Transversal Localised Surface Plamon Resonance

MALDI Matrix-Assisted Laser Desorption/Ionization

MB Methylene Blue

MC Metal Chalcogenide

MCF7 Michigan Cancer Foundation-7

MHz Megahertz

mM Milimolar

mmol Milimol

MNPs Noble Metal Nanoparticles

MS Mass Spectrometry

MTES Methyltriethoxysilane

MΩ Milliohm

N Rate of Nucleation

$\mathbf{N_A}$ Avogadro's Constant

NCW Near Critical Water

NIR Near Infra Red

nm Nanometer

NMR Nuclear Magnetic Resonance

NP Nanoparticle

NPs Nanoparticles

pAP p-aminophenol

Pj, PA, PB, PC Termed Depolarization Factors

PDI Polydispersity Index

pNP p-nitrophenol

PSPP Propagating Surface Plasmon Polariton

PSS Polystyrenesulphonate

Pt D-NPs Platinum Dendritic Nanoparticles

Pt NPs Platinum Nanoparticles

PTT Photothermal Therapy

PVP Polyvinylpyrrolidone

R Ideal Gas Constant

r Radius

RA Rod A

RB Rod B

$\mathbf{r_{crit}}$ Critical Radius

Re[ε] Real Part

RHE Reversible Hydrogen Electrode

RI Refractive Index

ROS Reactive Oxygen Species

RPM Revolutions per Minute

RT Room Temperature

S Supersaturation

S. Aureus Staphylococcus Aureus

SC Sodium Citrate

SCW Super Critical Water

SEM Scanning Electron Microscopy

SERS Surface Enhancement Raman Spectroscopy

SN Supernatant

SPR Surface Plasmon Resonance

STEM Scanning Transmission Electron Microscopy

t Time

T Temperature

TEM Transmission Electron Microscopy

TEOS Tetraethylorthosilicate

Tg Glass Transition Temperature

TGA Thermogravimetric analysis

THF Tetrahydrofuran

TOF Time-Of-Flight

TOF Turnover Frequency

TON Turnover Number

TSA Tryptic Soy Agar

U Activity Unit

US Ultrasounds

UV Ultraviolet

V Molar Volume of the Species

VdW Van der Waals

Vis Visible

$\mathbf{V_m}$ Molar Volume of the Particle

$\mathbf{V_{NP}}$ Volume of the Nanoparticles

WCR Wet Chemical Reduction

XPS X-ray Photoelectron Spectroscopy

XRD X-ray Diffraction

1 Chapter 1

Introduction

1.1 Material Chemistry

The International Union of Pure and Applied Chemistry (IUPAC) defines material chemistry as its application to the design, synthesis, characterisation, processing, understanding and utilisation of materials, particularly those with useful, or potentially useful, physical properties[1]. This definition perfectly fit the works related to nanomaterials, which are particles of any shape with dimensions in the 1 and 100 nm range. Exist several examples using nanomaterials in the history, and probably one of the most famous is the Lycurgus cup (**Figure** 1.1), a 4th-century Roman glass cage cup containing gold and silver nanoparticles in colloidal form, and showing a different colour depending on whether light is passing through it; red when lit from behind and green when lit from in front. Also, the use of different types of nanomaterials in the stained glass of the St Chapelle, in Paris (France) gives to the cathedral and stunning aspect.

Figure 1.1: Lycurgus cup in the British museum.

However, it was not until 1857 when Michael Faraday described, in the Bakerian Lecture to the Royal Society of London, the interaction of the light with metal particles that are "very minute in their dimensions"[2]. This lecture is considered the birth of modern colloid chemistry. Since then, several scientists have contributed to the study and development of the nanoscience and nanotechnology. Studies like the ones of Thomas Graham[3] (1861), John Tyndall[4] (1869), Wilhelm Ostwald[5] (1896) , Gustav Mie[6] (1908), Richard Gans[7] (1912), Knoll and Ruska[8] (1932), John Turkevich[9] (1951) or Richard

Feynman[10] (1959), just to cite few of them, helped to the understanding, developing and growth of the so-called nanotechnology.

The nanotechnology field is an increasing and essential area of research as can be noted for the number of scientific communications published in the last years, with more than 100.000 documents in total.

1.2 Classifications of nanoparticles

There are several ways to classify the nanomaterials. We can do the classification taking in consideration different aspects like the composition, the synthetical route, or their dimensions, among others. Here is presented a classification based on their composition that can cover a vast range of nanoparticles.

In this way, we can have organic based, carbon-based and inorganic-based nanoparticles, as well as composites.

1.2.1 Organic based nanoparticles

Polymer nanoparticles, dendrimers or liposomes are some of the examples that can be included in the organic-based materials.

1.2.1.1 Dendrimers

Dendrimers are highly-branched biomolecules with nanometre dimension. They present a globular structure with three different parts: i) the core, ii) the interior or branches and iii) the terminal groups. (**Figure** 1.2). They are widely used due to their exciting properties. It can host molecules or metal ions in the internal cavities and acting as carriers, while the external surface may be tailored with different functional groups. In this sense, the applications that could have varied from drug delivery, gene delivery or magnetic resonance imaging among others[11].

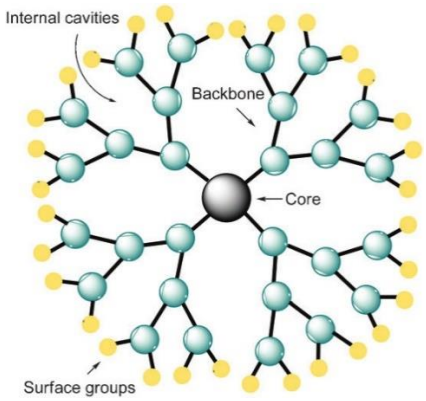

Figure 1.2: Illustration of a dendrimer structure. Reprinted from reference 11.

1.2.1.2 Liposomes

Amphiphilic phospholipids that are able to self-assemble into a spherical vesicle in which at least one lipid bilayer exist, are called liposomes. (**Figure** 1.3) In a usual conformation, the polar end is facing the outside, and the non-polar ends facing the core, forming the bilayers. They are useful in the delivery of hydrophobic drugs, and the surface can be easily functionalised[12].

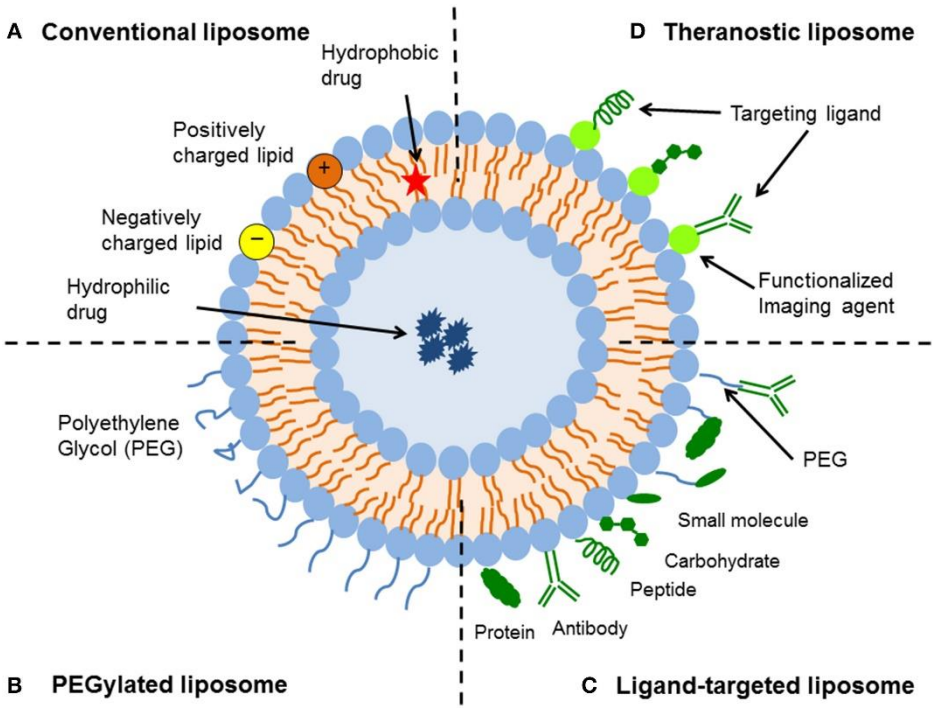

Figure 1.3: Representation of liposomes and functionalisation capabilities. Reprinted from reference 12.

1.2.1.3 Polymeric nanoparticles

Polymers are macromolecules organised in a chain like structure that presents many repeating units in their structure. It is possible to obtain polymeric nanoparticles with different types of polymers, natural or synthetic, giving to the system different properties. Nanocapsules, nanospheres or micelles can be formulated to specific applications. One of the most extended and important applications lies in the poorly soluble compounds encapsulation, used in a new drug formulation for biomedical delivery applications[13, 14].(**Figure** 1.4)

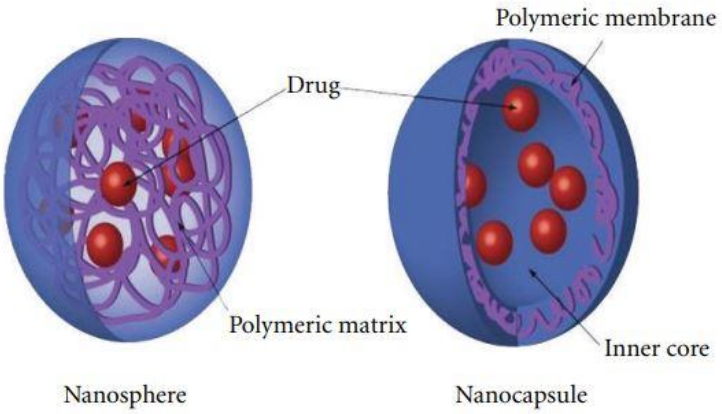

Figure 1.4: Representation of two polymeric nanoparticles, nanosphere and nanocapsule. Reprinted from reference 13.

1.2.1.4 Carbon based materials

Nanoparticles that are composed mostly of carbon can be included in this definition, as the fullerenes or carbon nanotubes. (**Figure** 1.5) Carbon-based nanomaterials present unprecedented physical and chemical properties. Their excellent resistance, high strength, stability and exceptional thermo-electrical conduction have allowed their implementation in a wide range of applications, from nanomedicine, to energy storage or biology[15,16].

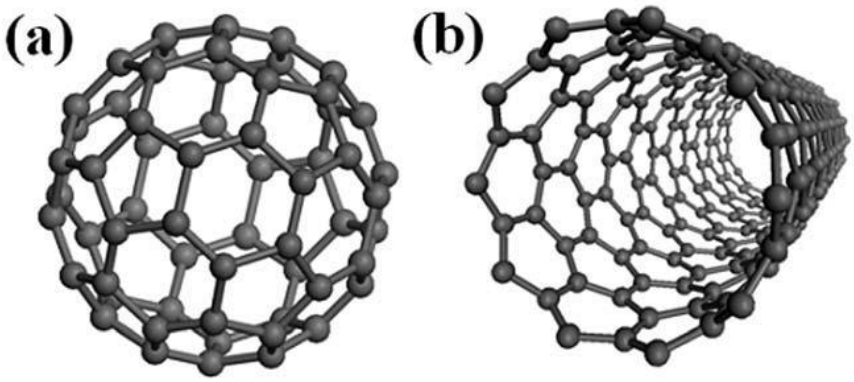

Figure 1.5: Representation of a) fullerene and b) carbon nanotube. Adapted from reference 15.

1.2.2 Inorganic based nanoparticles

We can find several types of inorganic-based nanoparticles, like the metal-based, silica nanoparticles or quantum dots.

1.2.2.1 Metal based

There exists a huge amount of work related to this type of nanoparticles. Gold, silver and platinum are ones of the most studied nowadays due to the properties that present in their nanometric form[17]. (**Figure** 1.6)

Metal oxides are also important, presenting useful properties, like the superparamagnetic iron oxide or the titanium dioxide capable of reflecting all the light in the visible region[18].

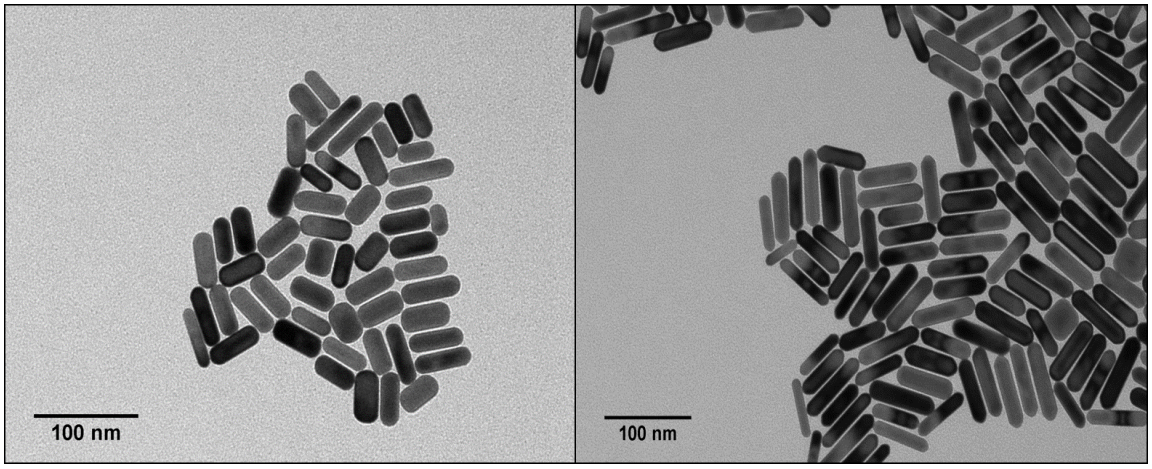

Figure 1.6: Microscopy images of Gold Nanorods with different sizes.

1.2.2.2 Silica nanomaterials

In general terms, the silica nanoparticles can be subclassified as amorphous or mesostructured silica, taking into account the different structural arrangements of the SiO_2 polymers that compose it. The first ones are characterised by the presence of mesostructured porous (2-50 nm pore size) (**Figure** 1.7), giving the ability to encapsulate different types of molecules. This structure is obtained using amphiphilic surfactants acting as templates, directing the growth and condensation of the precursors. The second ones do not present mesostructured porous; they are solid colloids with an empty or not core. Both cases offer an easy surface functionalization via siloxane chemistry, to conveniently create the desired nanomaterials[19,20].

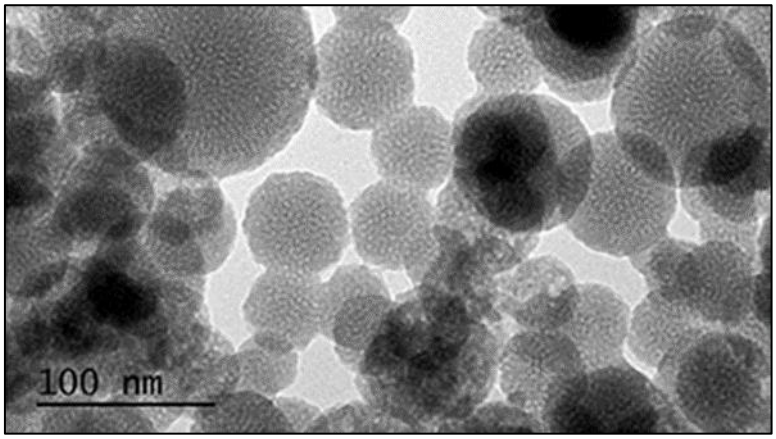

Figure 1.7: Microscopy image of Silica Mesoporous Nanoparticles. Reprinted from reference 20.

1.2.2.3 Quantum dots

Nanocrystals that are made mostly of semiconductor materials and that exhibit quantum mechanical effects are often called quantum dots. (**Figure** 1.8) The properties that present are a consequence of the composition and size. Several examples of quantum dots, like GaAs, PbS, CdSe, CdTe, ZnO or Silicon quantum dots exist. The applications vary from optical uses to photodetectors or photovoltaic, among others[21].

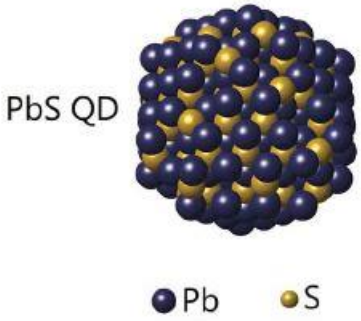

Figure 1.8: Representation of a colloidal quantum dot made of Pb and S. Adapted from reference 21.

1.2.3 Composites

Through the combination of two or more components in the nanometer scale arise the composites or nanocomposites. (**Figure** 1.9) Such combinations result in new properties that differ from the separate components that compose it. Core/shell materials are one of the most important composites, giving to the new material a surface with different functionalities, like protective biocompatibility, or allowing the dissolution in organic/non-organic solvents[22].

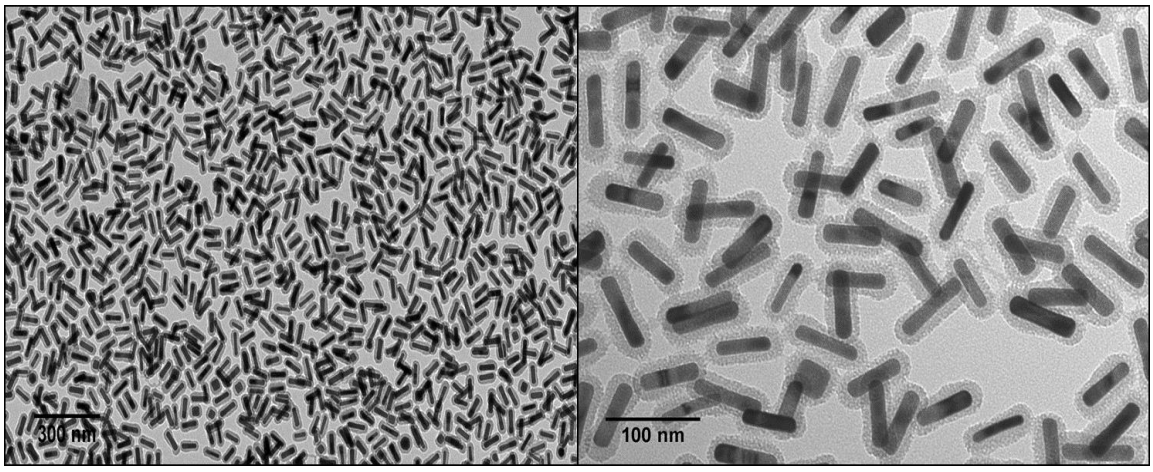

Figure 1.9: Microscopy images of Gold Nanorods@Mesoporous Silica nanocomposites.

1.3 Metals in colloidal chemistry

Metals have been used since a long time ago in human history. During the metal age, 3rd. 2nd and 1st millennia before common era (BCE), the bronze (an alloy composed mainly of copper) or the iron was started to be used in materials for practical objects, changing the population's life completely. In this sense, the use of metals in the nanoscale, due to the different properties that exhibit in comparison with the bulk material, can also lead to essential changes.

Regarding the inorganic nanomaterials, exists a vast variety of examples using different metals, however because the main body of this PhD thesis was based in three of them, we will center the introduction in Platinum (Pt), Silver (Ag) and Gold (Au).

1.3.1 Platinum

The platinum was first discovered in South America in 1735 by the Spanish navy officer and astronomer Antonio de Ulloa. It was named as platinum due to the visual similitude with the silver ("plata" in Spanish)[23].

Pt has an atomic number of **78** and an electronic configuration of [Xe] $4f^{14}$ $5d^{9}$ $6s^{1}$.

The dominant oxidation states for Platinum are Pt(II) and Pt(IV). Pt(II) forms almost exclusively low-spin, square planar complexes, while Pt(IV) forms a wide range of kinetically and thermodynamically inert octahedral complexes.

Bulk platinum has several applications, as catalysers for vehicles[24] , electrical applications[25] or in petroleum production[26]. Also, it is used in medical applications[27], e.g. as the cis-platinum, used worldwide for the cancer treatment.

We can find in the literature several examples of Platinum nanoparticles (Pt NPs). Different shapes can be obtained, and we can see that is possible do Pt NPs in a spherical[28], cubic[29], tetrahedral[29], octahedral[30], or dendrimer type[31], among others shapes. The most extended use to Pt NPs is in catalysis. Electrocatalytic applications, as well as hydrogenations, or electro-oxidation, are reported applications. Sensing is also a use of Pt NPs, and the use in biomedicine is related[32].

1.3.2 Silver

Silver has one of the most ancient names and has an uncertain origin. Berzelius accepted the Latin name Argentum and used the symbol Ag consequently. The name that is used in Galician, Portuguese or Spanish ("prata"/"plata") probably is a derivation from the Greek name "platys" (wide and plane). The

name in English ("silver") has an origin in the ancient German and Slavic languages ("silbar" in ancient German or "sirebro" in old Slavic)[23].

Silver (Ag) has an atomic number of **47** and an electron configuration of [Kr] $4d^{10}$ $5s^{1}$.

The only stable oxidation state of Silver is Ag(I). Their salts (except for AgF, $AgNO_3$ and $AgClO_4$) are sparingly soluble in water. Linear and tetrahedral complexes are common for Ag(I).

Silver is the best reflector of visible light, and was used in the fabrication of mirrors. The use in photography also was extended. Batteries, electrical contacts, or dental alloys are other uses of the silver.

The synthesis and applications of silver nanoparticles is a field in constant growth. The exciting properties of the silver in the nanometric range gives to these materials a vast range of applications. Different shapes can be obtained, such as spheres, platelets, cubes, or rods[33].

Silver nanoparticles have been used extensively for sensing, being used for detecting toxic ions like Hg(II), Pb(II) or As(V). Also, detection of Cu(II), Ni(II), Zn(II) or Co(III) is related[34,35]. They are also used as small molecule detector (e.g. cysteine or dopamine)[36]. The use of silver nanoparticles for Surface Enhancement Raman Spectroscopy (SERS) is an active field with brilliant results[37]. The studies of the antimicrobial property of the silver nanoparticles are also related in the literature, with a significant number of works reporting it[33].

1.3.3 Gold

The Latin name, "aurum", probably comes from the ancient word "ausom", which means yellow. In Galician, Portuguese or Spanish, "ouro"/"oro", the name comes from the Latin "aurum". In English, "gold", probably is a derivation from the Anglo-Saxon word "geolo", that can have the origin in the Sanskrit word "jual" (that shines)[23].

Gold (Au) has an atomic number of **79** and an electron configuration of [Xe] $4f^{14}$ $5d^{10}$ $6s^{1}$.

For gold, Au(I) and Au(III) are the most usual oxidation states, but Au(III) is the dominant due to be the most stable. Au(I) disproportionate in water to yield Au(III) and Au(0). For Au(III), square planar coordination is the predominant, while for Au(I) complexes linear coordination is usual.

Jewellery is one of the primary uses of gold. Is also used in computer and electric materials due to the excellent conductivity or in medicine to treat rheumatoid arthritis.

The synthesis and applications of gold nanoparticles is a relevant area of research in the nanomaterials field. The applications of gold nanoparticles are broad, and the properties are different depending on the size and shape, so that we can find different synthetic methodologies for spheres, rods, triangles, stars, nanocubes or nanocages, among others[38].

The applications vary from sensing, plasmonics, photodynamic and photothermal therapy or drug delivery, citing just a few of them[39].

1.4 General approaches to nanoparticles synthesis

Several approaches can be followed for the synthesis of nanomaterials. One of the most common synthetic routes to classifies them is in the "top-down" and "bottom-up" methodologies[40,41,42].

1.4.1 "Top-down"

Through this strategy, the bulk material is reduced in size to produce nanoparticles. Mechanical milling, where the macroscopic material is converted into smaller particles by attrition; or laser ablation, where high-energy laser light is used to remove and vaporize the material from a solid surface, are some of the most applied techniques.

1.4.2 "Bottom-up"

In this approach, the nanoparticles are produced assembling atoms or molecules in a liquid or gas phase. In Flame Synthesis the starting material is evaporated, mixed with fuel and an oxidizing agent, and injected in a flame, forming the nanoparticles within the flame.

Reducing metal precursors in a liquid phase to form nanoparticles, often called wet colloidal synthesis, is also one of the most commons methodologies. It is completed upon mixed solutions of different ions or molecules, under controlled conditions to form the final nanomaterials.

1.5 Nucleation, growth and stability of the nanoparticles

In general, the synthesis of metallic nanoparticles can be divided into two main stages, namely nucleation (related to the formation of a new phase) and growth (which involves the growth of the nuclei in the final NPs). Besides, a stabilisation mechanism must be present; otherwise, the growing NPs inevitably result in the formation of bulk material through aggregation.

1.5.1 Nucleation

Paying closer attention to the colloidal synthesis, we can distinguish between heterogeneous and homogenous nucleation[43,44,45].

Heterogeneous nucleation occurs at nucleation sites contacting the liquid or vapour. It has preferential sites as phase boundaries or impurities. This type of nucleation sees as the driving force in the seed-mediated synthesis.

Homogenous nucleation occurs spontaneously and randomly, but requires some factors, as a supersaturation state, that we will discuss below.

In base to the classical nucleation theory (CNT), and considering spherical particles as the final entity, the nucleation will take place when it lowers the Gibbs' free energy (**Equation** 1.1):

$$\Delta G = \frac{4}{3}\pi r^3 \Delta G_V + 4\pi r^2 \gamma \quad (1.1)$$

Here it is necessary to consider two critical parameters. First, Gibb's free energy of the bulk crystal, ΔG_V (which is expressed as per unit volume of newly formed particles), and secondly the surface energy, γ (expressed as per unit area of the material), with r as the nucleus radius. Both energies act in opposite directions. The ΔG_V produces an energy reduction due to the formation of the new volume, while γ result in an increase, as a consequence of the new surface created. Gibbs free energy will be the sum of these two parameters.

ΔG_V can be expressed as follow (**Equation** 1.2):

$$\Delta G_V = \frac{-k_B T \ln(S)}{V} \quad (1.2)$$

The crystal-free energy depends upon the Boltzmann constant (K_B), the temperature (T), the molar volume of the species (V) and the supersaturation of the solution (S). The supersaturation depends on the concentration, and it can be defined as (**Equation** 1.3):

$$S = \frac{(C - C_0)}{C_0} \quad (1.3)$$

Where C is the concentration of the solute and C_0 the equilibrium concentration or solubility.

Therefore, the supersaturation of the solution is a crucial factor in the nucleation process. Without supersaturation (i.e S = 0), the crystal free energy will be zero and the nucleation will not occur spontaneously. When $C > C_0$, ΔG_V is negative and nucleation occurs spontaneously.

Plotted ΔG vs r (nuclei radio), the graph reaches a maximum that corresponds with the critical radius (r_{crit}). (**Figure** 1.10) At the critical size, r = r_{crit}, dΔG/dr = 0, and the critical energy ΔG_{crit} and r_{crit} can be defined as the minimum size in which the nanoparticles could be formed (**Equations** 1.4 and 1.5). Smallest radius will cause the redissolution of the metal in the solution.

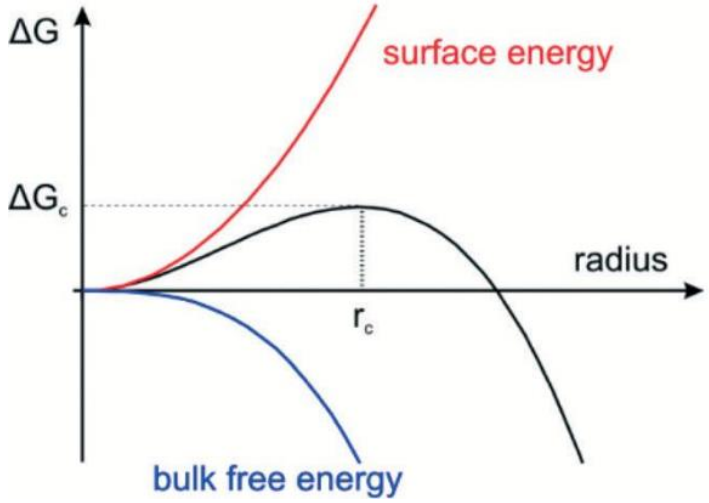

Figure 1.10: The dependence of the cluster free energy, ΔG, on the cluster radius, r_c according to the CNT. Adapted from reference 43.

$$\Delta G_{crit} = \frac{16\pi\gamma^3}{3(\Delta G_V)^2} = \frac{4\pi\gamma {r_{cri}}^2}{3} \quad (1.4)$$

$$r_{crit} = \frac{-2\gamma}{\Delta G_V} = \frac{2\gamma V}{k_B\, T \ln(S)} \quad (1.5)$$

In the base of these considerations, the nucleation ratio can be increased through:

A) Increasing the supersaturation level, leading to a decrease in the energy barrier to nucleation.

B) Increasing the temperature will increase the average atomic energy, favouring the critical energy overcoming.

C) With a variation in the surface free energy, that can be caused using different surfactants, the nucleation can be increased.

To describe easily the previously mentioned parameters, it is necessary to involve an Arrhenius type equation that relates the nucleation ratio (N) during the adjusted time (t) with a pre-exponential factor (A) (**Equations** 1.6 and 1.7):

$$\frac{dN}{dt} = A \exp\left(\frac{\Delta G_{crit}}{k_B T}\right) \quad (1.6)$$

$$\frac{dN}{dT} = A \exp \frac{16\pi\gamma^3 V^2}{3k_B^3 T^3 (\ln S)^2} \quad (1.7)$$

Therefore as remarked in the previous equations, there are only three experimental values that can be changed: the supersaturation (S), the temperature (T) and the surface free energy (γ).

When the concentration of monomers (i.e. atoms) falls below the critical supersaturation level, the nucleation ends. Therefore, the nucleation can be understood according to the atomic concentration with time.

1.5.2 Growth

Throughout the last decades, different theories have arisen to explain the phenomena that involve the growth of nuclei in final NPs. All of them can be subclassified into two large families. Growth mediated by atoms or growth mediated by nanoparticles. In the first family, atoms are used as building blocks through surface addition to influence growth. The second family comprises the formation of mesocrystalline nanoparticles in which the growth occur by initial nanoparticles addition rather than by atoms addition.

1.5.2.1 Atom-mediated growth

Within this family, it is possible to classify a multitude of theories that explain, in a consolidated way, the observed phenomenology for the great majority of NPs. The most relevant growth theories are described below:

1. **LaMer** mechanism, based on their research on aerosols and sulfur hydrosols[46], propose the separation between the nucleation and growth into three stages. The first stage is the formation of the metallic atoms. When they reach a certain level of saturation (C_{min}), the energy barrier for self-nucleation can be overcome, and nucleation starts. Afterwards, there is a drop in the concentration of metallic atoms below the minimum supersaturation level (C_{min}) and no more self-nucleation occurs, leading to the growth of the nanoparticles. (**Figure** 1.11) The Lamer process only describes the nucleation and growth, not answering in the evolution of the NPs, shapes or size distribution.

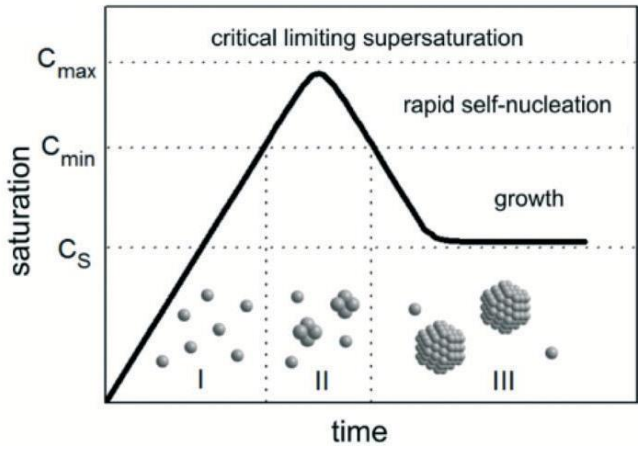

Figure 1.11: The principle of nanoparticle nucleation due to LaMer's mechanism of nucleation derived from CNT. Adapted from reference 43.

2. **Ostwald Ripening**. Taking into consideration that the solubility of nanoparticles is not independent of their size, according to the Gibbs-Thomson relation, which states that the nanoparticles become unstable when the size is decreased (**Equation** 1.8):

$$C(r) = C^0 \exp\left(\frac{2\gamma V_m}{rRT}\right) \quad (1.8)$$

Where C(r) is the solubility concentration of a particle with radius r, C^0 is the solubility of an atom taken from an infinite flat surface, γ the surface free energy, V_m is the molar volume of the particle, R is the ideal gas constant and T the temperature.

The Ostwald ripening theory proposes a mechanism of growing in which the nanoparticles of certain dimension go through a process of re-dissolution, leading to the growth of the big ones due to the new source of monomers. (**Figure** 1.12) It states that small particles are more soluble than big ones and tend to lose to re-precipitate into larger particles[47,48,49].

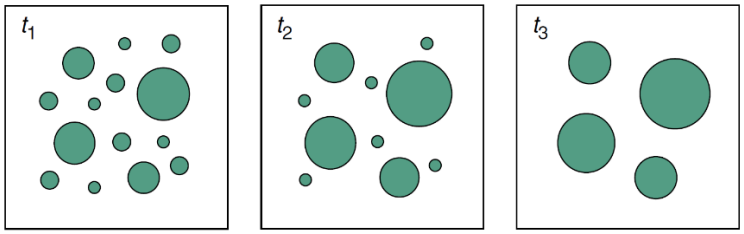

Figure 1.12: Schematic illustration of the Ostwald ripening with time (t1<t2<t3). Adapted from reference 49.

3. **Digestive ripening**, on the other side, can be considered as the opposite of Ostwald ripening. Small particles will grow at expenses of the biggest ones, which will re-dissolve and act as a source of

monomers to the smallest nanoparticles[50,51].(**Figure** 1.13) A more complex equation, derived from the Gibbs-Tomson relation, is necessary to explain the digestive ripening[52].

The overall process can be summarised in three steps: 1) The addition of a ligand (e.g. dodecanethiol) that will help to break the larger nanoparticles and narrowing the sizes, 2) the purification of the nanoparticle to obtain an isolate ligand-nanoparticle system and 3) the heating, usually in high boiling point solvents, with the presence of the ligand to obtain monodisperse nanoparticles.

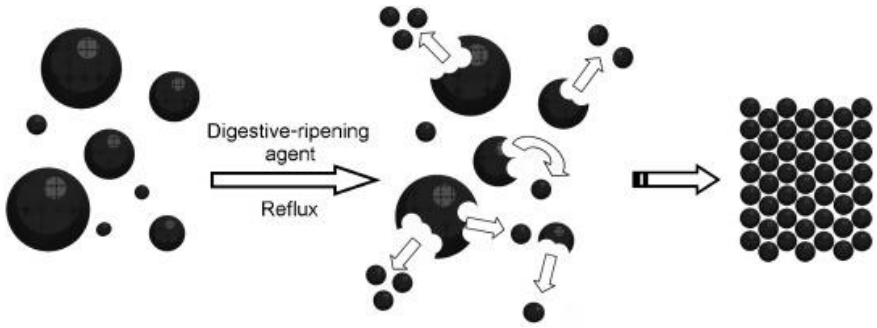

Figure 1.13: Representation of the digestive ripening process. Reprinted from reference 50.

4. The **Finke-Watzky** mechanism is a simultaneous process where the nucleation and growth happen at the same time, but still follow the condition of the critical size explained in the CNT. The nucleation occurs with a constant rate K_1, and the autocatalytic surface growth with a constant rate K_2[53,54,55].

$$A \overset{K1}{\rightarrow} B$$

$$A + B \overset{K2}{\rightarrow} 2B$$

1.5.2.2 Nanoparticle-mediated growth

Thanks to the development of modern electron microscopy techniques (among other technologies) in recent decades an increasing number of reports have emerged that inform the synthesis of metal nanoparticles for which it is difficult to explain their growth according to atom mediated theories. The final products obtained by these processes occur through the fusion of nanoparticles formed in the early stages of the reaction, usually evolve into mesocrystalline nanostructures. Attending to the nanoparticles attachment method, nanoparticle-mediated growth can be classified in:

1. **Coalescence.** During the formation of nanoparticles, they can present coalescence. Coalescence can be seen as the overall nanoparticle growth, where first occurs the aggregation of separate particles, followed by subsequent nanoparticle growth. For this process, there is no preference in the crystallographic planes[56,57].(**Figure** 1.14)

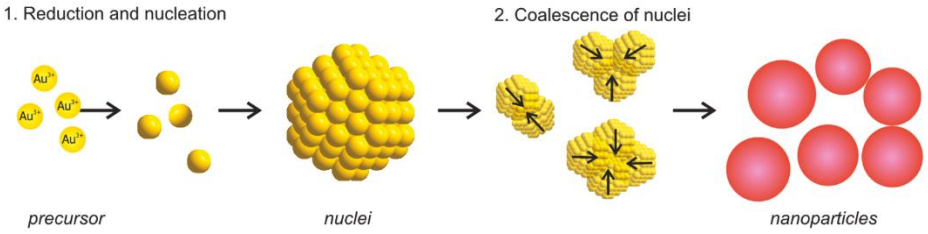

Figure 1.14: Representation of coalescence in the synthesis of gold nanoparticles. Adapted from reference 56.

2. In the **oriented attachment**, the growth involves a self-organization of adjacent particles, sharing a common crystallographic orientation, and following by joining this particles at a planar interface[58,59]. (**Figure** 1.15)

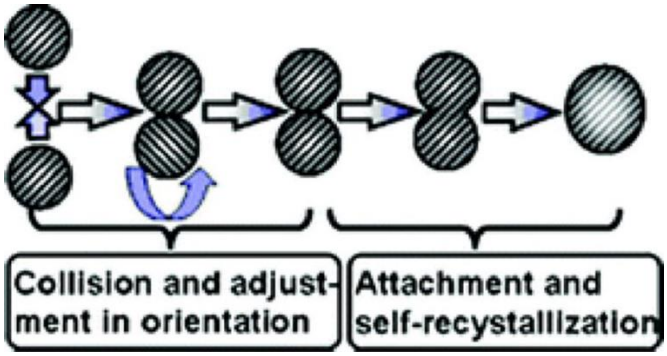

Figure 1.15: Representation of an oriented attached mechanism. Reprinted from reference 58

1.5.3 Stability

Once the nanoparticles forms, the colloidal stability in the dispersing medium plays an important role. Van der Waals (VdW), electrostatic or magnetic force can lead to nanoparticles agglomeration, aggregation or coalescence.

Van de Waals interactions[60] (**Figure** 1.16) govern nanoparticles aggregation at the most basic level. Permanent or induced dipoles within the nanoparticles can result in net attractive forces between them and posterior aggregation.

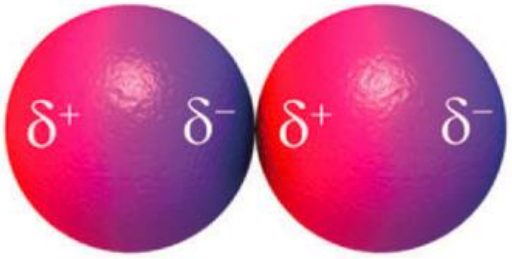

Figure 1.16: Representation of Van der Waals interactions that can lead to nanoparticle aggregation. Adapted from reference 60.

An electric double layer (EDL, **Figure** 1.17) formed by solvated ions or molecules can shield the surface charge, create repulsive interparticle forces and stabilise the system. We can distinguish two parts, the Stern layer, which consists of counter-ions adsorbed on the charged surface of the nanoparticle (NP), and the diffuse layer, an atmosphere of ions of opposite net charge surrounding the NP. The thickness of the EDL is called the Debye length.[60]

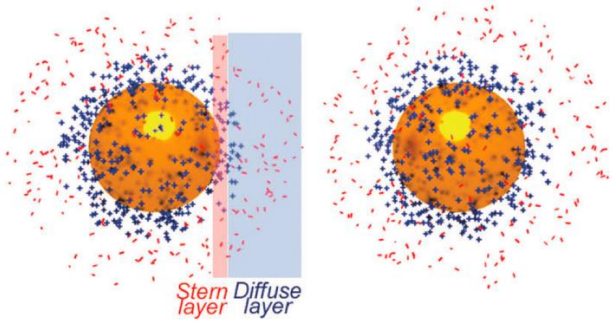

Figure 1.17: Representation of the EDL, composed by the Stern layer and the Diffuse layer. The total thickness of both is called the Debye length. Adapted from reference 60.

The DLVO theory (Derjaguin, Landau, Verwey and Overbeek, developers of the theory), for the colloidal stability, assumes that the total force between colloidal particles is composed for the van de Walls forces (attractive) and the EDL (repulsive). In **Figure** 1.18 we can see the combination of that forces, in which the maximum is the aggregation barrier and determine the colloidal stability.[44]

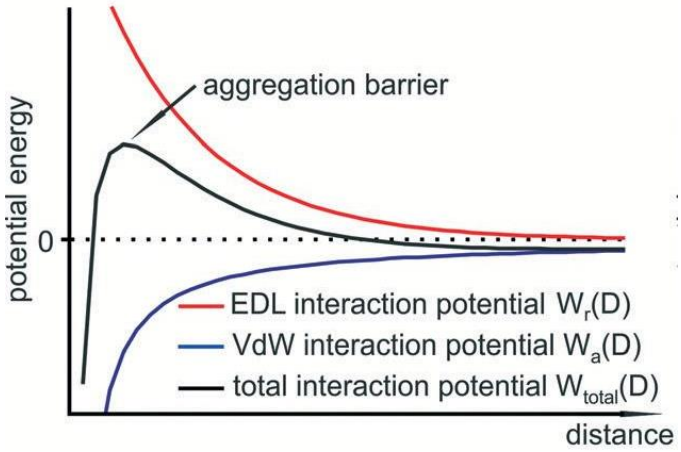

Figure 1.18: Representation of the Total Interaction Potential (TIP) from the DLVO theory. Adapted from reference 44.

On the other hand, the steric stabilisation can be carried out absorbing large molecules at the surface of the particles, which creates a physical barrier that prevents aggregation. (**Figure** 1.19) It can be used surfactants (e.g. hexadecyltrimethylammonium bromide, CTAB), polymers (e.g. Polyvinylpyrrolidone, PVP), proteins or other types of macromolecules. The stability is now determined by the solubility, average chain length, concentration or temperature, among others.[44,60]

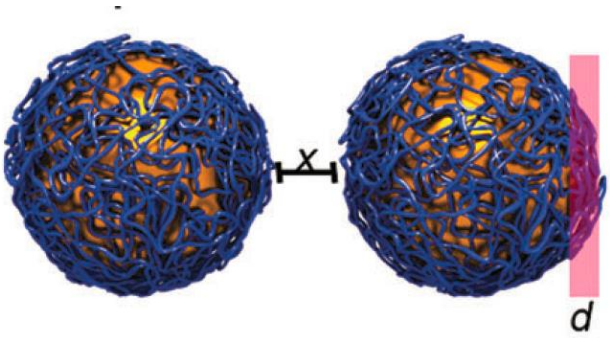

Figure 1.19: Representation of nanoparticles covered with a polymer avoiding particle interaction due to steric repulsion. Adapted from reference 60.

1.6 Surface Plasmon

The unique electronic properties of the nanomaterials arise from their interaction with an incident electromagnetic radiation[61,62,63,64,65,66].

Plasmons are the collective oscillations of free electrons in metals. In bulk materials, with an incident light, propagating surface plasmon polariton (PSPP) can occur under certain conditions. When the metals are in nanometres range, i.e. as a nanoparticle with a comparable size of a wavelength, and are illuminated with the appropriate wavelength (to produce resonance), the particle's free electrons participate in the collective oscillation, and it is called localised surface plasmon resonance (LSPR). LSPR in nanoparticles is strongly dependant on several factors, such as the metal type, size or shape of the nanoparticle, and also to the surrounding media. The existence of the LSPR makes that the nanoparticle behaviour changes drastically; for example, their optical properties will be greatly affected.

As a consequence of the formation of LSPR in metallic nanoparticles, the electromagnetic field near the surface of the nanoparticle is strongly increased and rapidly falls off with distance. Furthermore, noble metal NPs present an extinction cross section that can be much larger than their geometrical size. The optical extinction presents a maximum at the surface plasmon resonance frequency, and for gold and silver NPs is located at visible wavelengths.

The most convenient analytical treatment consist in the use of a homogenous and isotropic sphere, with radius a, using the quasi-static approximation, (where the particle is much smaller than the wavelength of light) located at the origin in a uniform, static electric field $E=E_0\hat{z}$, with ε_m as the dielectric constant of the medium and ε as the metal-dielectric function. (**Figure** 1.20 a) This electric field will create a dipole within the nanoparticles, where the charges are located in the surface. Only light with frequency in resonance with the oscillation can excite the local surface plasmon. (**Figure** 1.20 b)

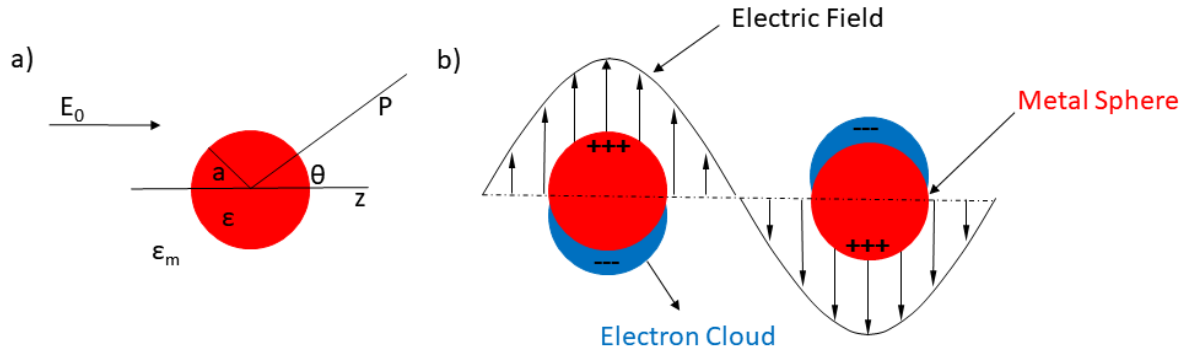

Figure 1.20: a) Representation of a homogeneous sphere set into an electrostatic field b) illustration of the surface plasmon resonance, with the collective oscillation of the conduction band electrons due to an incident light.

The metal polarizability (α) express the distortion of the electron cloud in the opposite direction to the electric field, and can be expressed as (**Equation** 1.9):

$$\alpha(\lambda) = 3\varepsilon_m(\lambda)V_{NP}\frac{\varepsilon\,(\lambda) - \varepsilon_m\,(\lambda)}{\varepsilon\,(\lambda) + 2\varepsilon_m\,(\lambda)} \quad (1.9)$$

Where ε (λ) is the dielectric function of the particle, ε_m (λ) dielectric constant of the surrounding media and V_{NP} is the volume of the nanoparticles.

With the analytical solutions of Maxwell's equations, Gustav Mie provided a solid description of the absorption and scattering produced in spherical metal particles. The section of a nanoparticle that absorb all the photons that reach its surface is defined as the absorption cross-section. Moreover, the section of a nanoparticle that scatters any photon that reaches its surface, is defined as the scattering cross-section. The sum of the absorption and scattering cross-section is defined as the extinction cross-section (σ_{Ext}), which represent the efficiency of the particle to remove photons from an incident beam. (**Figure** 1.21)

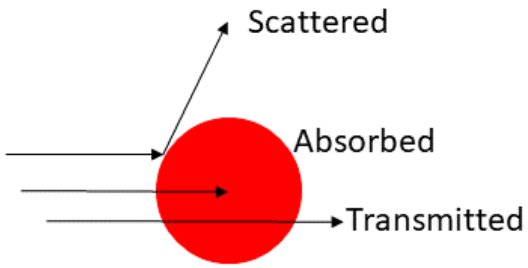

Figure 1.21: Representation of scatter, absorption and transmission process in a nanoparticle.

Considering a quasistatic regime (i.e. when the size of the nanoparticle is smaller than the further wavelength), the extinction cross-section in a spherical gold nanoparticle can be expressed as (**Equation** 1.10):

$$\sigma_{Ext} = \frac{18\pi[\varepsilon_m(\lambda)]^{3/2}}{\lambda}V_{NP}\frac{Im[\varepsilon(\lambda)]}{[Re[\varepsilon(\lambda)] + 2\varepsilon_m(\lambda)]^2 + Im[\varepsilon(\lambda)]^2} \quad (1.10)$$

Where λ is the light wavelength, V_{NP} the nanoparticles volume, ε the dielectric function of the particle and ε_m the dielectric constant of the medium.

It should be noted in Equation 1.10 that the LSPR extinction peak and metal polarizability are dependent on the dielectric function ε (λ), which correlates the response of a material to an electric field, as a function of the wavelength (λ). For this type of nanomaterials, the complex wavelength-dependent dielectric function can be expressed as (**Equation** 1.11):

$$\varepsilon(\lambda) = Re[\varepsilon(\lambda)] + iIm[\varepsilon(\lambda)] \quad (1.11)$$

Where the real part, Re[ε] is related with the resonance frequency of a plasmonic system, and the imaginary part iIm[ε] describe it losses (due to radiate damping, structural imperfections or intraband transitions, among other). (**Figure** 1.22)

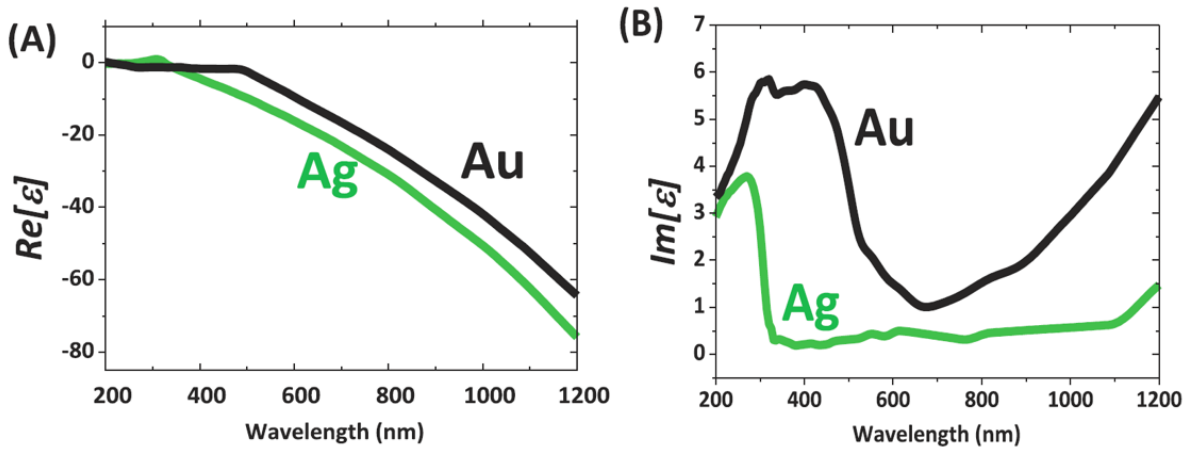

Figure 1.22: (A) Real and (B) Imaginary part for Au (black) and Ag (green). Adapted from reference 61.

The σ_{Ext} and α maximum will occur when met the Fröhlich condition (**Equation** 1.12), i.e. when the denominator is minimised, so the LSPR is excited at a frequency where:

$$Re[\varepsilon(\lambda)] = -2\varepsilon_m \quad (1.12)$$

For instance, for spherical 10 nm gold nanoparticles in water, with a $\varepsilon_m \approx 1.77$, and if we consider the Frölich condition, $Re[\varepsilon(\lambda)] = -2\varepsilon_m$, the expected wavelength will be about 520 nm (in consonance with experimental values), according to the real dielectric function of gold. For silver, the LSPR will present a blue shift when compared with gold.

The imaginary part also plays an important role in plasmon resonances, related to the resonance peak broadening. In **Figure** 1.22 B, we can see that the silver has lower losses than gold, resulting in a reduced plasmon intensity for gold nanoparticles. Despite this, gold is more used due to chemical stability and biocompatibility.

Platinum, on the other hand, present a small band in the ultraviolet (UV) region, ca. 215 nm, due to interband transitions which overlaps this region[67]. (**Figure** 1.23)

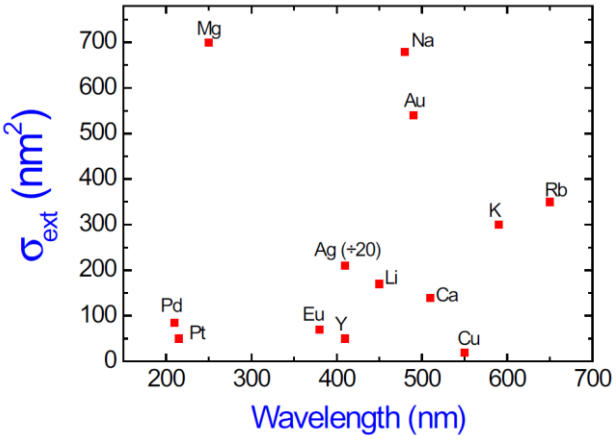

Figure 1.23: Resonant frequency and extinction cross section of various metallic nanoparticles with 10 nm size in air. For Ag, the extinction cross section was divided by 20. Reprinted from reference 63.

It is important to notice that the plasmonic properties of any material are defined by the dielectric function ε, and that σ_{Ext} scales with the particle volume. Due to the dependence of the dielectric function, refractive index (RI) of the surrounding media should play an essential role in the LSPR phenomenon.

Applying the Drude classical model of electronic transport in conductors, the relationship between the LSPR and the refractive index can be expressed as (**Equation** 1.13):

$$\lambda_{max} = \lambda_p \sqrt{2n_m^2 + 1} \quad (1.13)$$

Where λ_{max} is the LSPR peak wavelength, λ_p the wavelength corresponding to the plasmon frequency of the bulk metal, and n_m the metal refraction index. For visible and near infrared frequencies, and for small changes in the refractive index, the LSPR shift is nearly linear.

If we consider a nanomaterial with a non-spherical shape, in the quasi-static approximation, Richard Gans theory can be applied to calculate the LSPR, approximating the nanostructure to an ellipsoid. This is the case of gold nanorods. The extinction cross-section can be calculated (**Equation** 1.14):

$$\sigma_{Ext} = \frac{2\pi V_{NP} \varepsilon_m^{3/2}}{3\lambda} \sum_j \frac{\left(\frac{1}{P_j}\right)^2 Im[\varepsilon]}{\left(Re[\varepsilon] + \frac{1 - P_j}{P_j}\varepsilon_m\right)^2 + Im[\varepsilon]^2} \quad (1.14)$$

Pj represents de depolarization factor along the three Cartesian axes. For a prolate spheroid (an important type of ellipsoid, with volume $V=4\pi a^2 b/3$), Pj includes P_A, P_B and P_C, termed depolarization factors, where A>B=C.

With this theory, the LSPR spectra of gold nanorods have been described qualitatively applying the previous factors. Their LSPR were calculated, including the redshifts due to the increasing size of the nanoparticle. It can be seen comparing **Equations** 1.10 and 1.14. In **Equation** 1.10, the factor weighting ε_m is 2, while in **Equation** 1.14 is ((1-Pj)/Pj), which increase with the aspect ratio and can be greater than 2, resulting in a red-shift in the LSPR. Also, it will lead to an increased sensitivity of the surrounding medium ε_m.

Note that the extinction spectrum that arises from the previous **Equation** presents two peaks, one corresponding to the transverse plasmon mode, from the x and y contributions to the sum, and another due to the longitudinal plasmon mode from the z contribution. (**Figure** 1.24)

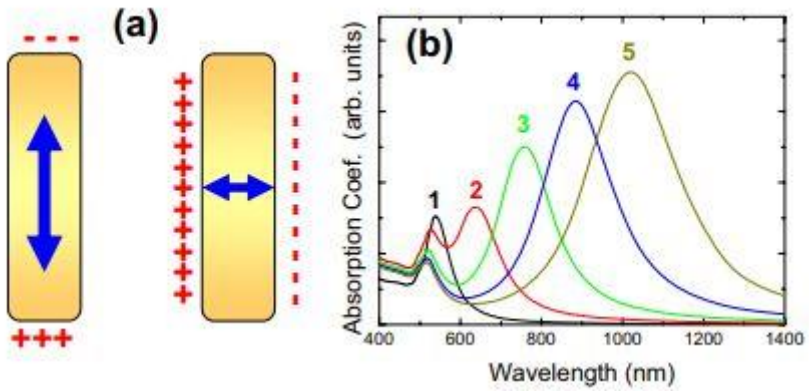

Figure 1.24: a) Representation of a gold nanorod with charge accumulation in the surface and b) absorption spectra of gold nanorods with different aspect ratio. Adapted from reference 63.

The particle shape plays an essential role in the extinction spectra. For other situations where the approximation to a sphere or ellipsoid is not possible, it is not feasible to obtain the LSPR analytically, and they should be studied numerically. Discrete Dipole Approximation (DDA), Finite Difference Time Domain (FDTD) or Finite Element Method (FEM), are some of the numerical methodologies developed to provide solutions for these more complicated situations.

1.7 General synthetic methodologies of gold and silver nanoparticles

Centring this introduction in the bottom-up methodologies due to be highly used at laboratory scales and the strategy employed in this thesis, we can differentiate two approaches for the obtaining of different types of nanomaterials: Direct (or *In Situ*) Synthesis and Seed-Mediated Synthesis.

1.7.1 Direct Synthesis

One-pot (also so-called direct synthesis) involves the production of metallic NPs only in one synthetic step, which requires the control of nucleation and growth simultaneously.

The two mains aspects in the one-pot strategy are the reduction of the metal precursor and the stabilisation of the newly formed nanoparticles. To achieve metal precursor reduction, usually, molecular agents with specific redox capabilities like sodium citrate (SC), sodium borohydride ($NaBH_4$), hydrazine (N_2H_4) or ascorbic acid (AA) are used. Also, metal reduction promoted by ultrasounds irradiation or temperature can be employed. The nanoparticles stabilisation can be done through molecular agents such as sodium citrate, sulphur ligands, polymers or surfactants.

Probably, one of the most used direct synthesis nowadays is the so-called Turkevich methodology for the obtaining of gold nanoparticles. In this process, the gold solution, usually tetrachloroauric(III) acid ($HAuCl_4$), is reduced and stabilised by trisodium citrate at 100 ºC in water. Using citrate as a reducing and stabilising agent is possible to get spherical gold nanoparticles with sizes around 20 nanometres. Despite being a synthesis that was first published in 1951, there are, still nowadays, several remarkable works going into explain the mechanism behind this process[68,69,70], as well as great efforts for improve the methodology[71,72,73].

Kumar *et al*.[68] proposed that the synthesis of gold nanoparticles with the Turkevich methodology can be seen as multiple steeps reaction, occurring in series and parallel, in which the initial step is the oxidation of the trisodium citrate to form acetonedicarboxylate and the reduction of the Au(III) to Au(I). (**Figure** 1.25)

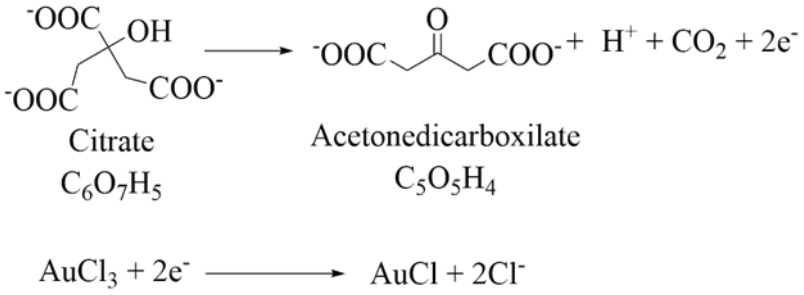

Figure 1.25: Scheme of the citrate oxidation.

The acetonedicarboxylate will form a coordination compound with the Au(I), facilitating the disproportionation of Au(I) into Au(0) and Au(III). This will lead to the nucleation and growth of Au (0) into gold nanoparticles. (**Figure** 1.26)

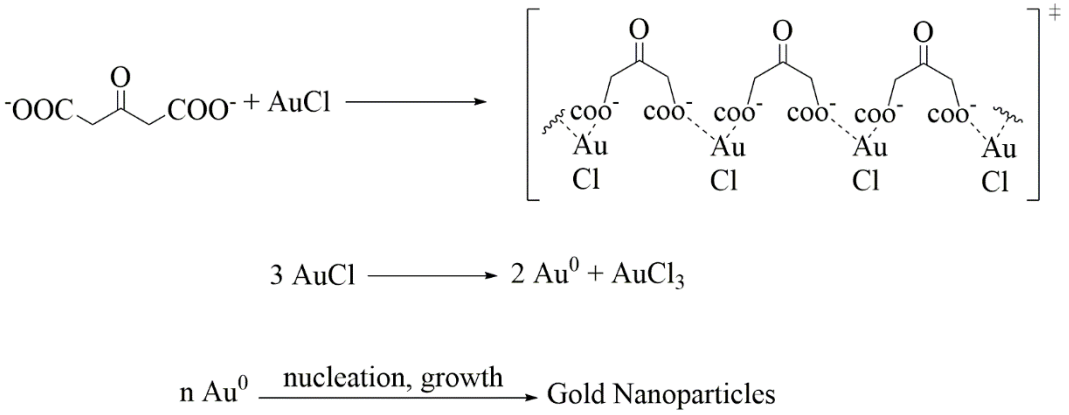

Figure 1.26: Scheme of the complex of dicarboxy acetone with the gold and formation of the nanoparticles.

Polte *et al*.[69] proposed a four step-process, where the first step is the partial reduction of gold precursor and formation of small clusters. They will form gold seed in the second step, which will attract the remaining ionic gold in solution, and lead to the reduction of the ionic metal and growth of the gold nanoparticle.

It is interesting to notice that a factor affecting the final outcome of the synthesis is the order of addition. In a standard synthesis, the sodium citrate is added to the pre-heated gold solution. Changing the order of addition (maintaining the final concentrations) can lead to smaller nanoparticles.[69,70]

It is also possible to obtain silver nanoparticles in the presence of citrate as a reductant and stabiliser, but this methodology leads to larger silver nanocrystal of various sizes and shapes. This result was attributed to the complexation of the first Ag nanoparticles with the citrate, making the reduction of the remaining Ag^+ slower, and leading to a growth methodology via Ostwald ripening.[74]. Taking this into consideration, a stronger reducing agents was used for the synthesis of more monodisperse silver nanoparticles.

Sodium Borohydride is a common reducing agent used in this type of synthesis. However, the reduction of metal ions with it is a complicated process. For metals with a positive redox potential the chemical **Equation** can be written as follow[75]:

$$M^{z+} + z\ BH_4^- + z\ 3\ H_2O \rightarrow M^0 + zB(OH)_3 + z\ 3.5\ H_2$$

Boric acid serves as Lewis acid giving place to the formation of tetrahydroxyborate anion:

$$B(OH)_3 + H_2O \leftrightarrow z\ B(OH)_4^- + z\ 3.5\ H_2 + z\ H^+$$

The overall reaction can be re-written as:

$$M^{z+} + z\ BH_4^- + z\ 4\ H_2O \rightarrow M^0 + zB(OH)_4^- + z\ 3.5\ H_2 + z\ H^+$$

But is also important take in consideration the hydrolysis of the borohydride anion in water:

$$BH_4^- + 4\ H_2O\ \rightarrow\ B(OH)_4^- + 4H_2$$

Polte *et al.*[76] proposed a mechanism for the growth of silver nanoparticles, in which the sodium borohydride plays an important role. They demonstrate that classical nucleation and growth process, like the LaMer model, is not applicable in this case. The growth of the nanoparticles is driven by two different coalescence processes. (**Figure** 1.27) The first one happens after the reduction of Ag^+ into Ag^0, which occurs in within less than 200 ms (faster than the growth process). The cluster coalesces and generate small nanoparticles. The next step is a metastable state in which the nanoparticles maintain the size. When most the BH_4^- is converted (due to the reduction and hydrolysis), a decrease in the colloidal stability is produced, and the second coalesce process begins, giving places to the final nanoparticles.

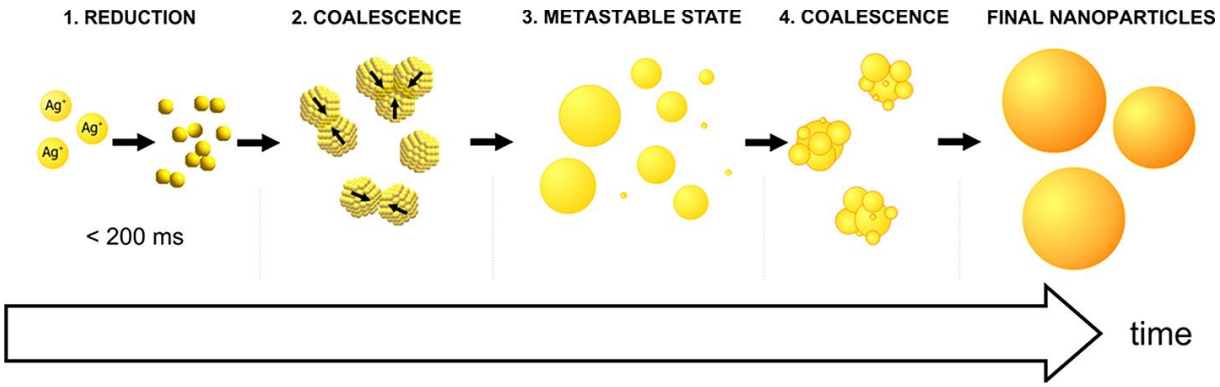

Figure 1.27: Schematic representation of the growth silver nanoparticles mechanism. Adapted from reference 76.

The addition of a steric stabilizing (like PVP) agent does not affect the growth mechanism, but has an impact in the size, reaction time, as well as, in the long-term stability.

In this sense, we followed a methodology[77] that contains sodium citrate as stabilizing agent and sodium borohydride as reductant. Taking as source of silver ion the silver nitrate ($AgNO_3$), the overall reaction can be described as:

$$NaBH_4(aq) + 8AgNO_3(aq) + 4\,H_2O\,(l) \rightarrow Na[B(OH)_4](aq) + 8\,Ag(s) + 8\,HNO_3(aq)$$

The citrate will not only help in the stabilisation of the newly formed nanoparticles, but is believed that act as a buffer, neutralizing the nitric acid formed and maintaining a less acid environment:

$$Na_3C_3H_5O(COO)_3\,(aq) + \,HNO_3\,(aq) \leftrightarrow \,Na_2HC_3H_5O(COO)_3\,(aq) + NaNO_3\,(aq)$$

Also, for the synthesis of different shapes (triangular or truncated triangular platelets) was added hydrogen peroxide (H_2O_2) as an etching agent. It will oxidize the less stable newly formed silver nanoparticles, allowing a shape control and avoiding overgrowth:

$$2Ag^0(s) + \,H_2O_2(aq) + 2H^+(aq) \leftrightarrow 2Ag^+\,(aq) + 2H_2O\,(l)$$

Potassium bromide (KBr), as a bromide ion source, can be used to stop the particle growth, being able to allow a size control. The bromide will bind to the silver surface, forming silver bromide and hampering the nanoparticle growth.

$$Ag^+ + \,Br^- \rightarrow AgBr$$

In this case, it is possible to obtain different sizes just varying the amount of bromide added to the reaction.

1.7.2 Seed mediated synthesis

This process involves the production of seeds (larger nuclei) and their growth into metallic NPs in differentiated steps.

The seed-mediated synthesis is an interesting technique in the obtaining of nanomaterials, due to the possibility of a high control in the final composition, size or shape. In 2001 Murphy *et al.*,[78] were among the first using the seed mediated methodology to synthetise nanoparticles, obtaining, with this technique, gold nanorods. Since then, many efforts have been made to improve and understand the synthesis.[79]

Using seed-mediated strategies, it is possible to obtain a large variety of gold and silver nanostructures with different geometry. Gold or silver triangles, cubes, stars or dendrimers have become accessible, also demonstrating greater control in size and dispersion.

Given that the only nanomaterial based on a seed-mediated strategy presented in the thesis is the Au nanorods, the following revision of this section will focus on this gold geometry specifically.

There are some critical parameters to take into consideration when the growth of gold nanorod is the final goal. The first one to have in consideration is the synthesis of the seeds. It was pointed out that different seeds will lead to different shapes, and they not only depend on the metal but on the surfactants or reductants.[79]

In the presence of CTAB as a surfactant and $NaBH_4$ as a reductant, the obtention of a good cuboctahedra structure is mainly achieved.[80]

The growth solution, in which the seeds are added, is composed by gold ($HAuCl_4$ as a gold source), a surfactant (CTAB), a week reductant (ascorbic acid) and silver (with $AgNO_3$ as the source).

The presence of silver is believed to have a role in the anisotropic growth and symmetry breaking of the seeds. Have been proposed more than one mechanism explaining the role of the silver. Some of them propose that the silver, alongside with the CTAB, will be absorbed preferentially in gold high-energy side facets and will slow down further gold deposition, leading to the formation of the gold nanorod. It can be in the reduced form, i.e. Ag(0), or in the silver complex with bromine, i.e. AgBr. Was even also proposed a mechanism involving the CTAB. Above ~1mM (the first critical micelle concentration of CTAB) the silver may alter the micellar structure and lead to the gold nanorod formation[81,82].

The presence of halides in the reaction media has an important role in the growth of gold nanorods. It was noticed that the change in the counter ion (cetyltrimethylammonium chloride, CTAC, with Cl^-, instead Br^- in the CTAB), or the presence of I^-, can change the product substantially.

In the presence of CTAB, the chloride ligand are replaced with the bromide:

$$[AuCl_4]^- \leftrightarrow [AuBr_4]^-$$

It can be seen due to a change in the colour from pale-yellow to dark-orange-yellow. The gold complex $AuBr_4^-$ has been identified as the main gold source into the growth solution, and with different amounts of Br^- ions in solution, there is a variation in the gold nanorods yield and aspect ratio. It can be added as an external source, but a minimum concentration (about 1mM) is required for the obtaining of the nanorods[83,84].

With an iodine concentration in the CTAB above 50 μM, the favoured product is not a rod, it will either be a prism or a nanoplate. For this reason, it is important not only the correct choice of the reagents, but also their purity. It was found that some reagents can present iodine contamination at a significant level, thus leading to a variation of the final shape of the product[85,86,87].

The reduction of the gold (III) complex anion, $AuBr_4^-$, can be carried out with mild reductants. One of the most used is ascorbic acid. Under acidic conditions, the ascorbic acid will be mostly in the form of L-ascorbate, and the net reaction can be described as seen in **Figure** 1.28. (Note that only Au(0) are adjusted, bromide ions are not.):

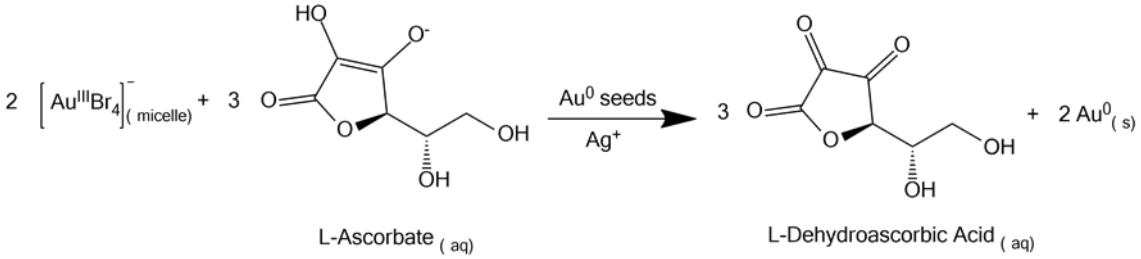

Figure 1.28: Scheme of the net redox reaction for the reduction of Au(III) to Au(0).

But the ascorbic acid is not strong enough to reduce the gold from Au^{3+} to Au^0 without a gold surface, and the reduction occurs in two steps. First, the ascorbic acid reduce the Au^{3+} to Au^{1+}, and Au^0 is achieved once the seeds are introduced in the growth solution.

It was noticed that, for a complete reduction of the Au^{3+} to Au^{1+}, also the radical anionic L-ascorbate has to participate in the reduction. (**Figure** 1.29)

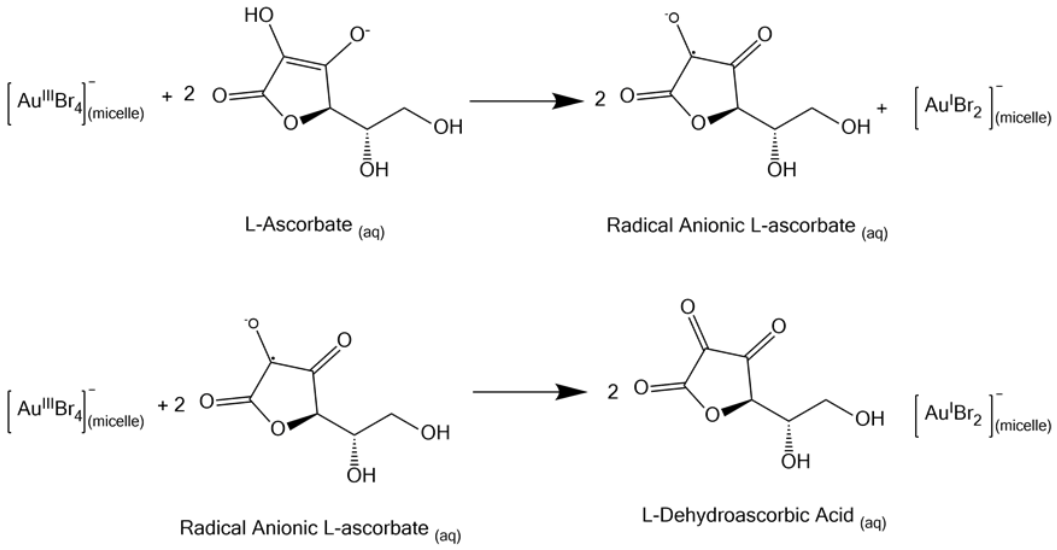

Figure 1.29: Scheme of reduction of Au(III) to Au(I) by ascorbic acid.

For the second step, the reduction of Au^{1+} to Au^0, were proposed two mechanism. The first mechanism (**Figure** 1.30) is the disproportionation of Au^{1+}, leading to Au^0 and Au^{3+}:

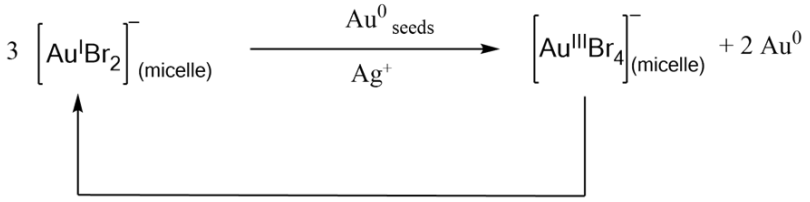

Figure 1.30: Scheme of the disproportionation of Au(I) to Au(0) and Au(III).

The second mechanism (**Figure** 1.31) is the direct reduction of Au^{1+} to Au^0:

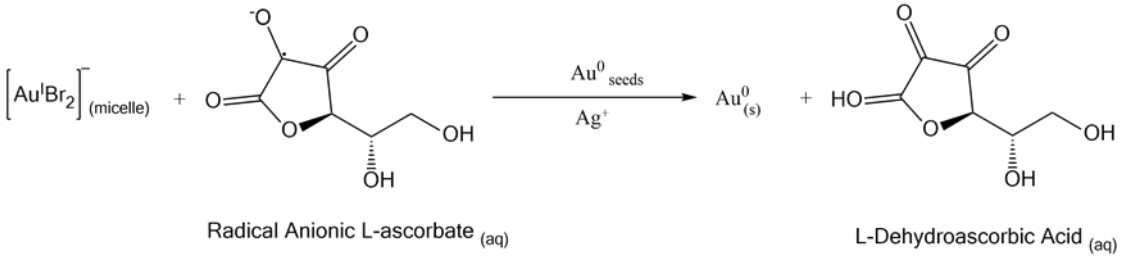

Figure 1.31: Scheme of the direct reduction of Au(I) to Au(0).

The complete oxidation of L-ascorbic acid can be seen in **Figure** 1.32:

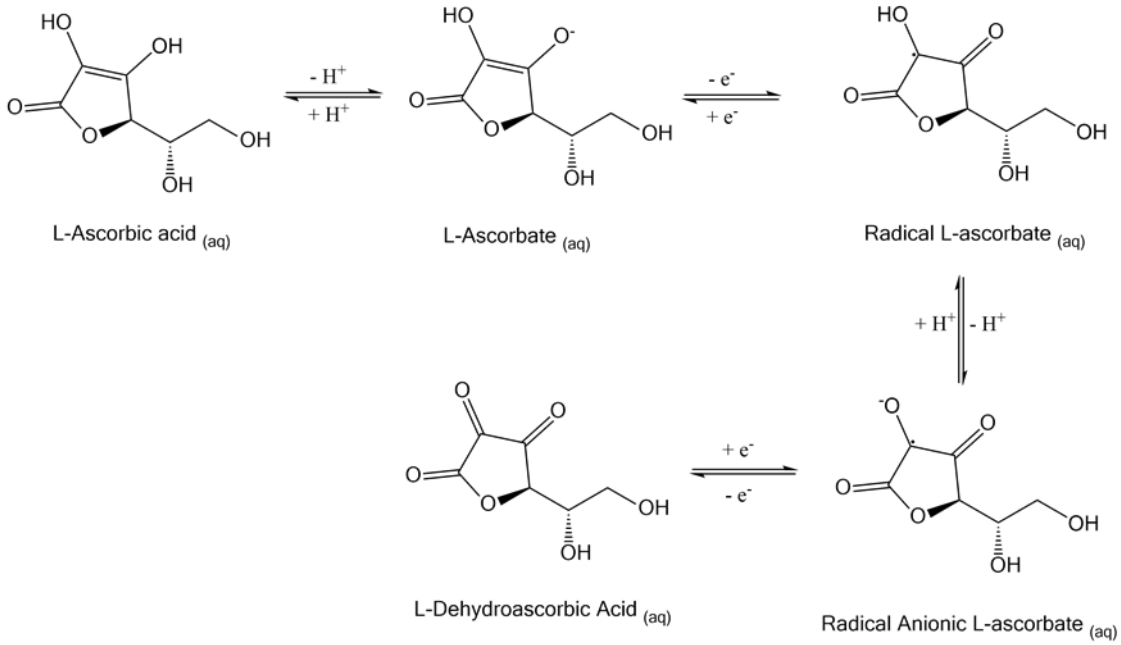

Figure 1.32: Scheme of the complex oxidation of L-ascorbic acid.

Other factors that have a direct relationship in the gold nanorod synthesis are the temperature and the pH.

Despite the fact that they can be synthesised at room temperature, the usual protocols use mild temperatures. The solubility of the CTAB marks the limit. With a concentration of 100 mM, temperatures above 27 ºC are necessary to avoid the crystallization in solution. Higher temperatures will lead to a fast reduction process, decreasing the size of the nanorods and presenting a higher polydispersity.[88].

With different pH conditions, the aspect ratio of the final gold nanorods can be tailored. Lowering the pH will slow the kinetic growth, and will be achieved higher aspect ratios. That is due to the dependence of the ascorbic acid reducing ability with the pH, which is weaker at acidic environments (pH 2.5) than in mild acidic ones (pH 6.5).[89]

Despite the fact that a lot of efforts have been made in order to understand the mechanism of the gold nanorods synthesis using the seed-mediated process, there are still factors that needs to be better understood, as well as different study parameters that can have an essential role in the final product, alone or in combination with the others[81].

1.8 General synthetic methodologies of Platinum nanoparticles

One of the most common synthetic routes to platinum nanoparticles is a wet chemical reduction (WCR). For the specific case of platinum, there are different synthetic routes for the obtention of a variety of structures[90,91]. Was El-Sayed *et al*. among the first synthetizing colloidal platinum nanoparticles using polymers capping agents. Since then, much research has been made with similar approaches for the obtention of different Pt nanoparticles due to their properties. In this sense, several synthetic routes for the formation and growth of Pt NPs can be applied.

The polyol methodology is one of the most used techniques. Polyols, such as ethylene glycol, propylene glycol or polyethylene glycol, present high boiling points as well as a reduction potential, making them good candidates for the synthesis of different kind of nanoparticles. With this methodology, cubic, cuboctahedra and octahedral particles with PVP as a stabilizing and $AgNO_3$ as a shape-directing agent has been synthetised.[92] Also, a polyol methodology with PVP as a protecting agent and methylamine as shape directing agent can lead to a concave polyhedral structure.

Different structures were obtained when the nanoparticles are synthetised in an N_2 atmosphere or an open-air environment, suggesting that the nitrogen can bind to the surface and act as a shape directing agent.[93] The addition of $NaNO_3$ to the reaction can alter the reaction kinetics causing a slow in the reduction process and changing the final structure of the particles.[94]

In water, different routes have been used. With Pluronic F127 copolymer and ascorbic acid as the reducing agent, dendritic nanoparticles were obtained. The presence of Pluronic is crucial, and it was acting as a structure directing-agent. The polymer, as well as the Pt concentration in the reaction synthesis method, plays also an important role in the synthesis.[95]

In this sense, several methodologies for the synthesis of Pt nanoparticles exist, but even small variations in the conditions can lead to a change in the structure and is likely that the control mechanism for each system is different.[96]

1.9 Silica coating

The implementation of silica as building blocks in hybrid nanomaterials construction has brought numerous advantages flowing from their intrinsic properties. Silica provided high stability, especially in aqueous media but also in polar organic solvents, it is chemically inert and optically transparent, which favours the retention of specific intrinsic properties of the metals coated with it.[97] Furthermore,

silica coatings offer the attractive possibility of easy functionalisation (via siloxane chemistry) with a wide variety of molecular agents with different functionalities.

One of the most used technique to cover metal nanoparticles with a silica layer is based on the so-called Stöber methodology. Using a silicon alkoxide like tetraethylorthosilicate (TEOS, $Si(OC_2H_5)_4$) or methyltriethoxysilane (MTES, $Si(OC_2H_5)_3CH_3$) as silica precursor, the controlled silica layer deposition with desired thickness can be achieved under controlled conditions (in the presence of a suitable catalyzer such as high pH condition or amine derivatives).

Interestingly, when the silica polymerisation process is completed in the presence of CTAB acting as a template, is possible to induce the formation of mesostructured porous in the silica layer with a size pore usually between 0.5 and 3 nm in diameter. For carrying out this procedure a base is employed as a catalyser, and a co-solvent methodology is applied, using water and an organic solvent like methanol, ethanol or isopropanol, due to the alkoxysilanes immiscibility with water. The process undergoes in two steps, hydrolysis and condensation:

$$Si(OC_2H_5)_4 + 4\,H_2O \rightarrow Si(OH)_4 + 4\,C_2H_5OH \text{ (Hydrolysis)}$$

$$Si(OH)_4 \rightarrow SiO_2 + 2\,H_2O \text{ (Condensation)}$$

Several parameters are affecting the hydrolysis and condensation of the alkoxysilanes. The temperature, solvents, concentration, reaction time or pH can have an influence in the final product[98,99,100].

1.10 Sustainable Chemistry

Were Anastas and Warner the catalyst within the scientific community for the development of sustainable chemistry. Was in 1998 when they published the 12 principles of green chemistry[101], which preceded the publication in 2003 by Anastas and Zimmerman of the 12 principles of green chemical engineering[102]. In those publications, it is brought to the attention of scientist and engineers the need for the development of a more sustainable scientific activity. We can list the 12 principles of sustainable chemistry as are listed in the green chemistry section of the American Chemical Society:

1. **Prevention**

It is better to prevent waste than to treat or clean up waste after it has been created.

2. **Atom Economy**

Synthetic methods should be designed to maximize the incorporation of all materials used in the process into the final product.

3. **Less Hazardous Chemical Syntheses**

Wherever practicable, synthetic methods should be designed to use and generate substances that possess little or no toxicity to human health and the environment.

4. **Designing Safer Chemicals**

Chemical products should be designed to affect their desired function while minimizing their toxicity.

5. **Safer Solvents and Auxiliaries**

The use of auxiliary substances (e.g., solvents, separation agents, etc.) should be made unnecessary wherever possible and innocuous when used.

6. **Design for Energy Efficiency**

Energy requirements of chemical processes should be recognised for their environmental and economic impacts and should be minimised. If possible, synthetic methods should be conducted at ambient temperature and pressure.

7. **Use of Renewable Feedstocks**

A raw material or feedstock should be renewable rather than depleting whenever technically and economically practicable.

8. **Reduce Derivatives**

Unnecessary derivatization (use of blocking groups, protection/ deprotection, temporary modification of physical/chemical processes) should be minimised or avoided, if possible, because such steps require additional reagents and can generate waste.

9. **Catalysis**

Catalytic reagents (as selective as possible) are superior to stoichiometric reagents.

10. **Design for Degradation**

Chemical products should be designed so that at the end of their function they break down into innocuous degradation products and do not persist in the environment.

11. Real-time analysis for Pollution Prevention

Analytical methodologies need to be further developed to allow for real-time, in-process monitoring and control prior to the formation of hazardous substances.

12. Inherently Safer Chemistry for Accident Prevention

Substances and the form of a substance used in a chemical process should be chosen to minimize the potential for chemical accidents, including releases, explosions, and fires.

Taking a close look at the 12 principles, we can use strategies that help to follow them, by using better solvents, energy sources that can faster the chemical process, obtaining better catalyst or obtaining new sensor that can drive to a fast recognition of toxic analytes.

1.10.1 Solvents

Solvents play an essential role in the reactions. They are used most of the times in more quantity than any reactive species and are one of the most important waste generators. Solvents like hexane or toluene are petroleum derivate, other can be volatile like acetone or flammable like diethyl ether, making dangerous the work with them. The easy dispersion, accumulation and toxicity of chlorinated solvents in the environment is an important source of contamination. A purely solvent-based process, avoiding mixing of solvents, can be a strategy to reduce the waste if we are able, for example, to recover and use it again. However, the use of preferentially water as well as new solvents can also have a positive impact in the environment as in the laboratory results.[103,104]

Water has several advantages. It is not dangerous, not toxic, cheap and non-flammable. It allows to work at moderate temperature conditions (0-100 ºC), but also in near critical conditions (near-critical water (NCW), 150-350 ºC, 4-200 bar) or supercritical conditions (supercritical water (SCW), >374 ºC, >221 bar), in which properties as density or polarity are strongly modified.

However, there are few organic compounds soluble in water, what makes that new solvents must be developed in order to improve the “classic” ones.

Those new solvents can include ionic liquids, perfluorinated compounds or supercritical fluids. All of them has advantages and drawback, showing that, nowadays, the perfect solvent does not exist, just the most convenient to the chemical process.

1.10.2 Catalyst

A catalyst is a compound that affects the reaction rate, speeding up or slowing down (also called inhibitors), but that does not appear in the stoichiometry of the reaction. The catalyst is not consumed during the reaction process and must be regenerated, so it can be reused in the reaction more than once.[105,106]

We can classify the catalyst in homogeneous and heterogeneous.

1.10.2.1 Homogeneous catalyst

The catalyst as well as the reagents are in the same phase (usually in dissolution). They can be acids, bases, or Lewis acids like $AlCl_3$, $TiCl_4$ or BF_3. The use of metals like Pd, Pt, Fe, Ni, Co or Cu with *d* orbitals partially occupied have also a widespread use. They have several advantages like a more homogeneous distribution within the solution, or the possibility to use a more specific catalyst.

One of the main problems is the separation of the catalyst and the reaction products with the consequent waste generation.

1.10.2.2 Heterogeneous catalyst

In this case, the catalyst and the reagents are in different phases (for example the catalyst as a solid and the reagents as a liquid).

Heterogeneous catalyst presents some advantages, such as an easy way to separate the products and the catalyst, or the thermally and chemically stable materials used. Zeolites are an important type of materials used in several catalytic processes.

The reaction conditions used to be more severe than with homogeneous catalyst.

1.10.3 Ultrasounds and Microwaves.

The use of ultrasounds and microwaves in the synthesis procedure can lead to improved methodologies, with the following lower use of time and energy in the process, making them more suitable for industrial scale.

1.10.3.1 Ultrasounds

Ultrasounds are acoustic waves with more than 20 KHz, until the 10 MHz. The use of high frequency and intensity waves can present several advantages in the synthesis of new products, like faster

conversions, mild reaction conditions or lowering the number of steps in a procedure. When the ultrasounds are applied in a liquid, they lead to the formation of microbubbles that collapse and give arise to temperatures in the order of 4.000-6.000 K and pressures of 1.000 - 2.000 bar[107,108,109].

They have been used extensively in analytical chemistry[110,111,112,113].

Ultrasounds can be considered as a clean source of energy, with no toxicity and with cheap equipment.

1.10.3.2 Microwaves

Microwaves are electromagnetic waves, with a wavelength range between 1 cm and 1 m. It corresponds to frequencies between 300 and 3.000 MHz. It is possible to introduce thermal energy in chemical reactions with the use of microwaves. It has several advantages like lowering the time of heating, present different temperatures in the mixture or a selective heating[114,115,116].

1.10.4 Electrochemistry and Photochemistry

Electrochemistry and photochemistry are called to have an important place in the development of greener process, giving rise to new products and methodologies with fewer wastes and use of energy than the usual procedures.

1.10.4.1 Electrochemistry

When a chemical process causes electrons to move, they give place to the oxidation-reduction (redox) reactions. If we do this process placing different electrodes connected with a saline environmental in a solvent, we are talking about an electrochemical reactor.

The electrochemical process offers several advantages like mild and easy control of the conditions, almost no risk process and high atom efficiency. Once the electrodes are usually in a dissolution, they can be considered as a heterogeneous catalyst. They are used to avoid the addition of oxidants or reducers that can lead to sources of contamination.

The main inconvenient can be the high cost of electrochemical reactors for laboratory scale or the high energy consumption in an industrial application[117,118,119].

1.10.4.2 Photochemistry

Taking advantage of the use of light, ultraviolet, visible or near infrared, to produce new chemical products, is a growing field of research. With the reasonable use of light and under certain conditions, it is possible to obtain new results in the chemical synthesis as well as produce or induce interesting

properties in some materials. Photovoltaics, the ability to convert sunlight into electricity, can be improved with the use of nanostructures and give a new option for solar cell devices.

The main advantages of the photochemical process are the possibility to reduce the number of reactive, the use of mild temperatures or being a selective process. Some molecule or materials interact at an electronic level with the light, and this can lead to specific reactions.

The photochemical process still presents several drawbacks, among them, the low absorption of the radiation or the higher price of apply the photochemistry to obtain the same product in comparison to another methodology[120,121].

1.10.5 Analytical methodologies

The development of new analytical methodologies is an essential field of research. The identification and quantification of analytes in a fast and reliable way is useful in several areas. The quick identification of toxic analytes, or precursors of toxic analytes, can lead to prevention or an implementation of a necessary action to minimise the adverse effects derived from their presence. For this reason, it is essential to develop new and fast strategies that can avoid the use of expensive equipment. Colourimetric methodologies that can give a response to a particular analyte with colour changes, or related fluorescence process (enhancement or quenching), can be fundamental in an *in-situ* analysis[122,123].

1.10.6 Toxicity

As we saw in the previous sections, it is highly vital to take into consideration the toxicity and toxicology effects, not only in the synthesis and manufacturing but also in the applications.

Metals like mercury where used in the past in several fields, as an antibacterial agent, to control plant diseases in the agriculture or for the manufacturing of hats. The ingestion or exposure to its vapours can lead to memory loss or hyperactivity, among others. Also, the organic mercury compounds, like methylmercury, can cause death. In this sense, the toxicity studies are highly essential to avoid the use of potentially toxic materials.[124]

Likewise, is well known that the toxicity of some substances depends on the dose, and when some substances may be innocuous, beneficial or even necessary for life at low doses, at high doses may be harmful. A notable case of toxicity can be seen in the chemotherapy compounds. The use of different drugs against cancer disease can have a harmful effect on the healthy parts of the body. An application or combination of new treatments that will eliminate or reduce the use of these drugs without compromising the beneficial effect would be preferred[125].

1.11 Material Chemistry and Green Chemistry

Taking in consideration the previous sections is interesting to notice that green chemistry is not a new field of research but is something that takes advantage of the fundamental pieces of knowledge of the organic and inorganic chemistry, as well as the physical and analytical chemistry. Moreover, with the help of new analytical methodologies, is possible, for example, to obtain new, cleaner and safer procedures at the laboratory or industrial scale. On this regard, material chemistry is not only called to have an essential role in the improvement of the actual methodologies, but also in the design and application of new ones, that can lead to better and sustainable science, and consequently, to a "greener" future.

In the present thesis work, we take advantage of the properties of nanomaterials, to help increase the scientific knowledge in systems that are capable of identifying toxic analytes (Chapter 2); in the realization of new materials with potential applications in catalysis (Chapters 3 and 4); or materials with applications in biomedical systems (Chapter 5)

1.11.1 Nanomaterials and Sensing

The use of noble metals in the detection or quantification of target analytes is a relevant research field. A colour change is produced when nanoparticle aggregation occurs, as was initially exploited by Mirkin *et al.*[126,127]. Exist several products in the market that are nanoparticle-based. The use of gold nanoparticles in pregnancy or drug-abuse test are well-known applications.[17] In this regard, and due to their properties, it can be used as fast colourimetric sensors.

On the other hand, polyamines are polycations that present a high biocompatibility[128], water solubility and flexibility. Polyamines also have shown an excellent sensing capacity against different metal and cations extensively[129]. This characteristic make them a useful component for the functionalization of different types of nanomaterials, and we can take advantage of the properties of both materials. On this topic, exists several works relating the functionalization of carbon quantum dots[130,131], silica[132], magnetic[133], silver[134] or gold nanoparticles[135] with different polyamines.

In Chapter 2, it has been exploited the binding ability of a polyamine molecular linker bearing different functional groups, which favours the self-assembling of silver nanoparticles (AgNPs) and gold nanoparticles (AuNPs) into 1D nano-chains in aqueous solution. The chainlike assemblies of AuNPs and AgNPs were structurally stable for an extended period, during which their characteristic optical properties remained unchanged and the sensing of Hg^{2+} in aqueous solution was carried out.

1.11.2 Nanomaterials and Catalysis

The synthesis and the use of Pt and Pt NPs have several advantages as was stated in the previous sections. With a reduction in the size, and consequently an increase in the surface area of the metal, we can have, for example, better catalytic properties using less amount of metal. Also, the combination of the platinum properties with other compounds, metals or semimetals, is of increasing interest. It will give to the system new properties that can be an advantage in fields like catalysis, sensing or biomedicine. For these reasons, the application of noble methodologies to the synthesis of nanomaterials is still a challenge in many different technological and scientific fields. New efficient and reproducible synthetic methods that produce fewer residues and reduce the cost of raw materials must be developed.

1.11.2.1 Platinum Composites

Combination of the platinum properties with other materials, can lead to characteristics that are distinct than its constituent materials. In this regard, tellurium compounds[136] has several uses, as in catalysis[137], antibacterial[138] or therapeutic applications[139]. Yang *et al.*,[140] demonstrated that when Te nanoparticles are below 120 nm, they perform like plasmonic nanoparticles, but when the size is bigger than 120 nm, behave like an all-dielectric material, having a potential application in solar cells. Thomas Webster group[141] synthesised Tellurium nanorods coated with PVP to test their antibacterial and anticancer properties. Similarly, Lin group[142] fabricated nanowires to use in antibacterial applications. Tiangfen Chen[143] group synthesised and applicate the tellurium nanorods as antioxidant and anticancer agents.

Several materials have been synthesised containing tellurium, like quantum dots of CdTe[144] or HgTe[145], $MoTe_2$ nanowires[146,147,148], ZnTe nanowires[149,150], SnTe nanoplates[151], Ag_2Te nanowires[152,153] or AuTe nanowires[142,154].

With platinum, we can find Pt-Te nanowires or nanotubes[155,156], with applications in catalysis or SERS,[136] which demonstrate the different properties that can achieve.

The synthesis often requires several steps reaction, long time procedures or elevated temperatures.[155]

In chapter 3 is reported the synthesis of new $PtTe_2$ multi-crystallite nanoparticles (NPs) in different sizes through an annealing process using new nanostructured Pt-Te organometallic NPs as a single source precursor. This precursor was obtained in a single reaction step using Ph_2Te_2 and H_2PtCl_6 and could be successfully size controlled in the nanoscale range. The resulting organometallic composite precursor could be thermally decomposed in 1,5 pentanediol to yield the new $PtTe_2$ multi-crystallite NPs. The final size of the multi-crystallite spheres was successfully controlled by selecting the nano precursor size. The sizes of the $PtTe_2$ crystallites formed using the large spheres were estimated to be in the range of 2.5–6.5 nm.

1.11.2.2 Platinum Nanoparticles

For the synthesis of Pt NPs, one of the most commonly methodologies is the polyol process. Using ethylene glycol, Tsuji *et al.*[157], Zang *et al.*[158], or Nogami *et al.*[159], reported the synthesis of different structures but with one common point, that is the use of high temperatures (up to 160 ºC) during times from half to several hours. Water in oil microemulsion, using water and n-heptane are also reported methodologies[160]. The reduction of the precursor can be achieved with Hydrogen (H_2), $NaBH_4$, Ascorbic acid or Hydrazine (N_2H_4), among others[161]

In chapter 4, the attractive possibility of applying the cheap iron (II) sulphate salt in the reduction process of the K_2PtCl_4 to produce colloids suspensions is studied. The synthesis took places in water at mild temperatures (60 ºC) and was assisted by sodium citrate (SC) using polyvinylpyrrolidone (PVP) as a surfactant. The adjustment of this novelty process allows obtaining well-dispersed and sub-20 nm dendrimer-type platinum nanoparticles (Pt D-NPs).

1.11.3 Nanomaterials and Biomedical Applications

Gold nanorods have several applications like photodynamic therapy, sensing or SERS. The unique properties arise from their LSPR which present two peaks. The transverse peak, at approximately 520 nm, and the longitudinal peak, that can be tuned from 650 to 1300 nm.[162,163] The interaction with the visible and near infra-red (NIR) light is an attractive property that can be exploited in biological applications. On this regard, near infra-red light can penetrate better the biological tissue than the visible light. As the NIR light can penetrate from mm to several centimeters[164,165,166], has the potential to interact with the nanoparticles in a non-invasive and non-harmful approach. Also, due to the fact that the first and second biological window for optical imaging, from 650-950 nm and 1,000-1,350 nm respectively, are separated from the major absorption peaks of blood and water, can be used as contrast agents.

When gold nanorods are exposed to laser light with a wavelength in resonances with their surface plasmon oscillations, they can absorb the light and convert into heat through a series of photophysical process. In biological media, temperature increases of 10 ºC, or 1000 ºC in local zones around the nanoparticles has been reported.[167,168]

The use of gold nanorods in biomedicine is in constant growth.[169] Applications in cancer cells[170] or against bacteria[171] have been reported. One of the most significant drawbacks in the use of gold rods is that the CTAB, the compound mostly used for the synthesis and stabilisation, can present cytotoxicity.[172] It lead us to have to make alterations for its replacement or elimination. The use of mesoporous silica is an exciting approach. Mesoporous silica covering brings new properties to the system, such as greater stability in an aqueous medium[173], and are being studied in several bio-applications methodologies[170,174,175,176,177,178,179].

In chapter 5 is reported the synthesis and characterization of gold nanorods with a longitudinal band centred approximately in 650 nm, covered with a mesoporous silica layer. The mesoporous silica was loaded with different molecules or drugs, such as Methylene Blue or Doxorubicin.

In this sense, the use of nanomaterials can have a positive impact on the treatment of diseases and infections, reducing the necessary amount of chemotherapeutic agents, and lowering the side effects related to them.

2 Chapter 2

Polyamine Ligand-Mediated Self-Assembly of Gold and Silver Nanoparticles into Chainlike Structures in Aqueous Solution: Towards New Nanostructured Chemosensors.

Published in: **Adrián Fernández-Lodeiro**, Javier Fernández-Lodeiro, Cristina Núñez, Rufina Bastida, José Luis Capelo, Carlos Lodeiro," Polyamine ligand-mediated self-assembly of gold and silver nanoparticles into chainlike structures in aqueous solution: Towards new nanostructured chemosensors". *ChemistryOpen*, **2**, 200-207 (2013) IF: 3.250. DOI: 10.1002/open.201300023

Candidate contribution: performed the synthesis, analysis and characterisation (UV/Vis, FT-IR, ζ-potential) of the nanomaterials. Performed the tritration experiments. Helped in the synthesis of the polyamine and helped in the discussion of all the analysed data and the writing of the final version of the manuscript.

Selected as Cover Issue Manuscrip

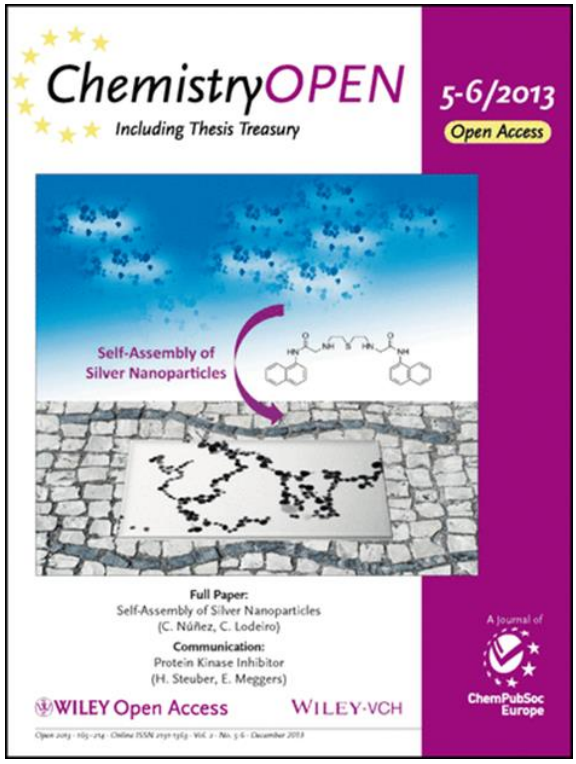

2.1 Introduction

Noble metal nanoparticles (MNPs) have been intensively pursued in recent years, not only for their fundamental scientific interest[180,181] but also for their technological applications, ranging from analytical sensors to catalysis and fuel cells[182,183]. Recently, the attention paid to one-dimensional (1D) nanomaterials has been increasing significantly, because of the need to fabricate alternative functional 1D nanostructures for applications in the fields of nanoelectronics and nanobiotechnology[184,185,186,187] due to the fact that they can act as interconnects between functional nanoscale components[188].

Several experimental routes have been recently proposed to efficiently self-assemble preformed MNPs into 1D chains: methods involving hard[189], polymeric[190] or surfactant-based[191] templates, molecular recognition[192,193,194], specific functionalization[195], and surface- or solvent-induced phase separation[196,197] have been successfully demonstrated[198]. Chains of MNPs also have been prepared by using linear macromolecular templates, such as, DNA[199,200,201,202], peptide[203,204,205,206,207,208,209], insulin fibrils[210], protein fibrils[211,212] or carbon nanotubes[213].

The growth mechanism of self-assembled metal nanostructures using (macro)molecular ligands has been also reported to exhibit common features with molecular step-growth polymerization[214]. Similar to functional monomers, metal nanostructures assemble to form chains. The assembly was performed by small molecules (< 2 nm), called molecular linkers, that contain at least two reactive ending groups, capable of attaching to a solid surface by chemisorption (thiol, amine) or interacting electrostatically with other functional groups (hydroxy, carboxyl, amine) present on the surface of nanoparticles (NPs)[214]. The governing factor in linker-mediated assembly of MNPs is the equilibrium between the attractive and repulsive forces[215]. In particular, fabrication of anisotropic 1D noble MNP chains to obtain integrated optics operating below the diffraction limit of light has attracted much attention[216,217,218].

Stellaci and co-workers[196] have introduced anisotropic properties on ligand-stabilised AuNPs. Face-centered cubic (fcc) metallic NPs exhibit no intrinsic electric dipole, however, heterogeneities in surface charge and polarity, associated for example with the non-uniform spatial distribution of capping ligands on different crystal faces[219,220,221], or nanophase separation in mixed-ligand stabilisation layers[222], are possible driving forces for anisotropic self-assembly[223]. In the case of spherical NPs, controlling the surface chemistry of the fabricated NPs allows the creation of an anisotropic ligand organization[224]. Enthalpy minimization, is obtained by promoting dipole alignment and reducing interdipole distances through the formation of linear chains of single NPs. This facilitates the orientation of specific interactions in one direction, which helps directing the selfassembly into 1D arrays. The self-assembly of the NPs into a well-defined 1D array is also influenced by interparticle chemical bonding, hydrogen bonding, van der Waals interactions, electrostatic forces, or any combination of these forces. In addition,

entropy can be maximised at finite temperature by introducing some disorder in the linear chain, which corresponds to the incorporation of branching junctions and to chain reticulation that should be favored at elevated temperature.

Aggregation of NPs induces variations in absorption spectra accompanied by significant color changes of solutions[225]. Similar color changes can be observed upon the addition of an analyte, which initiates the aggregation of noble MNPs, and this feature can be used for permitting their industrial application in biosensing, immunological, and biochemical investigations[226,227,228,229,127,230,231,232]. In the particular case of AgNPs, the geometrical shape also plays an important role in determining plasmon resonance properties[233]. For example, triangular, pentagonal, and spherical silver particles can be colored red, green, and blue, respectively. Consequently, it is important to develop approaches that can manipulate NPs into different shapes and dimensions. While many studies have tackled the synthesis and characterization of gold dimers and networks with peculiar plasmon resonance behavior[234,235], organization of AgNPs in two-dimensional (2D) superlattices is less common[236,237,238]. For example, Chang *et al*. Reported a variety of 1D and 2D-nanostructured assemblies formed from AgNPs by variations in pressure, temperature, and time in supercritical water without the need for any external linking agents[239].

To follow the group interest in new emissive materials, and functionalised NPs and to explore their applications[129,240,241,242,243,244], herein, we investigate the mechanism of AuNP and AgNP chain assembly associated with the induction of electric dipole–dipole interactions. The nano assembly capacity arises from the partial ligand exchange of surface-adsorbed negatively charged citrate ions, by covalently bound neutral molecular ligand L to produce a final mixed-ligand surface layer.

We show that exchange of surface adsorbed citrate with L, results in the formation of chain-like superstructures with topological features that are dependent on the extent of surface ligand substitution. We determine the time-dependent structural changes associated with the formation of 1D NP superstructures. Morphological and optical characteristics of various nanostructures were investigated by Transmission Electron Miscroscopy (TEM) and Ultraviolet/Visible (UV/Vis).

2.2 Experimental Section

2.2.1 General Instrumentation

Elemental analyses were carried out with Fisons Instruments EA1108 microanalyzer (Ipswich, UK) at the University of Vigo (CACTI), Spain. Fourier Transform infrared spectroscopy (FTIR) spectra were recorded in KBr windows using a JASCO FT/IR-410 spectrophotometer (Spain). ^{1}H and ^{13}C NMR (Nuclear Magnetic Resonance) were carried out on a Bruker Advance III 400 at an operating frequency

of 400 MHz for ^{1}H NMR and 100.6 MHz for ^{13}C NMR using the solvent peak as an internal reference at 25ºC. Matrix-Assisted Laser Desorption/Ionization-Mass Spectrometry (MALDI-MS) analyses were performer with a MALDI-TOF/TOF MS model Ultraflex II (Bruker, Germany) equipped with nitrogen from the BIOSCOPE group. Each spectrum represents accumulations of 5x50 laser shots. The reflection mode was used, and the ion source and flight tube pressure were less than $1.80x10^{-7}$ and $5.60x10^{-8}$ Torr, respectively. The MALDI mass spectra of the soluble samples (1 or 2 µgµL^{-1}) were recorded using the conventional sample preparation method for MALDI MS. One microliter was put on the sample holder on which the ligand had been previously spotted. The sample holder was inserted in the ion source. UV/Vis absorption spectra (220–900 nm) were performer using a JASCO-650 UV/Vis spectrophotometer (Oklahoma City, OK, USA) and fluorescence spectra on a HORIBA JOVIN-IBON Spectramax 4 (Irvine, CA, USA). All measurements were performer at 298 K.

2.2.2 Limit of detection

The limit of detection (LOD) for Hg^{2+} with the small fluorescent molecular systems L and the nano assembly system AgNPs@$(L)^{2-}$ (spherical) were performed having in mind their use for real ion detection and for analytical applications. The LOD was obtained using **Equation** 2.1:

$$ydl = yblank + 3std \quad (2.1)$$

where ydl=signal detection limit and std=standard deviation.

2.2.3 Concentration determination

Assuming a spherical shape and uniform face centered cubic structure, the molar concentrations of the silver nanoparticles (AgNP) and gold nanoparticles (AuNP) solutions was calculated using **Equations** 2.2 and 2.3.[245]

$$N = \frac{\pi \rho D^3}{6M} \quad (2.2)$$

where N is the number of atoms per AgNP or AuNP, ρ [g cm^{-3}] is the density of face centered cubic (fcc) silver (10.5 g cm^{-3}) of gold (19.3 g cm^{-3}), and M [gmol^{-1}] is the atomic mass of silver (107.86 gmol^{-1}) or gold (196.97 gmol^{-1}).

$$C = \frac{N_T}{NVN_A} \quad (2.3)$$

where C is the molar concentration of AgNPs or AuNPs, N_T is the total number of silver atoms added as $AgNO_3$ or gold atoms added as $HAuCl_4$, N is the number of NPs, V is the volume of the reaction solution in L, N_A is Avogadro's constant (number of atoms per mole).

2.2.4 Characterization of the assemblies of AgNPs and AuNPs

We characterised the AgNPs, AuNPs and the chainlike assemblies of AgNPs and AuNPs using a number of optical tools including, transmission electron microscopy (TEM) and dynamic light scattering (DLS). To collect TEM images, the samples were prepared dropping 1 µL of the colloidal suspension onto a copper grid coated with a continuous carbon film and allowing the solvent to evaporate. TEM images were obtained using a JEOL JEM 1010F TEM operating at 200 kV. To perform the Fourier transformations, we used the Digital Micrograph (Gatan) software[246]. The NP size distributions were measured using the DLS system, Malvern Nano ZS instrument (Worcestershire, UK) with a 633 nm laser diode. We investigated the optical properties of these structures using a JASCO-650 UV/Vis spectrophotometer.

2.2.5 Synthesis

2,2'-((Thiobis(ethane-2,1-diyl))bis(azanediyl))bis(N-(naphthalen-1-yl)acetamide) (L): A solution of 20% NaOH (3.4 g, 0.085 mol) was added to a stirred solution of 1-naphthylamine (9.34 g, 0.051 mol) in CH_2Cl_2 (30 mL). The mixture was cooled to 0 ºC and chloroacetyl chloride (9.29 g, 0.083 mol) was added dropwise for 45 min. After stirring at 0 ºC for 100 min, the mixture was allowed to warm to room temperature (RT). The aqueous layer was separated and extracted with CH_2Cl_2 (225 mL). The combined organic phases were washed with HCl (5% v/v), $NaHCO_3$ (5% v/v) and H_2O, dried over $MgSO_4$ and filtered to obtain a white solid. The crude product was purified by silica column chromatography and characterised as 2-chloro-N-(1-naphthyl) acetamide (74 %). A solution of 2-chloro-N-(1-naphthyl)acetamide (439.34 mg, 2 mmol) in tetrahydrofuran (THF; 25 mL) was added dropwise to a solution of 2,2'-thiobis(ethylamine) (120 mg, 1 mmol) and triethylamine (202.24 mg, 2 mmol) dissolved in THF (50 mL) over 1 h in an ice bath. After the addition was completed, the reaction mixture was kept at reflux for 4 h. The solvent was removed in vacuo, and the residue was washed with $H_2O/CHCl_3$ (1:3 *v/v*; 420 mL). The resulting organic phase was dried in vacuo to give L as a pink powder (407.05 mg,

84 %): ^{1}H NMR (500 MHz, $CDCl_3$): d=2.81 (t, 4 H), 3.12 (t, 4H), 3.72 (m, 4H), 5.84 (s, 2H), 7.41–7.59 (m, 2H), 7.72 (m, 2 H), 7.80 (m, 2H), 7.92 (m, 4 H), 8.10 (m, 4 H), 10.35 ppm (s, 2H); ^{13}C NMR (500 MHz, $CDCl_3$) d=30.32, 54.85, 58.37, 120.69, 124.80, 125.73, 125.90, 127.20, 128.05, 128.19, 133.03, 133.56, 169.83 ppm; IR (KBr): $\tilde{\nu}$=1436 ((C=C)ar), 1676 (C=O), 3262 cm^{-1} (N H); MALDI-TOF MS: m/z 487.21 $[M+H]^+$; Anal. calc for $C_{28}H_{30}N_4O_2S$: C 69.1, N 11.5, S 6.6, H 6.2, found: C 69.3, N 11.2, 6.4, H 6.6.

2.2.6 Preparation of AgNPs

Citrate-stabilised AgNPs of different shape (spherical and triangular) were synthesised in aqueous solution following the Frank methodology[77]. For the synthesis of AgNPs with triangular shape, sodium citrate (2.0 mL, $1.25x10^{-2}$ M), $AgNO_3$ (5.0 mL, $3.75x10^{-4}$ M), and H_2O_2 (5.0 mL, $5.0x10^{-2}$ M) were mixed. After that, freshly prepared $NaBH_4$ (2.5 mL, $5.0x10^{-3}$ M) was added. To obtain AgNPs with spherical shape, before the addition of $NaBH_4$, KBr (40 µL, $1.0x10^{-3}$ M) was added to the solution. Once all reagents were combined, the resulting solutions were carefully swirled to fully mix the reactants. Almost immediately, the progression of the reaction becomes evident through the visual changes consistent with the growth of silver nanoprisms. Yellow and blue colors were observed for the spherical and triangular AgNPs, respectively. (**Figure** 2.1)

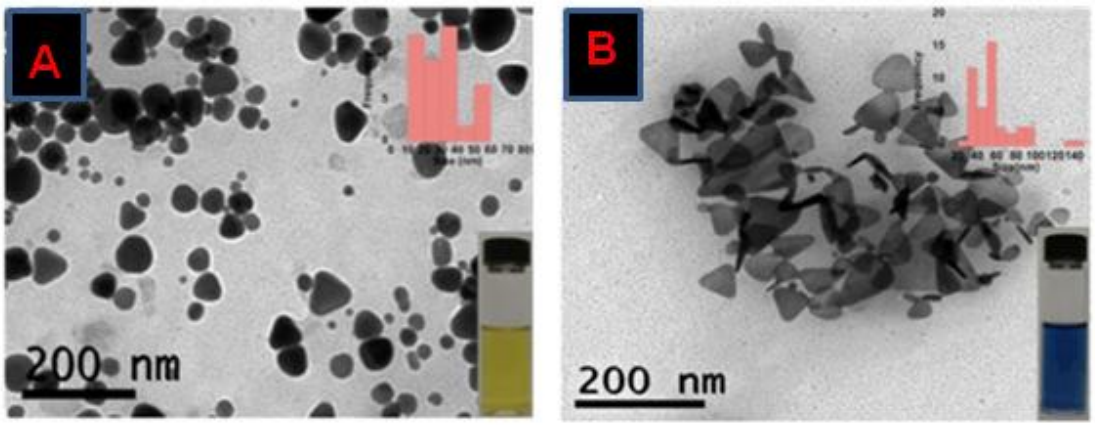

Figure 2.1: Transmission electron microscopy (TEM) images of AgNPs@citrate: A) yellow (25 ± 3 nm polidisperse quasispherical particles); B) blue (64 ±10 nm; average lateral dimension of triangular particles).

Using **Equations** 2.2 and 2.3, $N=30.70\ D^3$, and the resulting spherical AgNPs solution had a concentration of $C_{AgNP}=7.8x10^{-10}$ M with AgNPs of (25 ± 3) nm size.

2.2.7 Preparation of AuNPs

Preparation of AuNPs was performed following the Turkevish method[247,248,249,250] through reduction of tetrachloroaurate ions ($AuCl_4$) by boiling in aqueous sodium citrate solution. $HAuCl_4 \cdot 3H_2O$ (49.5 mg, 0.125 mmol) dissolved in nanopure H_2O (125 mL; 18.2 MΩ cm) was added to a preheated solution of sodium citrate (12.5 mL, 1 wt %). The resulting solution was heate to 100 ºC for 60 min and turned colorless before changing to violet and finally to ruby red. AuNPs obtained using this method appear as almost monodispersed globular structures with a size of (20±5) nm, which are stabilised by weakly bound citrate anions. Using **Equations** 2.2 and 2.3, $N=30.896D^3$ for AuNPs and the resulting AuNPs solution was found to have a of $C_{AuNPs}= 3.7x10^{-9}$.

2.2.8 Chainlike assemblies of AgNPs and AuNPs

We used the polyamine molecular probe L^{2-} to investigate the effect of the presence of different donor atoms in the AuNP assemblies and their optical properties. The formation of chainlike assemblies of AuNPs was controlled and modulated observing that the total formations were obtained by adding an acetonitrile solution of L^{2-} (5 µL, $1x10^{-3}$ M) into a suspension of AuNPs and AgNPs (circular and triangular) in nanopure H_2O (≈ 10^{-8}–10^{-9} M in 3 mL).

2.3 Results and Discussion

2.3.1 Formation of chainlike structures from AgNPs and AuNPs

1D metallic silver or gold nanostructures, can be obtained by exploiting the binding ability of the linear polyamine molecular probe L in water (**Figure** 2.2).

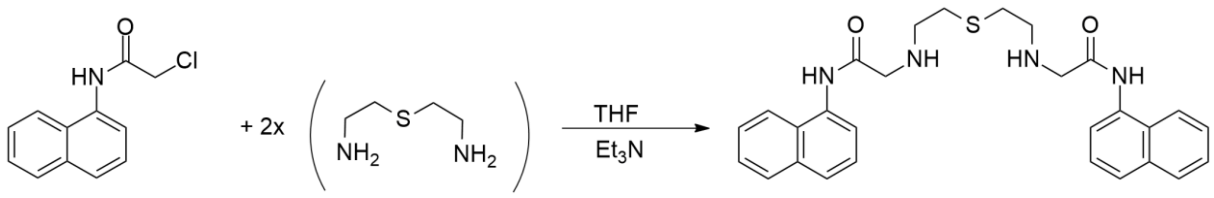

Figure 2.2 Scheme of the synthetic route to compound L.

The donor atoms presented in the structure of compound L could be responsible for the formation of NP chainlike aggregates and the partial removal of the citrate ion from the starting metal nanoparticle surface. This method is similar to that reported by Zhang *et al.*[251,252] and it is different to that in which

the assembly was induced by electrostatic interactions and the disassembly was labile in the presence of stronger chelating agents[253].

In that case, firstly, we assumed that the level of ionization (protonation-deprotonation of functional groups) of potential modifying compounds, might play a role in the process of MNP functionalization, and consequently, could affect the stability of their dispersions. Therefore, the pH of the mixture was modified with a NaOH solution, to an approximate value of pH 12, which leads to the change in the linker ionization degree. After the addition of base to a solution of L, this compound was dissociated bearing negative charges L^{2-} because of deprotonation of the amine groups. Second, we assumed that the chemisorption of the linker on the AuNP surface could take place through the sulfur atom and/or by deprotonated amine groups, leading to the modification of the ζ-potential from ζ_0 (initial potential) to ζ (potential that determines the equilibrium between attractive and repulsive forces).

Finally, it is well known that changing the medium surrounding the nanoparticles (NPs) for another medium, having a markedly different refractive index, strongly alters the surface plasmon resonance (SPR) band of the NPs in the UV/Vis spectrum. The position, intensity, and shape of SPR band strongly depends on the dielectric constant of surrounding medium, the size and shape of NPs as well as the electronic interaction between the stabilizing ligand and NP[254]. Therefore, UV/Vis absorption spectroscopy is an important analytical tool to probe the stability, surface chemistry, and aggregation behavior of AgNPs and AuNPs.

2.3.2 Formation of chainlike structures from AgNPs

2.3.2.1 Spherical shape

Initial characterization of spherical AgNPs prepared by citrate reduction of a silver nitrate solution revealed an absorption maximum (λ_{max}) of the SPR peak for single particles at ≈ 420 nm. (transverse SPR band; **Figure** 2.3 (A,B)) Analyses of TEM imaging shows that the prepared citrate-capped silver NPs (AgNPs@citrate) are nearly monodisperse spheres with an average size of about (25±3) nm. The AgNP concentration was estimated to be 7.8×10^{-10} in terms of molar concentration. This value was obtained taking into account that the entire mass of silver in AgNPs employed for colloidal dispersion preparation was fully transformed into NPs.

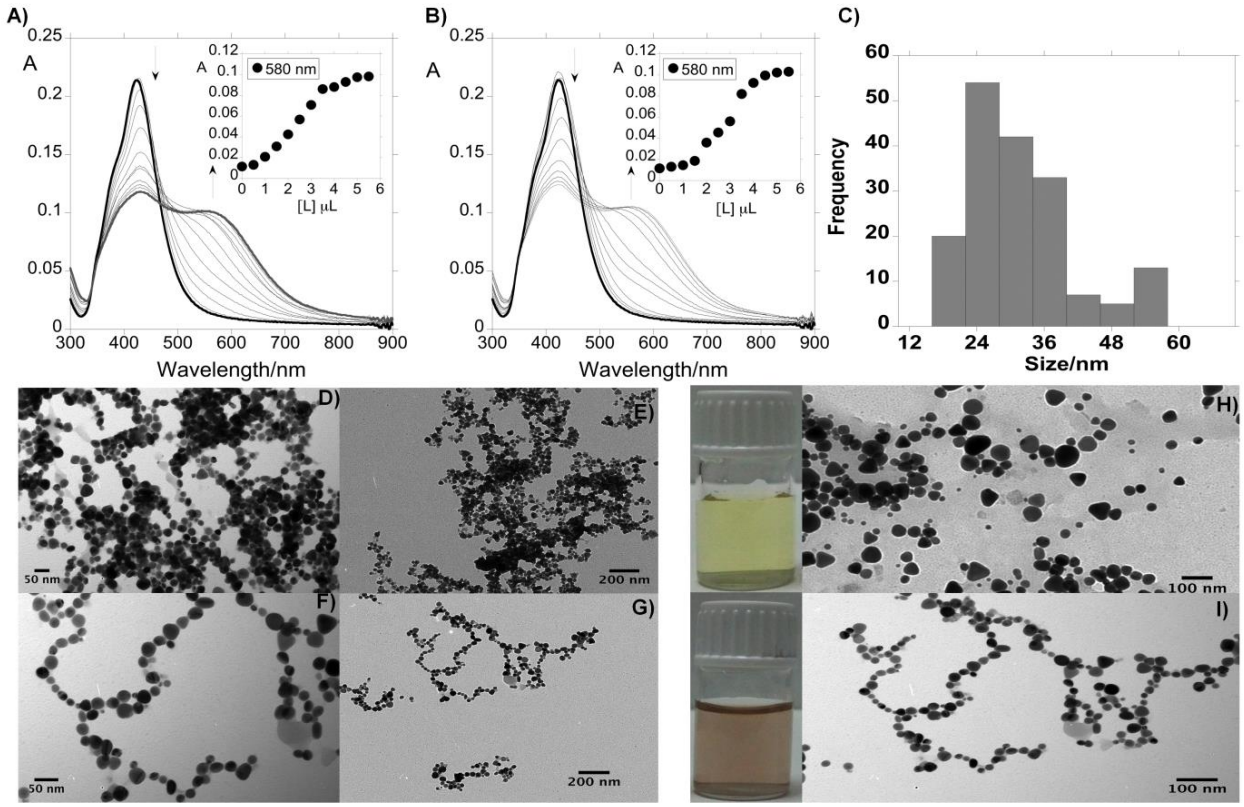

Figure 2.3: UV/Vis absorption spectra of spherical AgNPs@citrate during titration to A) AgNPs@L and B) AgNPs@$(L)^{2-}$. C) Size distribution diagram for AgNPs@$(L)^{2-}$. TEM images of silver nanowire formed from D,E) AgNPs@L and F,G) AgNPs@$(L)^{2-}$. Visual color changes and TEM images obtained H) before and I) after the addition of L^{2-} to an aqueous solution of spherical AgNPs@citrate.

Figure 2.3 A and 2.3 B show the absorption titration of spherical AgNPs@citrate with compound L and L^{2-}, respectively. As mentioned above, because AgNPs@citrate are highly dispersed in solution, the spectrum is characterised by a single SPR band at ≈420 nm (transverse SPR band). AgNPs@L and AgNPs@$(L)^{2-}$ exhibit two absorption bands, at 420 nm and a new band at ≈580 nm, respectively. In both cases, the appearance of the second band (longitudinal SPR band) is a clear evidence of the assembly of AgNPs in solution, and a color change from yellow (**Figure** 2.3 H) to deep red (**Figure** 2.3 I) was also observed.

Chainlike structure formations of AgNPs in aqueous solution were induced in both cases by L and L^{2-}, with the contact between AgNPs being easier at higher concentrations of L and L^{2-}. The ζ potential distribution plays the major role in linkermediated self-assembly of MNPs, and the development of linear chains and branched chain network is directed by the fact that the electrostatic double layer is rearranged around the dimers and becomes anisotropic.

The replacement of citrate ions most probably takes place after the addition of the negatively charged ligand L^{2-}. In that case, the amount of negative charge on the surface of NPs does not decrease significantly, and as a result, a slight change of the ζ-potential was observed from $\zeta_0 \approx$ -33.5 $mVcm^{-1}$ to

ζ_0 -27.8 mVcm^{-1}. The formations of chain-like superstructures with topological features are dependent on the extent of surface- ligand substitution. The replacement of citrate ions of the AgNPs surface by L^{2-} probably induces less electric dipole– dipole interactions, observing that the 1D NP assembly takes place less prominently (**Figure** 2.3 F,G) compared with that observed with L. (**Figure** 2.3 D, E)

In that case, IR spectra were recorded to demonstrate the replacement of citrate ions of the AgNP surface by polyamine ligand L. The IR spectrum of compound L shows peaks characteristic of the carbonyl group at 1676 cm^{-1} and the $\tilde{\nu}$ (C=C) stretching mode at 1436 cm^{-1}.(**Figure** 2.4)

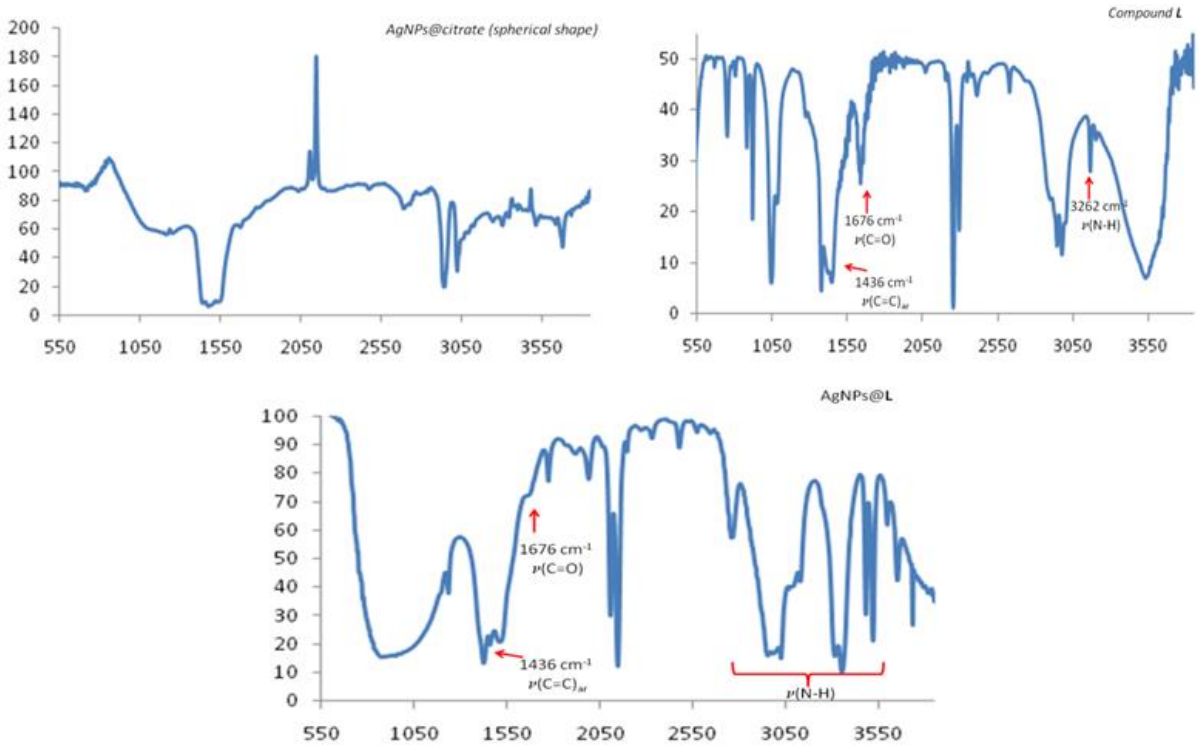

Figure 2.4: IR spectra of AgNPs@citrate, compound L and AgNPS@L in 550-4000 cm^{-1} region (x-axis = cm^{-1}, y-axis = intensity).

In addition, a peak at 3262 cm^{-1} is observed due to the $\tilde{\nu}$ (N-H) stretching mode. A decrease in the intensity of the $\tilde{\nu}$ (C=O) band was observed in the IR spectra of AgNPs@L in comparison with L. The most interesting part of the spectrum is the region from 3000 to 3200 cm^{-1} due to $\tilde{\nu}$ (N-H) stretching modes. The IR spectrum for AgNPs@L is very different from the spectrum of L in the same region. These results suggest the interaction of L with the MNP surface through the carbonyl and amine groups, confirming the replacement of the citrate ions from the NP surface.

2.3.2.2 Triangular shape

Because better results were obtained after titration of spherical AgNPs@citrate with the deprotonated ligand L^{2-}, we used the same method with the triangular AgNPs@citrate. The formation of triangular AgNPs@citrate in aqueous solution with sizes in the range of (64±10) nm was confirmed by the presence of the blue SPR band at ≈700 nm in the UV/Vis spectrum. (**Figure** 2.5 A)

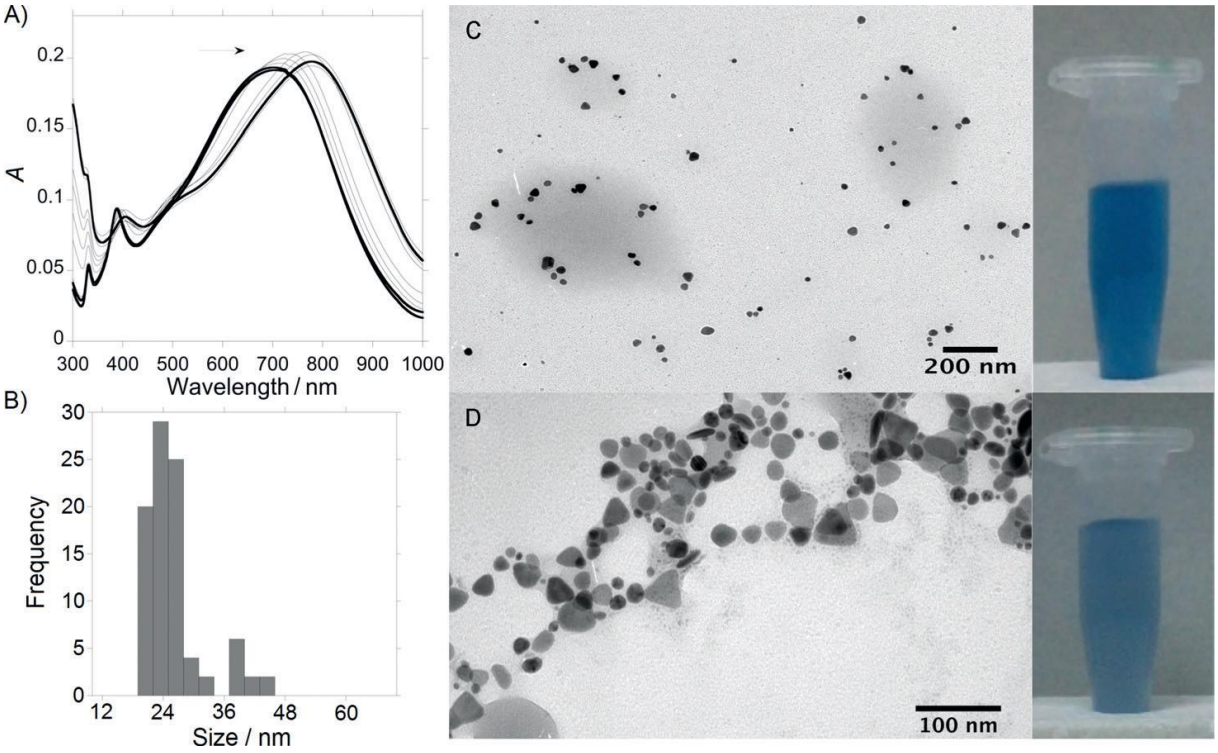

Figure 2.5: A) UV/Vis absorption spectra of triangular citrate@AgNPs during titration to AgNPs@$(L)^{2-}$ and B) size distribution diagram for AgNPs@$(L)^{2-}$. Visual color changes and TEM images obtained C) before and D) after the addition of L^{2-} to an aqueous solution of triangular AgNPs@citrate.

As shown in **Figure** 2.5 C, the triangular AgNPs@citrate were well dispersed in milli-Q water before adding L^{2-}, and they remained well separated on the TEM grid. After the addition of 5 µL of L^{2-} ($1x10^{-3}$ M) to a solution of triangular AgNPs@citrate in aqueous solution, a redshift in the absorption band was observed to ≈780 nm, due to the formation of chains in which L^{2-} ions played the role of connectors between the AgNPs (**Figure** 2.5 (D)). As shown in **Figure** 2.5 C,D, a slight color change from intense to pale blue was also observed.

2.3.3 Formation of chainlike structures from AuNPs

As a model experiment, we also used citrate-capped spherical gold NPs (AuNP@citrate) with a hydrodynamic diameter of (20±5) nm. (**Figure** 2.6)

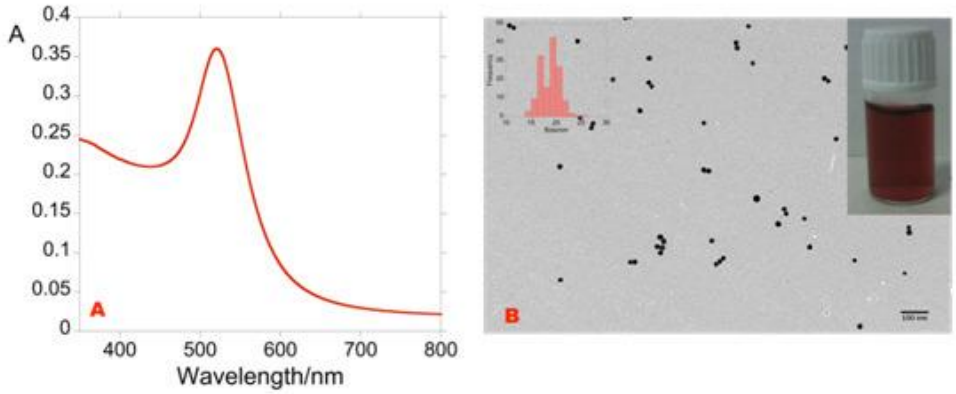

Figure 2.6: Absorption spectra and transmission electron microscopy (TEM) images of AuNPs in aqueous solutions.

The self assembly was performed using a AuNP@citrate solution with a C_{NP}=3.7x10^{-9}m (2.2x10^{15} particle L^{-1}) and a concentration of 1.6x10^{-6} M for L^{2-} (≈ pH 12) (C_L/C_{NP}≈4.5x10^2).

As we mentioned above, the assembly of AuNPs has a significant effect on the optical properties of the NPs, reflected by a dramatic change of the UV/Vis extinction value of the SPR band. As shown in **Figure** 2.6 A, single spherical AuNPs were characterised by an extinction transverse plasmon band at λ_1 ≈520 nm[255].

After addition of the linker L^{2-}, a second low energy longitudinal surface plasmon band (λ_2) appears at higher wavelengths (630–710 nm), which is a result of the plasmonic coupling of linearly assembled NPs. (**Figure** 2.7 (A)) The position of this longitudinal surface plasmon band (λ_2) could be modified in function of the topological distortions in the chains (Y-junction, zigzag defects defects, loop domains) in place of a strictly linear assembled superstructure. The second band shifts with time toward higher wavelengths and its intensity ($I_{\lambda 2}$) increases. As the interparticle spacing decreases, the first peak becomes weaker, while the second peak intensifies and shifts to longer wavelengths. The wide range of different chain morphologies observed in the extended networks accounts for the broadness of the emerging longitudinal plasmon band and the absence of isosbestic points in the time-dependent spectra [204].

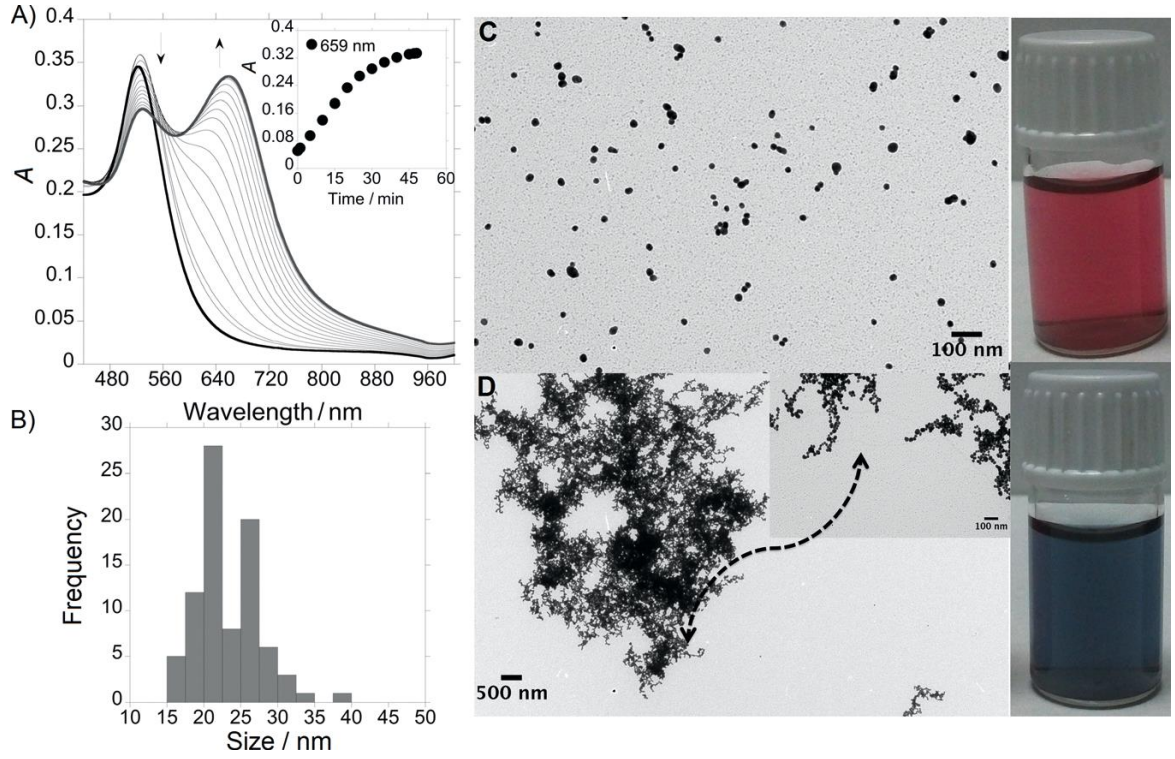

Figure 2.7: A) UV/Vis absorption spectra recorded in real-time (one spectrum per minute) during the self-assembly of AuNPs@citrate by L^{2-} to form AuNPs@$(L)^{2-}$. B) Size distribution diagram for AuNPs@$(L)^{2-}$. Visual color changes and TEM images of C) AuNPs@citrate and D) gold nanowire formed from AuNPs@$(L)^{2-}$.

The spectral change associated with the progressive aggregation of the NPs into chains and branched networks was also demonstrated by TEM. (**Figure** 2.7 C,D) Consequently, the number of single NPs progressively decreases, leading to a decrease in the intensity of the first peak ($I_{\lambda 1}$).

The ζ-potential of the original AuNPs@citrate solution was $\zeta_0 \approx$ -33.5 $mVcm^{-1}$, which is high enough (in absolute value) to keep the NPs electrostatically stable, and avoid aggregation due to repulsive forces between the negatively charged citrate ions. The use of citrate permits a controlled ligand exchange of the ions adsorbed on the surface. This spontaneous assembly is attributed to the electric dipole formed by the anisotropic organization of the ligands on the surface of the NP[256]. After the addition of L^{2-}, a destabilisation of the system was obtained with a value of ζ-potential ≈ -27.0 $mVcm^{-1}$. The effect of amine functionality on binding to the surface of AuNPs has been investigated[257], and recently Chegel *et al*. reported experimental and theoretically studies about the cooperative functionalities of amine and thiol groups for aggregation of AuNPs[258]. However, some authors have claimed that one type of amine group can readily bind to Au colloids, whereas others cannot[259]. In that case, an efficient surface displacement of citrate ions on the presence of L^{2-} could take place due to a cooperative functionality of the deprotonated amine groups, and the sulfur atom capable of forming stable chimica bonds with gold atoms.

In the absence of linker molecules, the aggregation of gold nanospheres could be mainly caused by van der Waals attraction, yielding random and irregular geometries and usually leading to rapid precipitation. The presence of a functional linker as L^{2-} in the surface of NPs minimizes the effect of van der Waals attractions by significantly increasing long-range interactions represented by electrostatic forces[260]. Experimentally speaking, the ζ-potential distribution seems to play the major role in linker-mediated self-assembly of AuNPs. As shown in **Figure** 2.7 C,D, a color change from intense red to blue was also observed.

In this particular case, the chainlike-structured AuNPs@$(L)^{2-}$ were observed after no longer reaction time (45 min) due to connection between one particle with other NPs from solution. These superstructures remained unchanged even for prolonged incubation times such as two weeks.

2.3.4 Interaction of AgNPs@$(L)^{2-}$ and AuNPs@$(L)^{2-}$ with Hg^{2+}

Trying to apply the obtained nanostructures as optical effective nano chemosensors, the sensing of Hg^{2+} using the colloidal systems AgNPs@L^{2-} and AuNPs@L^{2-} was carried out in aqueous solution. Changes in the absorption spectra of the colloidal systems AgNPs@$(L)^{2-}$ with spherical (**Figure** 2.8 (A,B)) and triangular (**Figure** 2.9) shapes were observed after the addition of increasing amounts of $HgCl_2$. In both cases, a shift of the SPR bands in the UV/Vis spectra suggest a continuous deformation of the chains, that is confirmed by TEM microscopy. (**Figure** 2.8 D,E and **Figure** 2.9 D,E) The ζ-potentials of the spherical and triangular AgNPs@$(L)^{2-}$ solutions were $\zeta_{spherical}$ -27.8 $mVcm^{-1}$ and $\zeta_{triangular}$ -19.1 $mVcm^{-1}$, respectively. In both cases, after the addition of Hg^{2+}, a destabilisation of the systems was observed, and the value of ζ-potentials changes to ζ spherical -22.5 $mVcm^{-1}$ and ζ triangular -17.0 $mVcm^{-1}$.

Given these results, we can conclude that the destabilisation of the spherical and triangular AgNPs@$(L)^{2-}$ systems and the loss of the assembly, could be due to the more favorable interaction of L^{2-} with Hg^{2+} to that observed for L^{2-} with AgNPs. The exchange of L^{2-} adsorbed on the surface produces a decrease of the negative net charge in the NP surface, which causes an increase of the ζ-potentials.

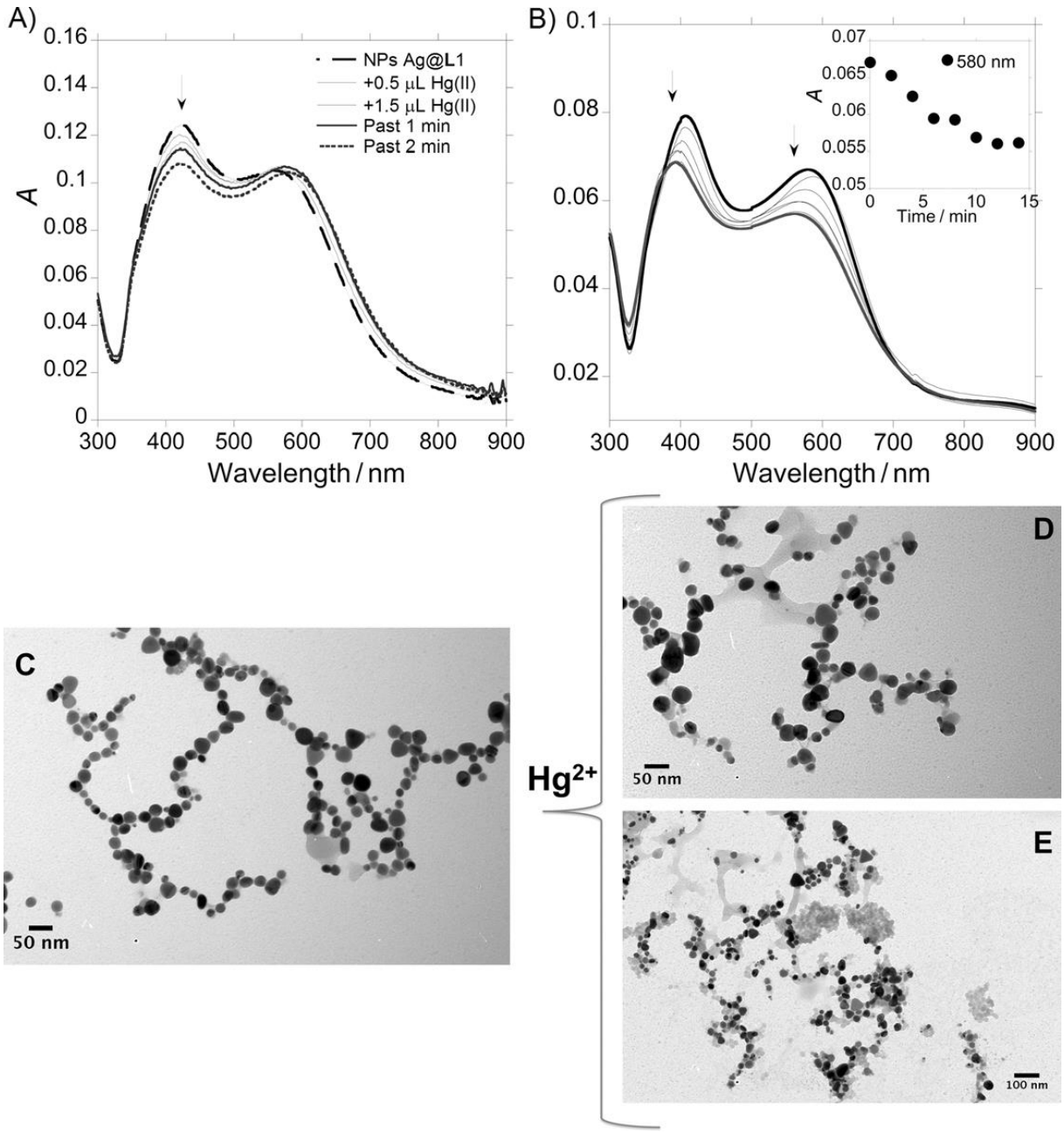

Figure 2.8: A) Spectrophotometric titration of spherical AgNPs@$(L)^{2-}$ with the addition of increasing amounts of $HgCl_2$ in aqueous solution. B) Modification with time in the absorption spectra of AgNPs@$(L)^{2-}$ with the addition of 6 μL of $HgCl_2$ (1:1 L/M). TEM images of an aqueous solution of spherical AgNPs@$(L)^{2-}$ C) before and D,E) after the addition of $HgCl_2$ (1 equiv, $[HgCl_2]=1.10x10^{-3}$ M).

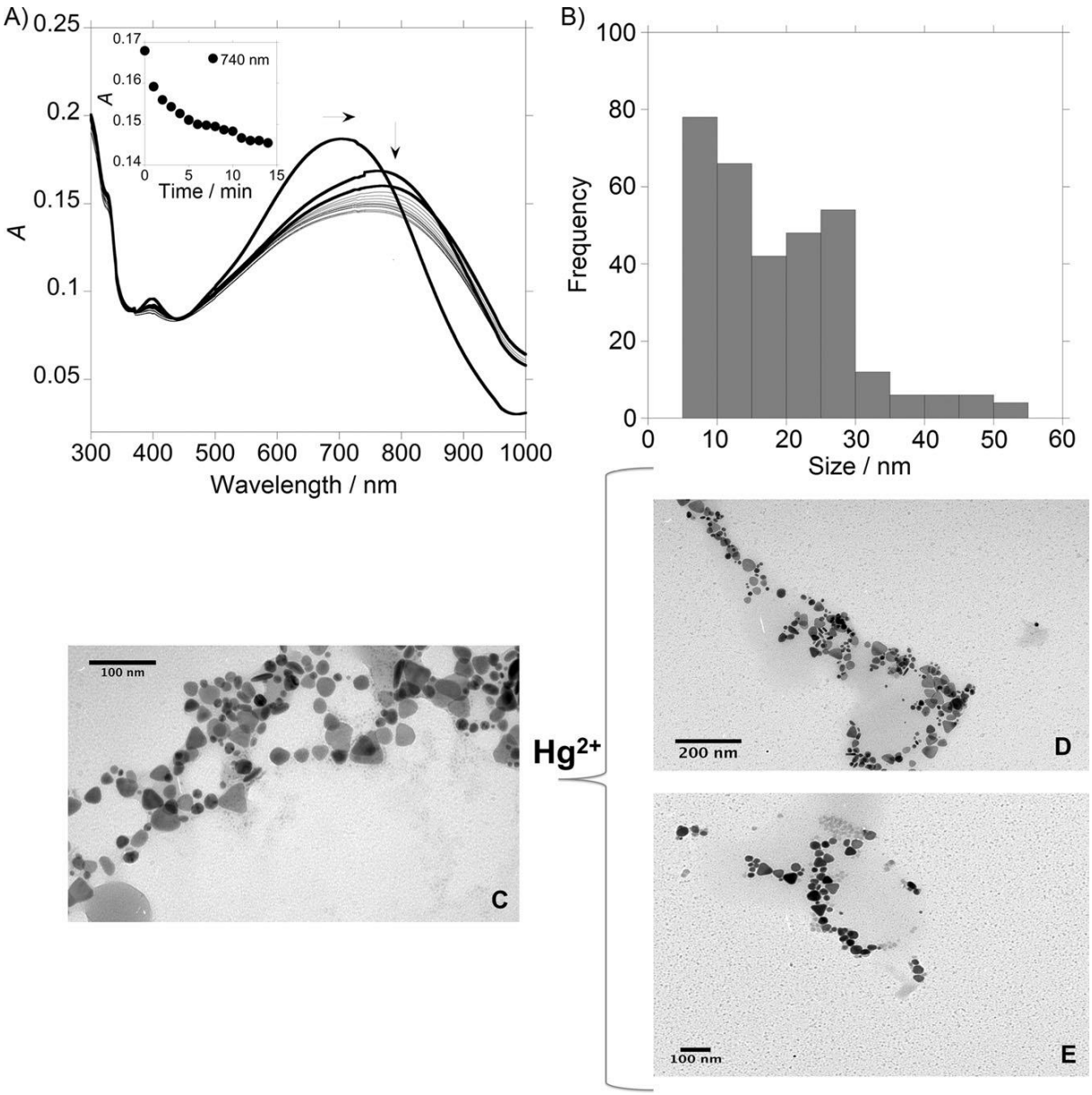

Figure 2.9: A) Modifications with time in the absorption spectra of triangular AgNPs@$(L)^{2-}$ with the addition of $HgCl_2$ (22 µL, 1:1 L/M). B) Size distribution diagram for an aqueous solution of triangular AgNPs@$(L)^{2-}$ after the addition of $HgCl_2$ (1 equiv, $[HgCl_2]=1.10x10^{-3}$ M). TEM images of an aqueous solution of triangular AgNPs@$(L)^{2-}$ C) before and D, E) after the addition of $HgCl_2$ (1 equiv, $[HgCl_2]=1.10x10^{-3}$ M).

On the other hand, different results were obtained for linker L^{2-} adsorbed on the AuNPs surface because a more stable bond is formed compared with that obtained for L^{2-} and Hg^{2+}, explaining that the AuNPs@$(L)^{2-}$ assembly remains unchanged after the interaction with this metal ion.

The sensitivity of this nanoassembly system AgNPs@$(L)^{2-}$ (spherical shape) toward Hg^{2+} was found to be comparable to the small fluorescent molecular system L. The value for the limit of detection (LOD)

shows that the best candidate for the detection of this metal ion is system AgNPs@$(L)^{2-}$, with the minimum amount of Hg^{2+} detectable being 8.3 ppm, whereas the LOD value with compound L was 19.0 ppm. The selectively of system L towards Hg^{2+} was also explored as shown in **Figure** 2.10 and **Figure** 2.11.

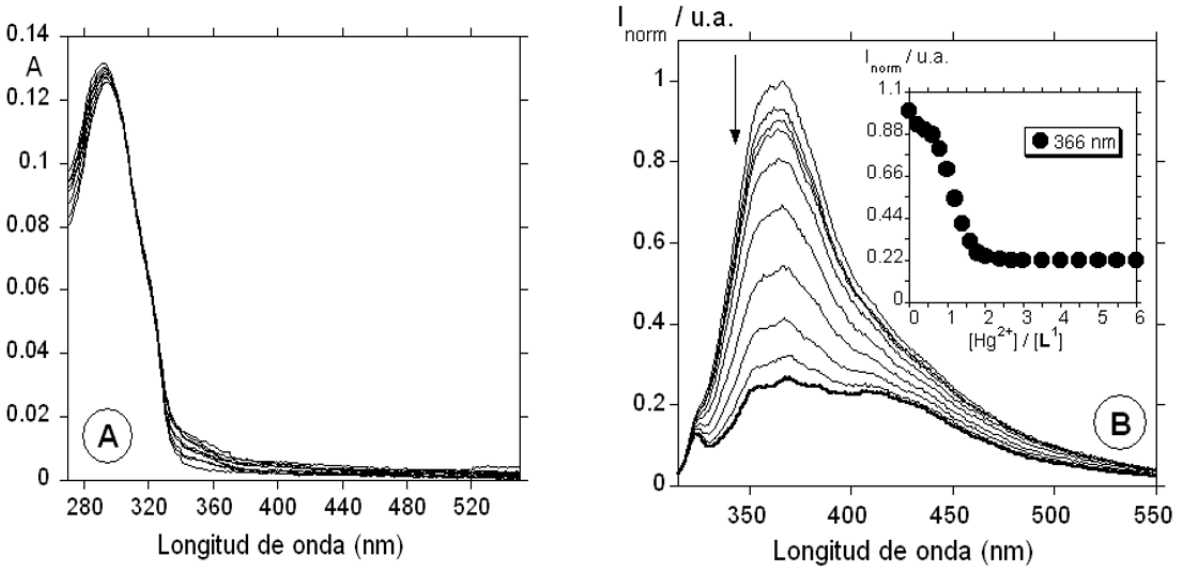

Figure 2.10: Spectrophotometric (A) and spectrofluorimetric (B) titrations of compound L as a function of added Hg^{2+} in absolute ethanol. The inset shows the normalised fluorescence intensity at 366 nm (B) λ_{exc} = 295 nm; λ_{em}= 366 nm, [L] = $1.00.10^{-5}$ M.

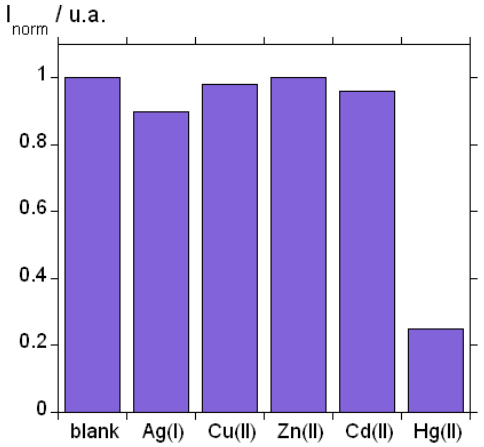

Figure 2.11: Normalised fluorescence intensity of receptor L in the absence and presence of one equivalent of different metal ions (Ag^{+}, Cu^{2+}, Zn^{2+}, Cd^{2+}, Hg^{2+}) in absolute ethanol. λ_{exc} = 295 nm; λ_{em}= 366 nm, [L] = $1.00x10^{-5}$ M.

2.4 Conclusions

This study of 1D self-assembly of silver nanoparticles (AgNPs) and gold nanoparticles (AuNPs) demonstrates direct evidence of the cooperative interaction between the metal nanoparticles (MNPs) and the deprotonated polyamine compound L^{2-} at the nanoscale in aqueous solution.

The unexpected symmetry-breaking that occurs when L^{2-} is added to an aqueous suspension of citrate-capped isotropic AgNPs and AuNPs was attributed to the ligand-mediated induction of a surface electrical dipole. At least three features of potentially modifying L^{2-} could influence citrate-stabilised AgNPs and AuNPs: (1) the presence of a sulfur atom, which can form covalent bonds with silver and gold atoms; (2) the presence of ionizable functional groups (amine); and (3) the charge (+/-) of ionizable functional groups. Electrostatic repulsion between AgNPs and AuNPs was progressively reduced, and the stability of the electric dipole associated with charge separation on the nanocrystal surface was potentially enhanced by spatial partitioning of L^{2-} and citrate-capping ligands. As a consequence, highly extended 1D NP assemblies in the form of discrete chains, bifurcated and looped chains, or interconnected chain networks are assembled spontaneously as the concentration of surface-adsorbed L^{2-} molecules increases.

Monoanionic compound L^{2-} causes shifts to the initial absorption spectra of AgNPs and AuNPs, and can be used for development of a surface plasmon resonance (SPR) chemical and biomolecular sensing platform because the interaction of citrate- stabilised AgNPs and AuNPs with the aforementioned compound is a very sensitive easy-to-visualize process.

The sensing of Hg^{2+} in aqueous solution using AgNPs@$(L)^{2-}$ and AuNPs@$(L)^{2-}$ was carried out. A destabilisation of the system AgNPs@$(L)^{2-}$ (spherical and triangular shape) and the loss of the assembly were observed due to the interaction of L^{2-} with Hg^{2+} is more favorable to that observed for L^{2-} with AuNPs. Linker L^{2-} binds to AuNP surfaces and forms a more stable bond compared with that obtained between L^{2-} and Hg^{2+}, explaining that the AuNPs@$(L)^{2-}$ assembly remains unchanged after the interaction with this metal ion.

3 Chapter 3

Synthesis and Characterisation of $PtTe_2$ Multi-Crystallite Nanoparticles using Organotellurium Nanocomposites

Published in: Javier Fernández-Lodeiro, Benito Rodriguez-Gonzalez, **Adrián Fernández-Lodeiro**, Fernando Novio, Daniel Ruiz-Molina, José Luis Capelo, Alcindo Dos Santos, Carlos Lodeiro. "Synthesis and Characterization of $PtTe_2$ Multi-Crystallite Nanoparticles using Organotellurium Nanocomposites." *Scientific Reports (NPG)*, **7**:9889 (2017), IF: 4.259. DOI: 10.1038/s41598-017-10239-8

Candidate contribution: helped in the synthesis, analysis and spectroscopic characterisation of the nanomaterials and helped in the discussion of all the analysed data and the writing of the final version of the manuscript.

3.1 Introduction

The development of materials at the nanoscale has attracted the attention of the scientific community because of their new and improved properties compared with those of their bulk counterparts[261]. Their physicochemical properties have been revealed to be dependent on their final composition, size and shape, among other factors[262,263,264]. In this regard, nanostructured metal chalcogenide (MC) materials are the subject of increasing research as a result of the numerous applications reported for these systems, primarily in electronics and energy conversion and storage[263,264,265,266], but also in catalysis[267], aerogel fabrication[268,269], semiconducting materials[270], among others.

Among the different MCs reported in the literature, binary systems containing tellurium have been extensively explored in recent years, largely due to their potential applications in memory devices[271], photovoltaic cells[272], thermoelectrics[273], catalysis[274] and biochemical[275] applications. Specifically, binary-phase systems based on Pt-Te provide an excellent combination of platinum as metal and tellurium as a semiconductor to provide enhanced thermoelectric properties in binary-phased nanocomposites[276] or photothermal therapy[277].

A convenient route for the production of MC materials is the use of organometallic derivatives as a *single source precursor* by thermal decomposition[278,279,280,281,282,283].

The chemistry of platinum with sulphur derivatives has been widely explored; to a lesser extent, so has that with selenium-containing ligands. By contrast, organic tellurium-based ligands have received less attention, such as in the case of organic ditellurites (R_2Te_2). This knowledge gap regarding the role of organic tellurides in coordination chemistry led to early assumptions that they behaviour similar to their chalcogenide counterparts S and Se; however, the rapid development of this field in recent decades has led to this preconception being discarded[284].

It is commonly accepted that R_2Te_2 produces a variety of tellurolate metal complexes with low-valent Pt precursors through different mechanisms, with the most common being Te-Te oxidative addition and/or Te-C reductive cleavage[284]. The evident structural differences between these platinum tellurolate complexes have revealed their large dependence on different experimental factors, such as the type of platinum precursor applied, the nature of the R group in the Te reagent, and the solvent or temperature used during the reaction[284,285,286,287,288]. However, reports about intact coordinated R_2Te_2 compounds are limited[289]. Moreover, to the best of our knowledge and in contrast to the commonly used low-valent platinum organometallic precursors, the use of platinum precursors in high oxidation states has been rarely reported.

Recently, Fernández-Lodeiro *et al*. reported on the spontaneous tendency of Ph_2Te_2 to reduce Au(III) into Au(0) nanoparticles[290]. This reaction presumably occurs via Te-Te cleavage with concomitant

formation of $PhTeCl_3$ and an Au(I) intermediate. This phenyl tellurium trihalide is prone to hydrolysis and could be transformed into oxohalides ($PhTe(O)X_n$), tellurinic acids (PhTeOOH) or their corresponding anhydrides [$PhTe(O)_n$] as a result of different hydrolysis stages[291292]. Additionally, in the presence of O_2 and H_2O as well as coordinative solvents, the photodecomposition of Ph_2Te_2 produced similar tellurinic acids or anhydride derivatives[293]. These organotellurium derivatives with a simple phenyl group usually evolve into a random polymeric structure via aggregation/condensation processes[294], producing an organometallic shell over gold cores. With these precedents in mind, we have now applied this novel organotellurium chemical approach to fabricate new monodisperse and size-modulated (nano- and micrometre scale) organometallic Pt-Te NPs, which can be easily dispersed in common organic and environmentally friendly solvents. Moreover, multi-crystallite $PtTe_2$ NPs with well-defined spherical shapes and dimensions (depending on the original size of the precursor) were obtained upon annealing the initial Pt-Te polymeric nanomaterial. These results provide an exciting opportunity to advance the knowledge of organotellurium chemistry applied to noble metal nanomaterial fabrication and offer the opportunity to better comprehend the properties of these new platinum/tellurium nanomaterials.

3.2 Experimental Section

3.2.1 Materials

Hydrogen hexachloroplatinate (IV) hydrate (99.99 % metal basis, CAS: 26023-84-7), Diphenyl ditelluride (98%, CAS: 32294-60-3), Calcium hydride (95%, CAS: 7789-78-8), Polyvinylpyrrolidone (PVP40, CAS: 9003-39-8), 1,5-Pentanediol (97%, CAS: 111-29-5) were purchased from Sigma Aldrich.

3.2.2 Synthesis of organometallic Pt-Te NPs.

The one-pot synthesis of the nanoparticles was performed as follows: an acetonitrile (2 mL) solution of Ph_2Te_2 (3×10^{-5} mol) was quickly added into a two-neck round bottom flask, coupled with a drying tube, containing $H_2PtCl_6.H_2O$ (1×10^{-5} mol) in boiling acetonitrile (48 mL).

The resulting dark red solution was maintained under reflux for an additional 1 h and then cooled on an ice/water bath. Immediately after cooling, the nanoparticles were isolated by centrifugation (8000 rpm × 30 min). The centrifugation procedure was repeated three times. To study the effects of water, light and/or oxygen on the formation of the organometallic Pt-Te NPs, this general procedure was performed in different conditions (summarised in **Table** 3-1).

Table 3-1: Experimental reaction conditions ([Reagent] in n/L and % H_2O in V/V; P= Presence and A= absence).

Sample	Media	$[Pt^{4+}]_{final}$	$[Te\text{-}Te]_{final}$	$\%H_2O$	O_2	Light
R1	CH_3CN	2×10^{-4}	6×10^{-4}	0	P	P
R2	CH_3CN	2×10^{-4}	6×10^{-4}	0.1	P	P
R3	CH_3CN	2×10^{-4}	6×10^{-4}	0.2	P	P
R2.1	CH_3CN	2×10^{-4}	6×10^{-4}	0.1	A	P
R2.2	CH_3CN	2×10^{-4}	6×10^{-4}	0.1	P	A
R4	CH_3CN	2×10^{-3}	6×10^{-3}	0.2	P	P
R5	CH_3CN/CH_2Cl_2	$8. \times 10^{-3}$	2.4×10^{-2}	0.2	P	P

The syntheses in the presence of oxygen was performed under an open atmosphere. For the synthesis in the absence of oxygen, the entire reaction occurred under nitrogen atmosphere, and the solvent was deoxygenated under US and nitrogen bubbling for 30 minutes prior to use.

3.2.2.1 Reverse order of reagent addition (entry R4).

A solution of 2 mL of acetonitrile containing 1×10^{-4} mol of H_2PtCl_4 was added to 48 mL of boiled acetonitrile solution containing 3×10^{-4} mol of Ph_2Te_2 (**Table** 3-1).

3.2.2.2 Synthesis in the presence of CH_2Cl_2/acetonitrile mixture (entry R5).

A dichloromethane/acetonitrile (1:1, 1 mL) solution of Ph_2Te_2 (3.6×10^{-4} mol) was quickly added to a flask containing a boiling acetonitrile (14 mL) solution of H_2PtCl_6 (1.2×10^{-4} mol). The solids were isolated by filtration on a sintered glass plate (No. 4) and washed repeatedly with acetonitrile and diethyl ether. The solid was then dispersed in acetonitrile (50 mL) under sonication and then isolated by centrifugation (3 cycles of 2000 rpm × 10 min). (**Table** 3-1)

3.2.2.3 Synthesis of multi-crystallite NPs.

The synthesis of $PtTe_2$ multi-crystallite NPs used an annealing process, which consisted of dissolving the organometallic Pt-Te NPs (11 mg) in 1,5-pentanediol (10 mL) under sonication. PVP_{40} (50 mg) was added to this brownish-red solution, and the sonication was maintained for an additional 10 minutes. The mixture was heated to 220 °C during 1 h. Colour changes from brownish-red to black developed during the heating process. After this heating time, the reaction mixture was cooled in an ice/water bath, and then the resulting crystalline nanoparticles were isolated by centrifugation 2 cycles (10000 rpm × 1 h) followed by washing with ethanol, ending the process by resuspending the clean $PtTe_2$ multi-crystallite NPs in absolute ethanol.

3.2.3 Fourier transform ion cyclotron resonance mass spectrometry analysis.

Fourier transform ion cyclotron resonance (FT-ICR) mass spectrometry (MS) studies were performed at the Scientific and Technological Research Assistance Centre (CACTI), University of Vigo using an APEXQe FT-ICR MS (Bruker Daltonics, Billerica, MA, USA), equipped with a 7 T actively shielded magnet. To follow the reaction by FT-ICR MS, 100 μL aliquots were removed directly from the reaction medium at different time intervals (1, 20 and 60 minutes). Each aliquot was diluted to 1 mL with 70:29.9:0.1 (v/v/v) CH_3CN/water/formic acid prior to injection into the mass spectrometer.

Ions were generated using a Combi MALDI-electrospray ionization (ESI) source. The mass spectra were obtained by ionization via an electrospray, using a voltage of 4500 V applied to the needle and a counter voltage of 300 V applied to the capillary.

3.2.4 Transmission electron microscopy analysis.

Microscopy analyses were performed at the CACTI, University of Vigo. A JEOL JEM1010 TEM working at 100 kV was used to obtain low-magnification TEM images. A JEOL JEM 2010F field-emission gun TEM working at 200 kV was used to obtain high resolution transmission electron microscopy (HRTEM) images. Energy Dispersive X-ray Spectrometry (EDS) maps were acquired by coupling the scanning unit of the microscope to an INCA 200 EDS system. Electron energy loss spectroscopy (EELS) spectra were collected in Scanning Transmission Electron Microscopy (STEM) mode using a Gatan GIF Quantum spectrometer with an energy resolution of 1.75 eV (Full width at half maximum (FWHM) Zero Loss peak), 0.5 eV/channel energy dispersion and an EELS collection semi-angle of 16 mrad. The EEL spectral background was subtracted using standard Digital Micrograph routines. All TEM samples were prepared by placing drop of the sample on a TEM copper grid coated with holey carbon thin film and then air dried. To avoid the interference due to the carbon foil grid, the EEL spectra were collected from areas of sample situated in a hole.

3.2.5 Scanning electron microscopy.

Scanning electron microscopy (SEM) images were taken using a Quanta environmental scanning electron microscope (FEI Quanta 650) operating between 20 and 5 kV with a spot size = 3.5. Samples dispersed in ethanol were deposited in aluminium holders used as support and metallised with platinum sputtering (sputter coating = 3 nm) before analysis.

3.2.6 X-ray photoelectron spectroscopy.

X-ray photoelectron spectroscopy (XPS) measurements were performed using a Phoibos 150 analyser (SPECS GmbH, Berlin, Germany) in ultra-high vacuum conditions (base pressure 1×10^{-10} mbar) with a monochromatic aluminium Kα X-ray source (1486.74 eV). All the spectra were referenced to aliphatic carbon at a binding energy of 284.8 eV.

3.2.7 UV/Vis and FT-IR spectroscopy studies.

The UV/Vis spectroscopy studies were performed using a JASCO 650 spectrophotometer provided by the PROTEOMASS-BIOSCOPE facility. A Bruker TENSOR (REQUIMTE-Chemistry Department, FCT-UNL) spectrophotometer was used to obtain the FT-IR spectra; All FT-IR experiments were performed in KBr disks.

3.2.8 Inductively coupled plasma analysis.

The Pt and Te contents in each studied sample were determined in the REQUIMTE-Chemistry Department, FCT-UNL analytical laboratory using an inductively coupled plasma (ICP) instrument from Horiba Jobin–Yvon (France, model Ultima), equipped with an RF of 40.68 MHz, a 1.00 m Czerny–Turner monochromator (sequential), and an AS500 autosampler.

3.2.9 Elemental analysis.

The elemental analysis (EA) was done in the REQUIMTE-Chemistry Department, FCT-UNL analytical laboratory by using an Elementar Thermo Finnigan-CE Instruments (Italy) Flash EA 1112 CHNS series.

3.2.10 Thermogravimetric analysis.

The thermogravimetric analysis (TGA) was performed in the CACTI, University of Vigo using a Setsys evolution (TG/DSC/DTA) Setaram instrument.

3.3 Results and Discussion

3.3.1 Synthesis and morphological characterization of organometallic Pt-Te NPs.

An acetonitrile solution of Ph_2Te_2 and H_2PtCl_6 was used as the starting material for the synthesis of Pt-Te NPs. The coordinating nature of this solvent plays a major role during the photodecomposition of the Ph_2Te_2 to form phenyltellurinic anhydride derivatives[293]. In a typical synthesis, a boiling acetonitrile solution containing H_2PtCl_6 was quickly added to an acetonitrile solution containing Ph_2Te_2. At the moment of addition, the dark red solution shifted to reddish brown, after which it was left for one hour at boiling temperature, resulting in the formation of a precipitate.

We also found a correlation between the water percentage during the reaction and the resulting organometallic nanocomposite; a distinctly lower yield and higher polydispersity were obtained at lower water contents. (**Figure** 3.1)

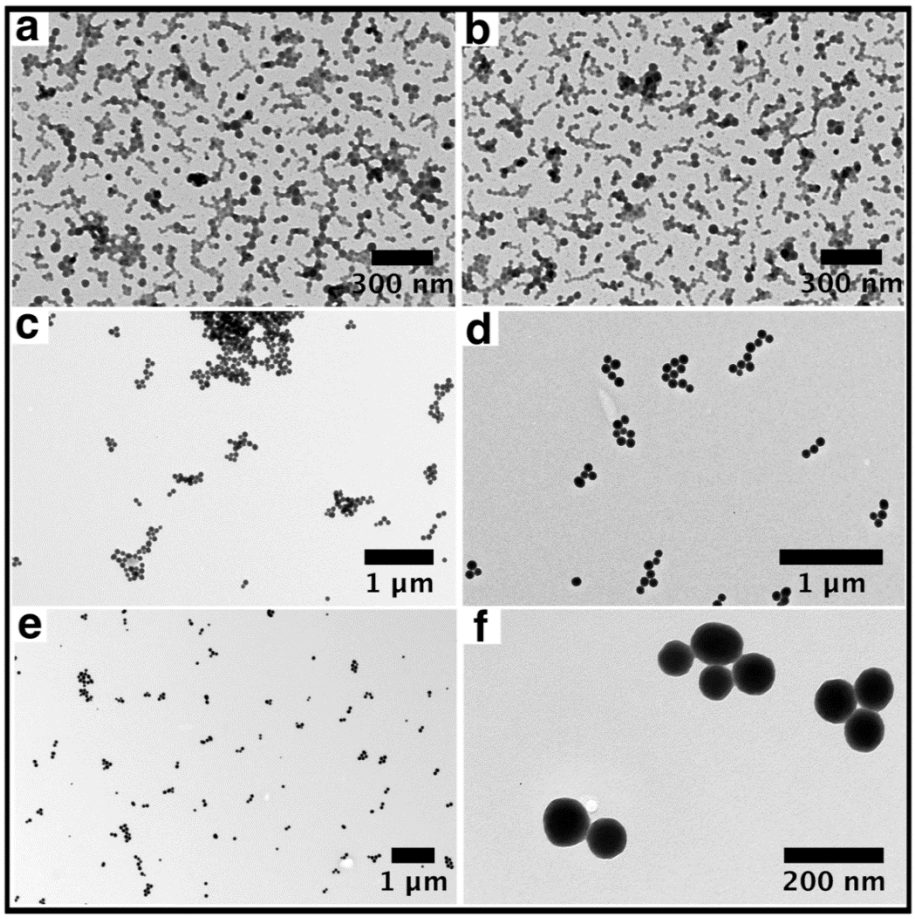

Figure 3.1: Low magnification electron transmission microscopy images obtained for R1 (a, b), R2 (c, d) and R3 (e, f).

Under low water-content conditions the crude reaction present red/Brown colour with transparent aspect. Only with centrifugation process at 14000 rpm x 1h was possible to obtain enough material for characterization. **R2** and **R3** were obtain in pure form with three centrifugation cycle at 8000 rpm x 30 min. in acetonitrile. This result can be correlated with the hydrolysis of phenyl tellurinyl chlorides ($PhTeCl_n$) formed as a sub-product of Ph_2Te_2 oxidation, similar to that observed for the previously reported gold system[290].

By contrast, no significant differences were observed for the reactions conducted under dark or inert atmosphere conditions. (**Figures** 3.2 to 3.5, **Table** 3-1)

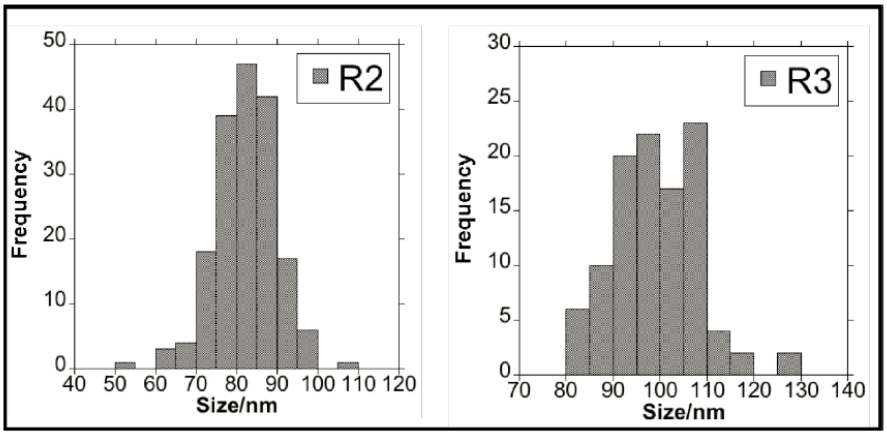

Figure 3.2: Histogram obtained for R2 and R3 samples. (Histogram was obtained counting a minimum of 100 particles per sample).

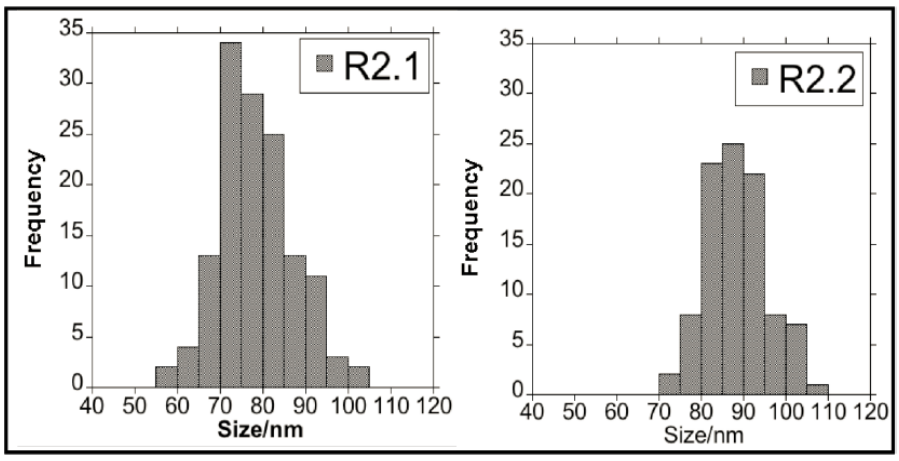

Figure 3.3: Histogram obtained for R2.1 (oxygen absence) and R2.2 (light absence) samples.

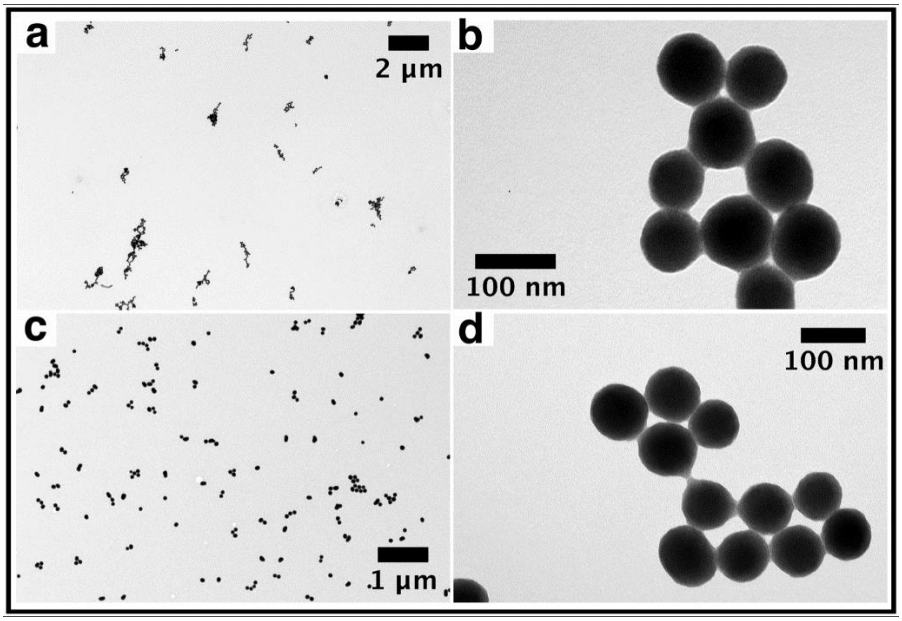

Figure 3.4: Low magnification TEM images obtained for R2.1 (a, b), R2.2 (c, d).

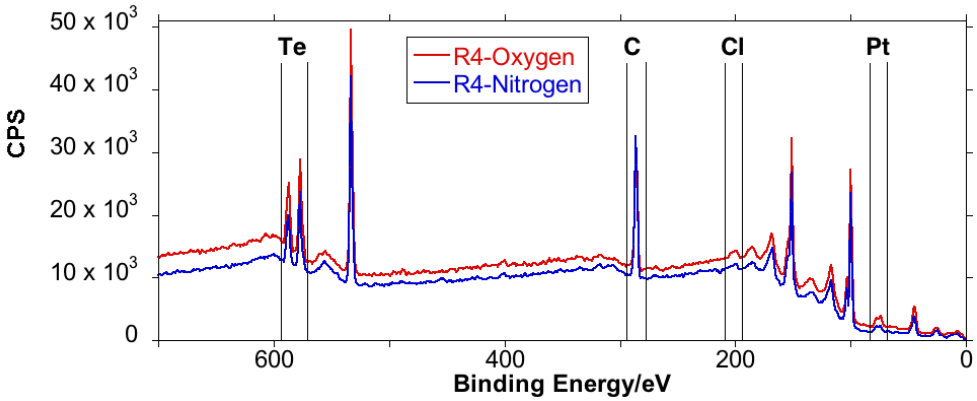

Figure 3.5: Overview X-ray photoelectron spectroscopy of R4 obtaining under N_2 or O_2 atmosphere.

In this respect, Ph_2Te_2 photodecomposition processes or additional oxidation by O_2 did not show any impact on the final nanostructuring of the obtained polymeric material.

Additionally, an increase in the initial reagent concentrations induced a size increase of the final nanoparticles, although with a higher resultant polydispersity. (**Figures** 3.6 to 3.9, **Table** 3-1)

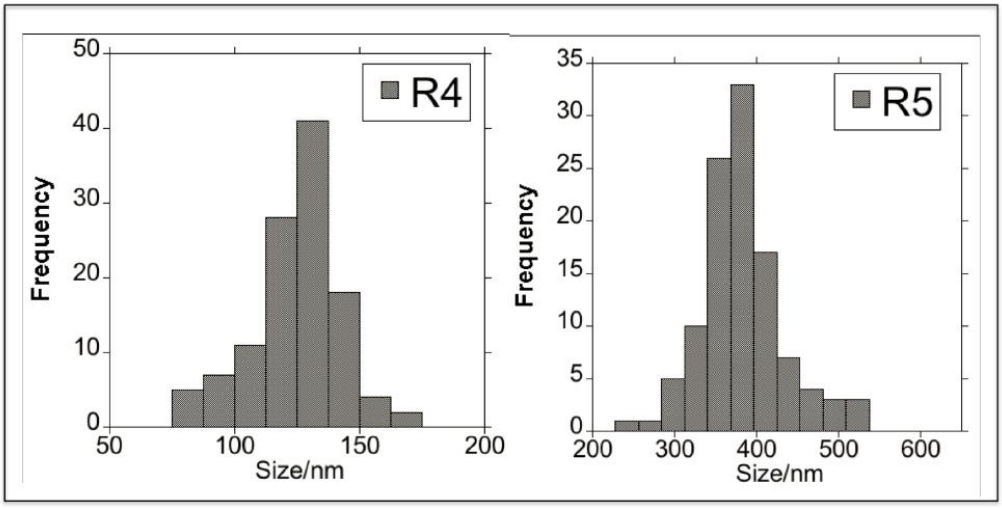

Figure 3.6: Histogram obtained for R4 and R5 samples.

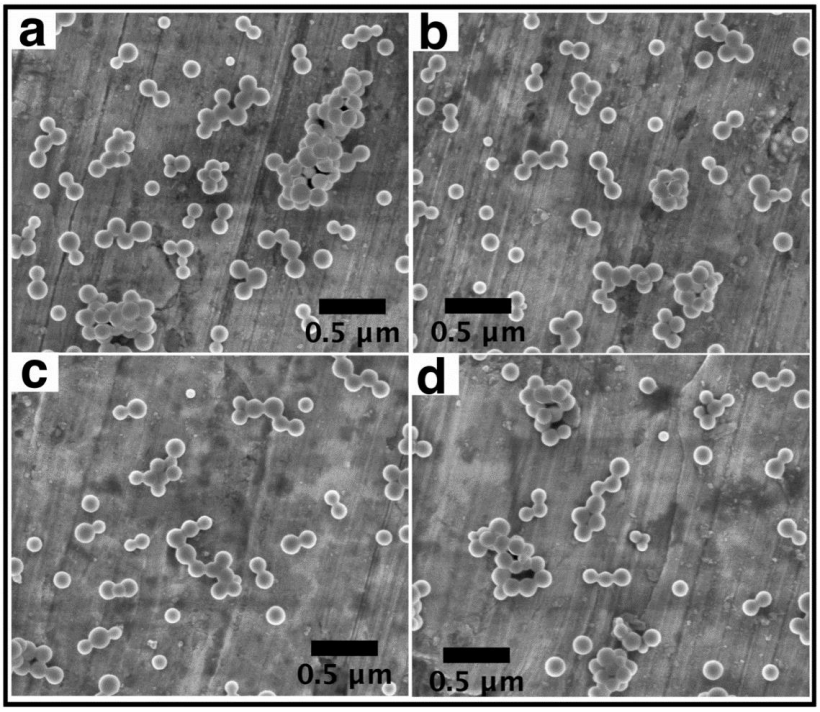

Figure 3.7: Low magnification SEM images obtained for R4.

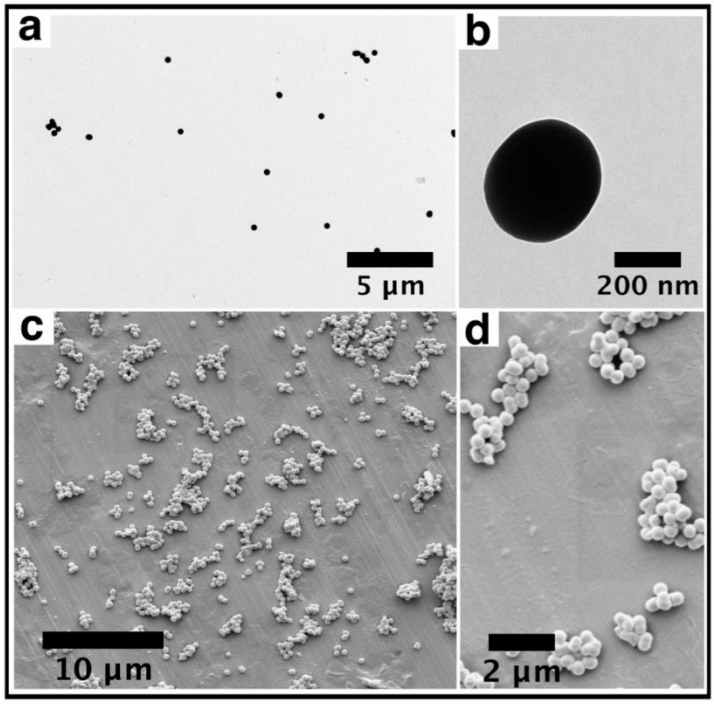

Figure 3.8: Low magnification TEM (a, b) and SEM (c, d) images obtained for R5.

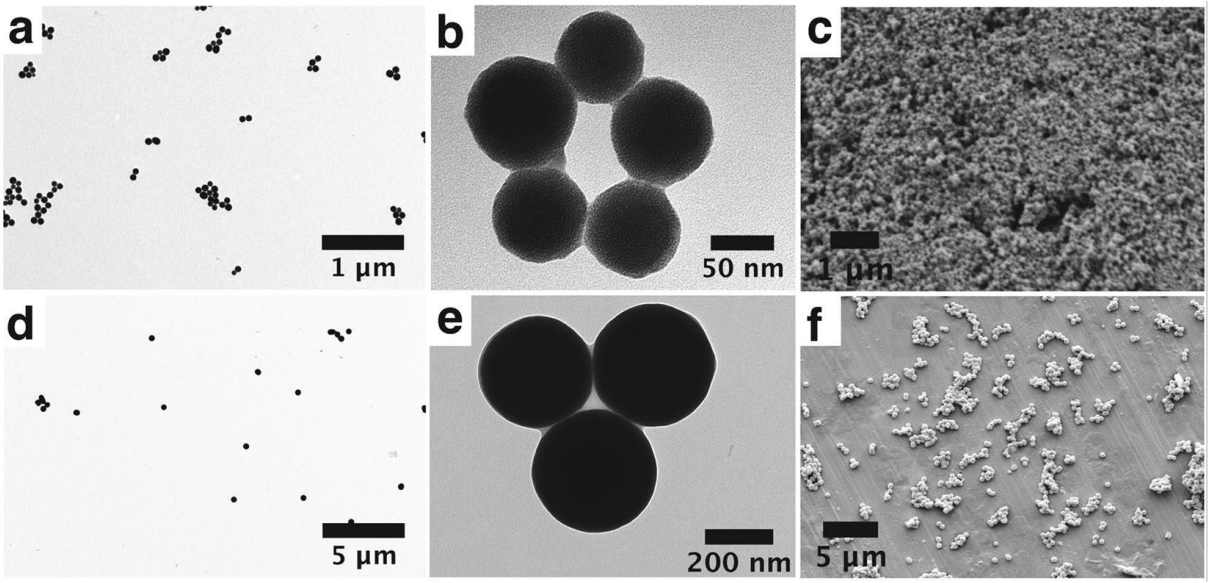

Figure 3.9: (a) Low magnification TEM (**a**,**b**,**d**,**e**) and SEM (**c**,**f**) images of different sizes of organometallic Pt-Te NPs obtained under higher initial reagent concentrations ([Pt(IV)] = 2.10^{-4} M, [Te-Te] = 6.10^{-4} M) (**a**,**b**,**c**) and ([Pt(IV)] = 8.10^{-3} M, [Te–Te] = $2.4.10^{-2}$ M) (**d**,**e**,**f**).

Modifying the reactant sequence addition also modified the reaction output, resulting in a more polydispersed material and a partial loss of the spherical morphology. (**Figure** 3.10)

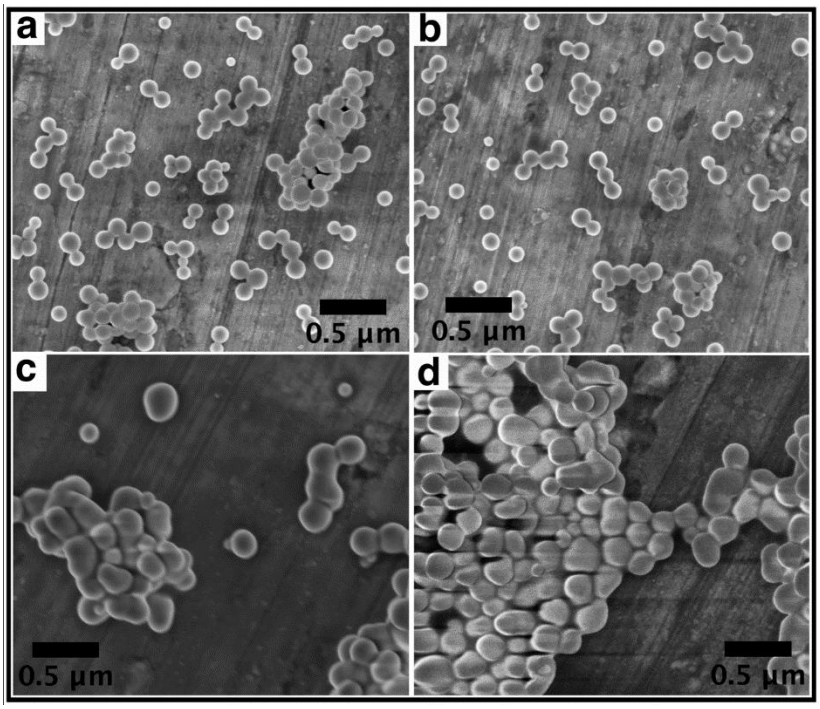

Figure 3.10: Low magnification SEM images obtained for R4 in normal condition (a and b) and modifying the reactant sequence addition (c and d).

The final organometallic Pt-Te NPs can be dispersed in absolute ethanol or water. (**Figure** 3.11)

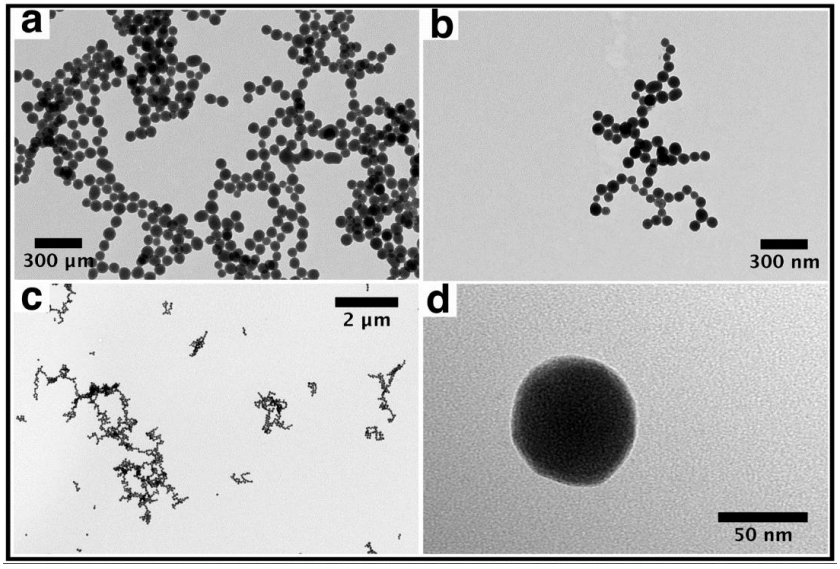

Figure 3.11: Low magnification electron transmission microscopy images obtained for R2 dispersed in absolute ethanol (a, b) and in water (c, d).

This observed behaviour with nucleophilic solvents is contrary to that observed with pure condensed tellurinic acid or anhydride derivatives formed in the previous reported gold system[290], indicating that in this case, the Pt ion was likely directly coordinated into the organometallic structures. This new polymeric material is not dissolved or disrupted in absolute ethanol as previously observed with the gold nanomaterial.

3.3.2 Chemical characterization of organometallic Pt-Te NPs.

Based on the electron microscopy evidence, the materials obtained in the presence or absence of oxygen and/or light have similar nanostructures; thus, we selected samples obtained in the presence of oxygen and light to perform a more complete characterization.

Figure 3.12 (panels 1 to 6) shows a High-Angle Annular Dark Field (HAADF) image together with five energy-dispersive EDS obtained for a group of Pt-Te NPs. These maps show that the major elements present in the particles are tellurium, platinum and carbon. In addition, the presence of oxygen and chlorine as minor elements was also confirmed.

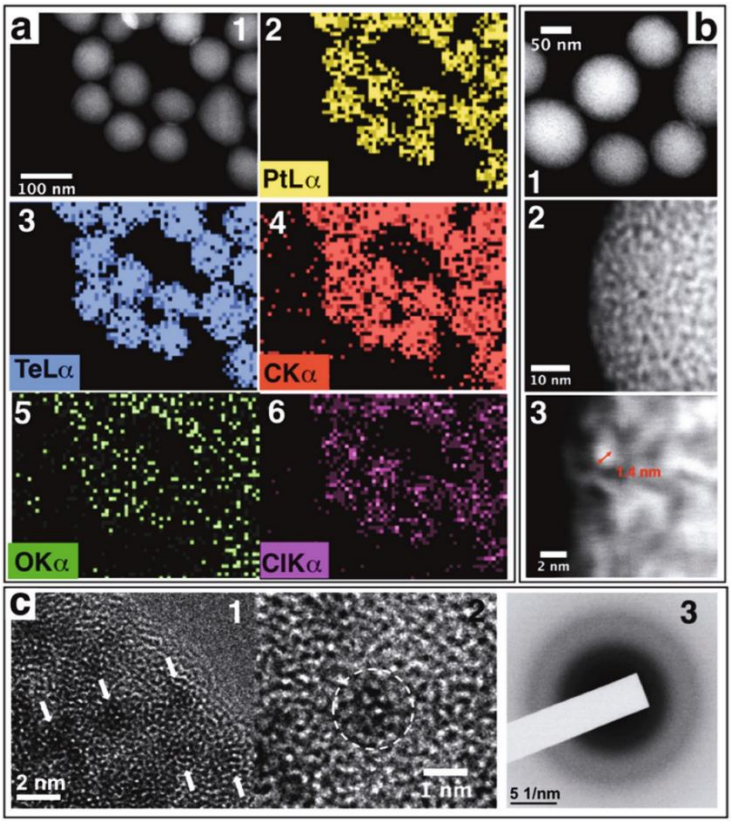

Figure 3.12: (a) STEM-HAADF image of a group of Pt-Te NPs and Te, Pt, C, O and Cl EDS elemental maps (1–6). (b) HAADF-STEM image: one group of isolated Pt-Te NPs (1) and two close ups (2) showing the complex structure and the nodules composed of high atomic-number elements (3). (c) HRTEM image and diffraction pattern showing the structure and demonstrating the lack of a crystalline structure in the nodules.

Similar results were obtained with the EDS X-ray microanalysis obtained from an individual particle. (**Figure** 3.13)

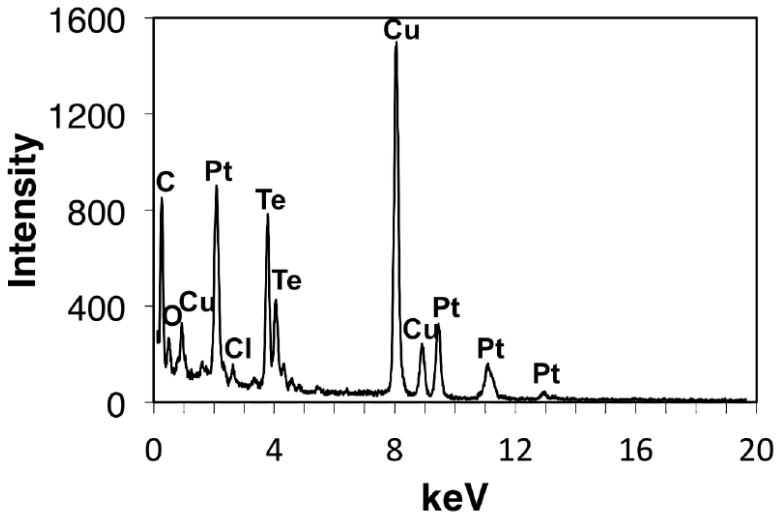

Figure 3.13: EDS X-ray microanalysis obtained from an individual particle.

Even though the spectrum shows a high Cu peak due to the contribution of the copper grid used in the TEM sample preparation, the main elements present in the particle are Te, Pt, C, O and Cl. Combined HRTEM and HAADF images were also obtained, as shown in **Figure** 3.12 (B 2,3). As seen in **Figure** 3.12 (B 1), the general trend indicates an increase in brightness from the outside to the centre of the particles, consistent with a spherical geometry and a mass-thickness contrast mechanism. The presence of a hole, or a non-uniform distribution of the elements within the particle, was discarded in light of the elemental profiles along the diameter of the particle. (**Figure** 3.14)

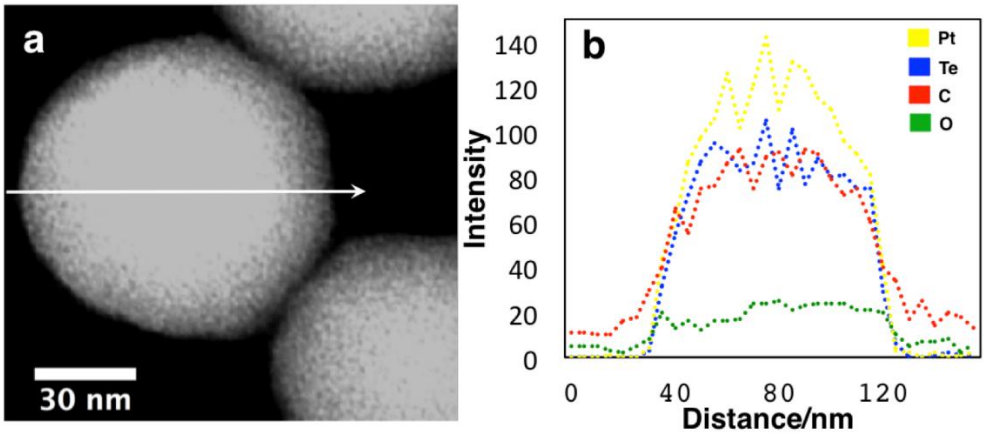

Figure 3.14: : (a) STEM-HAADF image of an as obtained organometallic Pt-Te NPs. (b) EDS intensity profiles of the PtLα1 signal (a), and O-Kα1, Pt-Lα1 Te-Lα1, and C-Kα1-2 along the white arrow marked in (a).

Images at higher magnification (**Figure** 3.12 B 2,3) showed the presence of a complex inner nanostructure; the contrast was not distributed evenly but showed grainy small nodules forming with

higher contrast levels. These images suggest that Te and/or Pt tend to concentrate in these approximately 1.4 nm nodules, and the other elements (C, O, and Cl) are mainly surrounding those nodules. Interestingly, TEM images at higher magnification (**Figure** 3.12 C) did not show the presence of lattice fringes in areas containing these nodules, nor any feature indicating the presence of a crystalline structure in the centre of the nodules. The amorphous character of the obtained Pt-Te NPs was confirmed by the electron diffraction pattern obtained from a group of those particles (**Figure** 3.12 C-3) and corroborated by the powder X-ray diffraction pattern obtained for the material. (**Figure** 3.15)

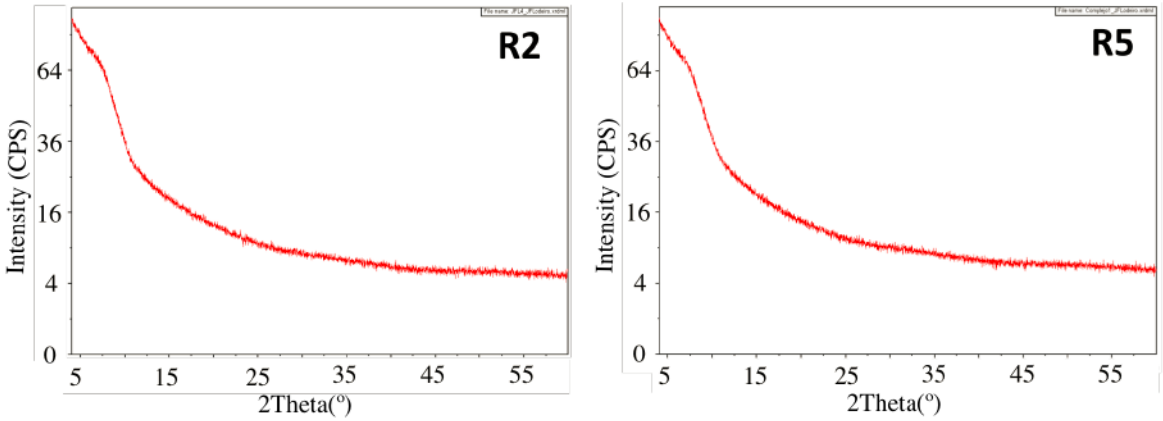

Figure 3.15: X-Ray diffraction pattern of organometallic Pt-Te NPs in different size.

Additionally, characterization using electron energy loss espectroscopy is displayed in **Figure** 3.16.

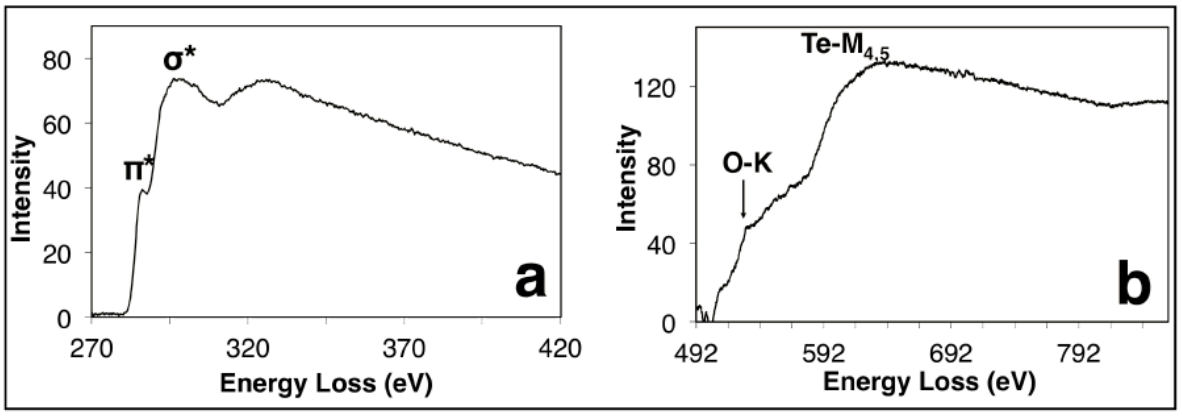

Figure 3.16: EEL spectrum in the region of the C K-edge (a) and Te, O edge (b) obtained for organometallic Pt-Te NPs.

The EELS spectrum in the carbon K-edge region shows two bands corresponding to two different electronic bonding states, one assigned to the π C=C bond peak at 285 eV and the other assigned to the σ C-C bond peak close to 297 eV. The oxygen and tellurium edges region is shown in **Figure** 3.16 B; in this region, the oxygen edge displays a relatively low intensity, especially compared with the intensity

and shape of the TeO_2 edges[295]. This result provides clear evidence of a large oxygen deficit compared with the relative content of oxygen in the TeO_2. Conversely, the Te edge shows an intense broad band, suggesting the presence of a large Te content and a mixture of electronic states in the Te bonds.

The X-ray photoelectron spectroscopy spectrum shown in **Figures** 3.5 and 3.17 shows a high Te (53%) percentage compared with those of C (35%), Pt (7%) and Cl (4.5%). Moreover, two signals can be assessed for Pt, namely, Pt $4f_{7/2}$ at 73.23 eV, Pt $4f_{5/2}$ at 76.58 eV and Pt $4f_{7/2}$ at 74.80, Pt $4f_{5/2}$ 78.15 eV.

Thus, the nanostructure contains mainly Pt(II) ($4f_{7/2}$ = 73.23 eV, $4f_{5/2}$ = 76.58 eV) with a small proportion of Pt(IV) ($4f_{7/2}$ = 74.80 eV, $4f_{5/2}$ = 78.15 eV), and the ratio of the areas of Pt(II):Pt(IV) is 4:1. (see **Figure** 3.17a)

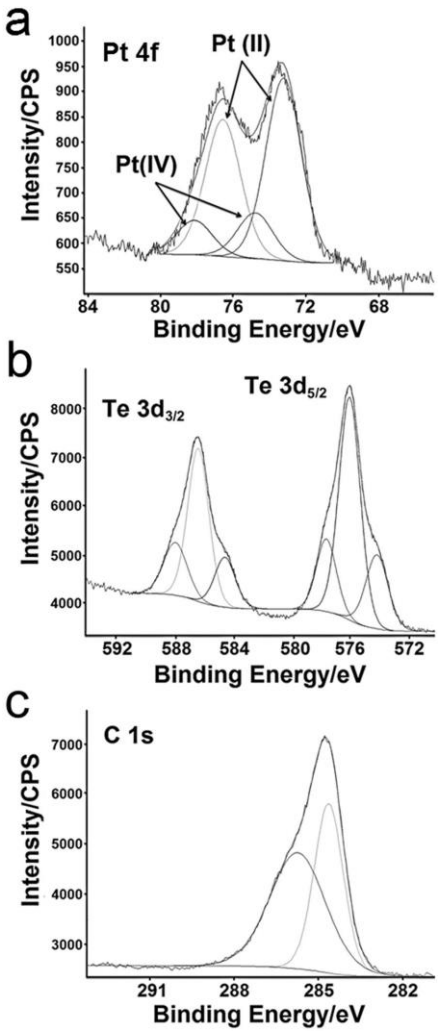

Figure 3.17: XPS spectrum of organometallic Pt-Te NPs. Binding energy spectrum of Pt 4 f (a), Te $3d_{3/2}$ and $3d_{5/2}$ (b), and C 1 s (c).

Three components were found for Te, presumably associated with the different oxidation states as revealed by EELS analysis. (**Figure** 3.17 B) The XPS chemical shifts for tellurium ($3d_{5/2}$ and $3d_{3/2}$) in different oxidation states appear in a narrow region. The main peaks appear at 576.1 ($3d_{5/2}$) and

586.4 ($3d_{3/2}$) eV, which correspond to telluroxide (TeO) functionalities[296,297]. If we focus on the $3d_{5/2}$ sub-spectrum of which one of the minor components (21%) at 574.2 ($3d_{5/2}$) and 584.6 ($3d_{3/2}$) eV could be attributed to (Ph_2Te_2)–Pt units, the other minor component (18%) at 577.7 ($3d_{5/2}$) and 588.0 ($3d_{3/2}$) eV should be attributed to oxidised species of telluride. Finally, two energy peaks appear in the C 1 s region associated with aromatic C-C bonds (284.6 eV) and the C-Te bond (285.7 eV). (**Figure** 3.17)

FT-IR spectroscopy of the Pt-Te NPs (**Figure** 3.18) show characteristic bands of phenyl C_{sp2}-H (3051 cm^{-1}), C=C stretches (1568 cm^{-1}, 1469 cm^{-1}, 1431 cm^{-1}), and C–H bending in-plane (1053 cm^{-1}, 1014 cm^{-1}) and out-of-plane (727 cm^{-1}, 686 cm^{-1}). Additionally, aromatic ring overtones can be observed in the region of 2000–1630 cm^{-1} [298,299].

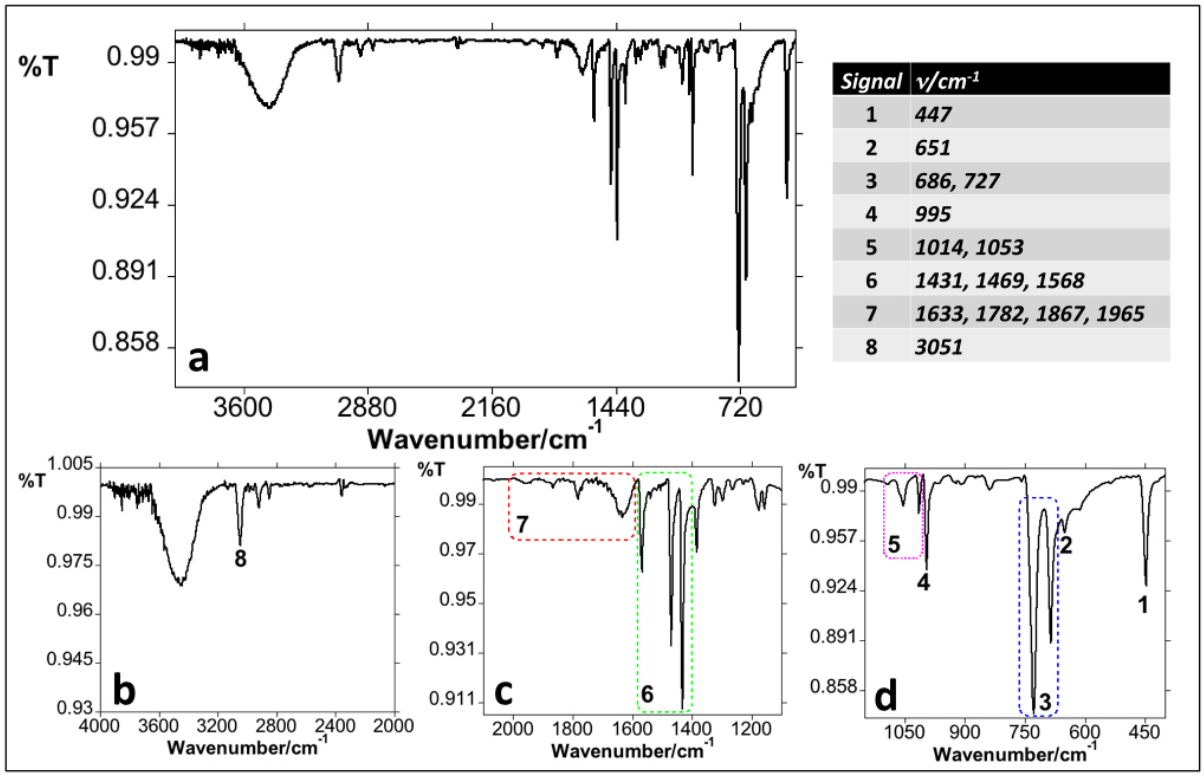

Figure 3.18: FT-IR spectrum (overview a, different spectra close-ups b, c, d) of organometallic Pt-Te NPs in KBr disk.

Attempts to characterize the nanomaterial with Raman spectroscopy were unsuccessful, as the nanocomposite was burned during the measurements by the action of the laser, and the results were inconclusive.

The composition of the material was studied by elemental analysis and inductively coupled plasma (ICP). We analysed two different particle sizes, denoted as R4 and R5. In this way, we obtained the following values, expressed as a percentage (R4/R5): %C (22.51/22.81), %H (1.52/1.59), %Pt

(26.03/24.37) and %Te (44.55/45.84). The slight difference in percentages obtained may be related to the partial change in the reaction conditions. (**Table** 3-1)

The composition differences obtained by XPS and ICP/EA show increased tellurium and carbon percentages for XPS analysis. The XPS spectrum gives information about the elemental composition of the shallow surface region. As photons possess a limited penetrating energy (up to 10 nm), only those electrons pertaining to atoms near the surface can be counted. This quantitative technique provides the average composition over an approximate 10 nm depth inside the nanoparticle. Taking into account these considerations inherent to the technique, the comparatively increased tellurium and carbon percentages can be explained as a result of the adsorption and/ or coordination of the remaining Ph_2Te_2 molecules on the surface-formed nanocomposite.

Using thermogravimetric analysis, we determined the thermal behaviour of organometallic Pt-Te NPs with the aim of delimiting the parameters for the annealing process. We observed that the decomposition occurred under multistage process between 25 °C and 1500 °C. The first mass loss (−37.22% completed above 400 °C) is associated with three exothermic changes, as seen in the differential thermogravimetry (dTGA) curve, with the first exothermic signal appearing near 200 °C. We believe that this first exothermic signal could be related to the crystallization of $PtTe_2$. (**Figure** 3.19)

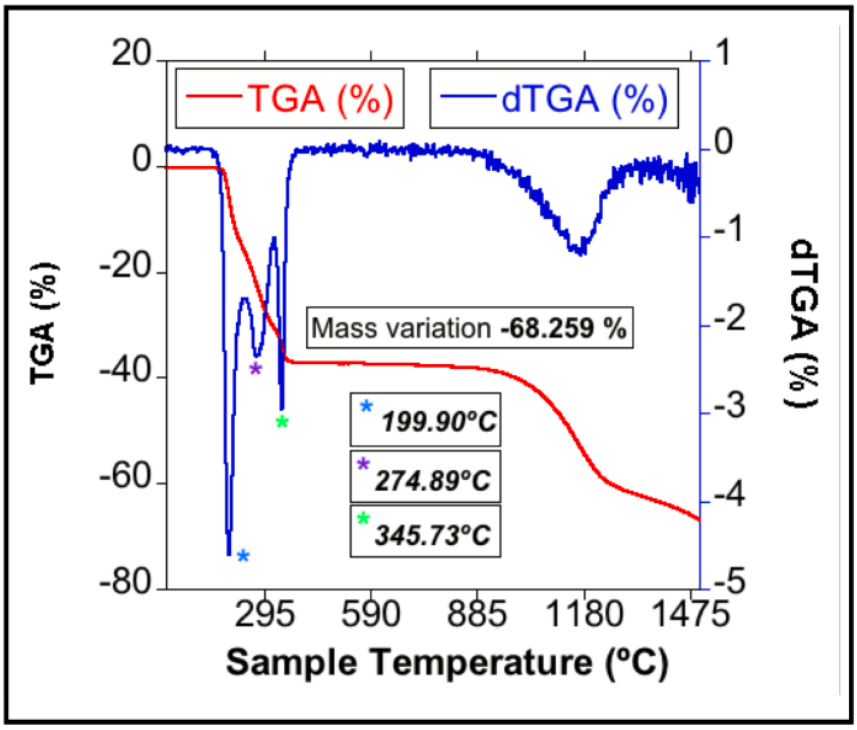

Figure 3.19: TG/dTG curves obtained for organometallic Pt-Te NPs.

3.3.3 Metal-ligand interaction during the reaction.

Metal-ligand interaction and the formation of the Pt-Te NPs was investigated using UV/Vis spectroscopy and FT-ICR-MS (Fourier transform ion cyclotron resonance mass spectrometry) studies. The spectroscopy profile of Ph_2Te_2 presents two absorption bands, one near 300 nm, which was assigned to the nTe-π* transition (phenyl group charge transfer band), and one near 397 nm, corresponding to the nTe-σ* transition (Te-Te charge transfer band)[300,301]. To study the interaction of the Te-Te residue with the Pt cation, we selected two ligand:metal stoichiometries (L:M = 3:1 and 1:1).

Upon addition of 1 equivalent of Pt^{4+} a new absorption band centred in 407 nm with a shoulder at *ca.* 500 nm is observed. The evolution of the absorption spectrum over time presents an increase in the region between ca. 320 and 600 nm, with an increase in base line as derived of organometallic Pt-Te nanocomposite formation. The interaction study upon addition of 1/3 equivalent of Pt^{4+} presents a similar time dependent behaviour, but with a lower increase of absorption between 300 and 600 nm. Additionally the formation of the band centred at 407 nm is not clearly observed. A slight blue shift in Te-Te charge transfer band from 397 to 395 nm is observed. In both cases, we observed a time-dependent Te–Te charge transfer band increase upon addition of the metal cation, indicating the coordination interaction between the Pt ions and the Ph_2Te_2 ligand. (**Figure** 3.20)

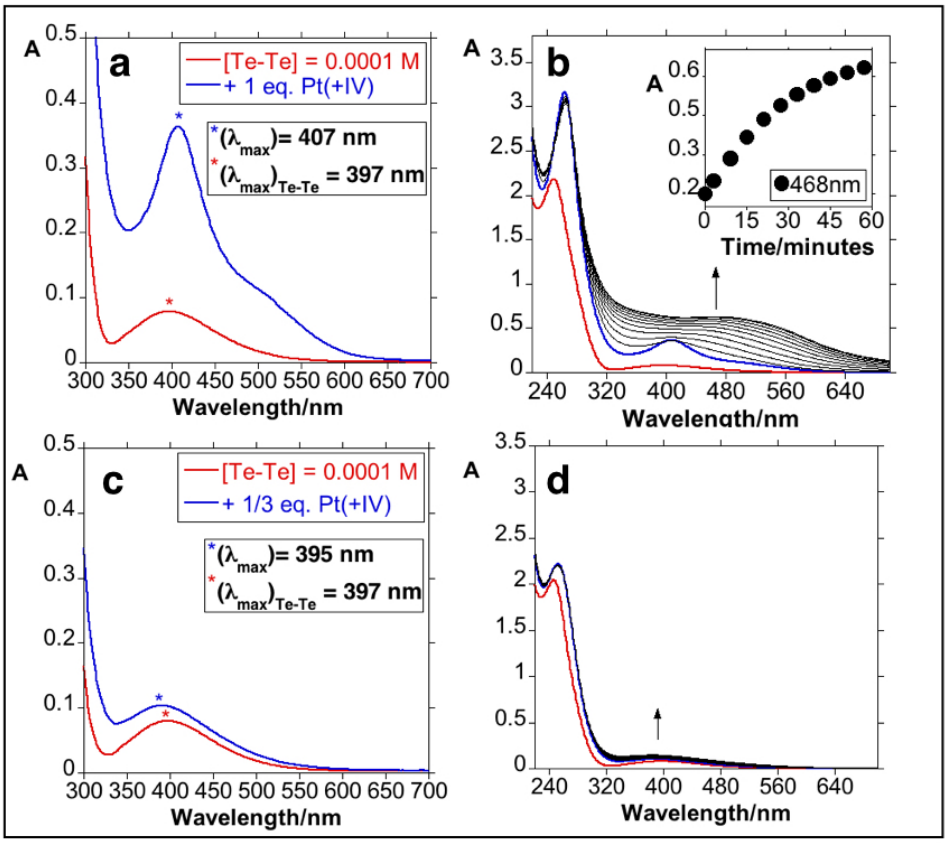

Figure 3.20: UV/Vis study of the time depend interaction of Ph_2Te_2 ([L] = 1.10^{-4} M) with addition of 1:1 (a, b) and 1:3 (c, d) equivalents of H_2PtCl_6 in acetonitrile solution.

Surprisingly, FT-ICR-MS analysis, performed just 1 minute after mixing the reagents, showed only the presence of some signals with clear Te isotopic distribution. Interestingly, we observed that the two most intense signals consistent with the Te isotopic distribution (at 616.833 and 853.398 *m/z*) are coincident with those observed in previous reported studies related to Au-Te nanoparticles[290]. (**Figure** 3.21)

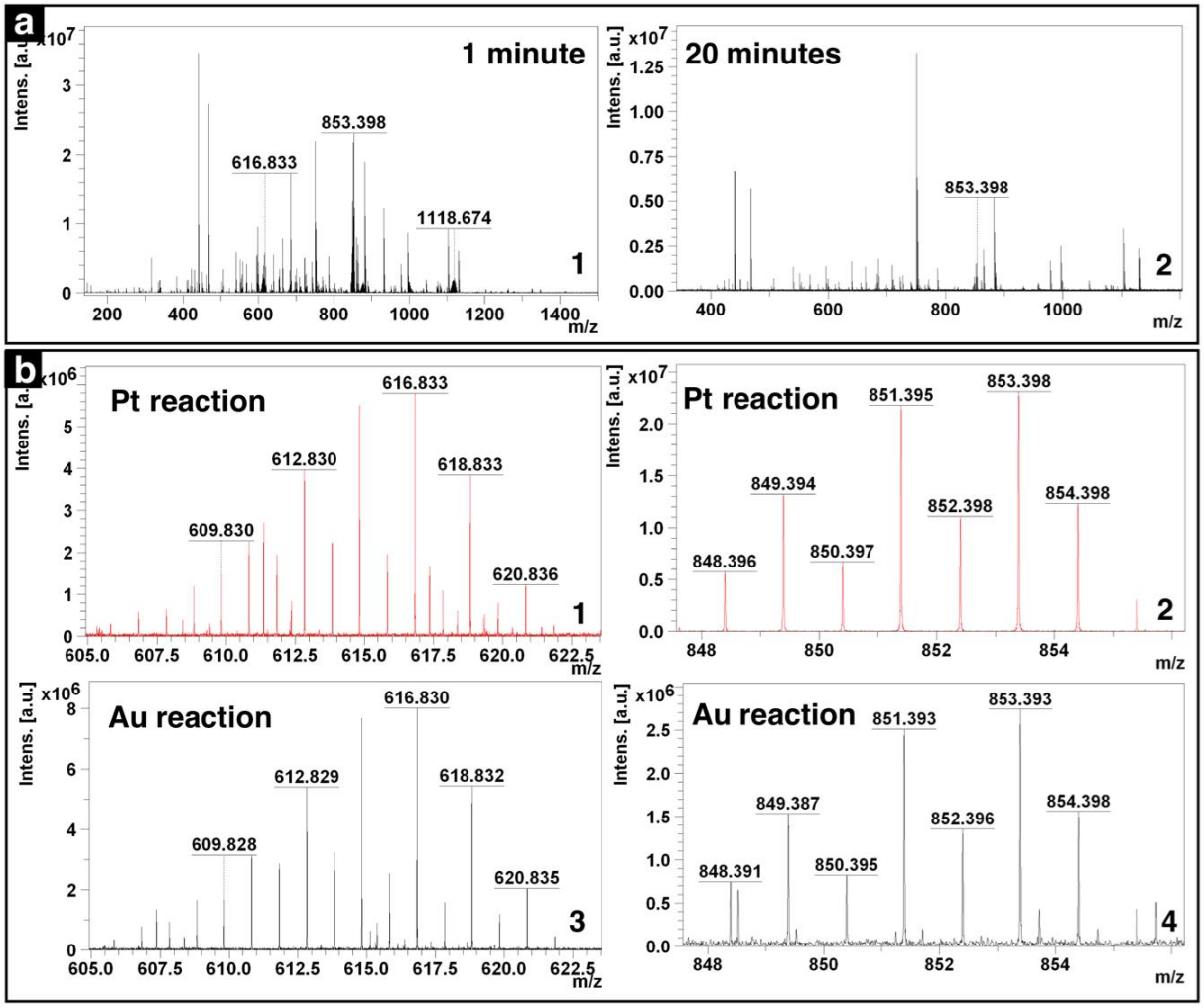

Figure 3.21: (a) FT-ICR MS (+) spectra of the reaction time at (1) 1 min, (2) 20 min. (b) Experimental isotopic mass spectra for the peaks at m/z 616.833 and m/z 853.398 for Pt and 616.830 m/z and 853.393 m/z for previously reported[290] gold reaction.

These results suggest that similar organotellurium derivatives are formed in both systems. Additionally, a signal was observed at 1118.674 *m/z* displaying a Te isotopic pattern. This signal was attributed to the empirical formula $[C_{24}H_{21}Cl_2O_2Te_4Pt]^+$, arising from the coordination of a Pt(II) cation with a Ph_2Te_2 molecule and a phenyl tellurium oxidised $(PhTeO)_2$ derivative resulting from the oxidation of Ph_2Te_2, along with two chlorine atoms remaining coordinated to the Pt atom. (**Figure** 3.22)

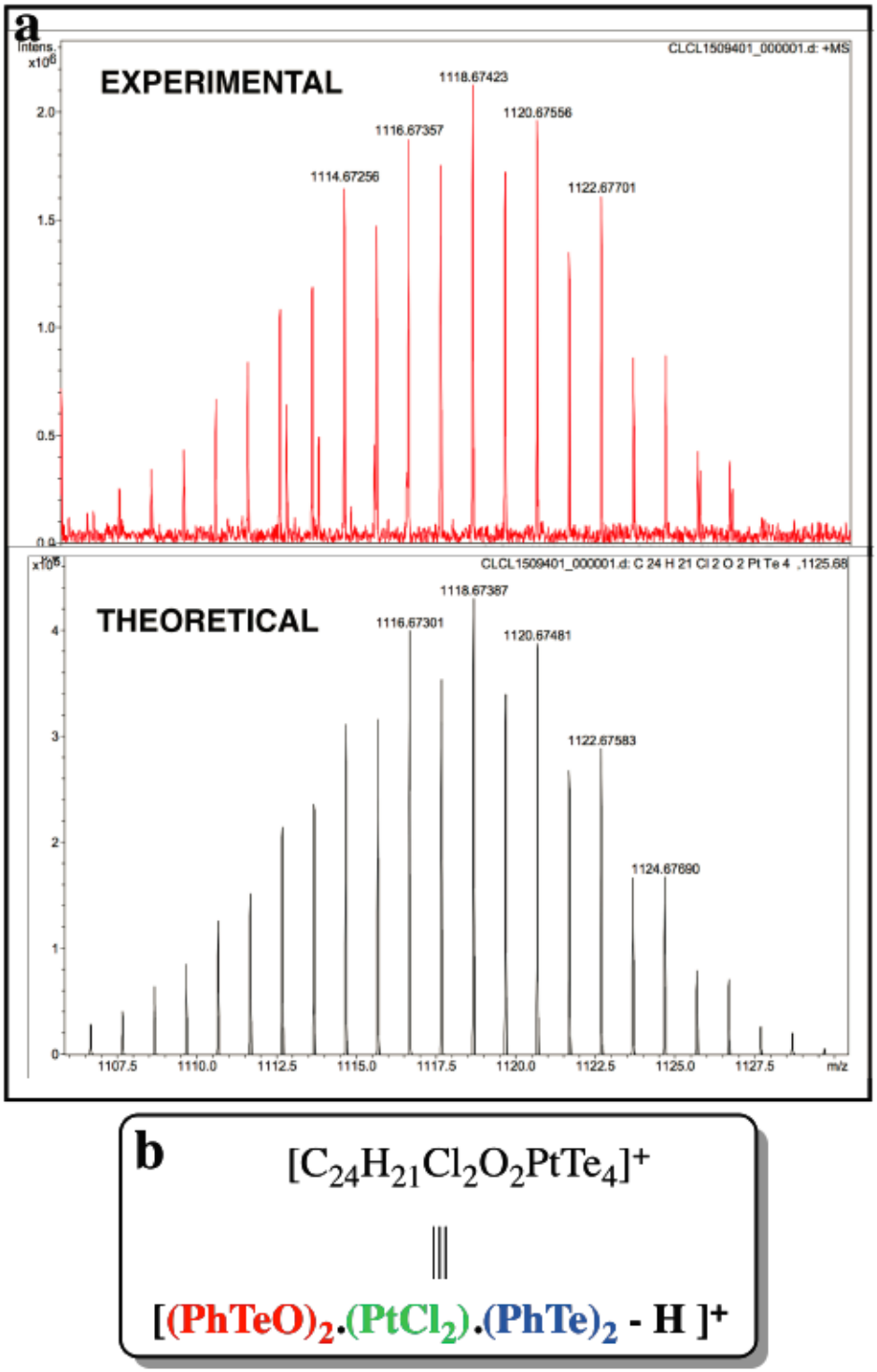

Figure 3.22: Experimental and theoretical isotopic pattern of 1118.674 m/z. This signal can be formed with one Pt(II) metal coordinated with one molecule of Ph_2Te_2 (blue) and one molecule of an derivative of phenyl tellurium oxidised (red) together to Cl atoms (green).

After 20 minutes of reaction, the mass spectrum signal intensities were drastically reduced. The limited literature related to this type of reaction, associated with the very high kinetics of the involved transformations, hinders a better interpretation of the mass spectrometry analysis, as only some plausible Te- and/ or Pt-containing isotopic patterns were detected. Moreover, the low solubility of the formed organometallic oligomers could be attributed to the signal decrease observed during the ESI ionization process.

Comparing the relative percentages of the structure proposed by theoretical FT-ICR-MS calculations with the experimental data, we assume that the final structure is not composed of pure units of $[C_{24}H_{21}Cl_2O_2Te_4Pt]^+$; this "structure-defect" may be attributed to a subsequent evolution of the proposed structure into oligomers/ polymers.

Based on previous reports[290,297,302] related to the ability of organic ditellurides to reduce Au(III) to Au(I), we propose here that Ph_2Te_2 should act as a Lewis base, reducing Pt(IV) to Pt(II) as was observed by XPS analysis. Consequently, oxidised phenyl tellurinyl chlorides should be formed. These halogenated tellurium derivatives are known to undergo different hydrolysis reactions under specific conditions, producing oxohalides (PhTe(O)Xn), tellurinic acids (PhTeOOH) or anhydride [(PhTeO)n] derivatives[291,292]. These oxygenated tellurium entities probably originate from the first obtained tellurium chloride species, which imputes high electrophilic character to the tellurium atom, being consequently more susceptible to react with water, for instance.

This hypothesis is linked with the low yield obtained at lower water contents, under which hydrolytic events are drastically reduced, hampering the progress of the nanoparticle formation. The low solubility of the organometallic structure formed in acetonitrile favours particle formation.

3.3.4 Synthesis and characterization of $PtTe_2$ multi-crystallite NPs.

As discussed, when the organometallic Pt-Te NPs were subjected to thermogravimetric analysis, an exothermic signal was observed at approximately 200 °C, which was believed to correspond to the crystallization process of a Pt-Te species. Thus, we decided to cover the nanoparticles with a stabilizing polymer, selecting PVP for this purpose. Examining high boiling point solvents (above 200 °C) in which the nanoparticles as well as the PVP could be solubilised, 1,5-pentanediol was found to be efficient for the annealing process. The thermal decomposition was completed at 220 °C in 1 h. The red/brown solution turned black, indicating the formation of metallic $PtTe_2$ nanoparticles.

The final size of these multi-crystallite metallic NPs was highly dependent on the organometallic precursor. As an example, annealing R2 (approximately 80 ± 20 nm) produced multi-crystallite metallic nanoparticles of approximately 45 ± 15 nm. (**Figure** 3.23)

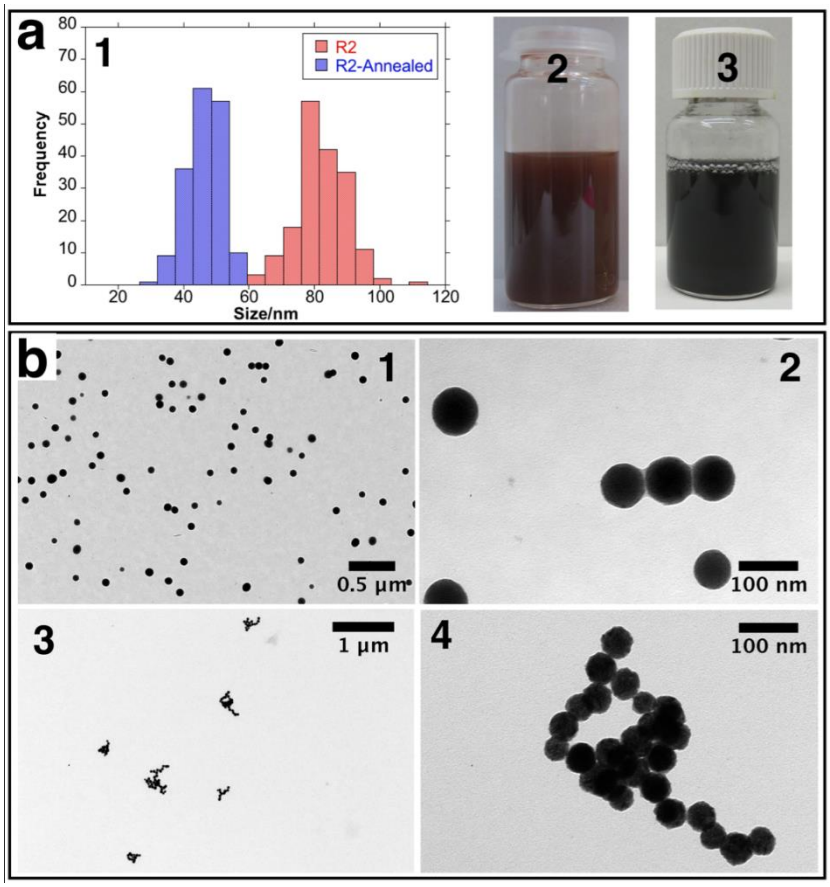

Figure 3.23: In panel a the histograms obtained for organometallic nanoparticles (sample R2) before and after the annealed process (1) and the colour solution of organometallic Pt-Te NPs (2) and annealed ($PtTe_2$ multi-crystallite) NPs (3) can be seen. In panel b images of organometallic Pt-Te NPs (1, 2) and the resulting $PtTe_2$ multi-crystallite NPs (3, 4).

The same effect was observed for R5. (**Figure** 3.24)

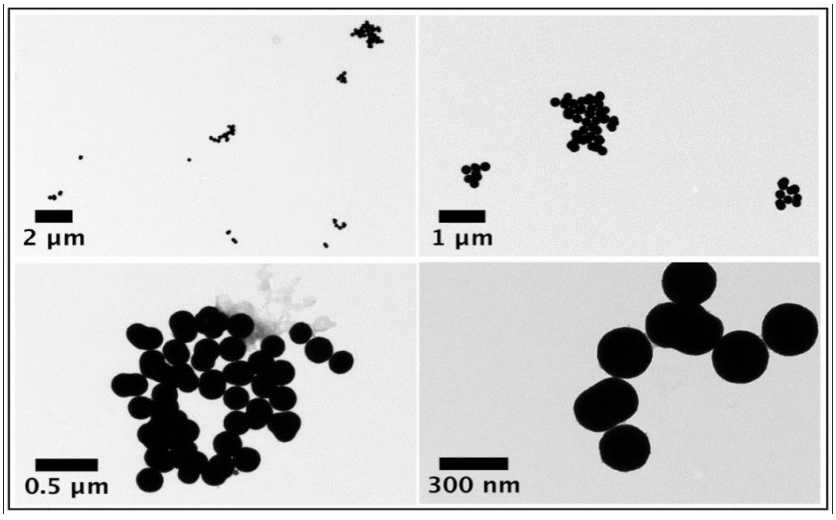

Figure 3.24: Low magnification electron transmission microscopy images $PtTe_2$ multi-crystallite particles obtained after annealing process of R5.

We strongly believe that the pre-adsorbed PVP polymer should prevent the aggregation of bulk $PtTe_2$ material during the thermal decomposition, thereby guaranteeing the final spherical shape of the $PtTe_2$ multi-crystallite NPs.

TEM and HRTEM micrographs are shown in **Figure** 3.25. Interestingly, these particles show clear lattice fringes, which reveals the crystalline nature of these nanoparticles.

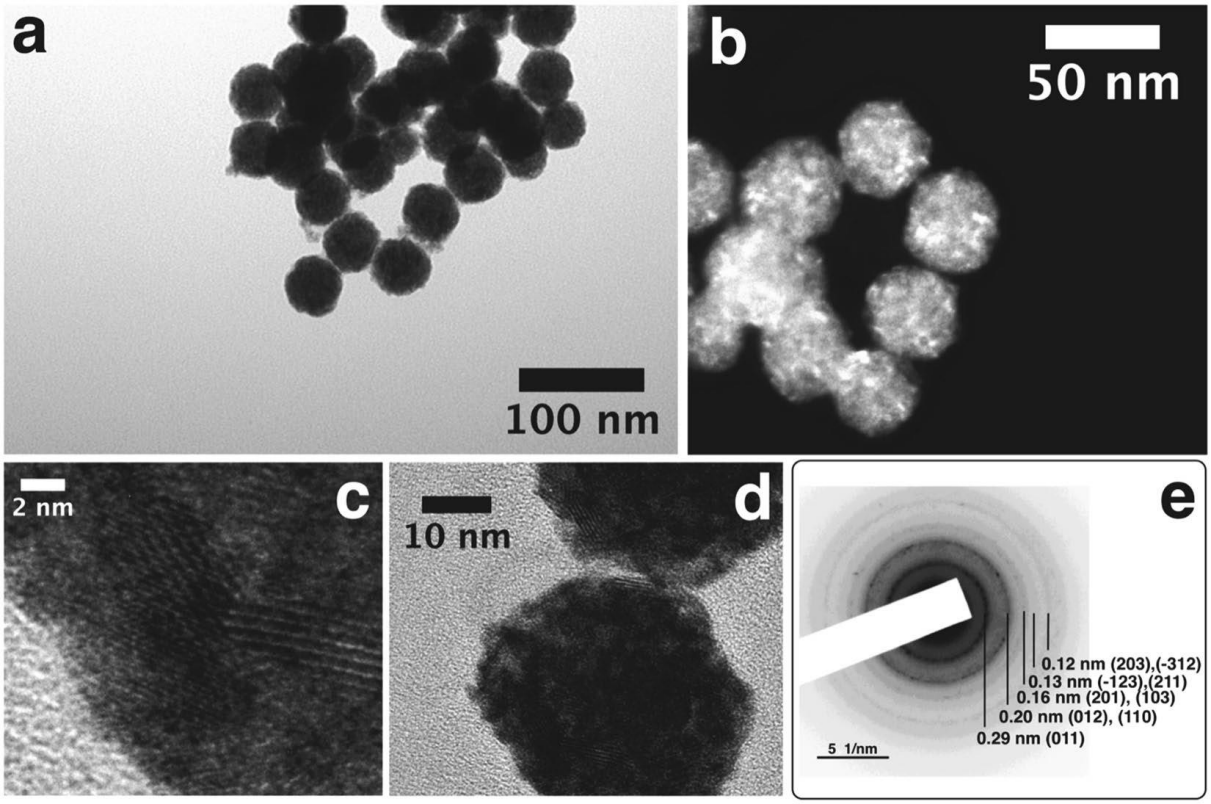

Figure 3.25: TEM (a), and STEM (b) images of $PtTe_2$ multi-crystallite NPs obtained after the annealing process, HRTEM images of isolated NPs showing lattice image fringes (c,d) and electron diffraction pattern obtained from a group of $PtTe_2$ multi-crystallite NPs showing clear diffraction rings; this pattern was indexed on the basis of the $PtTe_2$ crystalline structure (P −3 m 1, SG: 164) (e).

Their crystalline phase was clearly determined by indexing the electron diffraction pattern shown in **Figure** 3.25 (e); this pattern matches quite well with the $PtTe_2$ crystalline structure obtained from the database[303]. At this point, we firmly believe the annealed nanoparticles were formed of a $PtTe_2$ (P −3 m 1, SG: 164) crystalline structure. The annealing crystallization stage is characterised by two new features: first, a large drop in the intensity of the C-$K_{\alpha 1-2}$ intensity shown in **Figure** 3.26, and second, the presence of brighter areas in the STEM image showing crystalline contrast, contrary to the case of the Pt-Te organometallic polymeric particles. (**Figure** 3.25 b) These two features demonstrate the low carbon content of the $PtTe_2$ nanoparticles and indicate the presence of small crystallites in the spheres sized between 2.5–6.5 nm. (**Figure** 3.27)

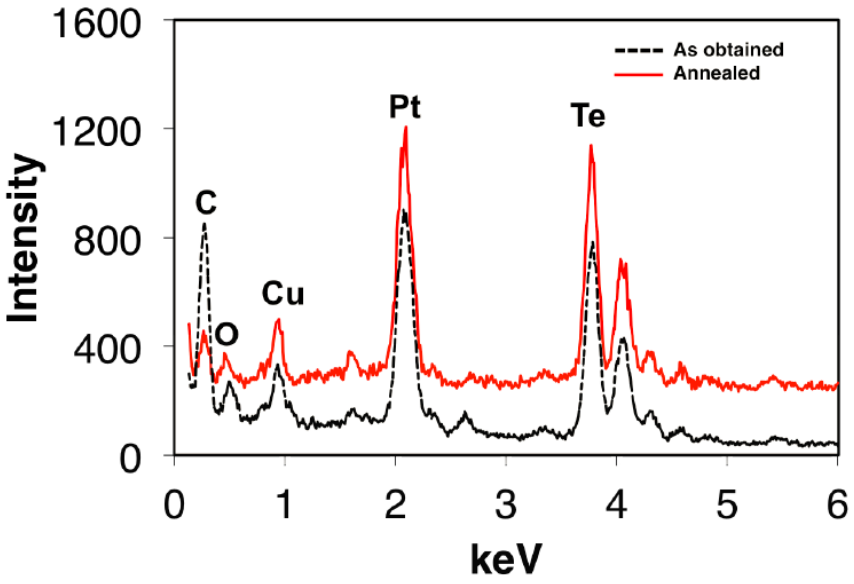

Figure 3.26: EDS X-ray microanalysis spectra of the as obtained organometallic Pt-Te NPs and of the annealed ($PtTe_2$ Multi-Crystallite) NPs, note the drop in the relative intensity of the C-Kα1-2 signal in the annealed NPs.

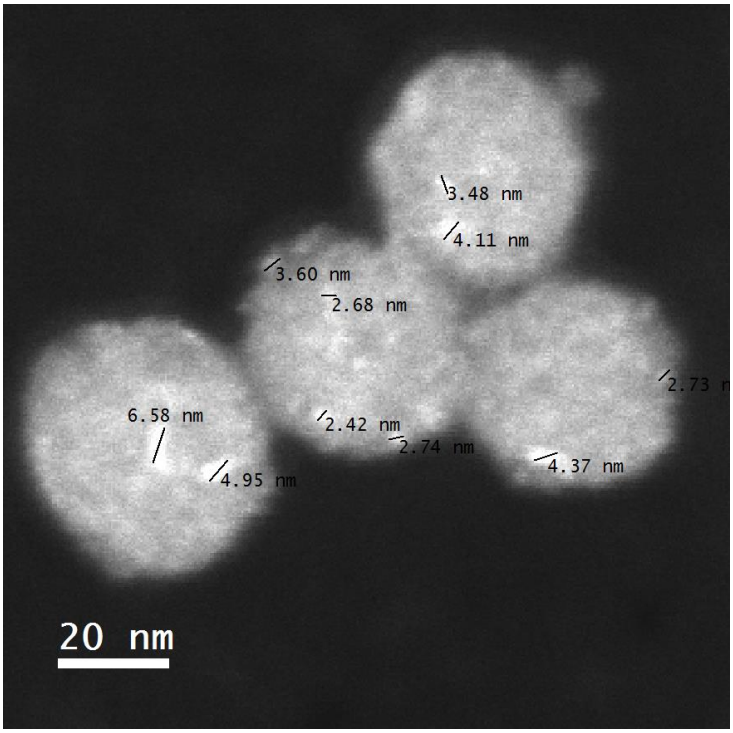

Figure 3.27: STEM image of a group of $PtTe_2$ multi-crystallite NPs showing crystalline contrast, brighter areas are due to the presence of small crystallites within the NPs. Numbers display the length of the black lines.

Similar results were obtained when annealing the R5 sample. (**Figure** 3.28)

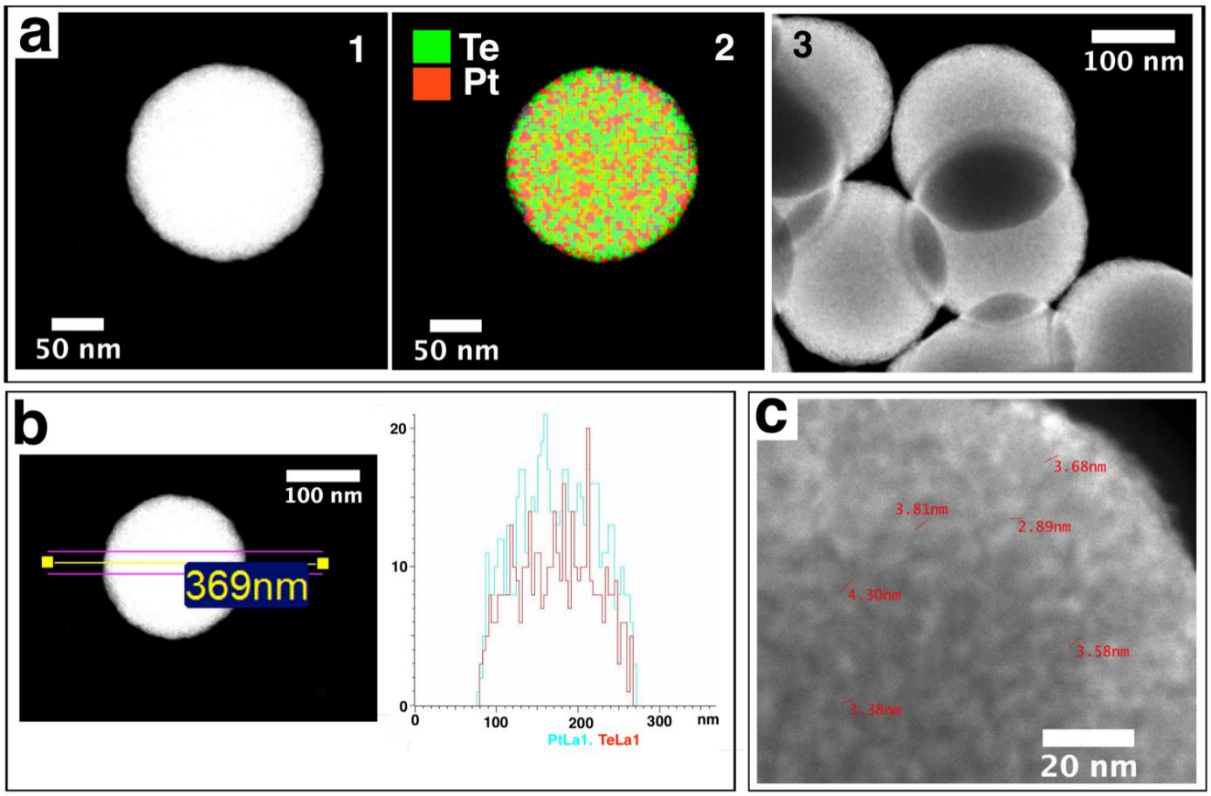

Figure 3.28: (a) STEM-HAADF image of a group isolated $PtTe_2$ multi-crystallite particles and Te, Pt EDS elemental maps (1,2) and STEM image of a group of particles. (b) EDS intensity profiles of the PtLα1 and Te-Lα1, signal along the yellow line. (c) STEM image in high resolution of an isolated particle showing crystalline contrast, brighter areas are due to the presence of small crystallites within the particles. Numbers display the length of the red lines.

These results clearly demonstrate that the annealing process transformed the initial amorphous organometallic Pt-Te nanocomposite into well-formed, spherical $PtTe_2$ multi-crystallite NPs.

3.4 Conclusion

Organotellurium chemistry was applied successfully to the construction of new platinum nanomaterials; this approach provides a versatile chemical tool in the assembly of novel nanostructured materials. The redox and hydrolytic properties shown by the organic tellurium-based entities were necessary for their role in the construction and stabilisation processes. The spontaneity of the Pt cation reduction promoted by the starting ditelluride reagent, associated with the easily adjustable experimental conditions to promote transformations based on the tellurium moiety, can be considered the key draw of this new synthetic strategy for obtaining well-defined nanoparticles.

New organometallic Pt-Te NPs were formed by a mixture of Te, Pt and C, plus minor amounts of O and Cl. This inhomogeneous mixture of elements produces Pt and Te nodules, conferring the final spherical shape to the particles. Each of the nodules is approximately 1.4 nm in diameter. Surrounding all the Pt-Te nodules are lighter elements, mainly C and O, acting as agglutinant agents. The interior of the nodules appears to be a mixture of organometallic Pt compounds, not crystalline Pt. EDS analysis demonstrates a low carbon content in the $PtTe_2$ multi-crystallite NPs relative to the initial composite NPs. The size of the $PtTe_2$ crystallites forming the large spheres was estimated to range from 2.5 to 6.5 nm. Further studies related to applications of these new nanoparticles are in progress.

4 Chapter 4

Highly accessible aqueous synthesis of well-dispersed dendrimer type platinum nanoparticles and their catalytic applications

Published in: **Adrián Fernández-Lodeiro**, Jamila Djafari, David Lopez-Tejedor, Carlos Perez-Rizquez, Benito Rodriguez-González, José Luis Capelo, Jose M. Palomo, Carlos Lodeiro, Javier Fernández-Lodeiro. "Highly accessible aqueous synthesis of well-dispersed dendrimer type platinum nanoparticles and their catalytic applications." *Nano Research*, **12**, 1083-1092 (2019). IF: 7.994. DOI: 10.1007/s12274-019-2350-7

Candidate contribution: performed the synthesis, analysis and characterisation (UV/Vis, FT-IR, DLS, ζ-potential) of the nanomaterials and helped in the discussion of all the analysed data and the writing of the final version of the manuscript.

4.1 Introduction

The remarkable advances that nanochemistry has undergone in recent decades have allowed the exponential expansion in the practical applications of metallic nanoparticles in different fields[304,305]. As a result of the interesting and unique physical and chemical properties that arise from the miniaturization of certain metals up to the nano-scale[306], metal NPs are being applied in several scientific and industrial applications, such as chemical detection[307], catalysis[308], biochemistry[309] or even medicine[310] among others.

In this sense, Pt NPs have shown potential to be applied not only in catalysis, but also in energy applications[311,312], green technologies, and recently in the biomedical field[313,314]. Among other advantages, the construction of Pt particles at nano-scale range results in a higher surface-to-volume ratio compared with their bulk counterparts. This property has been extensively exploited in catalytic purposes, not only because the amount of material consumed is reduced, but also due to the size-dependent catalytic activity reported for Pt NPs[314,315,316]. As a consequence of the low levels of this scarce precious metal, considerable effort has been devoted to developing synthetic strategies that allow the preparation of well-dispersed Pt nanoparticles with control in size[317,318,319].

Besides the size effects discussed above, the shape of NPs has been showed to play an important role in the catalytic properties of Pt NPs[320], due to that the different crystalline surfaces exposed exhibit different activity and/or selectivity for the same reaction[321,322]. Between the different shapes reported for Pt NPs such as spheres[319], cubes[318], triangular prisms[323], octahedrals[94], multi-octahedrals[324], or polyhedrals[325], hierarchical nanostructures such as branched or dendritic NPs[326,327,328,329,330,331], have shown improved catalytic properties, between other factors, thanks to their large number of edges and corners which increases the surface-to-volume ratio, and therefore the absorption sites available. Additionally, these three-dimensions porous structures should allow unlimited transport of molecules in the medium[332,333].

Up to date, different strategies have been reported to produce these fascinating nano-structures, including sonochemical synthesis[333], solvothermal method at high temperature[313], seed-mediated method[329], sacrificial template[334], interfacial synthesis using oleic acid in water[335], or apply organic dendrimer as template[336]. Most of these processes require considerable energetic contributions (high temperatures or ultrasound radiation), hard chemical compounds to reduce ion platinum to its metallic state, or present synthetic processes in consecutive steps. Therefore, there is a need to develop low-cost and more environmentally friendly strategies to produce dendrimer-type platinum nanoparticles (Pt D-NPs). In this respect, some simple one-pot synthetic processes, using common eco-friendly reagents, with minimal energy contributions have been developed. Furthermore, a size limitation between 30-50 nm with well-defined dendrimer structures has been achieved[328,331,337].

On the other hand, according to the published literature regarding the synthesis of Pt multi-branched nanoparticles in a polar medium, it can be noticed that the application of a weak reducer agent is usually necessary. For instance, Mohanty *et al*. showed that using ascorbic acid as a reducer, Au, Pd or Pt nano-flower while with sodium borohydride spherical NPs are obtained[338]. In this respect, it has been reported approaches that use organic weak reducers agents such as ascorbic acid[328,329,337], PVP[313,326] or ethylene glycol[327] among the most used. However, less attention has been paid to the application of metal cations as reducing agents in the synthesis of Pt NPs. It should be mentioned that the addition of metal cations such as Fe(III)/Fe(II) in trace amounts to a polyol or PVP assisted synthesis under high-temperature conditions (≥ 90 °C) has been successfully employed to manipulated redox kinetics during Pt hierarchical NPs synthesis[93,339]. However, to the best of our knowledge, Fe(II) has never been used as the main reducing agent during the synthesis of Pt NPs.

An important consequence that arises from the application of metallic redox pairs as a reducer is the attractive possibility to modulate the redox potential through complexation with chelating molecules[340]. For the case of redox pair Fe(III)/Fe(II), potentiometric studies showed changes towards more negative values through complex formation with, ethylenediaminetetraacetate (EDTA), citrate or oxalate among others[341,342].

In the present work, we have developed a new one-pot aqueous-phase, at relatively low-temperature (60 ºC) to obtain well-dispersed Pt D-NPs; using $FeSO_4$ in the presence of sodium citrate (SC) as reducing agent. This simple Fe(II)/SC-mediated synthesis in the presence of PVP as a surfactant, can be exploited to obtain well-dispersed Pt D-NPs in average sizes between 13-20 nm. We have carefully inspected the catalytic properties of Pt D-NPs through the analysis of aromatic compounds reduction and, particularly, as a new artificial metalloenzyme in the oxidation of L-DOPA.

4.2 Experimental Section

4.2.1 Materials

Potassium tetrachloroplatinate (K_2PtCl_4), iron (II) sulphate heptahydrate ($FeSO_4.7H_2O$), trisodium citrate dihydrate ($Na_3Cit.2H_2O$), polyvinylpyrrolidone (PVP 40K), polystyrene sulphonate (PSS 70k) and ethylenediaminetetraacetic sodium salt (EDTA-Na_4) were purchased from Sigma-Aldrich. Potassium bromide (KBr) was purchased from Alfa-Aesar. All reagents were used without further purification. Water was ultra-pure grade (type I) obtained with a Milli-Q Simplicity system.

4.2.2 Methods

Pt D-NPs were produced through reduction of K_2PtCl_4 applying $FeSO_4$ assisted by sodium citrate with/without the addition of PVP or PSS in aqueous solution.

4.2.3 Sodium citrate assisted synthesis

A round-bottom flask with 28 mL of ultrapure water containing SC (0.12 or 0.15 mmol) was immersed in a thermostated oil bath at 60°C. With the temperature stabilised and under vigorous magnetic stirring, 1 mL of an aqueous solution containing 0.03 mmol of K_2PtCl_4 was added. Then, 1 mL of an aqueous solution containing 0.12 mmol of $FeSO_4$ is rapidly injected. The reaction was allowed to elapse for 60 minutes, and then the solution was cooled to room temperature (RT) under stirring. Finally, the material was purified by three centrifugation steps at (8000 rpm x 15 min) in ultra-pure water (3 washing steps). The final NPs were resuspended in 8 mL of ultrapure water. Final concentrations explored: [K_2PtCl_4] = 1 mM, [$FeSO_4$] = 4 mM, [SC] = 4 mM or 5 mM).

4.2.4 Sodium citrate/PVP assisted synthesis

In all synthetic experiments in the presence of PVP, the molar ratio Pt/Fe/SC = 1/4/4 was maintained constant. In a typical experiment, a round-bottom flask with 28 mL of ultrapure water containing 0.12 mmol of SC and PVP (total concentrations explored between 0.25 mM and 5 mM) was immersed in a thermostated oil bath. Under vigorous magnetic stirring and temperature of reaction stabilised, 1 mL of an aqueous solution containing 0.03 mmol of K_2PtCl_4 was added. At this point, 1 mL of $FeSO_4$ water solution (0.12 mmol) is rapidly injected. The reaction was allowed to elapse for 60 minutes, and then the solution was cooled to room temperature under stirring. Finally, the material was purified by centrifugations at (14000 rpm x 60 min.) in ultra-pure water (3 washing steps). The final NPs were resuspended in 8 mL of ultrapure water.

Synthesis in the presence of polystyrenesulphonate (PSS_{70k}) were carried out with the same protocol previously explained at 60 °C with a molar ratio of Pt/PSS (1/5). Final concentrations explored: [K_2PtCl_4] = 1 mM, [$FeSO_4$] = 4 mM, [SC] = 4 mM and [PSS] = 5 mM). To obtain the sample under boiling conditions, we select molar relation Pt/PVP 1/1. The addition of iron salt solution was completed under boiling in a similar manner to the lower temperature reactions. The reaction medium was kept boiling for 60 minutes, cooled down under stirring and the material was purified in a similar way to previous reactions. Final concentrations: [K_2PtCl_4] = 1 mM, [$FeSO_4$] = 4 mM, [SC] = 4 mM and [PVP] = 1 mM).

4.2.5 Synthesis of Pt D-NPs for catalysis applications

The samples used in catalysis experiments were obtained through the SC/PVP assisted synthesis at 60 °C discussed in the previous experimental section.

4.2.5.1 Samples PtCat-1 and PtCat-2

We have selected molar ratio Pt/PVP 1/1 and 1/5 at 60 °C to obtain two new samples denoted as PtCat-1 and PtCat-2 respectively. In these cases, the materials were purified by centrifugations (14000 rpm x 60min.) using first EDTA solution 2 mM (1 step), and finally in ultra-pure water (2 additional steps). The final NPs were resuspended in 8 mL of ultrapure water.

4.2.5.2 Samples PtCat-3 and PtCat-4

Using a Pt/PVP molar ratio of 1/5 at 60 °C we have obtained the sample PtCat-3 increasing 5-fold the concentration of all the reagents (final concentrations: $[K_2PtCl_4]$ = 5 mM, $[FeSO_4]$ = 20 mM, [SC] = 20 mM, [PVP] = 25 mM). The NPs were purified by centrifugation (13000 rpm x 60 min) using first EDTA solution 5 mM (1 step), and in ultra-pure water (3 additional steps). The final NPs were resuspended in 12 mL of ultrapure water.

The sample denoted as PtCat-4 was obtained increasing the total concentration reagents by a factor of 10-fold (final concentrations: $[K_2PtCl_4]$ = 10 mM, $[FeSO_4]$ = 40 mM, [SC] = 40 mM, [PVP] = 5 mM). The NPs was purified by centrifugation (13000 rpm x 60 min) with EDTA 10 mM, and then 3 additional cycles in ultra-pure water. The final NPs were resuspended in 15 mL of ultrapure water.

4.2.6 Characterization of Pt D-NPs

All NPs have been characterised by spectroscopy and common chemical techniques:

DLS and ζ-potential analysis was done in a MALVERN model ZS instrument (PROTEOMASS Scientific Society, BIOSCOPE facility). Ultraviolet-visible (UV/Vis) was done in a Jasco-650 spectrophotometer with control temperature (PROTEOMASS Scientific Society, BIOSCOPE facility). Fourier Transform Infrared (FT-IR) spectroscopy was performed using a Bruker Tensor 27. Samples were prepared in KBr disks. To prepare the KBr disks to complete the FT-IR analyses, each sample were centrifuged (14000 rpm x 60 min) and washed twice in anhydrous EtOH. Then the solid obtained, from each sample, was resuspended in 100 µL of anhydrous EtOH and mixed with KBr powder. The solid was quickly dried in a vacuum pump for 6 h before preparing a concentrated KBr tablet. For PVP_{40k} analysis, the powder was directly mixed with KBr. Transmission electron microscopy (TEM) analysis

was performed using a TEM microscopy JEOL JEM1010 working at 100 kV to obtain low-magnification images. The high-resolution transmission electron microscopy (HRTEM) were performed on a JEOL 2100F microscope equipped with an EDS Inca Energy 200 (Oxford Instruments). All TEM samples were prepared by placing a drop of the sample onto a TEM copper grid and let air-dried (TED-PELLA Co.). Size of particles and dispersion histograms have been calculated from TEM micrographs using ImageJ package[343]. Interplanar spacings in the nanostructures were calculated by Fourier transform (FT) using the ImageJ digital micrograph suite. Inductively coupled plasma (ICP) analysis: The Pt content of each studied sample was determined in the REQUIMTE-LAQV Chemistry Department, FCT-UNL analytical laboratory using an ICP instrument from Horiba Jobin–Yvon (France, model Ultima), equipped with an RF of 40.68 MHz, a 1.00 m Czerny–Turner monochromator (sequential), and an AS500 autosampler. XRD analyses were obtained in X-ray diffraction system (XRD, PANalytical, model X´Pert Pro) in Bragg-Brentano geometry with Cu Kα line radiation (λ = 1.5406 Å). Samples were deposited in the form of a concentrated slurry and let dry before they were analysed.

4.3 Results and discussion

According to the standard redox potentials known for $[PtCl_4]^{2-}/Pt^0$ (+0.75 V vs RHE) and Fe(III)/Fe(II) (+0.77 V vs RHE) the reduction of Pt^{2+} mediated by Fe^{2+} is not a spontaneous process in normal conditions. However, the thermodynamics of the reaction should be altered upon addition of different chelating molecules such as oxalate, EDTA or citrate[341,342,344]. Based on this interesting concept, we have selected sodium citrate as a chelating agent for Fe(II) given its ability to alter the redox potential of Fe(III)/Fe(II) from 0.77 to 0.38 V, as has been previously reported[345]. With these considerations in mind, we have explored this reaction at colloidal level.

To develop the present synthetic protocol of Pt NPs, a workflow based on three principal work-packages has been adapted. Initially, the reduction reaction was studied using Ultraviolet-visible (UV/Vis) spectroscopy. Then the reaction was adjusted to obtain uniform and well-dispersed Pt D-NPs, using low-resolution transmission electron microscopy, dynamic light scattering (DLS) and Fourier transform infrared (FT-IR) spectroscopy. In a second work package, were produced four samples of Pt D-NPs under selected conditions to explore their catalytic properties. The detailed characterization of these samples was carried out, in addition to the techniques mentioned above, also with X-ray diffraction (XRD) and high-resolution transmission electron microscopy analysis.

4.3.1 Synthetic process adjustment

Initially, we explored the reduction reaction of Pt(II) mediated with Fe(II) in aqueous solution by UV/Vis spectroscopy. After the addition of an iron (II) sulphate solution, it does not observe any changes in the characteristics absorption bands of $[PtCl_4]^{2-}$ located at *ca*. 323, 388 and 472 nm[346,347].(**Figure** 4.1)

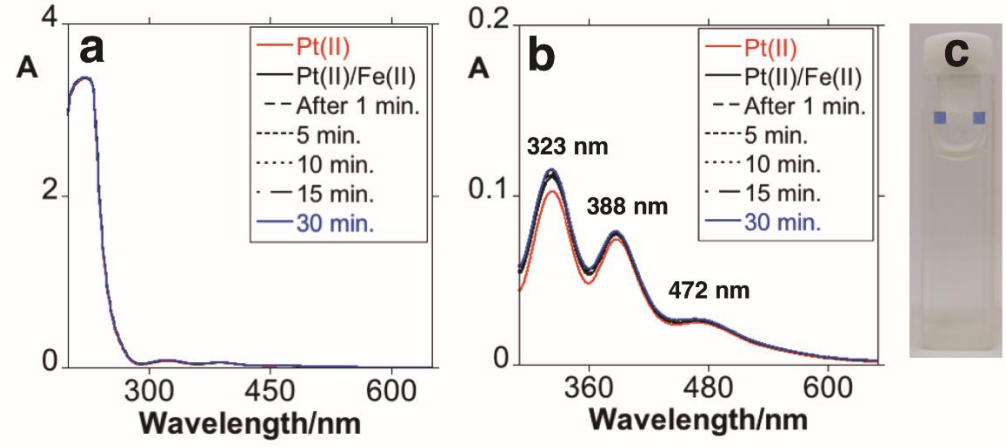

Figure 4.1: (a) UV/Vis kinetic study of the interaction of K_2PtCl_4 with $FeSO_4$ ($[Pt^{2+}]$ = 1 mM, molar ratio Pt/Fe = 1/4) at 22°C. (b) Extension on the y-axis showing $[PtCl_4]^{2-}$ absorption bands. (c) Colour solution at the end of the study.

Conversely, in the presence of SC, the production of Pt particles was evident even at room temperature (22 °C). Interestingly, we have observed that the process of reduction of Pt(II), and the consequent formation of particles in solution, depends not only on the molar ratio of Pt(II)/SC/Fe(II) used, but also, on the total concentration of the precursors. (**Figures** 4.2 and 4.3)

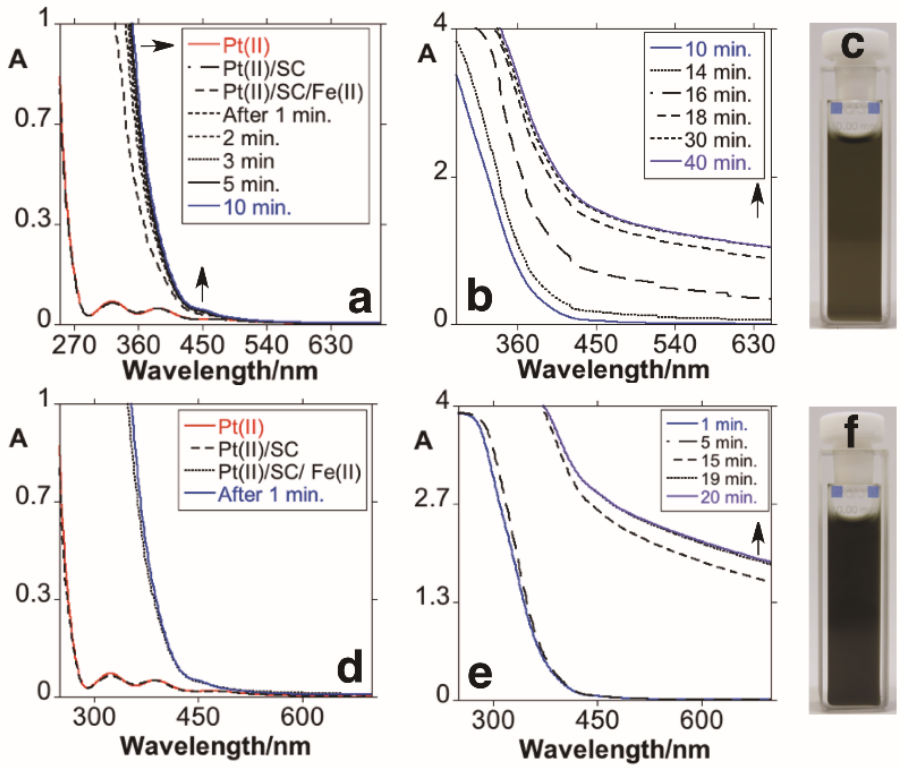

Figure 4.2: (a, b) UV/Vis kinetic study of the interaction of K_2PtCl_4 with $FeSO_4$ in presence of SC ($[Pt^{2+}]$ = 1 mM, molar ratio Pt/Fe/SC = 1/2/2) at 22°C and (c) colour solution at the end of the study. (d, e) UV/Vis kinetic study of the interaction of K_2PtCl_4 with $FeSO_4$ in presence of SC ($[Pt^{2+}]$ = 1 mM, molar ratio Pt/Fe/SC = 1/4/4) at 22°C and (f) colour solution at the end of the study.

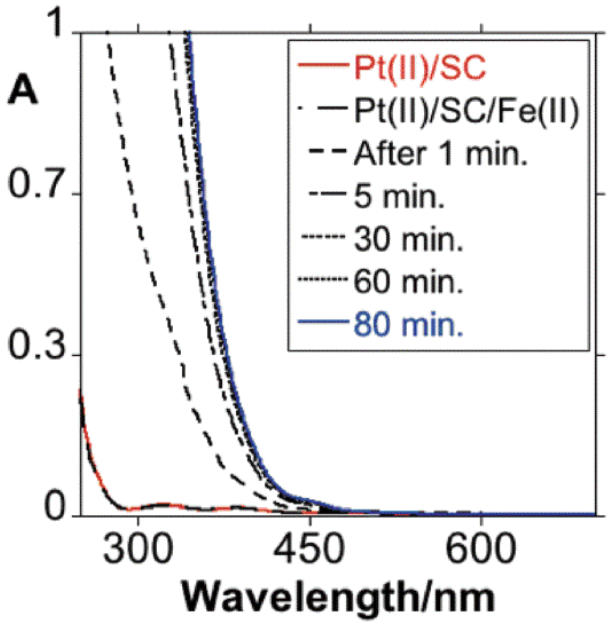

Figure 4.3: UV–vis kinetic study of the interaction of K_2PtCl_4 with $FeSO_4$ in presence of SC ($[Pt^{2+}]$ = 0.25 mM, molar ratio Pt/Fe/SC = 1/4/4) at T= 22°C.

We have noticed that, using the stoichiometric ratio 1/2/2, the reduction of Pt(II) with the formation of particles, seems to be favourable only for concentrations of 1 mM or higher. Otherwise, an excess of Fe(II)/SC is necessary to form particles in lower concentrations. (**Figure** 4.2) For instance, when the [Pt(II)] precursor was maintained in 0.5 mM for Pt/SC/Fe = 1/2/2 (**Figure** 4.4 (a,b)), a steady state was observed in which the UV/Vis spectra appeared identical for t ≥ 60 min. This steady state at the end of the study showed the absence of exponential features in UV/Vis spectra, that can be associated with the formation of structured bands as well as Pt particles[348,349]. The DLS measurements did not show the presence of particles in solution (data not show). When the stoichiometric ratio Pt/SC/Fe was increased to 1/4/4, the formation of Pt particles became evident starting from 20 minutes. (**Figure** 4.4 (d,e)) The colour of the solution changed from pale yellow to black at the end of the study. (**Figure** 4.4 f)

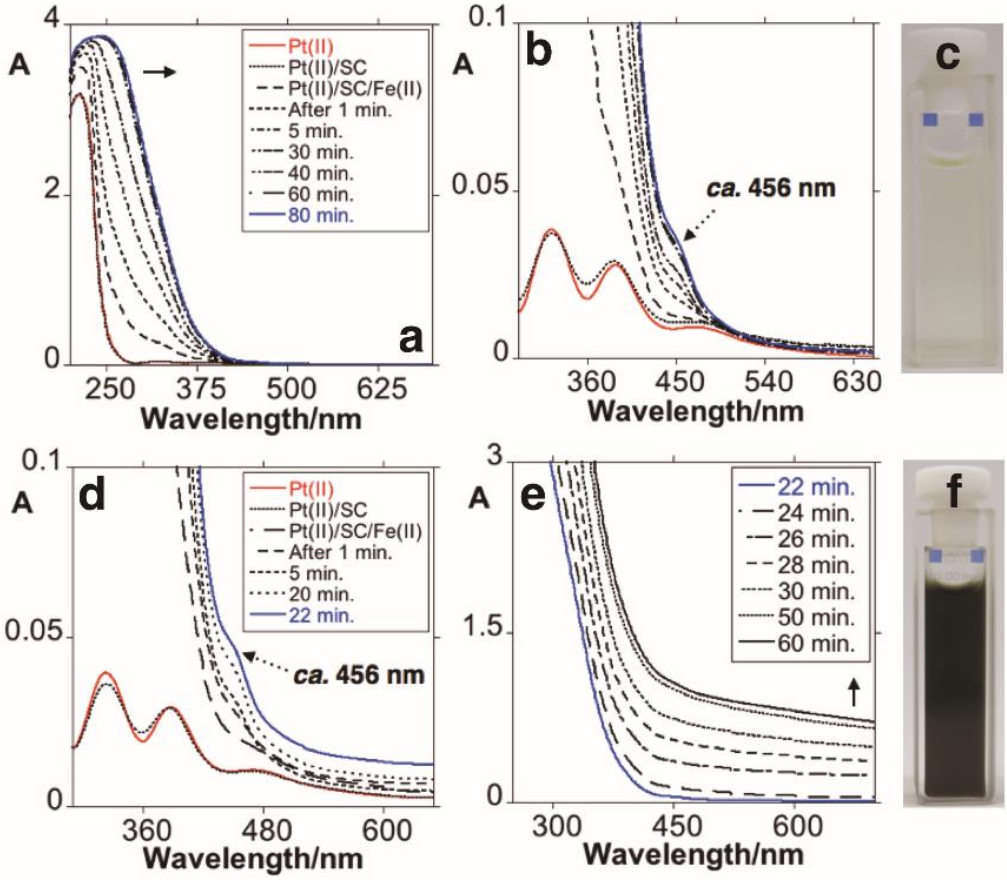

Figure 4.4: (a-c) UV/Vis kinetic study of the interaction of K_2PtCl_4 with $FeSO_4$ in presence of SC ($[Pt^{2+}]$ = 0.5 mM, molar ratio Pt/SC/Fe =1/2/2) (a), extension on the y-axis (b) and colour solution at the end of the study (c). (d-e) UV/Vis kinetic study of the interaction of K_2PtCl_4 with $FeSO_4$ in presence of SC ($[Pt^{2+}]$ = 1 mM, molar ratio Pt/SC/Fe =1/4/4) (d, e) and colour of the solution at the end of the study (f).

It can be noticed, that after the addition of iron sulphate over Pt(II)/SC solutions, independently of leading to effective reduction or not, marked spectral variations were observed between 200-460 nm

that evolve towards a red-shift and absorption increases over time. (**Figure** 4.2 to 4.4) This spectroscopic profile seems to be related with the different complex Fe(II)-Citrate formation or them subsequent oxidation[350,351]. To investigate this phenomenon, in our conditions, we have conducted similar interaction studies for Fe(II) and citrate interaction, but in the absence of Pt(II). The same spectral changes were observed without Pt(II), indicating that the changes observed in the early stages of the reaction are associated with complex formation events between Fe(II) and SC. The presence of a shoulder centred at ca. 456 nm observed in the interaction studies both in the presence or absence of Pt(II) confirm our hypothesis. (**Figure** 4.5)

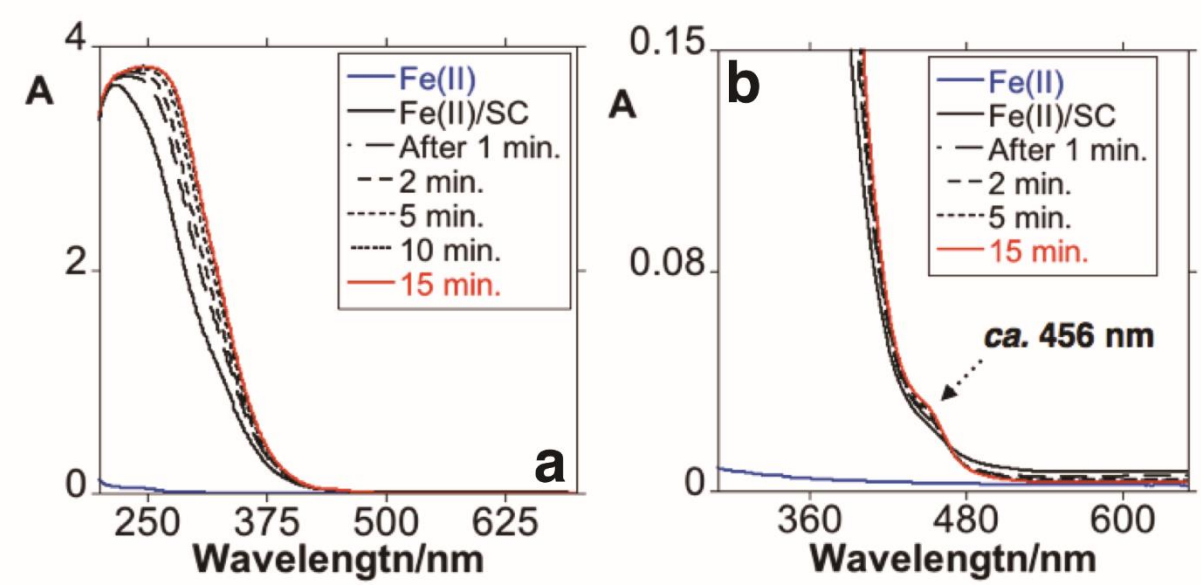

Figure 4.5: (a) UV/Vis kinetic study of the interaction of $FeSO_4$ ($[Fe^{2+}]$ = 2mM) upon addition of 1 equivalent of sodium citrate. (b) Extension spectra on the y-axis.

For the case of the interaction of Pt(II) (1 mM) in the stoichiometric ratio of Pt/SC/Fe 1/4/4 (which results in a high concentration Pt particles), we proceeded to isolate the supernatant (SN) obtained at the end of the study. The UV/Vis spectrum shows a similar profile to that obtained for a solution of $Fe_2(SO_4)_3$ (2 mM) with SC (2 mM). Furthermore, the characteristic shoulder to *ca.* 456 nm observed for the Fe(II)/SC solution was not detected. Besides, the reaction kinetics seems to be strongly affected by the reaction temperature, as revealed by the UV/Vis studies. An increase in the complexation kinetics between Fe(II) with citrate, as well as in the reduction and formation of particles was observed for slight increases of 18 ºC. (**Figures** 4.4 (d-e) and 4.6).

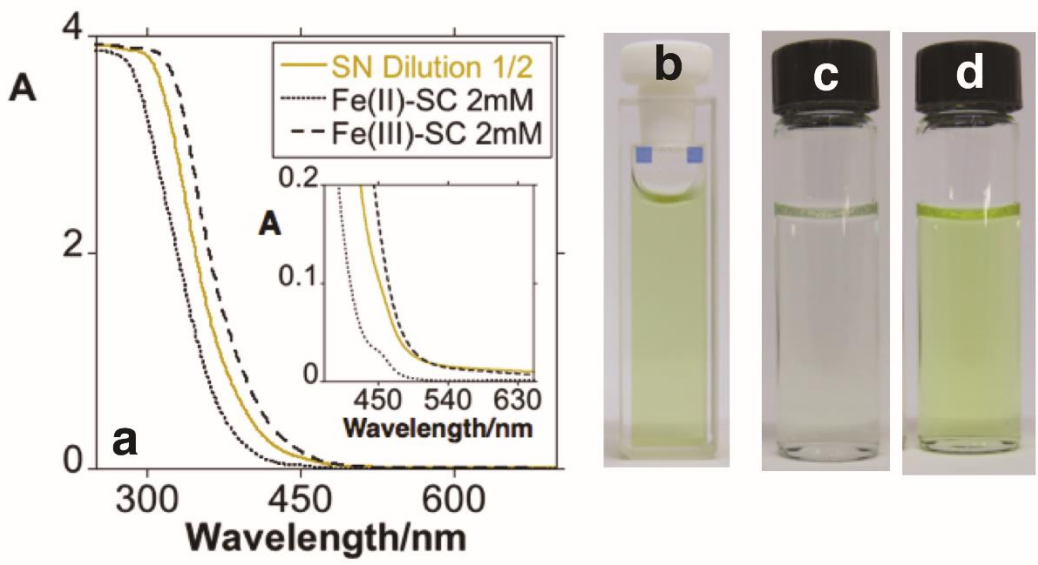

Figure 4.6: UV/Vis spectra of SN of the reaction in Pt/SC/Fe 1/4/4 with [Pt(II)]=1 mM (yellow line) and UV/Vis spectra of solution produced mixing $FeSO_4$ or $Fe_2(SO_4)_3$ in concentrations of 2mM with one equivalent of sodium citrate (denoted as Fe(II)-SC and Fe(III)-SC respectively). Colour solutions of SN (b), Fe(II)-SC (c) and Fe(III)-SC (d).

To promote a fast reduction of Pt(II), we have selected the molar ratio Pt/SC/Fe = 1/4/4 with the total concentration of K_2PtCl_4 of 1mM at 60 °C to explore the morphology and structure of the metallic materials obtained. In a typical experiment, after addition of $FeSO_4$ solution over the Pt^{2+}/SC, a colour change from yellow to black in the first 3 minutes of the reaction was observed. The reaction media turned to an intense black colour after 10 minutes from the start of the reaction. Transmission electron microscopy analysis showed the presence of nanoclusters aggregates in ill-defined form (see Fig. 4.7).

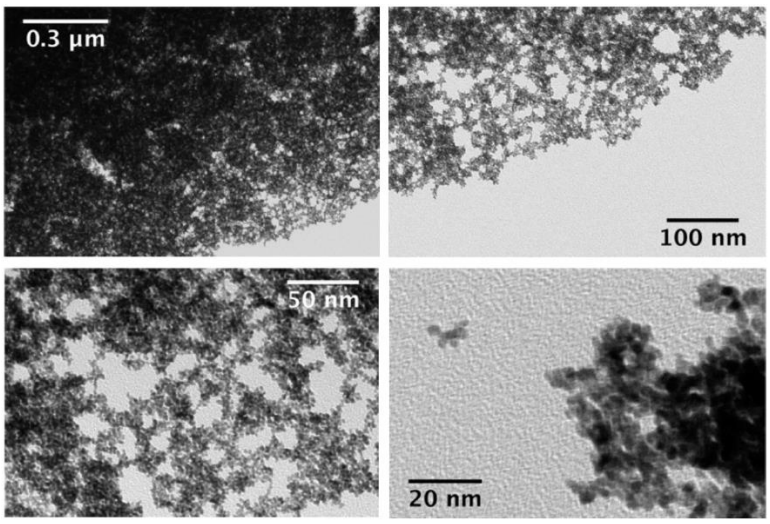

Figure 4.7: Transmission electron microscopy (TEM) images of the sample obtained under the molar ratio Pt /Fe/SC = 1/4/4.

As expected for the presence of citrate in the SN during the UV/Vis studies discussed above (**Figure** 4.6), the citrate molecules seem to remain mostly forming a stable complex with Fe(III). Because of this, effective stabilisation of the nanoparticles during the growth could be prevented, resulting in the formation of the aggregate material previously commented. An increase in the concentration of citrate to 5 mM (Pt/Fe/SC = 1/4/5) did not produce any improvement in the obtained material. (**Figure** 4.8)

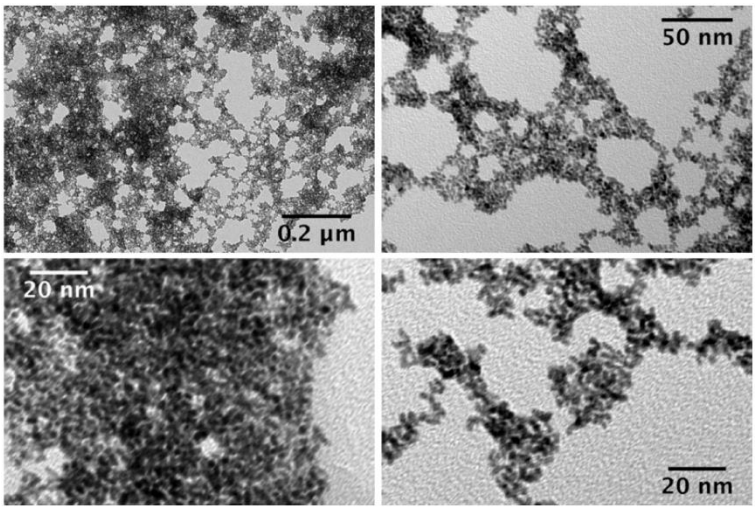

Figure 4.8: TEM images of sample obtained under the molar ratio Pt /Fe/SC = 1/4/5.

Therefore, under the studied conditions and despite the fact that the reduction of Pt(II) to Pt(0) using Fe(II) is a satisfactory process when assisted by citrate, the absence of an additional stabiliser does not allow to obtain well-defined Pt NPs under the explored conditions.

At this point, the water-soluble surfactant Polyvinilpyrrolidone (PVP_{40k}) has been selected because it provides control on the formation and deposition rates of metal particles[352], and has been widely used in synthesis of Pt NPs with catalytic or biomedical properties[313,326,327].

When the reaction was completed in the presence of PVP_{40k}, the size and morphology of the NPs showed important changes according to the molar ratio Pt/PVP used during the process (note that PVP concentrations have been expressed based on the monomeric unit of PVP). As it can be seen in **Figure** 4.9 (a), the low concentrations of PVP explored (Pt/PVP = 1/0.25) did not allow the obtaining of uniform NPs. Even so, this material, obtained in the presence of the polymer, showed a tendency to form circular aggregates of NPs with porous appearance. Analysis of size and behaviour in solution using DLS confirmed the aggregated character of the sample as revealed by the high polydispersity index (PDI) and Z-average (0.86 and 1447 nm respectively). (**Figure** 4.9 (a))

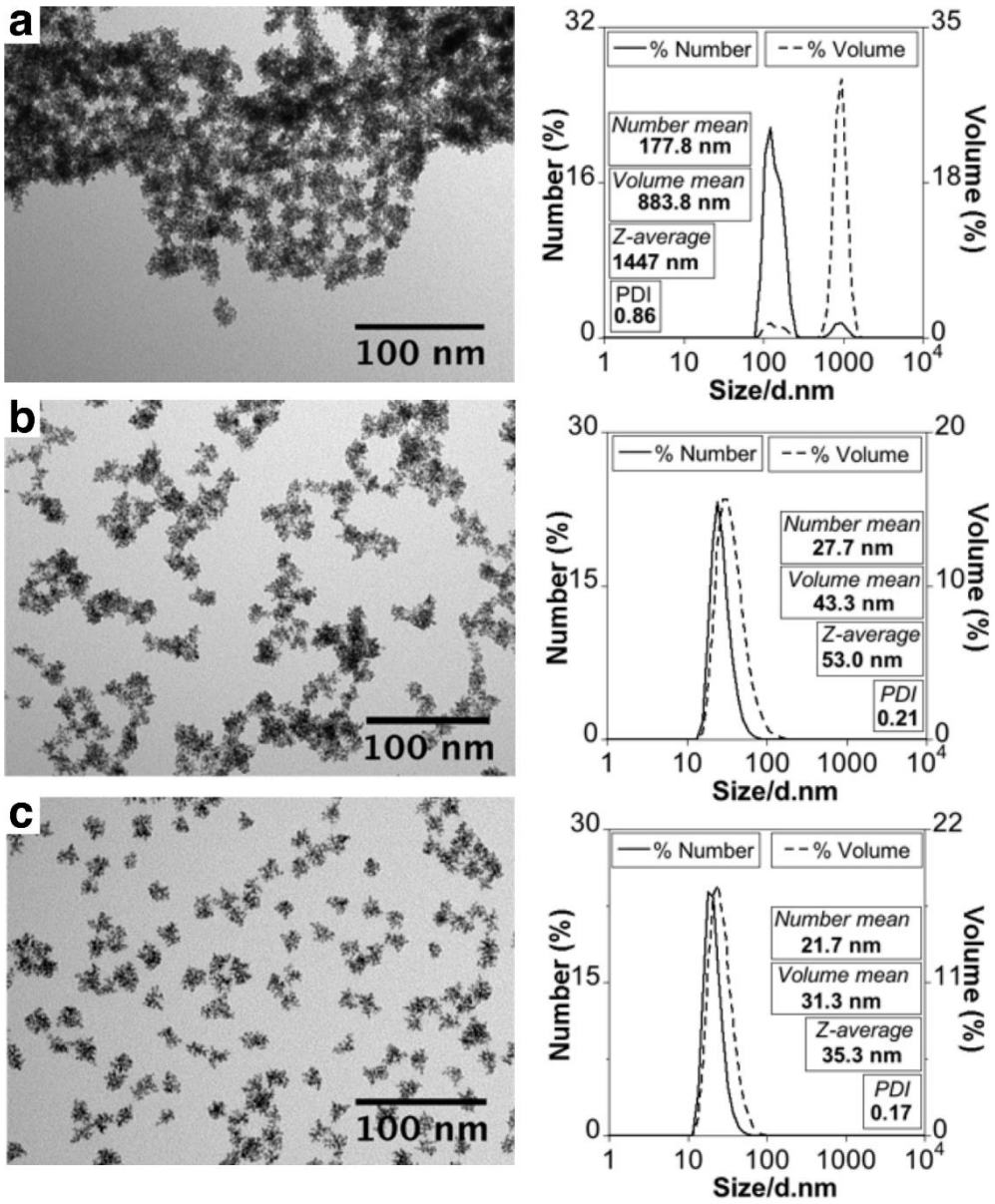

Figure 4.9: (a) Low-resolution TEM images of obtained Pt D-NPs in different Pt/PVP molar ratio: 1/0.25, (b) 1/1 and (c) 1/5 and the corresponding DLS analysis.

Conversely, for the sample obtained under [PVP] 1mM (Pt/PVP 1/1), the DLS analysis showed a lower degree of aggregation in solution, as well as a notable decrease in the average size, as evidenced by the ζ-average (53.0 nm) and PDI (0.21) obtained for these samples. (**Figure** 4.9 (b)) Under low-resolution TEM analysis, the samples showing the presence of abundant Pt NPs with a shape distribution of complete dendritic structure and particles sizes roughly distributed from 15-30 nm. For the highest [PVP] explored (Pt/PVP 1/5) the uniformity and dispersion of the nanoparticles obtained was greatly improved. (**Figure** 4.9 (c) and **Figure** 4.10)

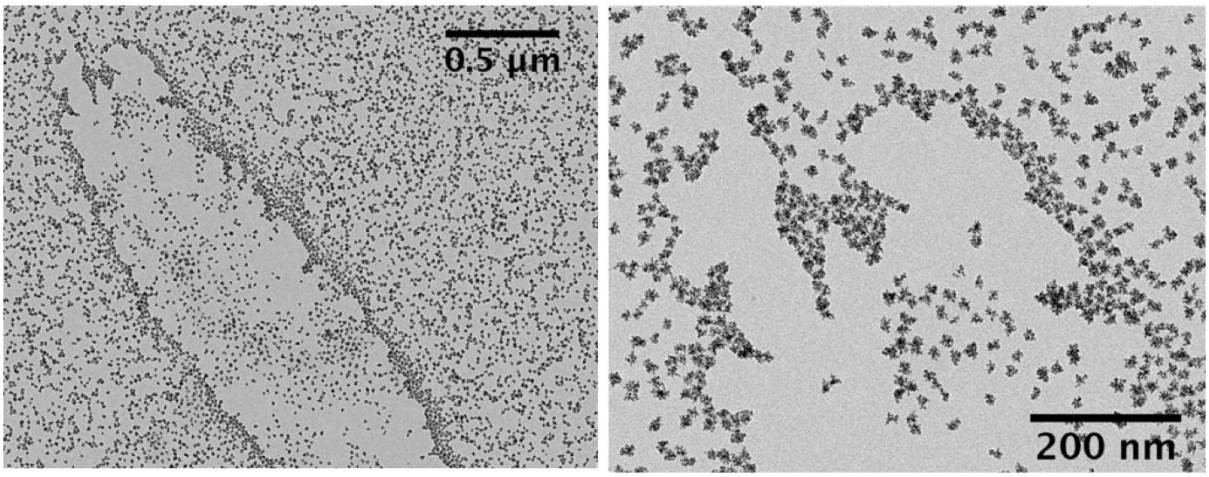

Figure 4.10: TEM images of sample obtained under the molar ratio Pt /Fe/SC/PVP = 1/4/4/5.

Aside from the increase in uniformity and well-dispersed character, the samples obtained in higher [PVP] seem to present open branched structure. Contrary, with 1mM of PVP, apparently the NPs presented a more compact structure. (**Figure** 4.9) Similar results about the optimal Pt/PVP molar ratio during the synthesis and stabilisation of Pt nanoflowers were reported by J. Yin *et al*. The authors produced monodisperse and strikingly uniform Pt nanoflowers in an iodine mediated synthesis using a polyol process (at 160 ºC). They have reported as optimal stoichiometric ratios of Pt/PVP between 1/2 and 1/10[158].

To further illustrate the essential role of PVP in the proposed approach, one reaction was performed by replacing PVP_{40k} with PSS_{70k}. The insufficient stabilisation given by the sulfonate subunits of PSS during the growth of the Pt D-NPs, seems to prevent the production of well-defined Pt D-NPs. Even so, the synthesis in the presence of PSS yields an ill-defined aggregate material but with an apparently porous structure. (**Figure** 4.11)

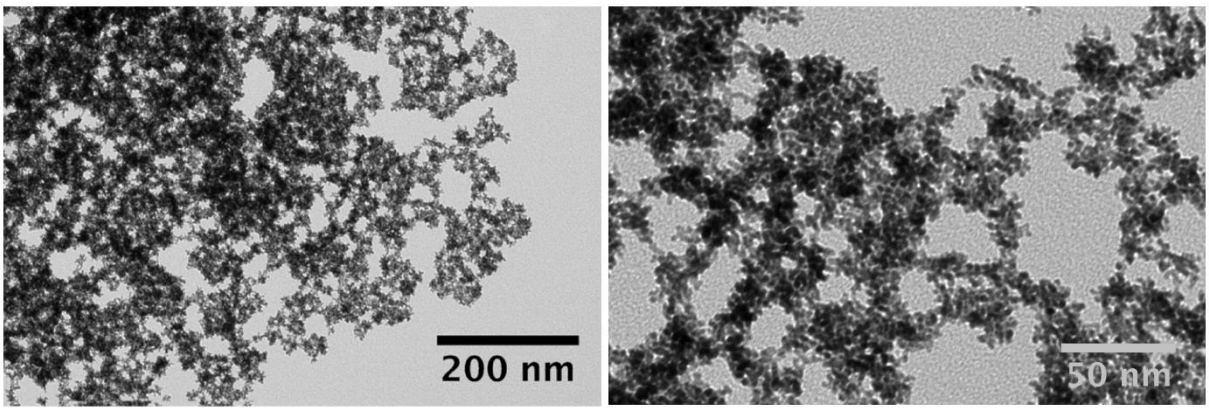

Figure 4.11: TEM images of sample obtained under the molar ratio Pt /Fe/SC/PSS = 1/4/4/5.

The effect of temperature on the final structure and morphology of Pt D-NPs was also investigated. We selected molar ratio Pt/PVP = 1/1 to produce a sample under boiling condition. (**Figure** 4.12 and **Figure** 4.13)

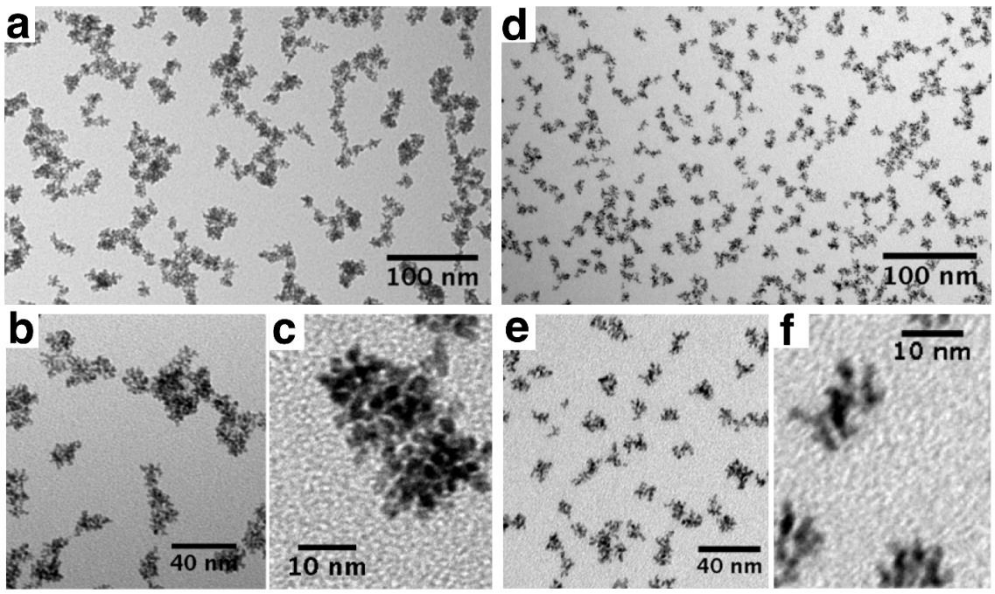

Figure 4.12: (a-c) Low-resolution TEM images of obtained Pt D-NPs obtained under molar relation Pt/PVP = 1/1 at 60 °C and (d-f) under boiling condition.

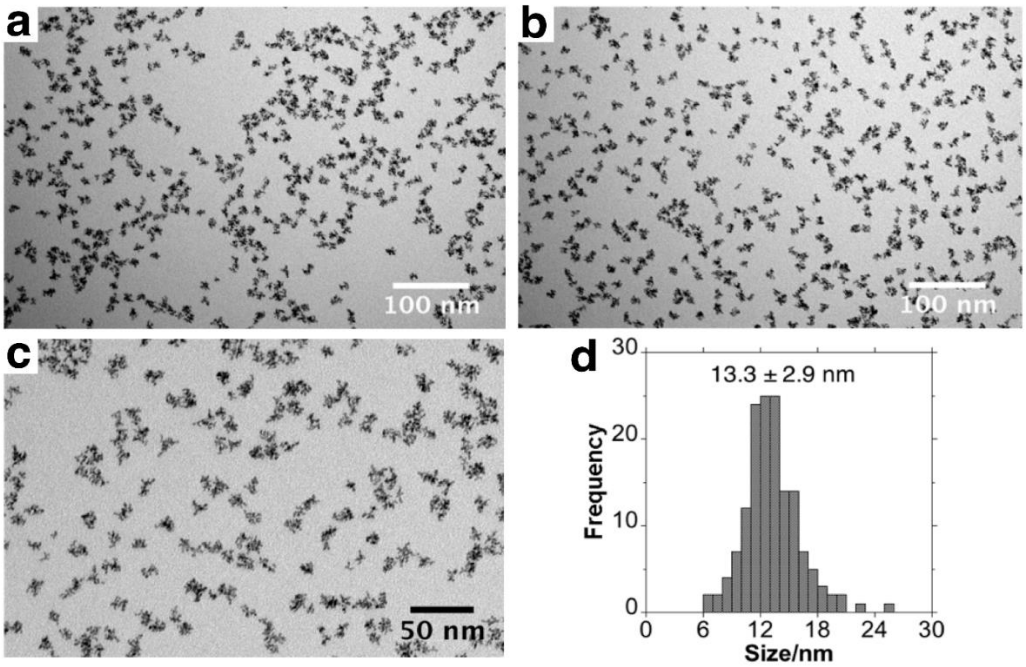

Figure 4.13: TEM images (a, b and c) and histogram (d) of sample obtained under molar ratio Pt/Fe/SC/PVP = 1/4/4/1 and under boiling condition.

It should be noticed that, under these conditions, well-dispersed Pt D-NPs of small dimensions (13.3± 2.9 nm) were obtained. More importantly, a more open branched structure was detected. This temperature-dependent particle sizes in our synthesis seems to indicate a faster reduction in early reaction stage under a higher temperature, favouring nucleation formation against growth. Our observations are in agreement with the recent studies reported by Y. Xia and co-workers. The authors report about the careful investigations related with how Pt(II) is reduced during the synthesis of Pt dendrimer nanoparticles using AA as reducers in presence of PVP at different temperatures (22-100 ºC).

Furthermore, similarly with Y. Xia work, we believe that in our process the growth of Pt D-NPs should not be related to the random aggregation of small crystals of Pt, otherwise, the synthesis under higher temperature conditions should produce larger sized nanocrystals, once a more significant number of Pt nanocrystals with smaller size, should be produced in the nucleation stage[353]. Note that in the present process, the reduction of Pt(II), and subsequent Pt particles, as highlighted in the UV/Vis studies, was favourable even at room temperature at reduced time lapses. This fact makes it difficult to perform a reliable *ex-situ* analysis of the materials obtained during their evolution applying common electron microscopy techniques. Currently, additional investigations are being conducted to explore this mechanism in more detail.

In order to understand in more detail the chemical structure and behaviour of the obtained Pt D-NPs, we have selected the sample obtained under Pt/PVP 1/5, which presents an increased structural definition and dispersion, to complete a more careful chemical characterization. As can be seen in **Figure** 4.10 and **Figure** 4.14 (a, b and d), under low-resolution TEM analysis, ≈100% of the NPs presented a well-defined dendritic structure with an average size of 15.3±2.9 nm. Analysis of the colloidal behaviour in solution using dynamic light scattering (DLS) revealed a well-dispersed character with PDI of 0.17 and ζ-average of 35.35 nm. (**Figure** 4.9(c)) To investigate the chemical surface composition of the obtained Pt D-NPs, Fourier Transform Infra-Red (FT-IR) spectroscopy analysis was performed. As can be noticed in **Figure** 4.14, the FT-IR spectra showed clearly the vibrational modes of C=O, C-N and CH_2 groups, that are attributed to the pyrrolidone ring of the PVP structure. (**Figure** 4.14(e-f) and **Figure** 4.15)

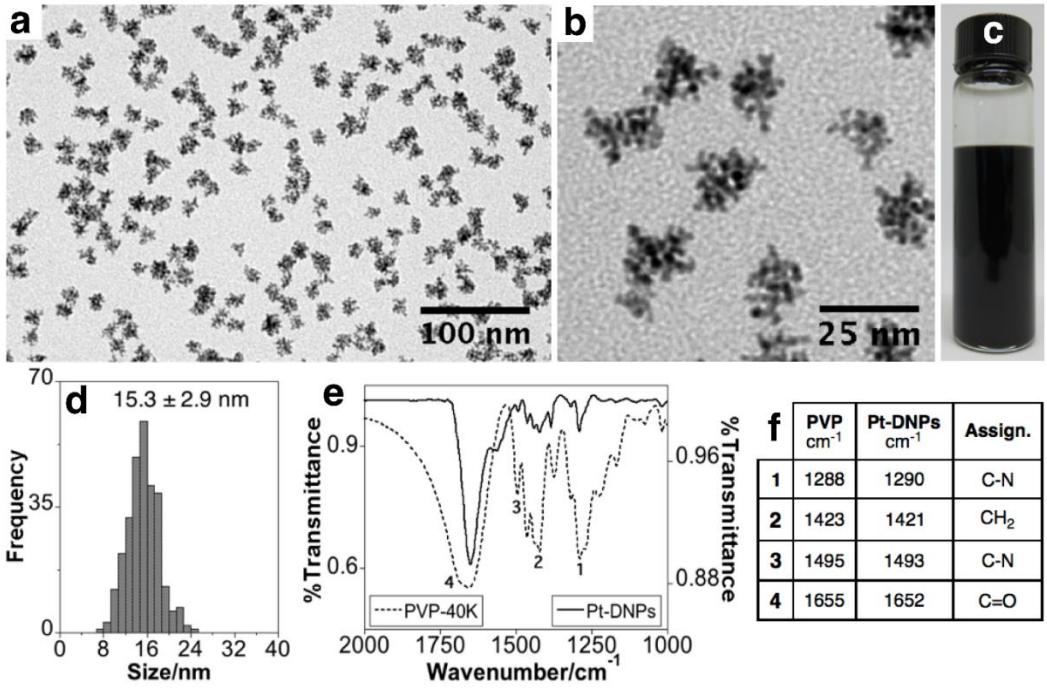

	PVP cm^{-1}	Pt-DNPs cm^{-1}	Assign.
1	1288	1290	C-N
2	1423	1421	CH_2
3	1495	1493	C-N
4	1655	1652	C=O

Figure 4.14: (a,b) Low-resolution TEM images, (c) colour solution, (d) histogram and (e and f) FT-IR study of sample obtained under Pt/PVP = 1/5.

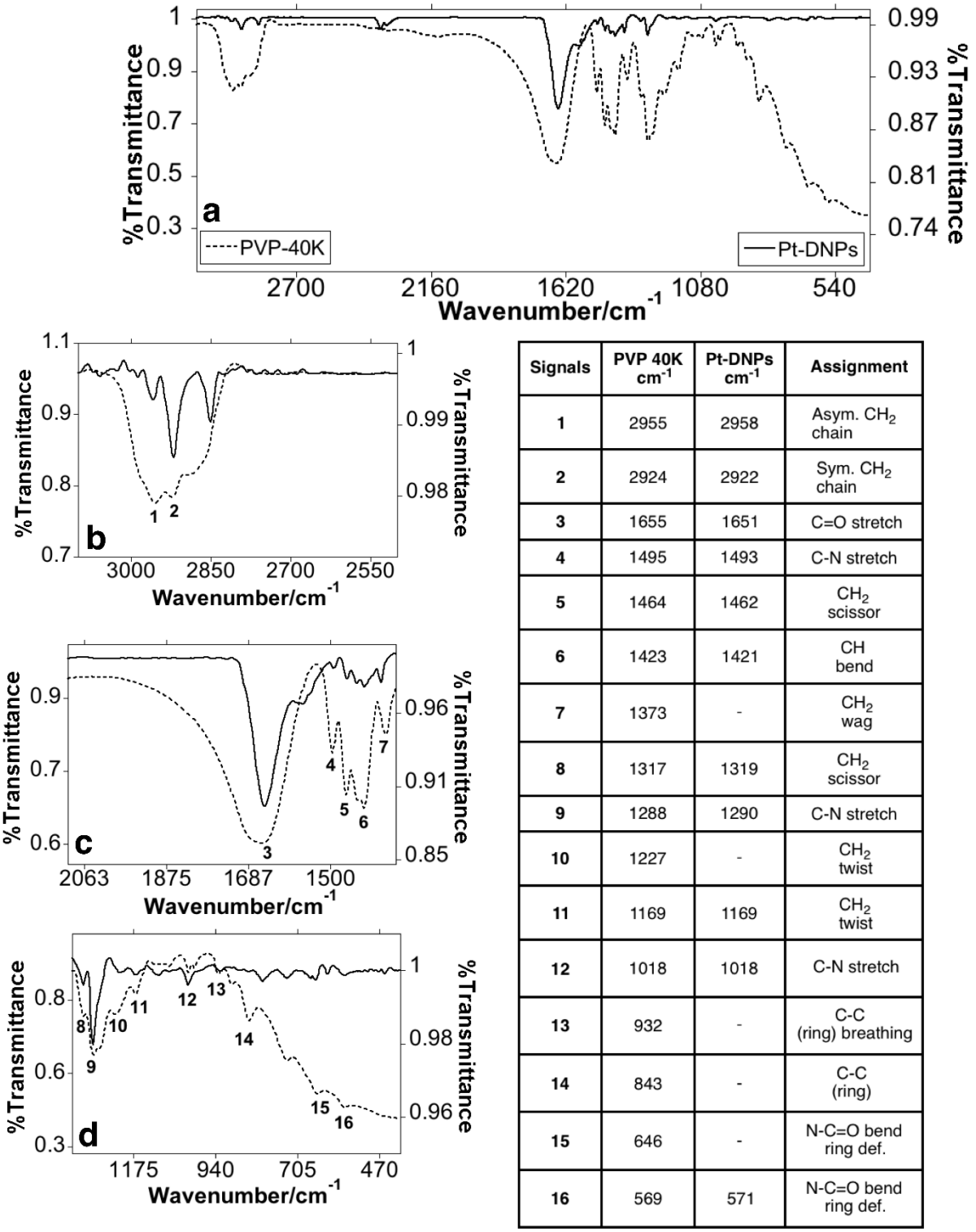

Signals	PVP 40K cm^{-1}	Pt-DNPs cm^{-1}	Assignment
1	2955	2958	Asym. CH_2 chain
2	2924	2922	Sym. CH_2 chain
3	1655	1651	C=O stretch
4	1495	1493	C-N stretch
5	1464	1462	CH_2 scissor
6	1423	1421	CH bend
7	1373	-	CH_2 wag
8	1317	1319	CH_2 scissor
9	1288	1290	C-N stretch
10	1227	-	CH_2 twist
11	1169	1169	CH_2 twist
12	1018	1018	C-N stretch
13	932	-	C-C (ring) breathing
14	843	-	C-C (ring)
15	646	-	N-C=O bend ring def.
16	569	571	N-C=O bend ring def.

Figure 4.15: FT-IR spectrum obtained for pure PVP (dotted line, Y axis left) and Pt D-NPs (sample obtained under relation Pt/PVP 1/5) (black line, Y axis right) in KBr disk. Complete spectra between 3100-400 cm^{-1} and different spectrum extensions. The table show different peaks detected with their corresponding assignments. Assignments of the signals have been based on previously detailed works on FT-IR analysis of, pure PVP and PVP/Pt nanocrystals [354,355,356].

4.3.2 Synthesis and characterization of samples for catalysis studies

Based on the analysis of structural changes produced by the different Pt/PVP molar ratio during the synthesis, we have selected 1/5 as the more suitable condition to obtain homogeneous and well-dispersed Pt D-NPs. Under these very same synthetic conditions, we have obtained the sample PtCat-1 with the aims of: first, to explore the catalytic properties, and second, to analyse the reproducibility of the process. As a comparative sample obtained in a lower Pt/PVP ratio, we obtained PtCat-2 under the ratio 1/1. In this way, we intended to analyse if the homogeneity and well-dispersed character of the NPs, and/or the [PVP] used during the synthesis can affect the catalytic properties of the obtained Pt D-NPs. Additionally, to further investigate the effect produced in response to the increasing of precursor concentration during the synthesis of Pt D-NPs obtained in ratio Pt/PVP 1/5, we produced the samples PtCat-3 and PtCat-4 with a total increase in the reagents concentration of 5-fold and 10-fold, respectively.

Firstly, we have noticed an excellent reproducibility in the size and structure of the Pt D-NPs obtained for the samples PtCat-1 and PtCat-2. As an example, PtCat-1 shows an average size of 16.0 nm, very close to the 15.3 nm obtained for the previous sample Pt/PVP 1/5. The behaviour in solution was also similar, as evidenced by the ζ-average and PDI values obtained. (**Figure** 4.16)

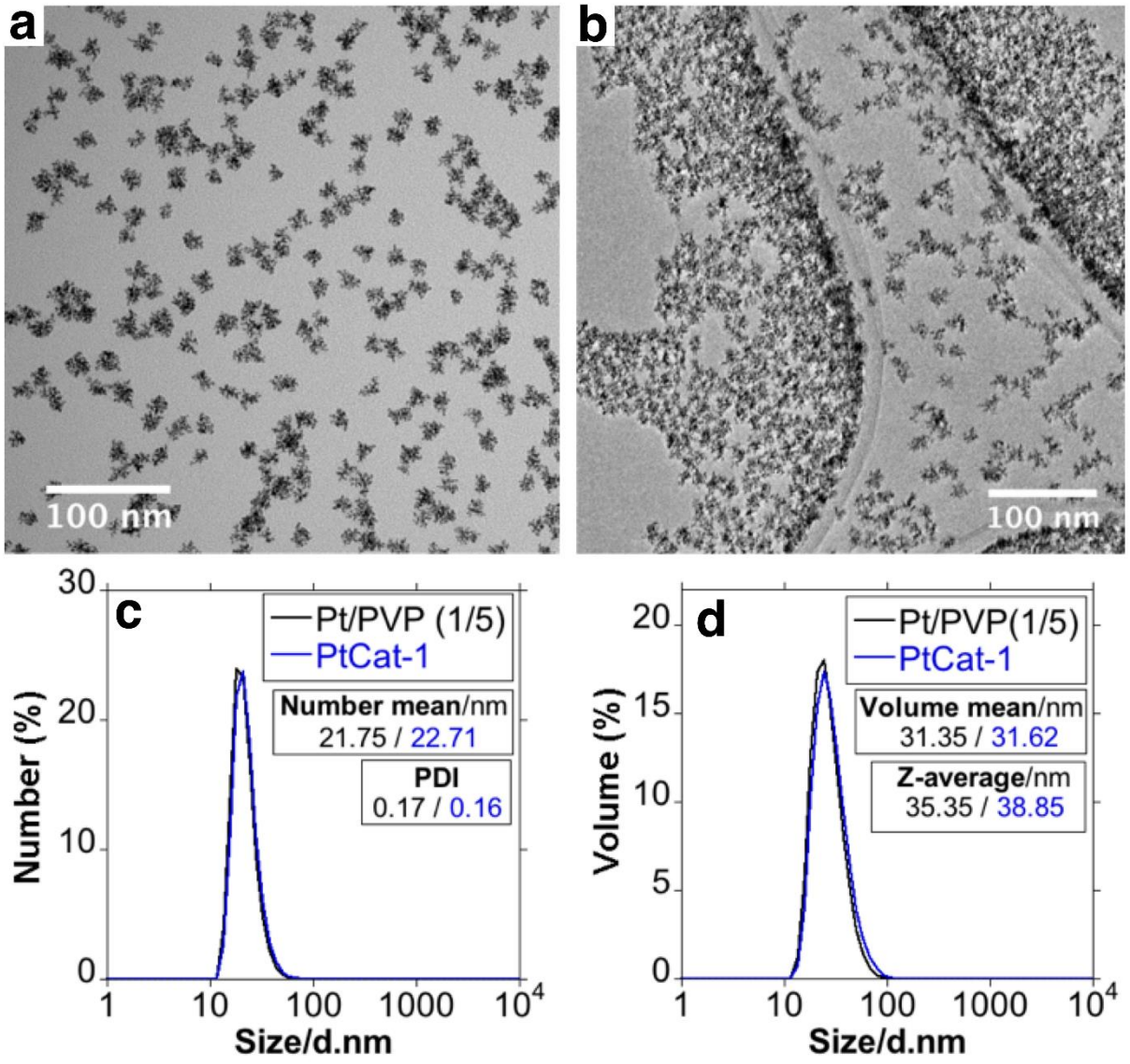

Figure 4.16: TEM images of Pt/PVP 1/5 (a) and PtCat-1 (b). DLS comparative analysis Pt/PVP 1/5 vs PtCat-1 samples, distribution by number (c) and by volume (d).

High-resolution TEM image indicates that single Pt D-NPs is an entire structure with its branches extending in random directions, (**Figure** 4.17) with a more open branched nanostructure for highest [PVP] used, PtCat-1 (Pt/PVP 1/5). (**Figure** 4.18)

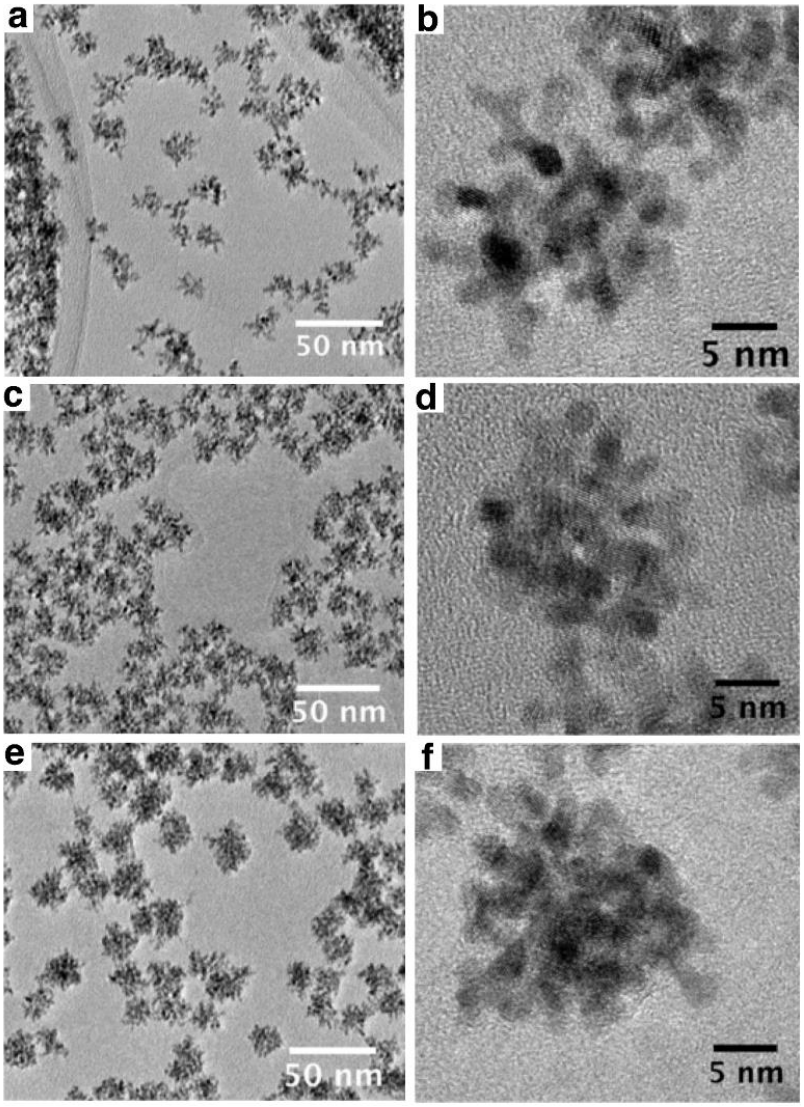

Figure 4.17: HRTEM images at different magnification of (a-b) PtCat-1, (c-d) PtCat-3 and (e-f) PtCat-4 synthesised with [K_2PtCl_4] 1, 5 and 10 mM respectively.

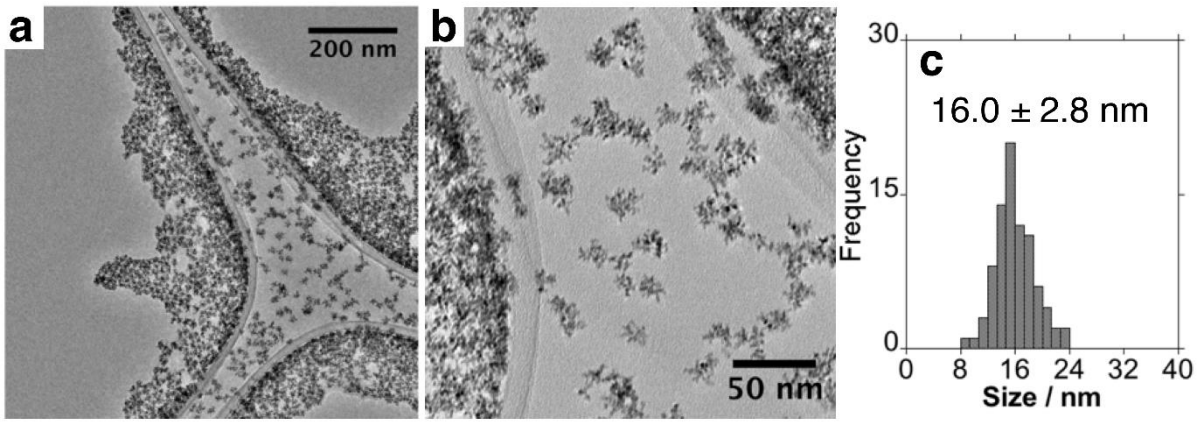

Figure 4.18: HR- TEM images at different magnification (a, b) and histogram (c) obtained for PtCat-1.

Secondly, we observed that the increase in the concentration of metal precursor during the synthesis, derived in an increase of the average size of Pt D-NPs moving from 16.0 ± 2.8 nm (for 1 mM) to 17.5 ± 2.4 nm and 20.1± 3.0 for 5 and 10 mM respectively. More important, as can be seen in **Figures** 4.16, 4.17, 4.18 and 4.19, high platinum precursor concentration promotes the obtainment of more branched and compact dendrimer structure.

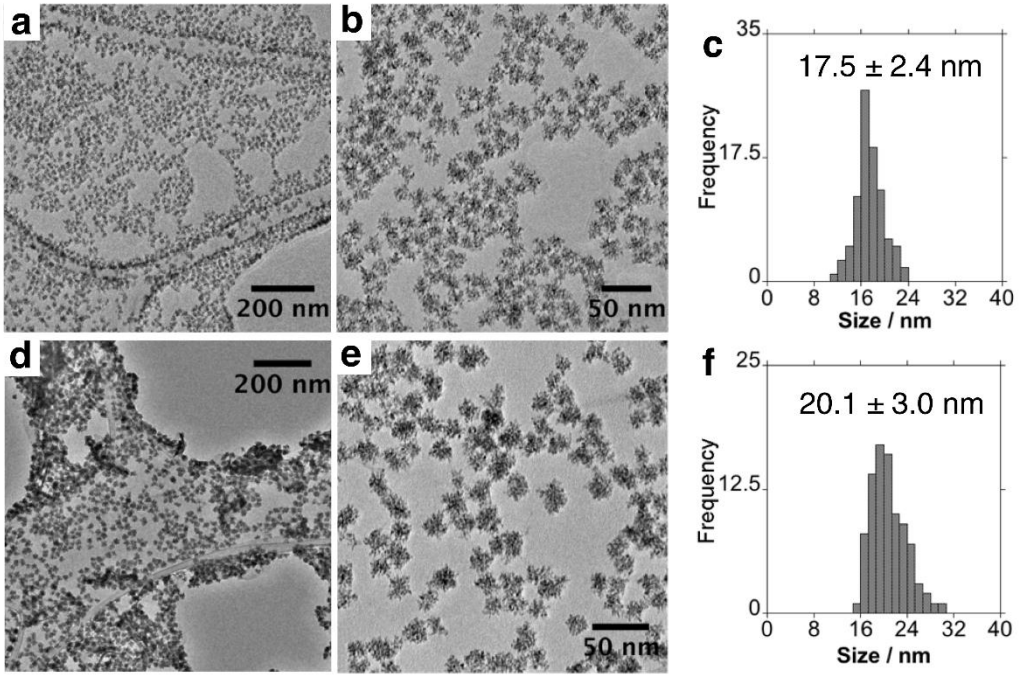

Figure 4.19: HR- TEM images at different magnification and histogram obtained for PtCat-3 (a-c), PtCat-4 (d-f).

The increase in precursor concentration is expected to favour the growth rate as a consequence of a higher monomers (growth species) concentration in solution, which are added more quickly than their subsequent surface diffusion[158,353,354,355,357,358]. High-concentration reactions in Pt NPs have shown grow, at much higher rates than low-concentration, under a kinetically controlled regime, leading to branched structures[358]. Similar structural dependences with metallic precursor were reported for the synthesis of Pt hierarchical nanostructures such as nanoflowers[158] or nanodendrimers[328,337,359,360].

HRTEM analysis at higher magnification were obtained to investigate the crystal structure in more detail. (**Figures** 4.20 to 4.23) We detected regular lattice fringes in HRTEM images with a regular inter-planar spacing of 0.225 nm, that is close to the inter-planar distance of the (111) Pt planes reported in the literature[313,329]. Apparently, domains with different crystallographic orientation are present within same NPs, those points to a polycrystalline character for the obtained NPs.

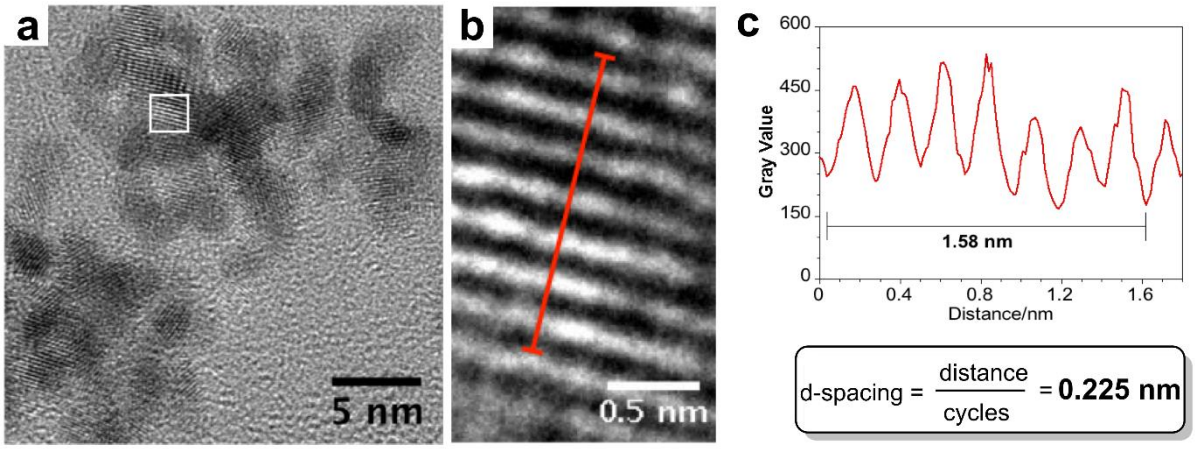

Figure 4.20: (a) HRTEM images at higher magnification, (b) representative lattice fringe under higher magnification and (c) determination of the inter-planar distance using plot profile.

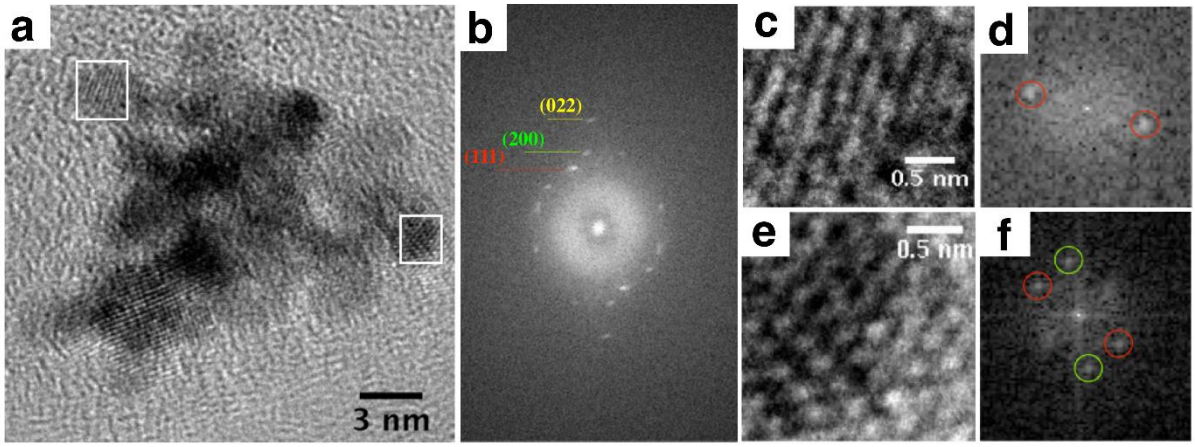

Figure 4.21: HRTEM images at higher magnification (a), and the corresponding FFT showing spots assigned to Pt (111) (marked as red), Pt (200) (marked as green) and Pt (022) (marked as yellow) (b). c and e shows two crystalline sections (marked with white box in a) and their corresponding FFT (d and f respectively) of sample PtCat-2.

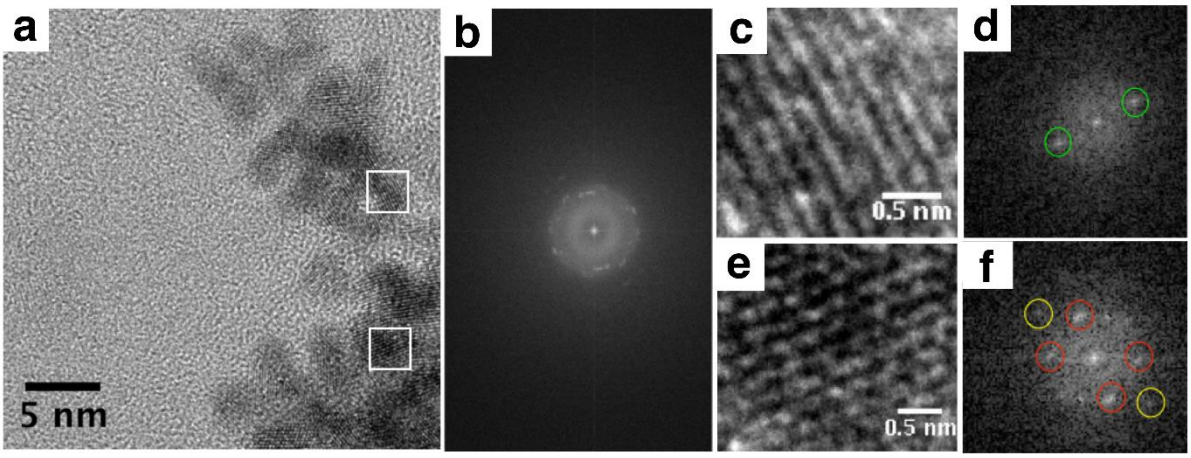

Figure 4.22 HRTEM images at higher magnification (a), and the corresponding FFT showing spots assigned to Pt (111) (marked as red), Pt (200) (marked as green) and Pt (022) (marked as yellow) (b). c and d show two crystalline sections (marked with white box in a) and their corresponding FFT (d and f respectively) of sample PtCat-4.

The FFT confirms the polycrystalline nature of Pt D-NPs (**Figure** 4.23). Also, after acquiring the FFT of the HRTEM images, we have obtained the spots at 0.22 nm, 0.19 nm, and 0.14 nm corresponding with the presence of the (111), (200) and (022) crystalline planes of Pt respectively[329], confirming the metallic character of our catalyst.

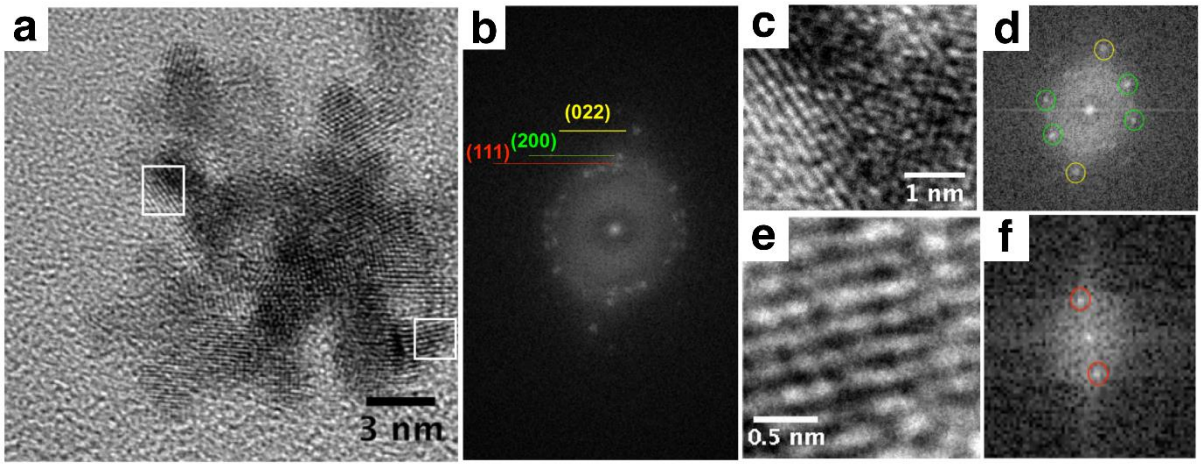

Figure 4.23: (a) HRTEM images at higher magnification and (b) the corresponding FFT showing spots assigned to Pt (111) (marked as red), Pt (200) (marked as green) and Pt (022) (marked as yellow). (c) and (e) shows two crystalline sections (marked with white box in a) and their corresponding FFT with the assignment of the bright spots (d and f respectively).

The analysis of XRD showed the same pattern in all cases. As can be seen in **Figure** 4.24, only the signal at 39.8° assigned to crystalline Pt (111)[329] was clearly detected.

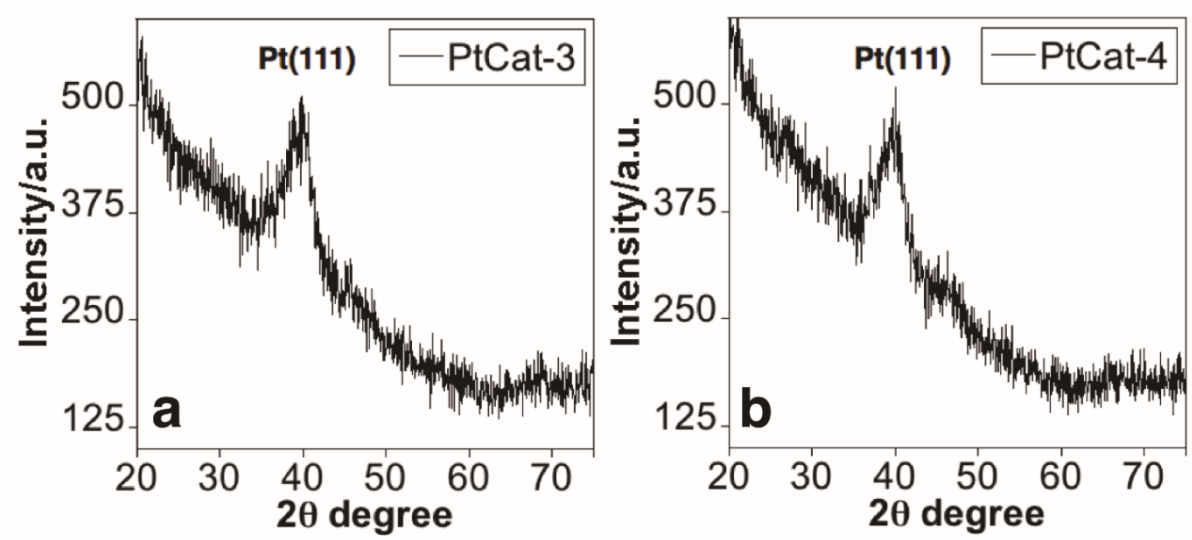

Figure 4.24: XRD spectra of PtCat-3 (a) and PtCat-4 (b) showing clearly the peaks at 39.8° corresponding with Pt (111) crystals planes.

Based on previously reported literature related to the interactions between Fe(III) ions and PVP[361], we washed with an EDTA solution the Pt D-NPs applied, before the successive washings with water.

We noticed that the samples purified previously with EDTA, showed a little decrease of the ζ-potential towards more negative values. (**Figure** 4.25)

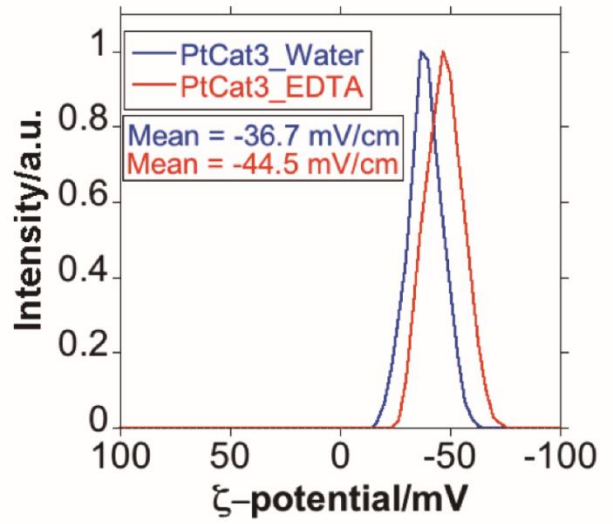

Figure 4.25: Graphic representation of ζ-potential analysis obtained for PtCat-3 purified only with water (denoted as PtCat-3_Water) or with EDTA and water process (denoted as PtCat-3_EDTA).

On the other hand, according to the transmission electron microscopy analysis, there were no structural morphology changes in the particles neither in their colloidal dispersion. (**Figure** 4.15) Likewise, the chemical composition on the surface of the NPs did not suffer modifications as revealed by the FT-IR analysis. (**Figure** 4.26)

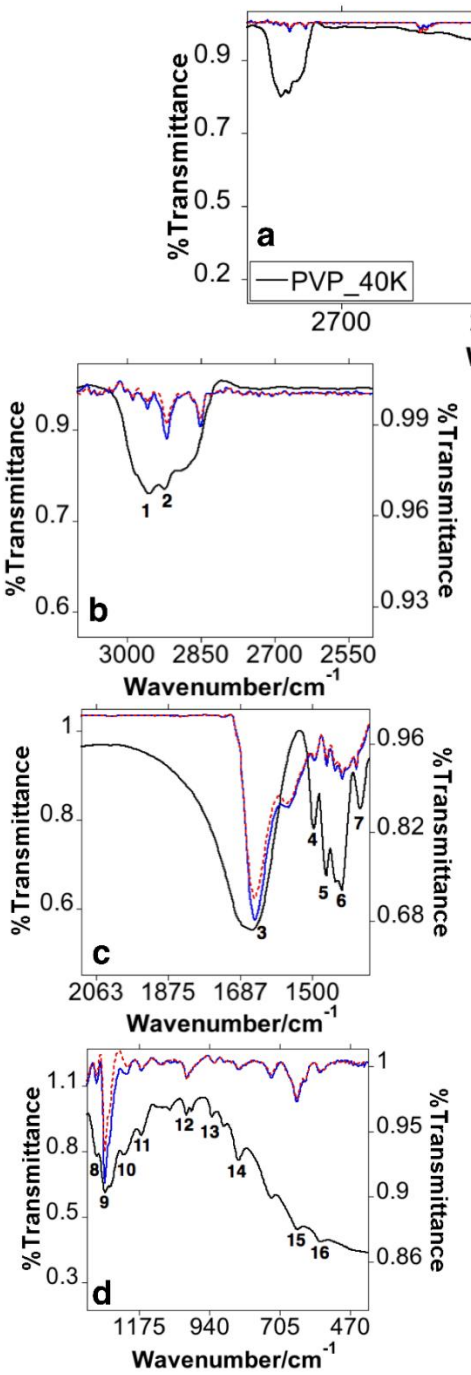

Signals	PtCat3_Water cm^{-1}	PtCat3_EDTA cm^{-1}
1	2959	2957
2	2918	2918
3	1449	1451
4	1493	1495
5	1462	1462
6	1421	1421
7	-	-
8	1317	1317
9	1290	1290
10	-	-
11	1169	1169
12	1016	1016
13	-	-
14	841	841
15	648	650
16	571	573

Figure 4.26: FT-IR spectrum obtained for pure PVP (black line, Y axis left) and PtCat-3 (sample purified only with water (blue line, Y axis right) or EDTA and water (red line, Y axis right) (black line, Y axis right) in KBr disk. Complete spectra between 3100-400 cm^{-1} and different spectrum extensions. The table show the different peaks detected. Assignments of the signals is showed in **Figure** 4.15.

Despite of EDTA purification process applied, ICP-MS analysis of different Pt D-NPs samples used in catalysis, a remanent Fe (%w) around 0.5 % was detected in all cases (concerning the total metallic mass).

4.3.3 Catalytic applications

First, the catalytic application of the Pt D-NPs was evaluated in the reduction of p-nitrophenol (pNP) to p-aminophenol (pAP) in aqueous media at room temperature. (**Figure** 4.27)

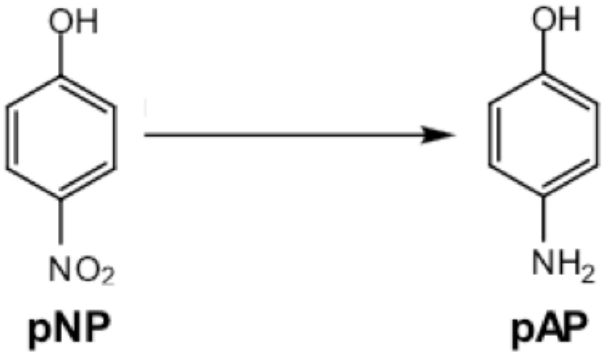

Figure 4.27: Scheme of the reduction of pNP to pAP.

All Pt D-NPs, specially PtCat-3 and PtCat-4, proved to be excellent catalysts in the reduction process, being able to reduce the totality of 5 mM (695 mg/L) of pNP to pAP in 90 seconds. (**Figure** 4.28)

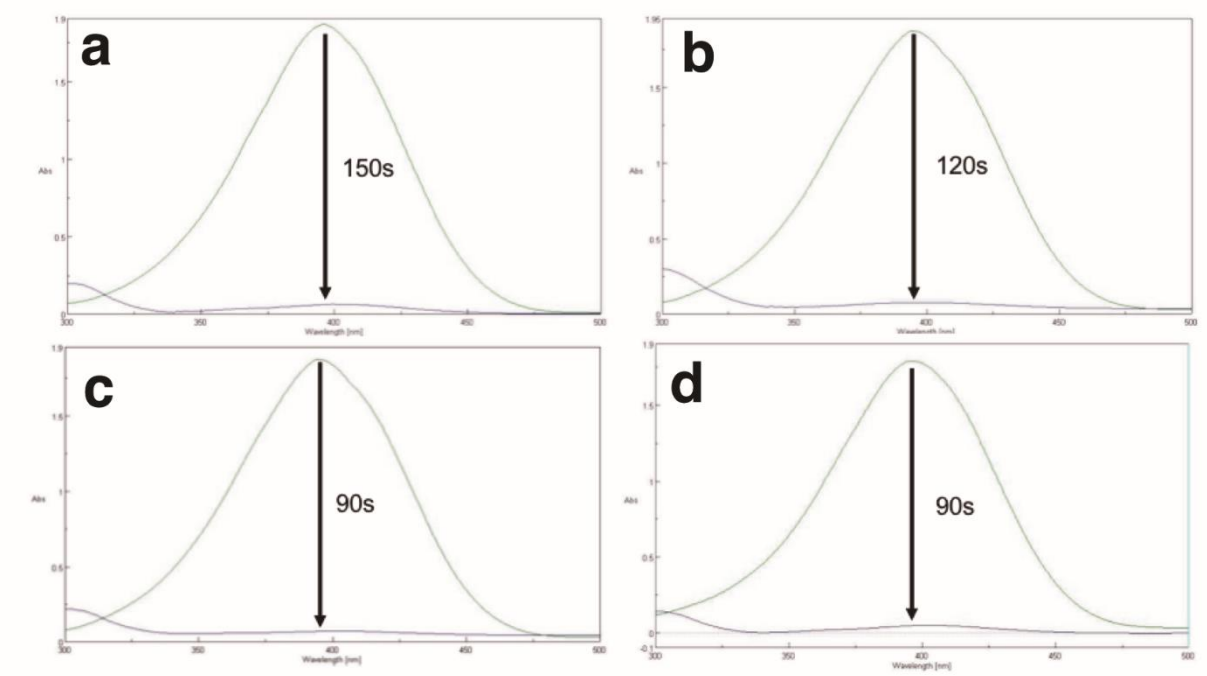

Figure 4.28: Time-dependent absorption spectra of the metal-catalysed reduction of 5 mM pNP in the presence of different Pt D-NPs and $NaBH_4$: a) PtCat-1 (60.6 µg Pt); b) PtCat-2 (89 µg Pt); c) PtCat-3 (71.8 µg Pt); D) PtCat-4 (75 µg Pt).

pNP is found as a contaminant of industrial effluents, soil and groundwater. It has been classified as a priority pollutant by the United States Environmental Protection Agency (US EPA), which recommends restricting pNP concentrations in natural waters. US EPA has established 1 µg/L as the Maximum Contaminant Level (MCL) for phenols in drinking water.

One important parameter for comparing the catalytic activity of the different Pt D-NPs is the turnover frequency (TOF) value. The produced pAP moles were calculated using the absorbance values. Afterwards, the turnover number (TON, **Equation** 4.1) and the turnover frequency (TOF, **Equation** 4.2) were calculated as follow:

$$\text{TON} = \frac{produced\ pAP\ amount\ (mmol)}{Pt\ amount\ (mmol)} \quad (4.1) \qquad \text{TOF}\ (min^{-1}) = \frac{TON}{time\ (min)} \quad (4.2)$$

In order to calculate the TON, the added Pt amounts was considered. A very diluted amount of catalysts was used for the reductive reaction and, adjusting the Pt amount of each catalyst, their catalytic profiles were determined (**Figure** 4.29).

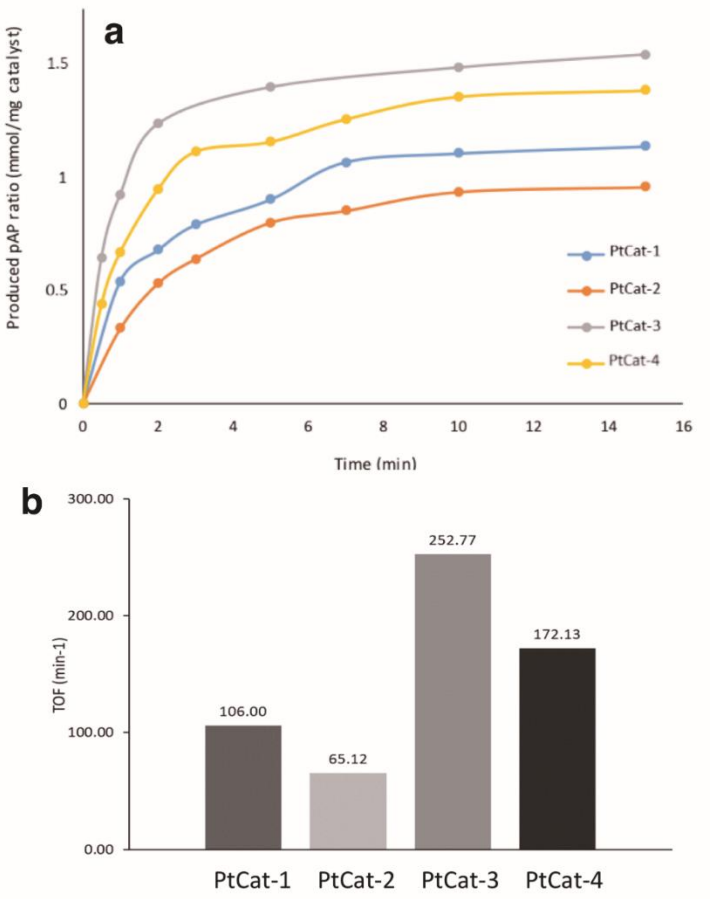

Figure 4.29: a) Catalytic activity of Pt D-NPs represented as the ratio of the produced pAP mmol per milligram of added Pt. b) Turnover frequency (TOF; min^{-1}) of Pt D-NPs.

According to the profiles, PtCat-3 is the most efficient catalyst (**Figure** 4.28), being able to reduce pNP at a higher rate per milligram of Pt, which translates into a TOF value of 253 min^{-1}.(**Figure** 4.29(b)) To the best of our knowledge, this is the highest value of Pt catalyst for this reaction and 1.5 times higher than the best value for a palladium catalyst described in literature[362]. PtCat-1 and PtCat-4 also showed a similar TOF value. (**Figure** 4.29(b))

Our results showed that the worst catalytic performance obtained was for the sample produced in the lower concentration of PVP (PtCat-2). In this sense, it can be noted that the average size and final dispersion of the NPs greatly influence the catalytic capabilities of nanodendrimers of Pt. On the other hand, between the catalysts, PtCat-1, PtCat-3 and PtCat-4, those obtained in higher Pt precursor concentration showed a clear improved catalytic performance, despite being in a similar size range (between 15-20 nm). We attribute these observations to the most significant number of branches by nanoparticles detected by TEM/HRTEM analysis for PtCat-3 and PtCat-4 when compared with PtCat-1. This increased number of branches, should lead to a greater number of available sites for catalysis reactions.

4.3.3.1 Temperature stability

The stability of the Pt D-NPs at different temperatures was studied. The four catalysts (PtCat-1 to PtCat-4) were incubated directly at 40, 60, 80 and 100 ºC. (**Figure** 4.30(a))

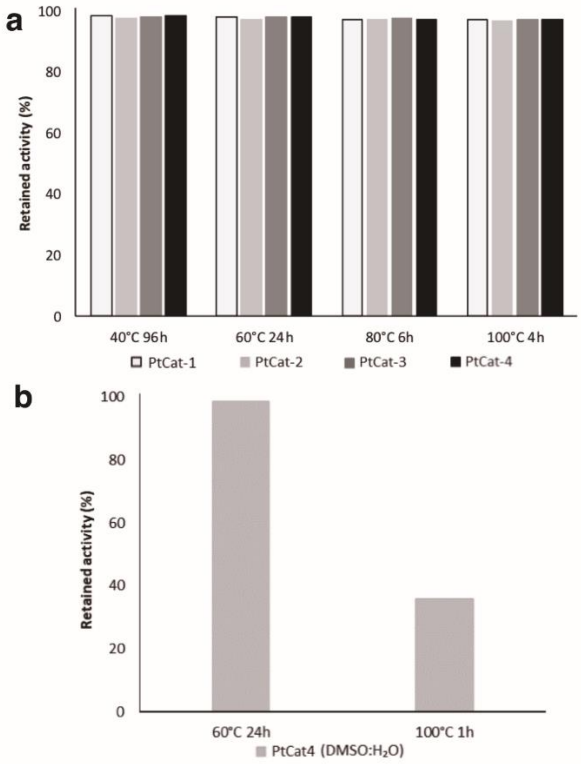

Figure 4.30: Thermostability at different T. b) Thermostability of the PtCat-4 in 50 % DMSO.

The stability was evaluated considering their activity in the reduction of pNP, taking the catalytic value of each catalyst at 25 ºC as 100% activity. pNP activity was evaluated at different times. In all cases, the four Pt nanodendrimers were completely stable and maintained more than 95% catalytic activity after 24 h incubation at 40 and 60 ºC. (**Figure** 4.30(a)) At 80 ºC, the catalysts were fully stable after 6 h of incubation and at 100 ºC after 4 h. In these two cases, the high value of T caused solvent evaporation, which prevented from acquiring further measurements. Also, stability of PtCat-4 in the presence of 50% DMSO as co-solvent was evaluated. (**Figure** 4.30(b)) The catalyst was stable at 60 ºC, but at 100ºC only 50 % of the activity was conserved after 1 h incubation.

4.3.3.2 Substrate concentration

In order to evaluate the catalyst suitability, PtCat-3 reductive activity was evaluated at different concentrations of pNP. (**Figure** 4.31) Using only 10 µL of PtCat-3 solution (28.72 µg of Pt) a full conversion was obtained even at high substrate concentrations. In 25 min, PtCat-3 catalyst was able to

complete the reduction of 20 mM pNP (2780 ppm). Plotting pNP concentration *versus* time, a linear tendency was observed. (**Figure** 4.31) These results illustrate this catalyst ability to degrade this pollutant, even at high concentrations.

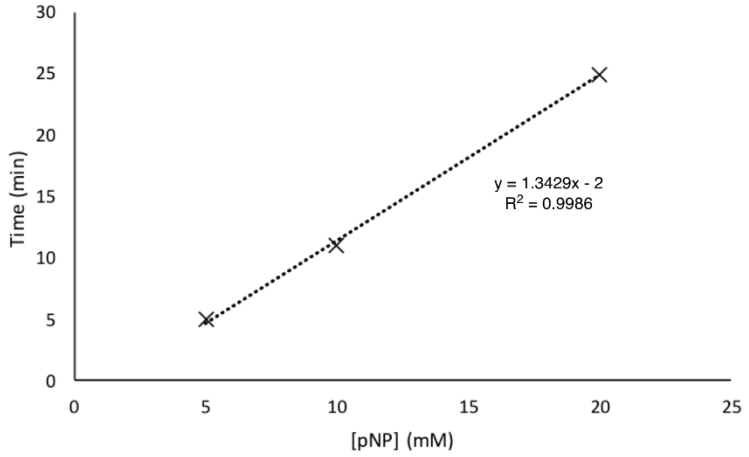

Figure 4.31: pNP concentration versus time using PtCat-3 as catalyst. Time value shown is the required to complete the reduction of substrate.

4.3.3.3 Application of the Pt D-NPs as an artificial metalloenzyme with catechol oxidase-like activity

Another exciting application of metal conjugate is mimicking biological catalytic activities, such as oxidases mimicry-for example, polyphenol oxidases, tyrosinases or catechol oxidases. Mushroom (*Agaricus bisporus*) tyrosinase can catalyze: (i) the o-hydroxylation of monophenols to o-diphenols as well as (ii) the oxidation of o-diphenols to produce o-quinones. In contrast, and by definition, catechol oxidase can only catalyze the oxidation of o-diphenols to their corresponding o-quinones. Here, catechol oxidase-like activity of the different Pt D-NPs was evaluated. Using L-DOPA as substrate this catechol oxidase activity was determined at two different pHs. At pH 7, PtCat-3 and PtCat-4 showed the highest catechol oxidase activity, with around 10000 U/mg, 2 times higher than the activity achieved by PtCat-1 and PtCat-2 and only 5 times less active than *A. bisporus* tyrosinase (**Table** 4-1).

Table 4-1: Oxidation of L-DOPA catalysed by the different PVP/Pt nanodendrimers.

Entry	Sample	Buffer (pH) [a]	ΔAbs/min	U [b]	U/mg [c]
1	PtCat-1	Na_3PO_4 (7)	0.0247 (15 µL)	12.35	2717.27
2	PtCat-1	NaOAc (4)	0 (15 µL)	0	0
3	PtCat-2	Na_3PO_4 (7)	0.0314 (15 µL)	15.7	2352.06
4	PtCat-2	NaOAc (4)	0.0027 (15 µL)	1.35	202.25
5	PtCat-3	Na_3PO_4 (7)	0.2104 (15 µL)	105.2	5049.19
6	PtCat-3	NaOAc (4)	0.0461 (15 µL)	23.05	1106.31
7	PtCat-4	Na_3PO_4 (7)	0.211 (15 µL)	105.5	4897.86
8	PtCat-4	NaOAc (4)	0.021 (15 µL)	10.8	501.4
9	Tyrosinase	Na_3PO_4 (7)	0.1237 (10 µL)	61.85	50284.55
10	Tyrosinase	NaOAc (4)	0.0017 (10 µL)	0.85	691.06

[a] Condition: 1 mM L-DOPA in 2 mL of 100 mM Na_3PO_4 at pH 7 or NaAcO at pH 4. [b]Activity Unit (U) was defined as the amount of enzyme/catalyst causing an increase in absorbance of 0.001/min at 25°C. Specific activity (U/mg) was calculated dividing the Units obtained in the reaction by the amount of either enzyme or platinum in mg. Added Pt amounts (mg) were: PtCat-1 0.00909, PtCat-2 0.01335, PtCat-3 0.04167, PtCat-4 0.04308. Added tyrosinase amounts (mg) were: 0.00246 mg.

Interestingly, activity seemed extremely affected by pH. On that subject, at acidic pH (pH 4) all the catalysts showed lower activities compared to pH 7 (**Table** 4-1). At pH 4, PtCat-3 showed the highest activity, two-fold higher than the one of PtCat-4, 5 times more than PtCat-2 and PtCat-1 was utterly inactive at this pH. Tyrosinase showed a substantial decrease of activity at this pH, becoming less active than PtCat-3 or PtCat-4 Pt D-NPs.

In order to evaluate in more detail, the pH effect, catechol oxidase activity of PtCat-4 and tyrosinase were tested at different pHs. (**Figure** 4.31)

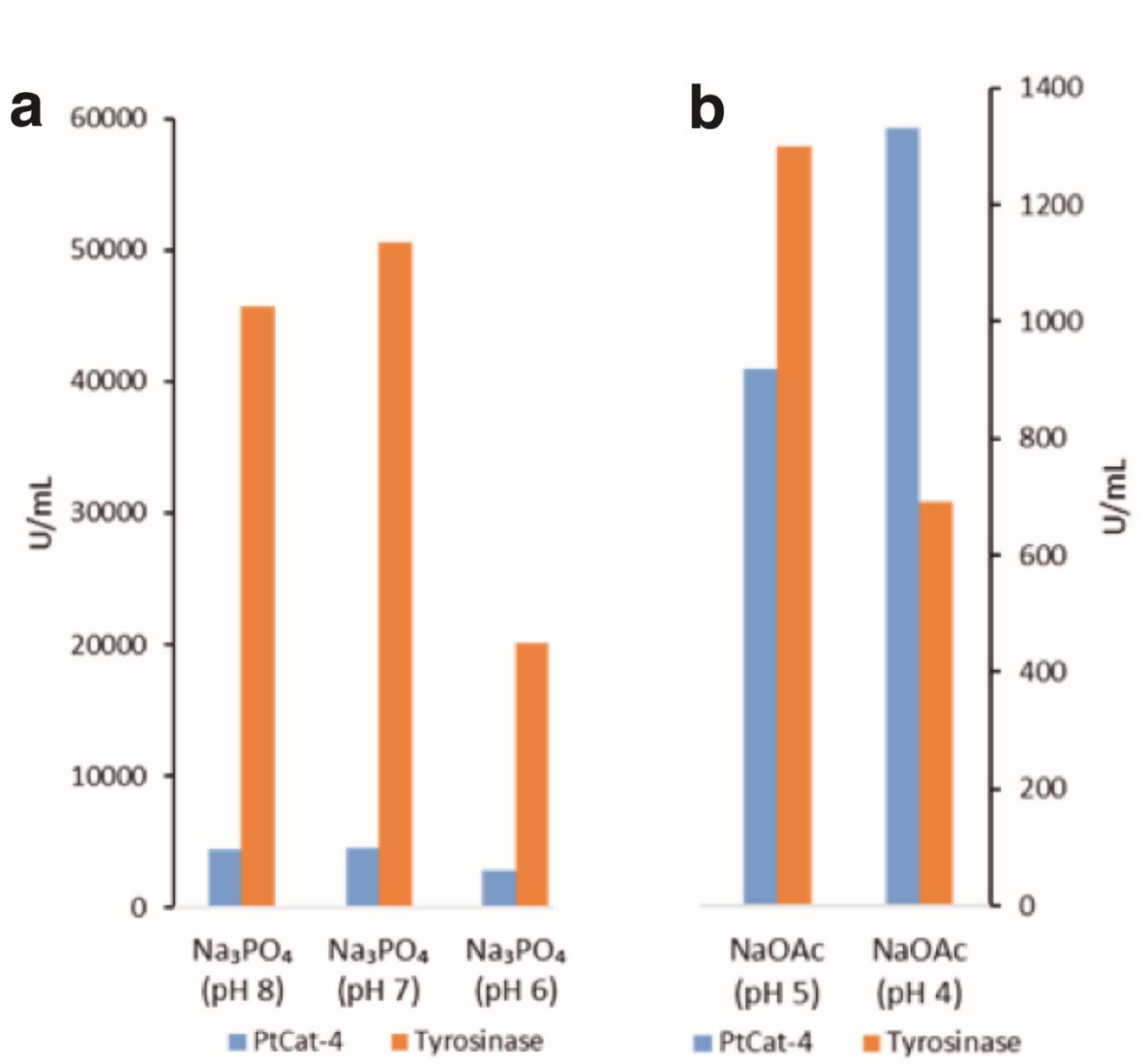

Figure 4.32: (a) Catechol oxidase activity assay of PtCat-4 catalyst and mushroom tyrosinase under 100 mM Na_3PO_4 at pH 8 to 6 or (b) NaOAc at pH 5 to 4 buffer and 1 mM of L-DOPA.

The highest activity of the tyrosinase was reached at pH 7, whereas for PtCat-4 the highest value was either pH 7 or 8 (it showed the same activity at both pHs). Decreasing the pH resulted in a consequent loss in activity for both tyrosinase and PtCat-4. The highest decrease was observed at pH 5 in both cases, being more accused in the enzyme. (**Figure** 4.32) Therefore, this seems to demonstrate that Pt D-NPs catalysts could be excellent candidates as catechol oxidase mimics at acidic pHs.

Another critical point for the application of enzyme as catalyst, is the effect of substrate saturation. Concerning this, tyrosinase and PtCat-4 activities were evaluated against different L-DOPA concentrations in sodium phosphate buffer pH 7. (**Figure** 4.33) Tyrosinase activity was affected by substrate concentration, shown by the clear saturation of the active site observed at 0.25 mM concentration of L-DOPA. However, the enzymatic activity still increased at higher concentrations (up

to 5 mM). In contrast, PtCat-4 was rapidly saturated and the activity resulted in almost the same from 0.25 to 5 mM of L-DOPA.

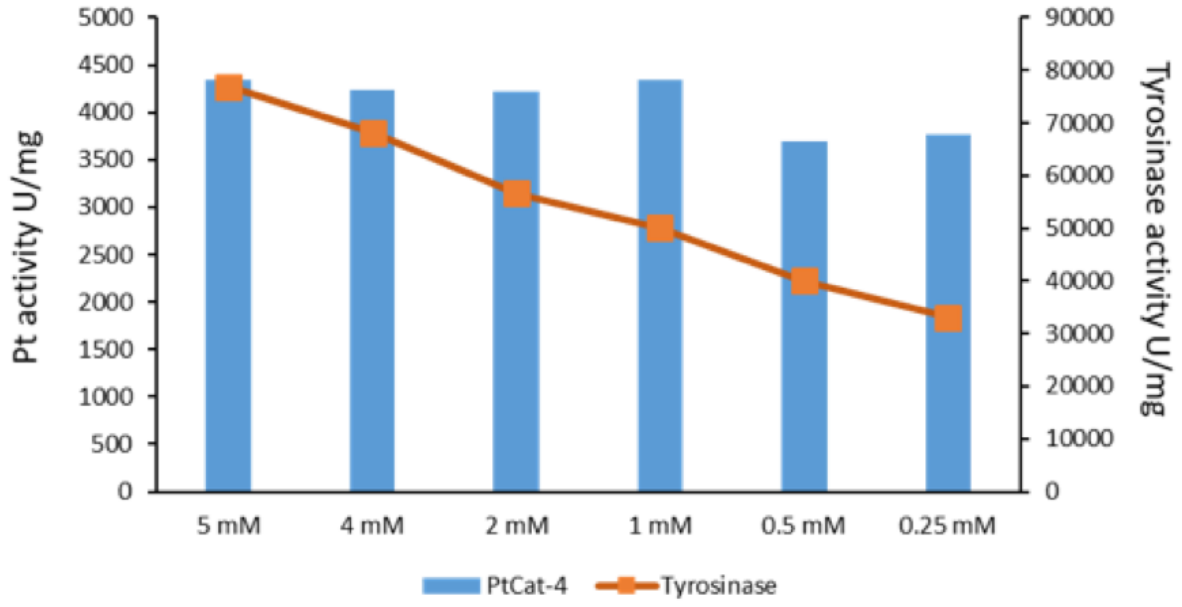

Figure 4.33: Catechol oxidase activity assay of the PtCat-4 catalyst and mushroom tyrosinase under 100 mM Na_3PO_4 at pH 7 and concentrations of L-DOPA from 5 to 0.25 mM. Pt amount was 0.02872 mg/mL and tyrosinase was 0.00246 mg/mL.

4.4 Conclusions

We have developed a new synthetic process to obtain Pt dendrimer nanoparticles (Pt D-NPs), based on the application of $FeSO_4$ in the presence of citrate as the principal reducing agent. This one-pot, aqueous based solution synthesis at relatively low temperature (60 ºC) and using PVP_{40k} as a surfactant, allows obtaining polycrystalline well-dispersed Pt D-NPs with sizes between 13 to 20 nm. The molar ratio Pt/PVP = 1/5 with the initial concentration of metal precursor (K_2PtCl_4) between 5 and 10 mM are the best conditions to obtain denser branched and quasi-spherical Pt D-NPs. The different dendrimers showed excellent catalytic properties in two different processes: reduction, and oxidation reactions. Furthermore, all of them were quite stable even at very high Tª (80 °C, or 100 °C). The results obtained in the reduction of p-nitrophenol, an organic pollutant, for PtCat-3 catalyst turned out to be most effective catalyst displaying *the highest TOF value* described in literature for a Pt catalyst in this reaction, being able to remove up to 2780 ppm of pNP in 20 min using only 10 microliters of catalyst, which contains 28.72 µg of Pt. Also, these Pt D-NPs exhibited catechol oxidase-like activity, showing around 5000 U/mg at pH 7. These Pt D-NPs were even more active than tyrosinase from *A. bisporus* at pH 4. Finally, we have observed that the optimum Pt D-NPs size to maximize the catalytic activity was found in the PtCat-3 sample around 17.5 nm.

5 Chapter 5

Synthesis of Gold Nanorods with mesoporous silica shell containing Doxorubicin and Methylene Blue as drugs, and their applications as anti-cancer and antimicrobial nanotools.

Adrián Fernández-Lodeiro, Jamila Djafari, Javier Fernández-Lodeiro, Julia Lorenzo, Sergi Rodriguez Calado, Maria Paula Duarte, Elisabete Muchagato Mauricio, José Luis Capelo, Carlos Lodeiro," Synthesis of Gold Nanorods with mesoporous silica shell containing Doxorubicin and Methylene Blue as drugs, and their applications as anti-cancer and antimicrobial nanotools". (2019). In preparation

Communicated in:

1.- **Adrián Fernández-Lodeiro**, Javier Fernández-Lodeiro, Jamila Djafari, Elisabete Oliveira, Hugo M. Santos, José Luís Capelo, Carlos Lodeiro. P52 Synthesis and studies of gold nanorods as nanocarriers for drug delivery in cancer cells. 3rd ST 2018 - International Caparica Christmas Conference on Sample Treatment, 03-06 December 2018, Caparica, Portugal.

2.- **Adrián Fernández-Lodeiro**, Javier Fernández-Lodeiro, Jamila Djafari, Elisabete Oliveira, Hugo M. Santos, José Luís Capelo, Carlos Lodeiro. P45 Synthesis and emission of gold-nanorods conjugated with three model drugs: Doxorubicin (Red), Rose Bengal Sodium Salt (Pink) and Methylene Blue (Blue). 3rd IC3EM 2018 - International Caparica Conference on Chromogenic and Emissive Materials, 03-06 September 2018, Caparica, Portugal.

3.- **Adrián Fernández-Lodeiro**, Javier Fernández-Lodeiro, Jamila Djafari, Elisabete Oliveira, Hugo M. Santos, José Luís Capelo, Carlos Lodeiro: "Synthesis of silica shell gold-nanorods conjugated with model drugs: Doxorubicin (Red), Rose Bengal Sodium Salt (Pink) and Methylene Blue (Blue)." International Symposium Ewha Chemistry and Nanoscience (ECNIS), 18-19 May 2017 Seoul, South Korea

Candidate contribution: performed the synthesis, analysis and characterisation (UV/Vis, FT-IR, ζ-potential) of the nanomaterials and helped in the discussion of all the analysed data and the writing of the final version of the chapter.

5.1 Introduction

Since the pioneering works on the synthesis of gold nanorods (AuNRs) using a wet chemistry approach,[78,363] a growing interest has been awakened in this fascinating nanostructures, mainly due to the intriguing optoelectronic properties that arise from this anisotropic nano-shape.[364]

AuNRs exhibit localised surface plasmon resonance which occurs from the interaction of an electromagnetic field with the free electrons confined in the gold metal nanostructure.[61,61] But, contrary to isotropic nanostructures, such as spheres which have a unique local surface plasmon resonance (LSPR) mode, in AuNRs, two LSPR modes are presents: transversal ($LSPR_{trans}$) and longitudinal $LSPR_{long}$, associated with the collective oscillations of the conduction free electrons in the transverse and longitudinal directions of the gold rod respectively.[365] The $LSPR_{trans}$ can be tuned in an electromagnetic range coincident with the biological tissue transparency window (650-900 nm). Furthermore, the plasmon energy of $LSPR_{trans}$ is strongly linked with the aspect ratio (AR) of AuNRs - unlike gold spheres, which have similar plasmon energy across 4-200 nm in diameter.[364] As a consequence, after coherent photo-excitation of surface plasmons, the efficient conversion in localised heat increments seem to be more pronounced for the case of AuNRs.[366,367]

Based on these properties, AuNRs are being widely explored in applications with several biochemical applications. For instance, AuNRs can act as photothermal therapy (PTT) agents.[186,368,369] After coherent excitation of AuNRs, hyperthermia process is produced, in which the biological media is exposed to temperatures ranging from 41 to 47 ºC, to produce strong damage into the cancer cells.[186,368,369]

Recently, also has been reported AuNRs as photodynamic therapy (PDT) agents, due to the generation of reactive oxygen species (ROS), especially singlet oxygen ($^1O_2$), directly by the metal surface.[370]

One of the main drawbacks in the direct use of AuNRs is the apparent cytotoxicity of the cetyltrimethylammonium bromide (CTAB)[371,372,373]. Also, the stability in biological media plays an important role, being prone to aggregation without additional stabiliser. In this regard, to decrease the toxicity and increase the stability in biological media, a variety of organic (polymers,[374,375] thiols terminated derivatives,[376] biomolecules[376] etc.) or inorganic (amorphous[377] or mesoporous[378] silica) stabilisers have been explored.

Among the different coatings aforementioned, mesoporous silica offers a series of advantages. With the replacement of the CTAB bilayer by a SiO_2 coating, cytotoxicity and the non-specific interactions should be reduced, as well as showing improved stability in biological media. Furthermore, mesoporous silica coating offers additional advantages, namely: high pore volume, high surface area, variable size or biocompatibility, among many others.[97,379,380,381]

Furthermore, the presence of pores in the nanostructured silica layer offers the possibility to load with molecular cargo for drug delivery approach. [379,380,382,383,384]

It has been demonstrated, therefore, the broad range of application that these nanostructures can have in different nano-medical strategies, which make AuNRs@Si_{mes} a convenient system for new biomedical applications.

Despite the numerous works in this line, the investigation about the applications of these hybrid nanostructures as antibacterial agents remains limited to organic coating.[171,385,386,387,388] It should be mentioned that relative to inorganic coatings, the application of metallic silver layers over AuNRs has shown interesting antimicrobial properties,[389] but to the best of our knowledge, a limited amount of research has been done to explore the application of AuNRs@Si_{mes} nanostructures in antibacterial applications[390,391]

To avoid the molecular cargo diffusion and possible degradation of the system in a water environment, and at the same time, to preserve the properties of the new nanomaterials, the lyophilisation in the presence of trehalose has been chosen as an excellent technique to improve the long-term stability. In this regard, the lyophilisation process presents a series of advantages over other dehydration techniques. The low temperature and high vacuum at which it operates limit thermal degradation or oxidation phenomena in the product. Also, the high porosity of the final product allows easy reconstitution of the sample with a simple addition of a specific solvent without the need for external energy inputs (e.g. ultrasound or thermal irradiation).[392] A large number of different nanomaterials have been successfully subjected to lyophilisation processes in specific conditions, without significant alteration of their intrinsic properties. Nanostructures such as polymeric NPs[393], mesoporous silica NPs[394] or even organic coating metal NPs like spherical gold nanoparticles[395] or AuNRs[396] have been reported, but less attention has been focused on AuNRs@Si_{mes}.

In the present work, we present the synthesis of AuNRs coated with mesoporous silica in two different silica thickness. Conjugation of AuNRs@Si_{mes} with the well-known drugs, Doxorubicin (DOX) and Methylene Blue (MB) for their application as an anticancer and antibacterial agent. The lyophilisation of these conjugated nanosystems was explored using trehalose as a cryogenic protector.

5.2 Experimental Section

5.2.1 Materials

Hexadecyltrimethylammonium bromide (CTAB), Methylene Blue, Sodium Borohydride ($NaBH_4$), D-(+)-Trehalose Dyhydrate and Tetraethyl orthosilicate (TEOS) were purchased from Sigma-Aldrich Hydrogen tetrachloroaurate (III) trihydrate ($HAuCl_4$ x $3H_2O$) and Silver Nitrate ($AgNO_3$) were purchased from Alfa Aesar. L(+)-Ascorbic Acid was purchased from Panreac. Doxorubicin Hydrochloride Salt was purchased from LC Labs. All reagents were used without further purification. Water was ultra-pure grade (type I) obtained with a Milli-Q Simplicity system

5.2.2 Synthesis of gold nanorods

AuNRs were synthesised according to a previously reported seed-mediated silver ion-assisted methodology, using CTAB as a template, with some minor modifications.[397] Briefly, CTAB solution (10 mL, 0.1M) was mixed with $HAuCl_4$ (50 µL, 0.05M) in a water bath at 30°C. Then, an ice-cold, freshly prepared solution of $NaBH_4$ (0.6 mL, 0.01M) was rapidly injected. The brownish-yellow seed solution was stirred during 30 seconds and left undisturbed at 30 °C. The seed solution was used within 2~5 hours. The growth solution consisted of a mixture of CTAB (80 mL, 0.1M), $HAuCl_4$ (4 mL, 0.01M), $AgNO_3$ (360µL, 0.01M), H_2SO_4 (1.6 mL, 0.5M) and ascorbic acid (640 µL, 0.1M). Growth was initiated after the addition of 192 µL of seeds solution, and the temperature of the reaction growth medium was kept at 30°C during the whole process. Two different reactions, **RA** and **RB,** were prepared with the same methodology. After 3 hours, both reactions were centrifuged 3 times (7000 rpm x15 min.). The pellets were re-dispersed in 50 and 100 mL of CTAB 1 mM respectively.

5.2.3 Silica coating of gold nanorods

The mesoporous silica coating process was carried out applying a modified Stöber methodology reported by Tracy and coworkers[397] with some modifications. The different silica thicknesses were produced trough change in starting concentration of AuNRs@CTAB and silica precursor.

5.2.3.1 Preparation of AuNRs_RA@Si$_{mes}$

To 50 mL of **RA** ([Au^0] = 0.76mM) in a round bottom flask, NaOH 0.1M in deionised water was added to obtain a pH between 10.5-11. After 15 minutes of gently agitation, 300 µL of 20 % v/v TEOS in

methanol were injected during a period of 6 minutes (50 µL each minute). The AuNRs were gently stirred for 30 minutes, and kept undisturbed during 20 hours at RT.

5.2.3.2 Preparation of AuNRs_RB@Si$_{mes}$

To 50 mL of **RB** ([Au^0] = 0.38mM) in a round bottom flask, NaOH 0.1M in deionised water was added to obtain a pH between 10.5-11. After 15 minutes of gently agitation, 360 µL of 20 % v/v TEOS in methanol were injected during a period of 6 minutes (60 µL each minute). The AuNRs was gently stirring for 30 minutes, and kept undisturbed during 20 hours at RT.

After 20 hours, both reactions were centrifuged (7000 rpm x12 min), and the pellets dispersed in MeOH. Then, the samples were centrifuged several times in MeOH at 6000 rpm for 12 min, and finally re-dispersed in 20 and 10 mL of MeOH for AuNRs_RA@Si$_{mes}$ and AuNRs_RB@Si$_{mes}$ respectively.

5.2.4 Drug Loading

Before the incubation, the AuNRs@Si$_{mes}$ were washed extensively in water through centrifugation at 7000 rpm for 12 min, to remove all MeOH. Finally the samples were dispersed in 20 or 10 mL of MilliQ (MQ) water for AuNRs_RA@Si$_{mes}$ and AuNRs_RB@Si$_{mes}$ respectively.

AuNRs_RA@Si$_{mes}$ were loaded with Doxorubicin (DOX), while AuNRs_RB@Si$_{mes}$ were loaded with Methylene Blue (MB). The procedure is identical for the two compounds.

To one milliliter of AuNRs@Si$_{mes}$ was added 1 mL with 0.1 mg of the different drugs prior to the immersion in a ultrasonic water bath of 35 KHz in agitation during one min. They were let 10 minutes undisturbed and centrifuged at 7000 rpm x 15 min, adding MQ water to the pellets, until the supernatant became clear. The AuNRs@Si$_{mes}$-Drugs were brought to a final volume of 1 mL in MQ water. All the supernatants were collected, and the entrapment efficiency of each drug was determined from the relation:

$$\%Entrapment\ Efficiency: \frac{Drug\ added - Free"untrapped\ drug"}{Drug\ added}\ x\ 100$$

5.2.5 Freeze Drying of AuNRs@Si$_{mes}$-Drug

To the system of AuNRs@Si$_{mes}$-Drugs, was added a solution of 1 mL with 30 mM of Trehalose, leading to a final volume of 2 mL, before to inmerse in liquid nitrogen during 5 minutes. The samples were

lyophilised and a blue powder was obtained. Empty AuNRs_RA@Si_{mes} and AuNRs_RB@Si_{mes} were treated equally but without the addition of the drugs.

5.2.6 Cell cytotoxicity assay

Cells were seeded into a 96-well plate at a cell density of 3.0 × 103 cell/well and incubated for 24 h before the addition of the nanorods in concentrations ranging from 0 to 200 µg/ml. The growth inhibitory effect was measured after 72 h treatment by the PrestoBlue assay. Briefly, 10 µL of PrestoBlue (resazurin-based solution) were added to each well. After 2 h incubation (37 ºC, 5 % CO2, 98% humidity), the fluorescence formed was quantified by a fluorescent multilabel plate reader (Victor3, PerkinElmer) exciting at 531 nm and recording at 572 nm wavelength. Cell cytotoxicity was evaluated in terms of cell-growth inhibition in treated cultures and expressed as % of the control conditions. Each experiment was repeated at least three times, and each concentration tested in at least three replicates.

5.2.7 In vitro photothermal assay

Human Breast Adenocarcinoma cells line (MCF7) were cultured in DMEM/F-12 containing 10 % fetal bovine serum at 37 °C under 5 % CO_2. MCF7 cells were seeded at 10,000 cells per well in 96-well plates for 24 hours to allow cell attachment. Next, cells were treated with doxorubicin-loaded nanorods at concentrations of 200 µg/ml and 500 µg/ml. After 16 hours incubation at 37 °C, the growth medium was removed, and the cells were washed with PBS and exposed to a continuous red-light laser at 650 nm (33.33 W/cm^2) for 30 minutes. After incubation for 72 hours at 37 °C, cell viability was determined. Cells exposed to the red light laser but unexposed to the nanorods were regarded as controls.

5.2.8 Antibacterial activity

Antimicrobial activity was assayed against *Escherichia coli* ATCC8739 (Gram-negative bacteria) and *Staphylococcus aureus* ATCC6538 (Gram-positive bacteria). Glycerol stock cultures stored at −80 ºC were inoculated in Tryptic Soy Agar (TSA) (Biokar, Allone, France) and incubated overnight at 35 ± 2 ºC. Subsequently, isolated colonies were transferred to 0.85 % NaCl solution and the turbidity of the suspension was adjusted to 0.5 on the McFarland scale (Mc-Farland densitometer, Model Den-1B, Grant Instruments, England), corresponding to 1 to 2 x 10^8 CFU/mL (CLSI, 2012).

Samples (AuNRS_RB@Si_{mes}, and AuNRS_RB@Si_{mes}-MB), were dissolved in double-distilled water (2 mg/mL). MB solutions were also prepared in double-distilled water, at a concentration similar to that

found in samples, namely 0.02 mg/mL for MB. All solutions were prepared and handled under light-restricted conditions.

The antibacterial assays were performed according to the procedure described by Pérez-Laguna *et al.*[398] with little modifications. Briefly, the bacterial suspensions (0.5 McFarland) were deposited in 96-well microplates and mixed with the same volume of the different samples under study (AuNRS_RB@Si_{mes}, AuNRS_RB@Si_{mes}-MB and MB) or, in the case of the control, with double-distilled water. Microplates were prepared in duplicate being one of them kept in the dark and the other irradiated with a red laser (JD-850, max output power 200 mW, wavelength 650 nm ± 10), at a distance of 2.5 cm from the top of each well, during 4 min. Then, irradiated and non-irradiated bacterial suspensions were diluted in 0.85% NaCl (from 10^{-1} to 10^{-5}), cultured on TSA and incubated overnight at 35 ± 2 ºC. Viable bacteria, colony-forming unit (CFU), were determined by colony counting in TSA plates containing between 30 and 300 colonies. All experiments were carried out at least three times.

5.2.9 Statistics in bacterial samples

As the assumptions of normality and homogeneity of variance (Cochran, Hartley and Bartlett tests) were verified, one-way analysis of variance (ANOVA) followed by Tukey's test were used to identify significant differences between results. Statistical analyses were tested at 0.05 level of probability with the software STATISTICA™ 7.0 (StatSoft).

5.3 Results and discussion

5.3.1 Synthesis of gold nanorods

The present work has been focused on the synthesis and application of hybrid nanomaterials based on AuNRs and mesoporous silica for cellular or bactericidal applications. It was stated out that the amount of heat that a plasmon nanoparticle can produce increase as nanoparticle size is decreased.[229,399] Additionally, smaller sized NPs should offer better cell uptake when compared with the bigger ones[229,400]

Based on these considerations, first, gold nanorods (AuNRs) were synthesised using the well-known seed-mediated surfactant directed synthesis. Two different reactions, **RA** and **RB** were prepared with the same methodology.

As showed in **Figure** 5.1(a), the as prepared **RA** sample presented two absorption bands, one weak band centred at ca. 514 nm and a strong band centred in ca. 662 nm assigned to transverse ($LSPR_{trans}$) and longitudinal ($LSPR_{long}$) plasmon band respectively.

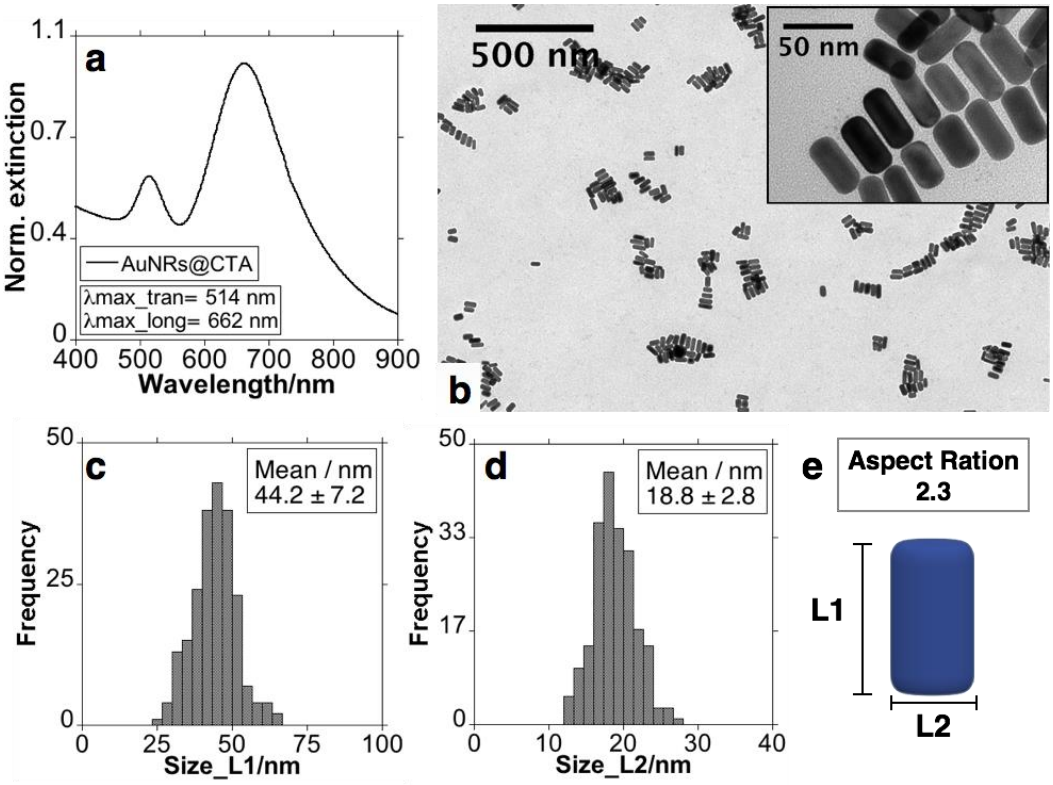

Figure 5.1 Normalised extinction spectra (A), representative TEM images (B), histograms and graphic representation of obtained AuNRs (C-E).

Transmission electron microscopy (TEM) images showed a colloidal solution essentially composed of rod-shaped gold nanoparticles with a length of 47.4±8.7 nm and a width of 21.1±3.5 nm. With these dimensions the AuNRs presented an aspect ratio of ≈2.3. (**Figure** 5.1) Similar results were obtained for the sample **RB**. In **Figure** 5.2 can be noticed that little difference in AR between the two samples is produced, being AuNRs of sample RB with a length and width of 42.4 nm and 19.2±3.8 nm respectively (AR ≈ 2.2).

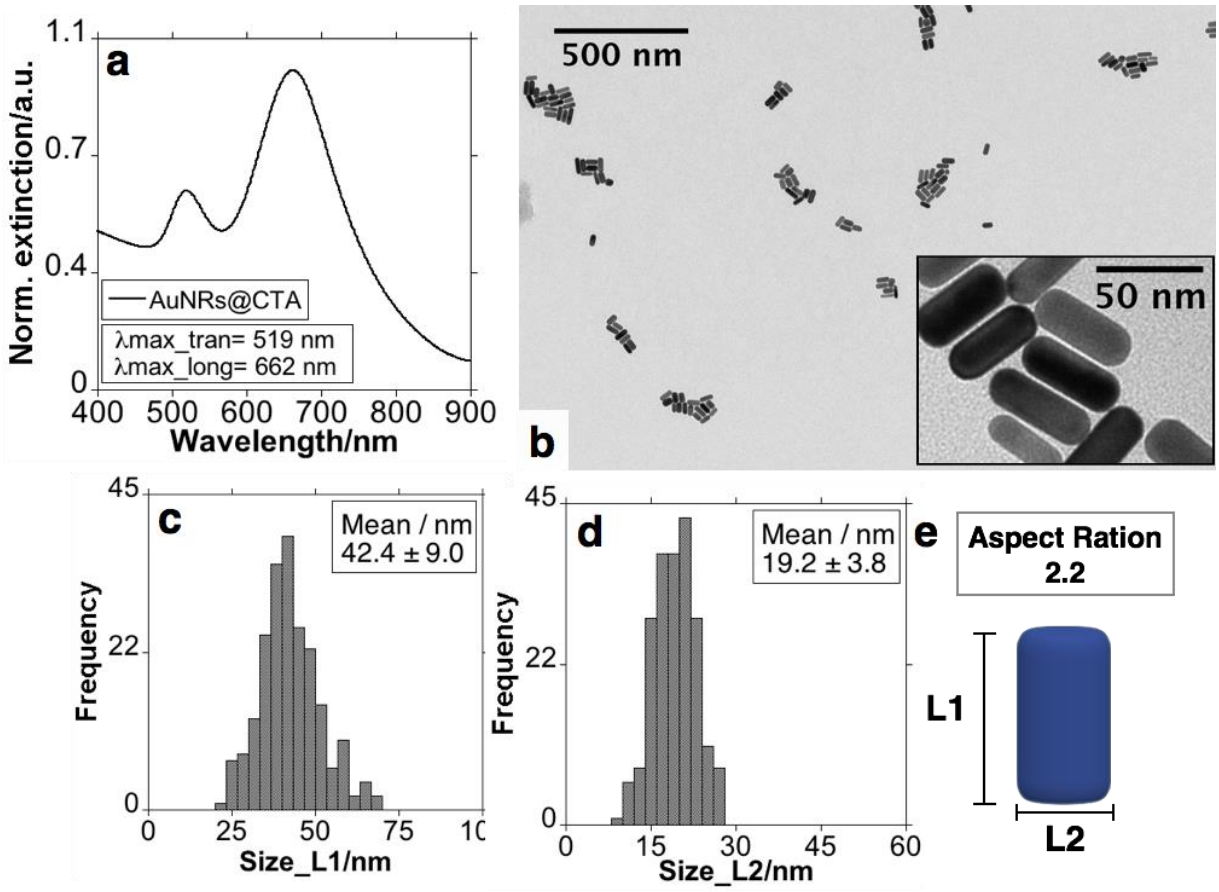

Figure 5.2 Normalised extinction spectra spectra (A), representative TEM images (B), histograms and graphic representation of AuNRs sample RB obtained (C-E).

Both colloidal solutions solution were purified using CTAB solution (1 mM). The purified colloids (**RA** and **RB**) were used as precursor in the subsequent mesoporous silica coating process.

5.4 Synthesis and purification of AuNRs@Si_{mes}

Mesoporous silica coating was achieved using a modified Stöber methodology as reported by Tracy *et al*. with some modifications.[397] The controlled deposition of mesoporous silica was completed using TEOS as silica precursor in basic medium (pH≈10.5-11). The presence of CTAB in the colloidal solution of AuNRs serves as a template to obtain mesostructured silica growth. Two different silica shell thickness were obtained using slightly different methods (see experimental section). This allowed us to obtain two-shell thickness (denoted as AuNRs_RA@Si_{mes} and AuNRs_RB@Si_{mes}).

Both samples were obtained using the same experimental conditions, with difference in the initial concentration of AuNRs and silica precursor concentration.

5.4.1 The case of AuNRs_RA@Si$_{mes}$

To complete the silica coating on **RA**, we used a starting concentration of AuNRs equal to 0.76 mM (referred to [Au^0])[84] and 300 µL of TEOS (20 %) solution. After the process of deposition of silica on RA, AuNRs_RA@Si_{mes} presented a relatively homogeneous coating with thickness of 8.4±2.1 nm. More important, silica free core NPs were not detected in the TEM images. (**Figure** 5.3)

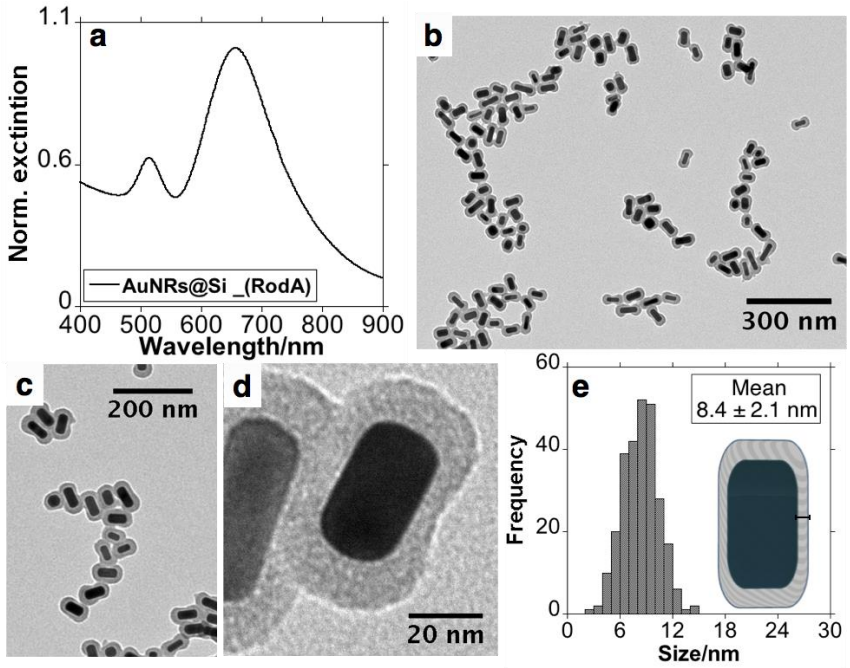

Figure 5.3: Normalised extinction spectra spectra (A), representative TEM images (B, C and D), histograms and graphic representation of AuNRs_RA@Si_{mes} (E).

In order to eliminate the CTAB, due to its toxicity, the AuNRs were subjected to a purification process through subsequent centrifugation steps. The purification of the sample using water resulted in a red-shift the $LSPR_{long}$ to ca. 670 nm.

Conversely, upon successive MeOH and water washes, the $LSPR_{long}$ of the colloid solution resulted in a slight blue-shift, bringing the LSPR near to that of AuNRs without mesoporous silica shell. The analysis of the ζ-potential of sample purified in water showed a positive potential (+7 mV), while in the other case, the purification in MeOH, showed negative values (-20 mV). This behaviour has been

conveniently explained recently by J. B. Tracy and coworkers.[401] The authors attributed this blue-shift to the dissolution of CTAB molecules that remain as a template in the mesostructured silica shell. [401]

Alternatively, it has been pointed out in numerous works that a successful methodology to remove CTAB molecules from mesostructured silica materials is based on the treatment of silica derivative with methanolic boiling solutions of Ammonium nitrate.[402] As can be seen in **Figure** 5.4 the purification through a methanolic solution of boiling ammonium nitrate (1h), or exhausts MeOH washes offer similar results, visible in the LSPR shift and ζ-potential values. Under these results, and to limit the possible presence of residues such as ammonium or nitrates in the purified AuNRs, we applied only MeOH to complete the purification in all cases.

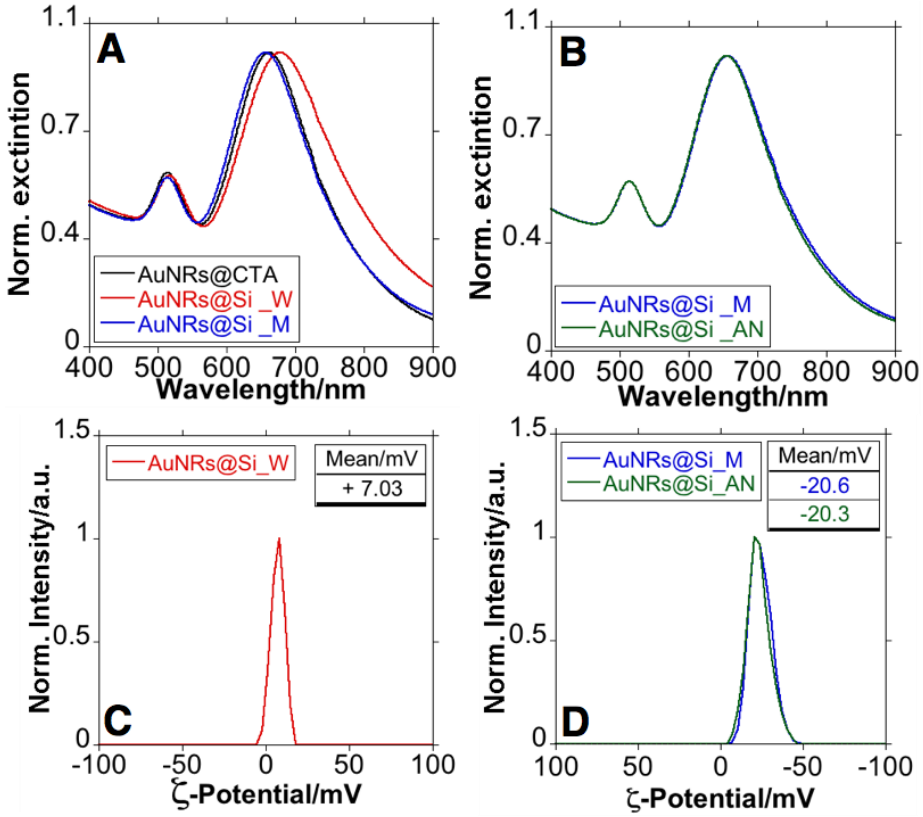

Figure 5.4: Normalised extinction spectra spectra (A) and (B), and graphic representation of the ζ-potential obtained for AuNRs@Si_{mes} purified with water (red), ammonium nitrate (green) and successive MeOH whased (blue) (C-E).

To further demonstrate the convenient purification of CTAB molecules through successive MeOH washes, we investigated the chemical composition of AuNRs_RA@Si_{mes} after purification with water or MeOH using Fourier-transform infrared spectroscopy (FT-IR) spectroscopy. FT-IR spectra of CTAB alone and AuNRs_RA@Si_{mes} purified with water or MeOH are showed in **Figure** 5.5. CTAB spectra showed clearly the typical vibrational modes previously reported in literature associated with the $-CH_2$, $-CH_3$ or $[-N(CH_3)_3]^+$ groups that form the molecule. (**Figure** 5.5)[403,404,405,406]

On the other hand, FT-IR spectra of AuNRs_RA@Si_{mes}, regardless of the purification method, showed the signal of about 3448 cm^{-1}, which can be assigned to the O-H stretch of surface silanol groups or adsorbed water molecules. Deformational vibrations of adsorbed water molecules produce the bands located at 1634 cm^{-1}. The signals generated by the Si-O-Si and Si-O groups located between 1094-1044 and 471-456 cm^{-1} respectively were clearly detected. More importantly, the signals from CTAB groups are only evident in the spectrum obtained from the sample purified in water. (**Figure** 5.5)

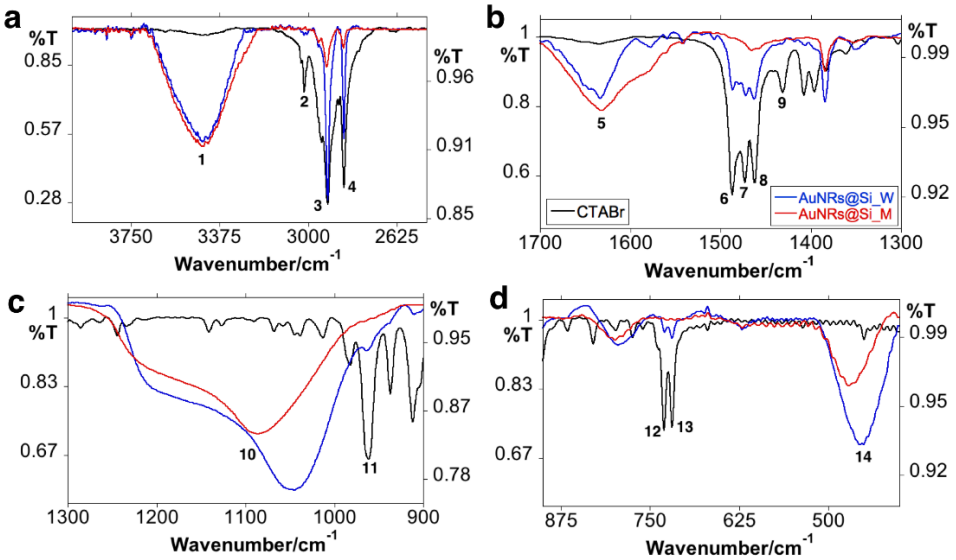

e

Signals	CTABr cm^{-1}	AuNRs@Si_Water cm^{-1}	AuNRs@Si_MeOH cm^{-1}	Assignment
1	-	3448	3449	ν(Si—OH) *surface silanol*
2	3017	-	-	$\nu(CH_3)$ anti-symm.
3	2917	2918	2923	$\nu(CH_2)$ symm.
4	2851	2850	2852	$\nu(CH_2)$ assymm.
5	1635	1634	1632	ν(O-H) adsorbed water
6	1487	1487	-	Assymm. and symm. ν(C-H) scissoring in $(H_3C\text{-}N^+)$ group
7	1473	1472	-	
8	1462	1463	-	
9	1431	-	-	
10	-	1094	1044	ν(Si—O—Si) asymm.
11	961	964	-	ν $(C\text{-}N^+)$
12	730	729	-	$\nu(CH_2)$ in-plane swinging
13	719	719	-	
14	-	456	471	ν(Si—O) bending

Figure 5.5: FT-IR spectra (a-d) of CTAB (black line), AuNRs@Si_{mes} only purified with water (blue line) and AuNRs@Si_{mes} purified with MeOH and water (red line). The table show the different peaks detected (e).

The blue shift in the $LSPR_{long}$ in agreement with previous reports,[401,407] the negative ζ-potential and the marked decrease in the signals produced by CTAB groups in FT-IR analysis for AuNRs_RA@Si_{mes} purified in MeOH, suggest a substantial CTAB removal.

5.4.2 The case of AuNRs_RB@Si_{mes}

The colloidal suspension of AuNRs_RB@Si_{mes} was used as a precursor to obtaining the hybrid nanomaterial used with the antimicrobial approach.

J. Tracy and coworkers[401] showed a modulation on the silica thickness deposited on AuNRs through variation in starting concentration of AuNRs, or [TEOS] used. Based on these considerations, in our case, we have decreased the initial concentration of AuNRs from 0.76 mM (RA) to 0.38 mM (RB) together with an increase in silica precursor (see experimental section).

After the mesoporous silica deposition on **RB**, a relatively homogeneous coating was obtained with an increase in the silica thickness to 20.1 ± 5.7nm. The displacement of the LSPR, ζ-potentials and FT-IR analysis obtained yielded similar behaviour to those obtained for AuNRs_RA@Si_{mes} (data not shown).

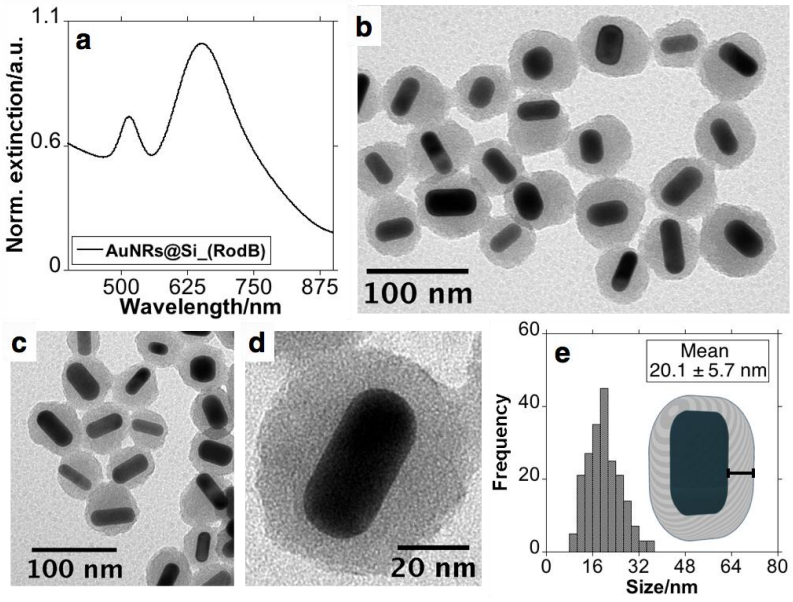

Figure 5.6: Normalised extinction spectra (A), representative TEM images (B, C and D), histograms and graphic representation of AuNRs_RB@Si_{mes} (E).

AuNRs_RA@Si_{mes} and AuNRs_RB@Si_{mes} were used to complete the drug loading experiments with the selected molecules. Both colloidal solutions were gently washed in water to remove any remaining MeOH.

5.5 Drug loading experiments

With the aim to explore the anticancer effect, we have selected the drug Doxorubicin (DOX). DOX and its bioactive derivatives, which are among the most used anticancer drugs in chemotherapy strategies.[408,409] On the other hand, Methylene blue, a cationic hydrophilic dye, is one of the most widely used antimicrobial photosensitizer.[410] We further investigated the drug loading capacity exploring the encapsulation of these two different drugs; doxorubicin in AuNRs_RA@Si_{mes} and methylene blue in AuNRs_RB@Si_{mes} using an ultra-sound assisted technique in 15 min. The entrapment efficiency was calculated analysing the UV/Vis supernatants from the calibration curve. (**Table** 5-1)

Table 5-1: Encapsulation efficiency obtained for AuNRs_RA@Si_{mes} and AuNRs_RB@Simes with the different drugs explored.

	Doxorubicin (%)	**Methylene Blue (%)**
AuNRs_RA@Si_{mes}	11.6 ±5.1	-
AuNRs_RB@Si_{mes}	-	13.6±3.2

After the loading process and the corresponding purification, the $LSPR_{long}$ suffered a red-shift in both cases. It can be explained due to the sensitivity of the AuNRs to the refractive index of the medium, in agreement with previous reports, where the $LSPR_{long}$ also were modified after the internalization of the different molecules in the mesoporous matrix[380,407].

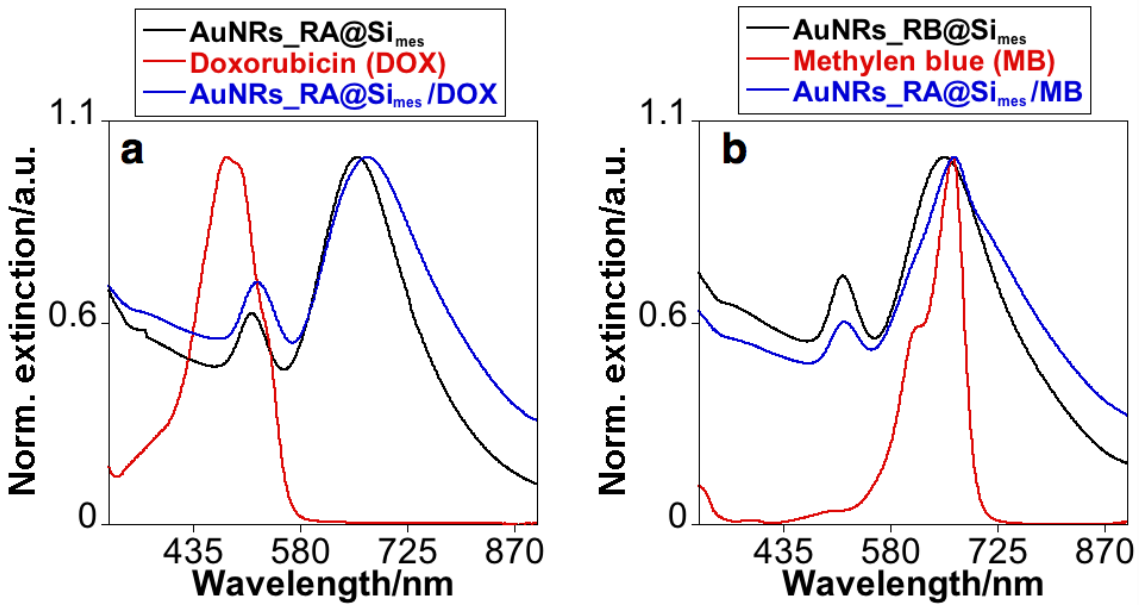

Figure 5.7: Normalised extinction spectra (a and b), with the representation of the initial spectra of the AuNRs (black), the two different molecules (red) and the final spectra of the AuNRs@Si$_{mes}$-Drug (Blue).

5.6 Freeze drying experiments of AuNRs@Si$_{mes}$-Drug

The composite AuNRs@Si$_{mes}$-Drug was subject to a freeze-drying process. Sugars, and specifically trehalose, are known to be excellent candidates to lyophilise pharmaceutical products, due to the absence of internal hydrogen bonds, less hygroscopicity, low chemical reactivity or higher glass transition temperature (Tg)[411,412,413,414]. Nanoparticles encased in high Tg amorphous carbohydrates, allow us to store the products at room temperature. Trehalose was stated as the best cryoprotectant for lyophilising mesoporous silica nanoparticles when compared against other common cryoprotectants, like mannitol or sorbitol. The presence of trehalose can avoid the aggregation, and allows an easy reconstruction, maintaining the same size and polydispersity index (PDI) in comparison with the prior wet formulation[415,416].

After the lyophilisation process, blue powders were obtained. The powders offered an easy redispersion in water without the need to apply external inputs. As can be seen in **Figures** 5.8 and 5.9, regardless of the thickness of silica or encapsulated drug, the optical and nanostructural characteristics were not appreciably affected. Similar spectroscopic profiles and nanostructure cores were detected before and after the lyophilisation process.

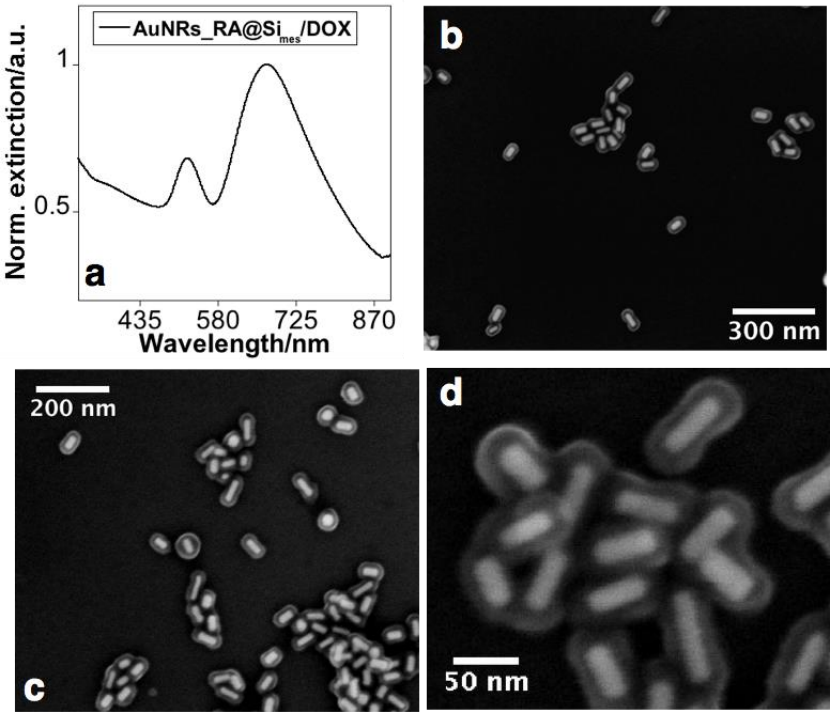

Figure 5.8: Normalised extinction spectra of AuNRs_RA@Si$_{mes}$-DOX after resuspension (a), and representative SEM images (b, c and e).

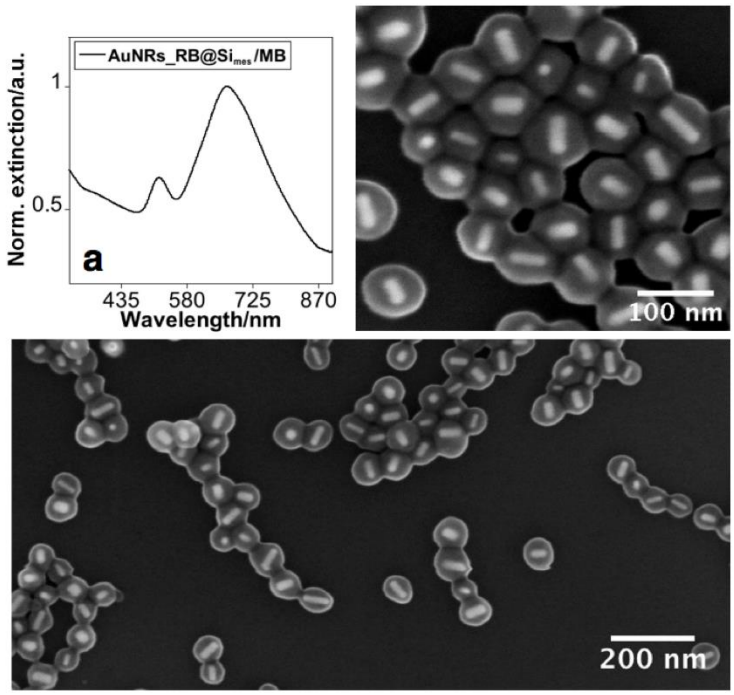

Figure 5.9: Normalised extinction spectra of AuNRs_RB@Si$_{mes}$-MB after resuspension (a), and representative SEM images (b and c).

5.7 Exploring the application of AuNRs_RA@Si$_{mes}$-DOX in cell experiments

As a first step, the toxicity of empty AuNRs_RA@Si$_{mes}$ against MCF7 cell was tested. They were incubated with several concentrations (from 0 to 200 µg/mL) during 72 hours. After this time, the cytotoxity assays were performed. **Figure** 5.10 shows that no citotoxity on MCF7 cells in any of the tested concentration is visible.

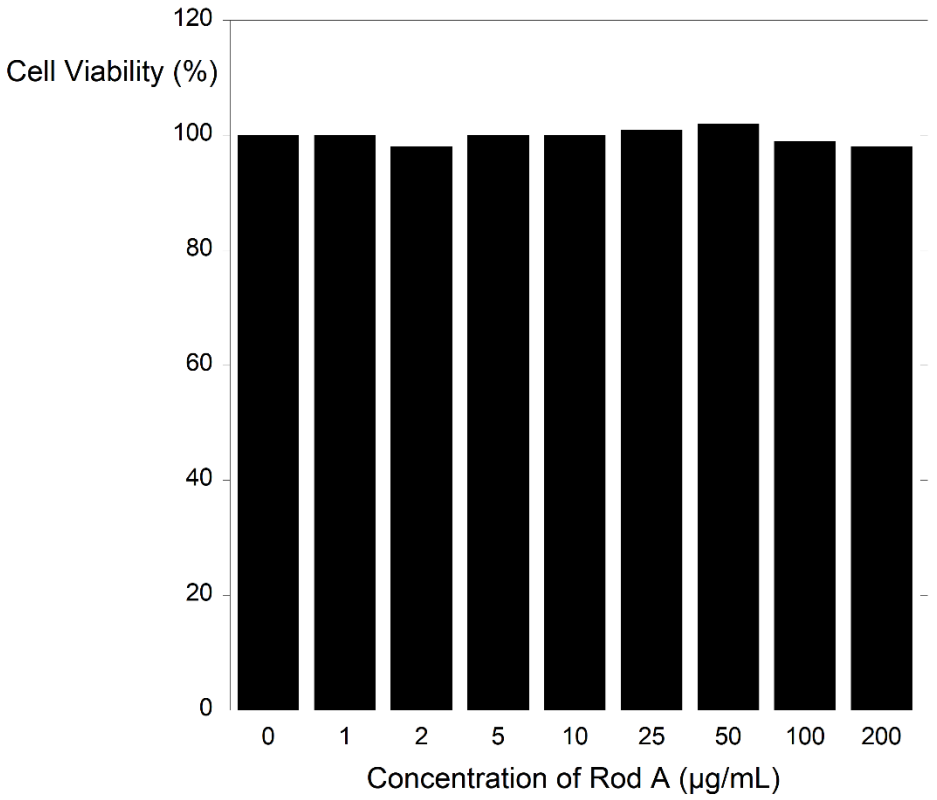

Figure 5.10: Effect of various concentrations of AuNRs_RA@Si$_{mes}$ without doxorubicin for 72 h on viability of MCF-7 cells as measured by Presto Blue assay.

Once was determined that AuNRs_RA@Si$_{mes}$, with the absence of drug and a laser exposure were nontoxic, was carried out the experiment with the laser and the drug. For this, two different amounts of sample were used (200 µg/mL and 500 µg/mL), and were exposed to the laser (see experimental section). Control samples were used, without nanoparticles. **Figure** 5.11 shows that there is no

significant toxicity even after the laser treatment with the higher dose of nanoparticles, in comparison with the control treated with the laser beam.

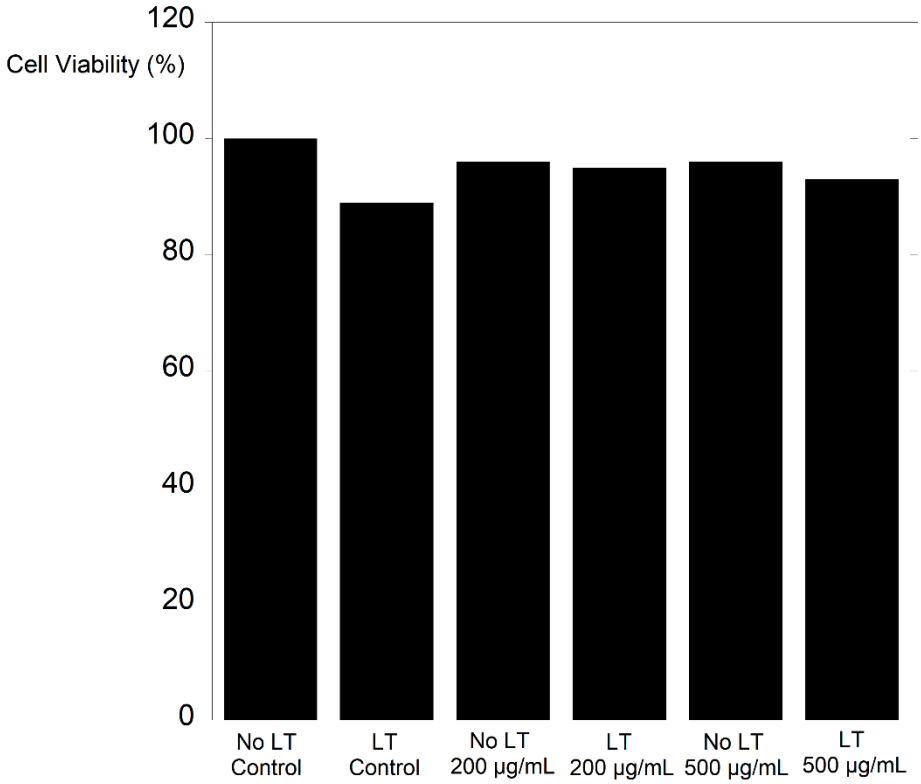

Figure 5.11: Effect of various concentration of AuNRs_RA@Si_{mes}/DOX, in the presence and absence of the laser treatment (LT). Control states for cells without nanoparticles.

The unexpected results, showing no toxicity even after long laser exposures, can be explained for the presence of the trehalose in the nanoparticle formulation.

Trehalose, even at low concentrations, can protect the cells against the heat-shock, reducing aggregation of denatured proteins.[417,418] Recent reports using the trehalose to functionalize gold nanoparticles for application in neuronal cells, or in combination with silver nanoparticles in a prostatic cancer cell line, relate that the presence of the trehalose enhances the cell survival.[419]

This is in concordance with our experiments, in which we think that the presence of trehalose, even in low concentrations, can hamper the effect of the photothermal therapy associated to the gold nanorods, as well as to the chemotherapy-associated to the doxorubicin.

5.8 Exploring the application of AuNRs_RB@Si_{mes}-MB in antibacterial applicattions

Bacteria can be classified into Gram-negative and Gram-positive cells based on their cell wall composition. Gram-positive bacteria contain a thicker peptidoglycan layer with wall teichoic acids and lipoteichoic acids covalently attached; Gram-negative bacteria contain a thinner peptidoglycan layer involved by an outer membrane. The outer membrane is a lipid bilayer, where the inner leaflet is composed of phospholipids and the outer leaflet of highly negatively-charged lipopolysaccharides (LPS)[420]. Gram-negative bacteria tend to be more resistant to antimicrobial agents than Gram-positive bacteria, because of the presence of the additional protection afforded by the outer membrane[421].

Based on these differences in composition and sensitivity, the antibacterial activity of AuNRs_RB@Si_{mes}-MB was assayed against gram-negative (*Escherichia coli*) and gram-positive bacteria (*Staphylococcus aureus*) (**Table** 5-2). Neither *Escherichia coli (E. coli)* nor *Staphylococcus aureus (S. aureus)* was affected by laser irradiation as no significant differences were observed between the numbers of CFU/mL and between irradiated and no irradiated controls.

Regarding AuNRs_RB@Si_{mes}-MB and MB, the results obtained showed that the antibacterial activities of both samples were strongly affected by the exposure to the red laser. Accordingly, after irradiation, both MB and AuNRs_RB@Si_{mes}-MB showed a pronounced antibacterial activity (~ 8 Log_{10} unit reduction) against *E. coli* and *S. aureus*. However, MB without laser exposure reduced the number of CFU/mL of *E. coli* in about 2 log_{10} cycles, an effect that was not observed with AuNRs_RB@Si_{mes}-MB without laser (**Table** 5-2). This effect can indicate that there is nor release nor a significant interaction of the MB without a laser exposure in our system, making possible a potential use in control release.

Table 5-2 Antibacterial activity of samples against *E. coli* and *S. aureus*. Different letters within the same column indicate statistically significant differences among samples ($p < 0.05$).

Sample	*E. coli*		*S. aureus*	
	$Log_{10}CFU/mL$	Log Reduction	$Log_{10}CFU/mL$	Log Reduction
Control *Irradiated*	7.58 ± 0.20^{a}	-	7.55 ± 0.11^{a}	-
Control *Non-irradiated*	7.70 ± 0.24^{a}	-	$7.51 \pm 0.06^{a,b}$	-
AuNRs_RB@Si$_{mes}$ (1mg/mL) Irradiated	7.88 ± 0.03^{a}	< 1	6.70 ± 0.26^{d}	< 1
AuNRs_RB@Si$_{mes}$ (1mg/mL) Non-Irradiated	7.98 ± 0.09^{a}	< 1	$6.97 \pm 0.13^{c,d}$	< 1
AuNRs_RB@Si$_{mes}$/MB (1 mg/mL) Irradiated	< 1	>7.58 ± 0.00	< 1	>7.55 ± 0.00
AuNRs_RB@Si$_{mes}$/MB (1 mg/mL) Non-Irradiated	7.87 ± 0.04^{a}	< 1	$7.15 \pm 0.26^{b,c}$	< 1
MB (0.02 mg/mL) *Irradiated*	< 1	>7.58 ± 0.00	<1	>7.55 ± 0.00
MB (0.02 mg/mL) *Non-Irradiated*	5.57 ± 0.02^{b}	2.13 ± 0.02	$6.98 \pm 0.06^{b,c,d}$	< 1

The results obtained suggest that *E. coli* has a higher sensitivity to MB than *S. aureus*. Positively charged photosensitizers are expected to be more effective bacterial inactivators than neutral molecules against Gram-negative bacteria, whose outer membranes are composed of negatively charged lipopolysaccharides. In contrast, Gram-positive bacteria may be inactivated more effectively by neutral or negatively charged agents[422].

According to the above, under the same experimental conditions, *E. coli* proved to be more sensitive to the bactericidal effects of AuNRs_RB@Si_{mes}/MB than S. aureus (**Figure** 5.12) as a more pronounced log_{10} unit decrease was achieved with the same concentration of AuNRs_RB@Si_{mes}-MB (3 and 4 log_{10} unit decrease with 0.5 mg/mL for *S. aureus* and for *E. coli*, respectively).

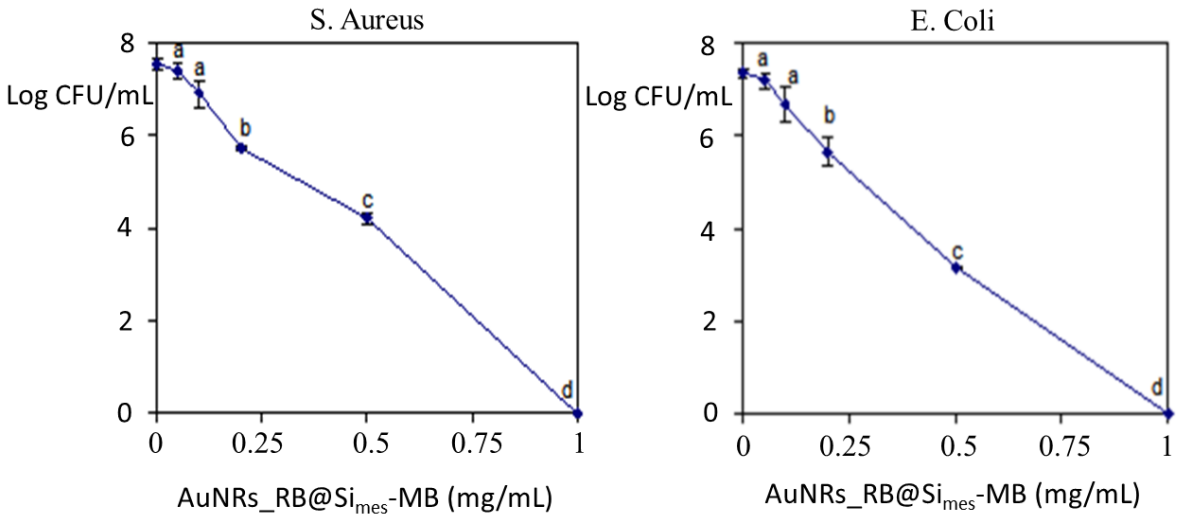

Figure 5.12: Inactivation of *S. aureus* (left) and *E. coli* (right) using different concentrations of ROD_MB after exposure to red laser. Different letters within the same curve indicate statistically significant differences among Log10 CFU/mL ($p < 0.05$).

5.9 Conclusions

We have successfully synthesised AuNRs@CTAB in aqueous solution with aspect ratio 2.3. The controlled deposition of mesoporous silica with two different thicknesses (around 8 o 20 nm) on AuNRs was successfully produced.

Conjugation with DOX and MB was obtained proceeding to its subsequent lyophilisation in the presence of trehalose as a cryo-preservation molecule. We have observed that after resuspension, there were no substantial changes in the core@shell structures studied.

The anticancer and antibacterial properties of the final nanoformulations obtained were analysed against MCF7 cells and S. aureus and E. coli bacteria. Despite the lack of toxicity in the cells, the antibacterial result shows that the nanoformulation is effective against the two bacterial strains studied. The absence of toxicity in the AuNRs system without the laser exposure, even with the presence of MB, as well as the toxicity after the laser exposure, indicates the possibility to use this system as an external drug delivery system

6 Chapter 6

General Conclusions and Future Work

Chapter 2

Polyamine Ligand-Mediated Self-Assembly of Gold and Silver Nanoparticles into Chainlike Structures in Aqueous Solution: Towards New Nanostructured Chemosensors.

In chapter two, the synthesis of different systems of nanoparticles is presented. Spherical, gold and silver, as well as triangular silver nanoparticles, were successfully synthesised.

The functionalization with a new polyamine ligand was carried out, leading to the formation of 1D assemblies, and the consequent changes in the UV/Vis band as well as the physical aspect.

The use of the assemblies as nano chemosensors was investigated, being selective for Hg^{2+} among all the ions tested, and being able to improve the polyamine limit of detection by itself.

The use of nano-assemblies can produce faster recognition systems for the detection of toxic analytes. In this sense, functionalization of nanoparticles with different ligands with specific recognition abilities can be a successful tool for biosensing. Changing the type of structures, and doing the functionalization with other nanoparticles like gold nanorods, can change the properties of the systems, as well as their sensing capabilities.

Chapter 3

Synthesis and Characterisation of $PtTe_2$ Multi-Crystallite Nanoparticles using Organotellurium Nanocomposites.

In chapter three, a spherical nanocomposite based on platinum and tellurium was successfully synthesised and characterised. It was successfully done using a new approach based on the reduction and stabilisation of platinum cations with organotellurium derivates.

The methodology present easily adjustable experimental conditions.

Nowadays, platinum metal has a key-role due to the excellent properties as a catalyser. The obtention of well-defined platinum nanoparticles and doing it in combination with other elements like the semiconductor tellurium can give to the systems useful applications in several technological fields. A mesoporous silica cover of the nanoparticles, being able to provide more stability to the system can be investigated. Also, the versatility of the procedure may be possible the obtention of other

nanocomposites just varying the metal cation. In this sense, it can be carried out new nanocomposites applying the same methodology.

Chapter 4

Highly accessible aqueous synthesis of well-dispersed dendrimer type platinum nanoparticles and their catalytic applications.

In chapter four, dendritic type platinum nanoparticles were successfully synthesised.

A new methodology was applied using the inexpensive and environmentally friendly iron in a water environment.

The reaction shows good reproducibility.

The catalytic activity test of the obtained platinum nanoparticles was carried out, showing excellent performance in reduction and oxidation reactions.

The results obtained in the reduction of p-nitrophenol displayed to have the highest TOF value described in the literature for a platinum catalyst.

The use of platinum, as stated above, is, nowadays, of great importance. The improvement and change in the methodology of the reaction, with the aim to obtain new PtNPs with different morphologies, can be studied. The functionalisation with ligands or polymers can modify and give to the nanomaterials better properties for specific catalytic applications. Moreover, the use of iron seems to be a feasible procedure, fast, inexpensive and environmentally friendly. It can be applied to the synthesis of other types of nanomaterials, leading to new clean methodologies.

Chapter 5

Synthesis of Gold Nanorods with mesoporous silica shell containing Doxorubicin and Methylene Blue as drugs, and their applications as anti-cancer and antimicrobial nanotools.

In chapter five, the synthesis of gold nanorods is presented. The successfully covering with mesoporous silica, and the variation in the thickness with small modifications in the synthetic procedure was reported.

The elimination of the cytotoxic component CTAB was studied.

The combination with the drugs was carried out using an ultrasound assisted technique.

To preserve their properties, a lyophilisation process was carried out with the cryoprotectant trehalose. After resuspension of the obtained powder, the nanomaterials retained their properties.

The new systems were tested with an anti-cancer and antibacterial approach.

The bacterial tests show that they can be activated remotely with the use of laser light (red), being good candidates for drug delivery systems.

The properties of the gold nanorods are well known, in photothermal and photodynamic therapy. Their combination with a mesoporous silica layer, where can carry different molecules or drugs, can be a new system for use in the future nano biomedicine. In this sense, the work realised varying the size and composition of a gold nanorod, as well as the introduction of new active compounds, can give the gold nanorods new exciting uses. The lyophilisation process is a fascinating technique for the preservation of the nanoparticles, being able to be stored and used when needed for long periods. Also, it can provide new forms of administration, once in the powder can be administrated easily, e.g., via oral.

7 Bibliography

1. Day, P., Interrante, L. V. & West, A. R. Towards defining materials chemistry (IUPAC Technical Report). *Pure Appl. Chem.* **81,** 1707–1717 (2009).
2. Edwards, P. P. & Thomas, J. M. Gold in a metallic divided state - From Faraday to present-day nanoscience. *Angew. Chemie - Int. Ed.* **46,** 5480–5486 (2007).
3. Mokrushin, S. G. Thomas Graham and the definition of colloids. *Nature* 861 (1962).
4. Graham, T. Classics and Classicists of Colloid and Interface Science. John Tyndall. *J. Colloid Interface Sci.* **119,** 602–604 (1987).
5. Zhang, Z. *et al.* Redox reaction induced Ostwald ripening for size- and shape-focusing of palladium nanocrystals. *Chem. Sci.* **6,** 5197–5203 (2015).
6. Horvath, H. Gustav Mie and the scattering and absorption of light by particles: Historic developments and basics. *J. Quant. Spectrosc. Radiat. Transf.* **110,** 787–799 (2009).
7. Sprünken, D. P., Omi, H., Furukawa, K., Nakashima, H. & Sychugov, I. Influence of the local environment on determining aspect-ratio distributions of gold. *J. Phys. Chem. C* **111,** 14299–14306 (2007).
8. Ruska, E. The development of the electron and of electron microscopy microscope. *Biosci. Rep.* **7,** (1987).
9. Turkevich, J., Stevenson, P. C. & Hillier, J. A study of the nucleation and growth process in the synthesis of colloidal gold. *Discuss. Faraday Soc.* **55,** 55–75 (1951).
10. Toumey, C. Plenty of room, plenty of history. *Nat. Nanotechnol.* **4,** 783–784 (2009).
11. Castonguay, A., Ladd, E., Van De Ven, T. G. M. & Kakkar, A. Dendrimers as bactericides. *New J. Chem.* **36,** 199–204 (2012).
12. Sercombe, L., Veerati, T., Moheimani, F., Wu, S. Y. & Hua, S. Advances and Challenges of Liposome Assisted Drug Delivery. *Front. Pharmacol.* **6,** 1–13 (2015).
13. Christoforidis, J. B., Chang, S., Jiang, A., Wang, J. & Cebulla, C. M. Intravitreal devices for the treatment of vitreous inflammation. *Mediators Inflamm.* **2012,** (2012).
14. Fabienne Danhier, Eduardo Ansorena, Joana M. Silva, Régis Coco, Aude Le Breton, V. P. PLGA-based nanoparticles: An overview of biomedical applications. *J. Control. Release* **161,** 505–522 (2012).
15. Ma, L., Hart, A. H. C., Ozden, S., Vajtai, R. & Ajayan, P. M. Spiers memorial lecture: Advances of carbon nanomaterials. *Faraday Discuss.* **173,** 9–46 (2014).
16. Chaenyung Cha, Su Ryon Shin, Nasim Annabi, Mehmet R. Dokmeci, and A. K. Carbon-Based

Nanomaterials: Multi-Functional Materials for Biomedical Engineering. *ACS Nano* **7,** 2891–2897 (2013).

17. Erik C. Dreaden, Alaaldin M. Alkilany, Xiaohua Huang, C. J. M. and M. A. E.-S. The golden age: gold nanoparticles for biomedicine. *Chem. Soc. Rev.* **41,** 2740–2779 (2012).

18. Zhou, Z. *et al.* Iron/iron oxide core/shell nanoparticles for magnetic targeting MRI and near-infrared photothermal therapy. *Biomaterials* **35,** 7470–7478 (2014).

19. Ravera, M. *et al*. Functionalized nonporous silica nanoparticles as carriers for Pt(IV) anticancer prodrugs. *Dalt. Trans.* **45,** 17233–17240 (2016).

20. Nuti, S. *et al.* Engineered nanostructured materials for ofloxacin delivery. *Front. Chem.* **6,** 1–14 (2018).

21. García De Arquer, F. P., Lasanta, T., Bernechea, M. & Konstantatos, G. Tailoring the electronic properties of colloidal quantum dots in metal-semiconductor nanocomposites for high performance photodetectors. *Small* **11,** 2636–2641 (2015).

22. Nooney, R. I., Thirunavukkarasu, D., Chen, Y., Josephs, R. & Ostafin, A. E. Self-assembly of mesoporous nanoscale silica/gold composites. *Langmuir* **19,** 7628–7637 (2003).

23. Bermejo, M. R., González-Noya, A. M. & Vázquez, M. *O nome e o símbolo dos elementos químicos*. (Xunta de Galicia, 2006).

24. Reşitoglu, I. A., Altinişik, K. & Keskin, A. The pollutant emissions from diesel-engine vehicles and exhaust aftertreatment systems. *Clean Technol. Environ. Policy* **17,** 15–27 (2015).

25. Chiu, W. T. *et al.* Platinum coating on silk by a supercritical CO_2 promoted metallization technique for applications of wearable devices. *Surf. Coatings Technol.* **350,** 1028–1035 (2018).

26. Nassar, N. T. Limitations to elemental substitution as exemplified by the platinum-group metals. *Green Chem.* **17,** 2226–2235 (2015).

27. Wang, X., Wang, X. & Guo, Z. Functionalization of platinum complexes for biomedical applications. *Acc. Chem. Res.* **48,** 2622–2631 (2015).

28. Pandey, S. & Mishra, S. B. Catalytic reduction of p-nitrophenol by using platinum nanoparticles stabilised by guar gum. *Carbohydr. Polym.* **113,** 525–531 (2014).

29. Wang, C., Daimon, H., Lee, Y., Kim, J. & Sun, S. Synthesis of monodisperse Pt nanocubes and their enhanced catalysis for oxygen reduction. *J. Am. Chem. Soc.* **129,** 6974–6975 (2007).

30. Gong, X. *et al.* Controlled synthesis of Pt nanoparticles via seeding growth and their shape-dependent catalytic activity. *J. Colloid Interface Sci.* **352,** 379–385 (2010).

31. Ye, W. *et al.* Green synthesis of Pt-Au dendrimer-like nanoparticles supported on polydopamine-functionalized graphene and their high performance toward 4- nitrophenol reduction. *Appl. Catal. B Environ.* **181,** 371–378 (2016).

32. Lin, X. Q. *et al.* Platinum nanoparticles/graphene-oxide hybrid with excellent peroxidase-like activity and its application for cysteine detection. *Analyst* **140,** 5251–5256 (2015).

33. Helmlinger, J. *et al.* Silver nanoparticles with different size and shape: Equal cytotoxicity, but different antibacterial effects. *RSC Adv.* **6,** 18490–18501 (2016).

34. Ban, D. K. & Paul, S. Rapid colorimetric and spectroscopy based sensing of heavy metal and cellular free oxygen radical by surface functionalized silver nanoparticles. *Appl. Surf. Sci.* **458,** 245–251 (2018).

35. Zhang, J. J., Cheng, F. F., Li, J. J., Zhu, J. J. & Lu, Y. Fluorescent nanoprobes for sensing and imaging of metal ions: Recent advances and future perspectives. *Nano Today* **11,** 309–329 (2016).

36. Sabela, M., Balme, S., Bechelany, M., Janot, J. M. & Bisetty, K. A review of gold and silver nanoparticle-based colorimetric sensing assays. *Adv. Eng. Mater.* **19,** 1–24 (2017).

37. Reguera, J., Langer, J., Jiménez De Aberasturi, D. & Liz-Marzán, L. M. Anisotropic metal nanoparticles for surface enhanced Raman scattering. *Chem. Soc. Rev.* **46,** 3866–3885 (2017).

38. Yang, X., Yang, M., Pang, B., Vara, M. & Xia, Y. Gold nanomaterials at work in biomedicine. *Chem. Rev.* **115,** 10410–10488 (2015).

39. Deng, H. H. *et al.* Fabrication of Water-Soluble, Green-Emitting Gold Nanoclusters with a 65 % Photoluminescence Quantum Yield via Host-Guest Recognition. *Chem. Mater.* **29,** 1362–1369 (2017).

40. Uskoković, V. Entering the era of nanoscience: Time to be so small. *J. Biomed. Nanotechnol.* **9,** 1441–1470 (2013).

41. Shenhar, R. & Rotello, V. M. Nanoparticles: Scaffolds and building blocks. *Acc. Chem. Res.* **36,** 549–561 (2003).

42. Morag, A. & Jelinek, R. "Bottom-up" transparent electrodes. *J. Colloid Interface Sci.* **482,** 267–289 (2016).

43. Thanh, N. T. K., Maclean, N. & Mahiddine, S. Mechanisms of nucleation and growth of nanoparticles in solution. *Chem. Rev.* **114,** 7610–7630 (2014).

44. Polte, J. Fundamental growth principles of colloidal metal nanoparticles - a new perspective. *CrystEngComm* **17,** 6809–6830 (2015).

45. You, H. & Fang, J. Particle-mediated nucleation and growth of solution-synthesized metal nanocrystals: A new story beyond the LaMer curve. *Nano Today* **11,** 145–167 (2016).

46. Lamer, V. K. & Dinegar, R. H. Theory, Production and Mechanism of Formation of Monodispersed Hydrosols. *J. Am. Chem. Soc.* **72,** 4847–4854 (1950).

47. Ivanskii, B. V. & Vengrenovich, R. D. To the theory of Ostwald ripening in metallic alloys. *Phys. Met. Metallogr.* **117,** 756–765 (2016).

48. Gentry, S. T., Kendra, S. F. & Bezpalko, M. W. Ostwald ripening in metallic nanoparticles: Stochastic kinetics. *J. Phys. Chem. C* **115,** 12736–12741 (2011).

49. Werz, T., Baumann, M., Wolfram, U. & Krill, C. E. Particle tracking during Ostwald ripening using time-resolved laboratory X-ray microtomography. *Mater. Charact.* **90,** 185–195 (2014).

50. Park, J., Joo, J., Soon, G. K., Jang, Y. & Hyeon, T. Synthesis of monodisperse spherical nanocrystals. *Angew. Chemie - Int. Ed.* **46,** 4630–4660 (2007).

51. Shimpi, J. R., Sidhaye, D. S. & Prasad, B. L. V. Digestive ripening: A fine chemical machining process on the nanoscale. *Langmuir* **33,** 9491–9507 (2017).

52. Hwang, N.-M. & Lee, J.-S. J. and D.-K. Thermodynamics and kinetics in the synthesis of monodisperse nanoparticles. *Thermodyn. - Fundam. Its Appl. Sci.* 371–388 (2012).

53. Besson, C., Finney, E. E. & Finke, R. G. A mechanism for transition-metal nanoparticle self-assembly. *J. Am. Chem. Soc.* **127,** 8179–8184 (2005).

54. Siva, R. K. P. S. On the two-step mechanism for synthesis of transition-metal nanoparticles. *Langmuir* **30,** 12703–12711 (2014).

55. Stein, B. *et al*. Kinetics of aggregation and growth processes of PEG-stabilised mono- and multivalent gold nanoparticles in highly concentrated halide solutions. *Faraday Discuss.* **181,** 85–102 (2015).

56. Polte, J. *et al*. Nucleation and growth of gold nanoparticles studied via in situ small angle X-ray scattering at millisecond time resolution. *ACS Nano* **4,** 1076–1082 (2010).

57. Ingham, B. *et al*. How nanoparticles coalesce: An in situ study of Au nanoparticle aggregation and grain growth. *Chem. Mater.* **23,** 3312–3317 (2011).

58. Nasilowski, M., Mahler, B., Lhuillier, E., Ithurria, S. & Dubertret, B. Two-dimensional colloidal nanocrystals. *Chem. Rev.* **116,** 10934–10982 (2016).

59. Zhang, J., Huang, F. & Lin, Z. Progress of nanocrystalline growth kinetics based on oriented attachment. *Nanoscale* **2,** 18–34 (2010).

60. Moore, T. L. *et al.* Nanoparticle colloidal stability in cell culture media and impact on cellular interactions. *Chem. Soc. Rev.* **44,** 6287–6305 (2015).

61. Amendola, V., Pilot, R., Frasconi, M., Maragò, O. M. & Iatì, M. A. Surface plasmon resonance in gold nanoparticles : a review. *J. Phys. Condens. Matter* **29,** 203002 (2017).

62. Mayer, K. M. & Hafner, J. H. Localized surface plasmon resonance sensors. *Chem. Rev.* **111,** 3828–3857 (2011).

63. Garcia, M. A. Surface plasmons in metallic nanoparticles: Fundamentals and applications. *J. Phys. D. Appl. Phys.* **44,** (2011).

64. Myroshnychenko, V. *et al*. Modelling the optical response of gold nanoparticles. *Chem. Soc. Rev.* **37,** 1792–1805 (2008).

65. Miller, M. M. & Lazarides, A. A. Sensitivity of metal nanoparticle surface plasmon resonance to the dielectric environment. *J. Opt. A: Pure Appl. Opt.* **8,** S239–S249 (2006).

66. Gulati, A., Liao, H. & Hafner, J. H. Monitoring gold nanorod synthesis by localized surface plasmon resonance. *J. Phys. Chem. B* **110,** 22323–22327 (2006).

67. Gharibshahi, E., Saion, E., Ashraf, A. & Gharibshahi, L. Size-controlled and optical properties

of platinum nanoparticles by gamma radiolytic synthesis. *Appl. Radiat. Isot.* **130,** 211–217 (2017).

68. Kumar, S., Gandhi, K. S. & Kumar, R. Modeling of formation of gold nanoparticles by citrate method. *Ind. Eng. Chem. Res.* **46,** 3128–3136 (2007).

69. Wuithschick, M. *et al.* Turkevich in new robes: Key questions answered for the most common gold nanoparticle synthesis. *ACS Nano* **9,** 7052–7071 (2015).

70. Ojea-Jiménez, I., Romero, F., Bastús, N. G. & Puntes, V. Small gold nanoparticles synthesized with sodium citrate and heavy water: insights into the reaction mechanism. *J. Phys. Chem. C* **114,** 1800–1804 (2010).

71. Schulz, F. *et al.* Little adjustments significantly improve the Turkevich synthesis of gold nanoparticles. *Langmuir* **30,** 10779–10784 (2014).

72. Kimling, J. *et al.* Turkevich method for gold nanoparticle synthesis revisited. *J. Phys. Chem. B* **110,** 15700–15707 (2006).

73. Ojea-Jiménez, I., Bastús, N. G. & Puntes, V. Influence of the sequence of the reagents addition in the citrate-mediated synthesis of gold nanoparticles. *J. Phys. Chem. C* **115,** 15752–15757 (2011).

74. Pillai, Z. S. & Kamat, P. V. What factors control the size and shape of silver nanoparticles in the citrate ion reduction method? *J. Phys. Chem. B* **108,** 945–951 (2004).

75. Wuithschick, M. *et al.* Size-controlled synthesis of colloidal silver nanoparticles based on mechanistic understanding. *Chem. Mater.* **25,** 4679–4689 (2013).

76. Tuaev, X. *et al.* Formation mechanism of colloidal silver nanoparticles: Analogies and differences to the growth of gold nanoparticles. *ACS Nano* **6,** 5791–5802 (2012).

77. Frank, A. J., Cathcart, N., Maly, K. E. & Kitaev, V. Synthesis of silver nanoprisms with variable size and investigation of their optical properties: A first-year undergraduate experiment exploring plasmonic nanoparticles. *J. Chem. Educ.* **87,** 1098–1101 (2010).

78. Jana, N. R., Gearheart, L. & Murphy, C. J. Wet chemical synthesis of high aspect ratio cylindrical gold nanorods. *J. Phys. Chem. B* **105,** 4065–4067 (2001).

79. Xia, Y., Gilroy, K. D., Peng, H. C. & Xia, X. Seed-mediated growth of colloidal metal nanocrystals. *Angew. Chemie - Int. Ed.* **56,** 60–95 (2017).

80. Walsh, M. J., Barrow, S. J., Tong, W., Funston, A. M. & Etheridge, J. Symmetry breaking and silver in gold nanorod growth. *ACS Nano* **9,** 715–724 (2015).

81. Burrows, N. D., Harvey, S., Idesis, F. A. & Murphy, C. J. Understanding the seed-mediated growth of gold nanorods through a fractional factorial design of experiments. *Langmuir* **33,** 1891–1907 (2017).

82. Meena, S. K. & Sulpizi, M. From gold nanoseeds to nanorods: The microscopic origin of the anisotropic growth. *Angew. Chemie - Int. Ed.* **55,** 11960–11964 (2016).

83. Garg, N., Scholl, C., Mohanty, A. & Jin, R. The role of bromide ions in seeding growth of Au

nanorods. *Langmuir* **26,** 10271–10276 (2010).

84. Scarabelli, L., Sánchez-Iglesias, A., Pérez-Juste, J. & Liz-Marzán, L. M. A 'tips and tricks' practical guide to the synthesis of gold nanorods. *J. Phys. Chem. Lett.* **6,** 4270–4279 (2015).

85. Millstone, J. E., Wei, W., Jones, M. R., Yoo, H. & Mirkin, C. A. Iodide ions control seed-mediated growth of anisotropic gold nanoparticles. *Nano Lett.* **8,** 2526–2529 (2008).

86. Murphy, C. J., Burrows, N. D., Liz-Marzán, L. M., Lohse, S. E. & Scarabelli, L. Anisotropic noble metal nanocrystal growth: The role of halides. *Chem. Mater.* **26,** 34–43 (2013).

87. Xu, Y. *et al.* Cooperative interactions among CTA^+, Br^- and Ag^+ during seeded growth of gold nanorods. *Nano Res.* **10,** 2146–2155 (2017).

88. Liu, X. *et al.* Effect of growth temperature on tailoring the size and aspect ratio of gold nanorods. *Langmuir* **33,** 7479–7485 (2017).

89. Wei, Q., Ji, J. & Shen, J. pH controlled synthesis of high aspect-ratio gold nanorods. *J. Nanosci. Nanotechnol.* **8,** 5708–5714 (2008).

90. Leong, G. J. *et al.* Shape-directed platinum nanoparticle synthesis: Nanoscale design of novel catalysts. *Appl. Organomet. Chem.* **28,** 1–17 (2014).

91. Song, H., Kim, F., Connor, S., Somorjai, G. A. & Yang, P. Pt nanocrystals: Shape control and Langmuir-Blodgett monolayer formation. *J. Phys. Chem. B* **109,** 188–193 (2005).

92. Huang, X., Zhao, Z., Fan, J., Tan, Y. & Zheng, N. Amine-assisted synthesis of concave polyhedral platinum nanocrystals having {411} high-index facets. *J. Am. Chem. Soc.* **133,** 4718–4721 (2011).

93. Chen, J., Herricks, T. & Xia, Y. Polyol synthesis of platinum nanostructures: Control of morphology through the manipulation of reduction kinetics. *Angew. Chemie - Int. Ed.* **44,** 2589–2592 (2005).

94. Herricks, T., Chen, J. & Xia, Y. Polyol synthesis of platinum nanoparticles: Control of morphology with sodium nitrate. *Nano Lett.* **4,** 2367–2371 (2004).

95. Wang, L. & Yamauchi, Y. Block copolymer mediated synthesis of dendritic platinum nanoparticles. *J. Am. Chem. Soc.* **131,** 9152–9153 (2009).

96. Lee, J., Yang, J., Kwon, S. G. & Hyeon, T. Nonclassical nucleation and growth of inorganic nanoparticles. *Nat. Rev. Mater.* **1,** (2016).

97. Guerrero-Martínez, A., Pérez-Juste, J. & Liz-Marzán, L. M. Recent progress on silica coating of nanoparticles and related nanomaterials. *Adv. Mater.* **22,** 1182–1195 (2010).

98. Wong, Y. J. *et al.* Revisiting the Stöber method: Inhomogeneity in silica shells. *J. Am. Chem. Soc.* **133,** 11422–11425 (2011).

99. Hongmei, J., Zhen, Z., Zhiming, L. & Xinling, W. Effects of temperature and solvent on the hydrolysis of alkoxysilane under alkaline conditions. *Ind. Eng. Chem. Res.* **45,** 8617–8622 (2006).

100. Montaño-Priede, J. L., Coelho, J. P., Guerrero-Martínez, A., Peña-Rodríguez, O. & Pal, U. Fabrication of monodispersed $Au@SiO_2$ nanoparticles with highly stable silica layers by ultrasound-assisted Stöber method. *J. Phys. Chem. C* **121,** 9543–9551 (2017).

101. Anastas, P. T. & Warner, J. C. *Green Chemistry*. (Oxford University Press: Oxford, 2000).

102. Anastas, P. & Zimmerman, J. B. Through the 12 Principles GREEN Engineering. *Environ. Sci. Technol.* **37,** 94A–101A (2003).

103. Mestres, R. *Química Sostenible*. (Editorial Sintesis, 2010).

104. Mestres, R. Química Sostenible: Naturaleza, fines y ámbito. *Educ. Quim.* **24,** 103–112 (2013).

105. Housecroft, C. E. & Sharpe, A. G. *Inorganic Chemistry*. (Pearson, 2012).

106. Sheldon, R. A., Arends, I. & Hanefeld, U. *Green Chemistry and Catalysis*. (WILEY-VCH Verlag GmbH & Co. KGaA, Weinheim, Germany, 2007).

107. Sillanpää, M., Shrestha, R. A. & Pham, T.-D. *Ultrasound Technology in Green Chemistry*. (Springer, 2011).

108. Capelo-Martinez, J. L. *Ultrasound in Chemistry: Analytical Applications*. (Wiley-VCH, 2009).

109. T. J. Mason & Lorimer, J. P. *Applied sonochemistry: Uses of power ultrasound in chemistry and processing*. *Wiley-VCH* (WILEY-VCH Verlag GmbH & Co. KGaA, Weinheim, Germany, 2002).

110. Capelo, J. L., Maduro, C. & Vilhena, C. Discussion of parameters associated with the ultrasonic solid-liquid extraction for elemental analysis (total content) by electrothermal atomic absorption spectrometry. An overview. *Ultrason. Sonochem.* **12,** 225–232 (2005).

111. Ramos, J. J., Rial-Otero, R., Ramos, L. & Capelo, J. L. Ultrasonic-assisted matrix solid-phase dispersion as an improved methodology for the determination of pesticides in fruits. *J. Chromatogr. A* **1212,** 145–149 (2008).

112. Araújo, J. E. *et al.* A journey through PROTEOSONICS. *Talanta* **121,** 71–80 (2014).

113. Jesus, J. R. *et al.* Ultrasonic-based membrane aided sample preparation of urine proteomes. *Talanta* **178,** 864–869 (2018).

114. Keglevich, G. *Milestones in Microwave Chemistry*. (Springer, 2016).

115. Bogdat, D. & Prociak, A. *Microwave-Enhanced Polymer Chemistry and Technology*. (Wiley, 2013).

116. Serpone, N. & Horikoshi, S. *Microwaves in Nanoparticle Synthesis. Fundamentals and Applications*. (WILEY-VCH Verlag GmbH & Co. KGaA, Weinheim, Germany, 2013).

117. Brett, C. M. A. & Brett, A. M. O. *Electrochemistry: Principles, methods, and applications*. (Oxford University Press Inc., New York, 1993).

118. Santos, E. & Schmickler, W. *Catalysis in electrochemistry from fundamentals to strategies for fuel cell development*. (John Wiley & Sons, Inc., Hoboken, New Jersey, 2011).

119. Radjenovic, J. & Sedlak, D. L. Challenges and opportunities for electrochemical processes as

next-generation technologies for the treatment of contaminated water. *Environ. Sci. Technol.* **49,** 11292–11302 (2015).

120. Vincenzo Balzani, Ceroni, P. & Juris, A. *Photochemistry and Photophysics. Concepts, Research, Applications*. (WILEY-VCH Verlag GmbH & Co. KGaA, Weinheim, Germany, 2014).

121. Hamblin, M. R. & Avci, P. *Applications of Nanoscience in Photomedicine*. (Woodhead Publishing, Elsevier, 2015).

122. Skoog, D., Crouch, S. R., Holler, F. J. & Anzures, M. B. *Principios de Analisis Instrumental - (Spanish Edition)*. (Cengage Learning, 2008).

123. Peng, L. *et al.* "Naked-eye" recognition: Emerging gold nano-family for visual sensing. *Appl. Mater. Today* **11,** 166–188 (2018).

124. Hobman, J. L. & Crossman, L. C. Bacterial antimicrobial metal ion resistance. *J. Med. Microbiol.* **64,** 471–497 (2015).

125. Zhao, C. Y., Cheng, R., Yang, Z. & Tian, Z. M. Nanotechnology for cancer therapy based on chemotherapy. *Molecules* **23,** (2018).

126. Elghanian, R., Storhoff, J. J., Mucic, R. C., Letsinger, R. L. & Mirkin, C. A. Selective colorimetric detection of polynucleotides based on the distance-dependent optical properties of gold nanoparticles. *Science (80-.).* **277,** 1078–1081 (1997).

127. Mirkin, C. A., Letsinger, R. L., Mucic, R. C. & Storhoff, J. L. A DNA-based method for rationally assembling nanoparticles into macroscopic materials. *Nature* **382,** 607–609 (1996).

128. Park, M. H. & Igarashi, K. Polyamines and their metabolites as diagnostic markers of human diseases. *Biomol. Ther.* **21,** 1–9 (2013).

129. Lodeiro, C. *et al.* Light and colour as analytical detection tools: A journey into the periodic table using polyamines to bio-inspired systems as chemosensors. *Chem. Soc. Rev.* **39,** 2948–2976 (2010).

130. Dong, Y. *et al.* Polyamine-functionalized carbon quantum dots as fluorescent probes for selective and sensitive detection of copper ions. *Anal. Chem.* **84,** 6220–6224 (2012).

131. Lin, H.-J. *et al.* Synthesis of self-assembled spermidine-carbon quantum dots effective against multidrug-resistant bacteria. *Adv. Healthc. Mater.* **5,** 2545–2554 (2016).

132. Pi, M. *et al.* Biomimetic synthesis of raspberry-like hybrid polymer-silica core-shell nanoparticles by templating colloidal particles with hairy polyamine shell. *Colloids Surfaces B Biointerfaces* **78,** 193–199 (2010).

133. Huang, S. H. & Chen, D. H. Rapid removal of heavy metal cations and anions from aqueous solutions by an amino-functionalized magnetic nano-adsorbent. *J. Hazard. Mater.* **163,** 174–179 (2009).

134. Qu, F., Li, N. B. & Luo, H. Q. Transition from nanoparticles to nanoclusters: Microscopic and spectroscopic investigation of size-dependent physicochemical properties of polyamine-functionalized silver nanoclusters. *J. Phys. Chem. C* **117,** 3548–3555 (2013).

135. Zhang, Y., Li, R., Xue, Q., Li, H. & Liu, J. Colorimetric determination of copper(II) using a

polyamine-functionalized gold nanoparticle probe. *Microchim. Acta* **182,** 1677–1683 (2015).

136. He, Z., Yang, Y., Liu, J. W. & Yu, S. H. Emerging tellurium nanostructures: Controllable synthesis and their applications. *Chem. Soc. Rev.* **46,** 2732–2753 (2017).

137. Petragnani, N. & Stefani, H. A. Advances in organic tellurium chemistry. *Tetrahedron* **61,** 1613–1679 (2005).

138. Lin, Z. H., Lee, C. H., Chang, H. Y. & Chang, H. T. Antibacterial activities of tellurium nanomaterials. *Chem. - An Asian J.* **7,** 930–934 (2012).

139. Seng, H. L. & Tiekink, E. R. T. Anti-cancer potential of selenium- and tellurium-containing species: Opportunities abound! *Appl. Organomet. Chem.* **26,** 655–662 (2012).

140. Ma, C., Yan, J., Huang, Y., Wang, C. & Yang, G. The optical duality of tellurium nanoparticles for broadband solar energy harvesting and efficient photothermal conversion. *Sci. Adv.* **4,** 1–10 (2018).

141. Brown, C. D., Cruz, D. M., Roy, A. K. & Webster, T. J. Synthesis and characterization of PVP-coated tellurium nanorods and their antibacterial and anticancer properties. *J. Nanoparticle Res.* **20,** (2018).

142. Chou, T. M., Ke, Y. Y., Tsao, Y. H., Li, Y. C. & Lin, Z. H. Fabrication of Te and Te-Au nanowires-based carbon fiber fabrics for antibacterial applications. *Int. J. Environ. Res. Public Health* **13,** (2016).

143. Huang, W., Wu, H., Li, X. & Chen, T. Facile one-pot synthesis of tellurium nanorods as antioxidant and anticancer agents. *Chem. - An Asian J.* **11,** 2301–2311 (2016).

144. Yu, H. W. *et al.* Preparation of quantum dots CdTe decorated graphene composite for sensitive detection of uric acid and dopamine. *Anal. Biochem.* **519,** 92–99 (2017).

145. Chen, M. & Guyot-Sionnest, P. Reversible electrochemistry of mercury chalcogenide colloidal quantum dot films. *ACS Nano* **11,** 4165–4173 (2017).

146. Pradhan, N. R. *et al.* Field-effect transistors based on few-layered α-$MoTe_2$. *ACS Nano* **8,** 5911–5920 (2014).

147. Qiu, L., Pol, V. G., Wei, Y. & Gedanken, A. A two-step process for the synthesis of $MoTe_2$ nanotubes: Combining a sonochemical technique with heat treatment. *J. Mater. Chem.* **13,** 2985–2988 (2003).

148. Qiu, L., Wei, Y., Pol, V. G. & Gedanken, A. Synthesis of α-$MoTe_2$ nanorods via annealing Te-seeded amorphous MoTe2 particles. *Inorg. Chem.* **43,** 6061–6066 (2004).

149. Shaygan, M. *et al.* In situ observation of melting behavior of ZnTe nanowires. *J. Phys. Chem. C* **118,** 15061–15067 (2014).

150. Rueda-Fonseca, P. *et al.* Structure and morphology in diffusion-driven growth of nanowires: The case of ZnTe. *Nano Lett.* **14,** 1877–1883 (2014).

151. Shen, J. *et al.* Synthesis of SnTe nanoplates with {100} and {111} surfaces. *Nano Lett.* **14,** 4183–4188 (2014).

152. Som, A., Samal, A. K., Udayabhaskararao, T., Bootharaju, M. S. & Pradeep, T. Manifestation of

the difference in reactivity of silver clusters in contrast to its ions and nanoparticles: The growth of metal tipped Te nanowires. *Chem. Mater.* **26,** 3049–3056 (2014).

153. Jao, Y.-T., Li, Y.-C., Xie, Y. & Lin, Z.-H. A self-powered temperature sensor based on silver telluride nanowires. *ECS J. Solid State Sci. Technol.* **6,** N3055–N3057 (2017).

154. Lin, Z. H. & Chang, H. T. Preparation of gold-tellurium hybrid nanomaterials for surface-enhanced raman spectroscopy. *Langmuir* **24,** 365–367 (2008).

155. Guo, S., Dong, S. & Wang, E. Novel Te/Pt hybrid nanowire with nanoporous surface: A catalytically active nanoelectrocatalyst. *J. Phys. Chem. C* **114,** 4797–4802 (2010).

156. Dong, M., Chen, H., Xu, J., Chen, Z. & Cao, J. Synthesis of Cu-decorated PtTe nanotubes with high electrocatalytic activity for oxygen reduction. *J. Alloys Compd.* **770,** 76–81 (2019).

157. Tsuji, M. *et al*. Toward to branched platinum nanoparticles by polyol reduction: A role of poly(vinylpyrrolidone) molecules. *Colloids Surfaces A Physicochem. Eng. Asp.* **317,** 23–31 (2008).

158. Yin, J., Wang, J., Li, M., Jin, C. & Zhang, T. Iodine ions mediated formation of monomorphic single-crystalline platinum nanoflowers. *Chem. Mater.* **24,** 2645–2654 (2012).

159. Long, N. V. *et al*. Synthesis and characterization of polyhedral Pt nanoparticles: Their catalytic property, surface attachment, self-aggregation and assembly. *J. Colloid Interface Sci.* **359,** 339–350 (2011).

160. Vidal-Iglesias, F. J., Arán-Ais, R. M., Solla-Gullón, J., Herrero, E. & Feliu, J. M. Electrochemical characterization of shape-controlled Pt nanoparticles in different supporting electrolytes. *ACS Catal.* **2,** 901–910 (2012).

161. Singh, H. P., Gupta, N., Sharma, S. K. & Sharma, R. K. Synthesis of bimetallic Pt-Cu nanoparticles and their application in the reduction of rhodamine B. *Colloids Surfaces A Physicochem. Eng. Asp.* **416,** 43–50 (2013).

162. Alkilany, A. M., Thompson, L. B., Boulos, S. P., Sisco, P. N. & Murphy, C. J. Gold nanorods: Their potential for photothermal therapeutics and drug delivery, tempered by the complexity of their biological interaction. *Adv. Drug Deliv. Rev.* **64,** 190–199 (2012).

163. Wu, X., Wang, J. & Chen, J. Y. The effect of aspect ratio of gold nanorods on cell imaging with two-photon excitation. *Plasmonics* **8,** 685–691 (2013).

164. Smith, A. M., Mancini, M. C. & Nie, S. Second window for in vivo imaging. *Nat. Nanotechnol.* **4,** 710–711 (2010).

165. Weissleder, R. A clearer vision for in vivo imaging. *Nat. Biotechnol.* **19,** 316–317 (2001).

166. Gao, X., Cui, Y., Levenson, R. M., Chung, L. W. K. & Nie, S. In vivo cancer targeting and imaging with semiconductor quantum dots. *Nat. Biotechnol.* **22,** 969–976 (2004).

167. Pissuwan, D., Valenzuela, S. M., Killingsworth, M. C., Xu, X. & Cortie, M. B. Targeted destruction of murine macrophage cells with bioconjugated gold nanorods. *J. Nanoparticle Res.* **9,** 1109–1124 (2007).

168. Zharov, V. P., Mercer, K. E., Galitovskaya, E. N. & Smeltzer, M. S. Photothermal

nanotherapeutics and nanodiagnostics for selective killing of bacteria targeted with gold nanoparticles. *Biophys. J.* **90,** 619–627 (2006).

169. Khlebtsov, N. *et al.* Analytical and theranostic applications of gold nanoparticles and multifunctional nanocomposites. *Theranostics* **3,** 167–180 (2013).

170. Moreira, A. F. *et al.* Functionalization of AuMSS nanorods towards more effective cancer therapies. *Nano Res.* **12,** (2019).

171. Liu, M. *et al.* An efficient antimicrobial depot for infectious site-targeted chemo-photothermal therapy. *J. Nanobiotechnology* **16,** 1–20 (2018).

172. Zhang, Y., Xu, D., Li, W., Yu, J. & Chen, Y. Effect of size, shape, and surface modification on cytotoxicity of gold nanoparticles to human HEp-2 and Canine MDCK Cells. *J. Nanomater.* **2012,** (2012).

173. Han, B. *et al.* Ultra-stable silica-coated chiral Au-nanorod assemblies: Core–shell nanostructures with enhanced chiroptical properties. *Nano Res.* **9,** 451–457 (2016).

174. Chen, D. *et al.* Gold nanorods/mesoporous silica-based nanocomposite as theranostic agents for targeting near-infrared imaging and photothermal therapy induced with laser. *Int. J. Nanomedicine* 4747 (2015).

175. Gao, Z. *et al.* In solution SERS sensing using mesoporous silica-coated gold nanorods. *Analyst* **141,** 5088–5095 (2016).

176. Cui, Q. *et al.* Gold nanorod-based multifunctional nanocarrier for synergistic chemo-photothermal therapy in tumors. *RSC Adv.* **8,** 41454–41463 (2018).

177. Zhang, L. *et al.* Gold nanorod embedded large-pore mesoporous organosilica nanospheres for gene and photothermal cooperative therapy of triple negative breast cancer. *Nanoscale* **9,** 1466–1474 (2016).

178. Prasad, R., Agawane, S. B., Chauhan, D. S., Srivastava, R. & Selvaraj, K. In Vivo Examination of Folic Acid-Conjugated Gold-Silica Nanohybrids as Contrast Agents for Localized Tumor Diagnosis and Biodistribution. *Bioconjug. Chem.* **29,** 4012–4019 (2018).

179. An, N., Lin, H. & Qu, F. Synthesis of a GNRs@mSiO_2-ICG-DOX@Se-Se-FA Nanocomposite for Controlled Chemo-/Photothermal/Photodynamic Therapy. *Eur. J. Inorg. Chem.* **2018,** 4375–4384 (2018).

180. Daniel, M. & Astruc, D. Gold nanoparticles : Assembly , supramolecular chemistry , quantum-size-related properties , and applications toward biology , catalysis , and nanotechnology. *Chem. Mater* **104,** 293–346 (2004).

181. Sau, T. K. & Rogach, A. L. Nonspherical noble metal nanoparticles : Colloid-chemical synthesis and morphology control. *Adv. Mater.* **22,** 1781–1804 (2010).

182. Hutchings, G. J., Brust, M. & Schmidbaur, H. Gold-an introductory perspective. *Chemical Society Reviews* **37,** 1759–1765 (2008).

183. Guo, S. & Wang, E. Noble metal nanomaterials: Controllable synthesis and application in fuel cells and analytical sensors. *Nano Today* **6,** 240–264 (2011).

184. Kumar M., A., Jung, S. & Ji, T. Protein biosensors based on polymer nanowires, carbon nanotubes and zinc oxide nanorods. *Sensors* **11,** 5087–5111 (2011).

185. Ratto, F., Matteini, P., Centi, S., Rossi, F. & Pini, R. Gold nanorods as new nanochromophores for photothermal therapies. *J. Biophotonics* **4,** 64–73 (2011).

186. Stone, J., Jackson, S. & Wright, D. Biological applications of gold nanorods. *Wiley Interdiscip. Rev. Nanomedicine Nanobiotechnology* **3,** 100–109 (2011).

187. Kim, F. S., Ren, G. & Jenekhe, S. A. One-dimensional nanostructures of π-conjugated molecular systems: assembly, properties, and applications from photovoltaics, sensors, and nanophotonics to nanoelectronics. *Chem. Mater.* **23,** 682–732 (2011).

188. Pruneanu, S. *et al.* Nanostructures based on metallic nanoparticles and biomolecules Nanostructures Based On Metallic Nanoparticles And Biomolecules. *AIP Conf. Proc.* **144,** 144–147 (2012).

189. Teranishi, T. Fabrication and electronic properties of gold nanoparticle superlattices. *Comptes Rendus Chimie* **6,** 979–987 (2003).

190. Zhang, D. F. *et al.* Branched gold nanochains facilitated by polyvinylpyrrolidone and their SERS effects on p-aminothiophenol. *J. Phys. Chem. C* **112,** 16011–16016 (2008).

191. Yang, Y., Matsubara, S., Nogami, M., Shi, J. & Huang, W. One-dimensional self-assembly of gold nanoparticles for tunable surface plasmon. *Nanotechnology* **17,** 2821–2827 (2006).

192. Chen, C., Zhang, P. & Rosi, N. L. A new peptide-based method for the design and synthesis of nanoparticle superstructures: Nanoparticle double helices construction of highly-ordered gold. *J. Am. Chem. Soc.* **130,** 13555–13557 (2008).

193. Chang, J., Wu, H., Chen, H., Ling, Y. & Tan, W. Oriented assembly of Au nanorods using biorecognition system. *Chem. Commun.* 1092–1094 (2005).

194. Tian, H. *et al.* Electrochemically triggered Au nanoparticles "sponges" for the controlled uptake and release of a photoisomerizable dithienylethene guest substrate. *ACS Nano* **5,** 5936–5944 (2011).

195. Thomas, K. G., Barazzouk, S., Ipe, B. I., Joseph, S. T. S. & Kamat, P. V. Uniaxial plasmon coupling through longitudinal self-assembly of gold nanorods. *J. Phys. Chem. B* **108,** 13066–13068 (2004).

196. DeVries, G. A. *et al.* Divalent metal nanoparticles. *Science (80-.).* **315,** 358–361 (2007).

197. Nie, Z. *et al.* Self-assembly of metal-polymer analogues of amphiphilic triblock copolymers. *Nat. Mater.* **6,** 609–614 (2007).

198. Li, M., Johnson, S., Guo, H., Dujardin, E. & Mann, S. A generalized mechanism for ligand-induced dipolar assembly of plasmonic gold nanoparticle chain networks. *Adv. Funct. Mater.* **21,** 851–859 (2011).

199. Ding, B., Deng, Z., Yan, H., Cabrini, S. & Zuckermann, R. N. Supporting online information gold nanoparticles self-similar chain structure organized by DNA origami. *J. Am. Chem. Soc.* **132,** 1–16 (2010).

200. Kim, H. J., Roh, Y., Kim, S. K. & Hong, B. Fabrication and characterization of DNA-templated conductive gold nanoparticle chains. *J. Appl. Phys.* **105,** (2009).

201. Ongaro, A. *et al.* DNA-templated assembly of conducting gold nanowires between gold electrodes on a silicon oxide substrate. *Chem. Mater.* **17,** 1959–1964 (2005).

202. Wei, G. *et al.* Type I collagen-mediated synthesis and assembly of UV-photoreduced gold nanoparticles and their application in surface-enhanced Raman scattering. *J. Phys. Chem. C* **111,** 1976–1982 (2007).

203. Higuchi, M., Ushiba, K. & Kawaguchi, M. Structural control of peptide-coated gold nanoparticle assemblies by the conformational transition of surface peptides. *J. Colloid Interface Sci.* **308,** 356–363 (2007).

204. Zhong, Z., Patskovskyy, S., Bouvrette, P., Luong, J. H. T. & Gedanken, A. The surface chemistry of Au colloids and their interactions with functional amino acids. *J. Phys. Chem. B* **108,** 4046–4052 (2004).

205. Zhong, Z. *et al.* Controlled organization of au colloids into linear assemblies. *J. Phys. Chem. B* **108,** 18119–18123 (2004).

206. Selvakannan, P. R. *et al.* Water-dispersible tryptophan-protected gold nanoparticles prepared by the spontaneous reduction of aqueous chloroaurate ions by the amino acid. *J. Colloid Interface Sci.* **269,** 97–102 (2004).

207. Shao, Y., Jin, Y. & Dong, S. Synthesis of gold nanoplates by aspartate reduction of gold chloride. *Chem. Commun.* 1104–1105 (2004).

208. Zhong, Z., Subramanian, A. S., Highfield, J., Carpenter, K. & Gedanken, A. From discrete particles to spherical aggregates: A simple approach to the self-assembly of Au colloids. *Chem. - A Eur. J.* **11,** 1473–1478 (2005).

209. Polavarapu, L. & Xu, Q. H. A single-step synthesis of gold nanochains using an amino acid as a capping agent and characterization of their optical properties. *Nanotechnology* **19,** (2008).

210. Hsieh, S. & Hsieh, C. W. Alignment of gold nanoparticles using insulin fibrils as a sacrificial biotemplate. *Chem. Commun.* **46,** 7355–7357 (2010).

211. Lee, D. *et al.* Photoconductivity of pea-pod-type chains of gold nanoparticles encapsulated within dielectric amyloid protein nanofibrils of α-synuclein. *Angew. Chemie - Int. Ed.* **50,** 1332–1337 (2011).

212. Qin, L. X. *et al.* Electrodeposition of single-metal nanoparticles on stable protein 1 membranes: Application of plasmonic sensing by single nanoparticles. *Angew. Chemie - Int. Ed.* **51,** 140–144 (2012).

213. Correa-Duarte, M. A. & Liz-Marzán, L. M. Carbon nanotubes as templates for one-dimensional nanoparticle assemblies. *J. Mater. Chem.* **16,** 22–25 (2006).

214. Liu, K. *et al.* Step-Growth polymerization of inorganic nanoparticles. *Science (80-.).* **329,** 197–200 (2010).

215. Nel, A. E. *et al.* Understanding biophysicochemical interactions at the nano-bio interface. *Nat. Mater.* **8,** 543–557 (2009).

216. Sharma, N., Top, A., Kiick, K. L. & Pochan, D. J. One-dimensional gold nanoparticle arrays by electrostatically directed organization using polypeptide self-assembly. *Angew. Chemie - Int. Ed.* **48,** 7078–7082 (2009).

217. Brongersma, M. L., Hartman, J. W. & Atwater, H. A. Electromagnetic energy transfer and switching in nanoparticle chain arrays below the diffraction limit. *Phys. Rev. B - Condens. Matter Mater. Phys.* **62,** 356–359 (2000).

218. Quinten, M., Leitner, A., Krenn, J. R. & Aussenegg, F. R. Electromagnetic energy transport via linear chains of silver nanoparticles. *Opt. Lett.* **23,** 1331–1334 (1998).

219. Shipway, A. N., Lahav, M., Gabai, R. & Willner, I. Investigations into the electrostatically induced aggregation of Au nanoparticles. *Langmuir* **16,** 8789–8795 (2000).

220. Nikoobakht, B. & El-Sayed, M. A. Evidence for bilayer assembly of cationic surfactants on the surface of gold nanorods. *Langmuir* **17,** 6368–6374 (2001).

221. Johnson, C. J., Dujardin, E., Davis, S. A., Murphy, C. J. & Mann, S. Growth and form of gold nanorods prepared by seed-mediated, surfactant-directed synthesis. *J. Mater. Chem.* **12,** 1765–1770 (2002).

222. Jackson, A. M., Myerson, J. W. & Stellacci, F. Spontaneous assembly of subnanometre-ordered domains in the ligand shell of monolayer-protected nanoparticles. *Nat. Mater.* **3,** 330–336 (2004).

223. Glotzer, S. C. & Solomon, M. J. Anisotropy of building blocks and their assembly into complex structures. *Nat. Mater.* **6,** 557–562 (2007).

224. Ling, A. P. K., Kok, K. M., Hussein, S. & Ong, S. L. Effects of plant growth regulators on adventitious roots induction from different explants of Orthosiphon stamineus. *Am. J. Sustain. Agric.* **3,** 493–501 (2009).

225. Faraday, M. The Bakerian Lecture: Experimental Relations of Gold (and Other Metals) to Light. *Phil. Trans. R. Soc. L.* **147,** 145–181 (1857).

226. Thaxton, C. S., Georganopoulou, D. G. & Mirkin, C. A. Gold nanoparticle probes for the detection of nucleic acid targets. *Clin. Chim. Acta* **363,** 120–126 (2006).

227. Witlicki, E. H. *et al.* Molecular logic gates using surface-enhanced raman-scattered light. *J. Am. Chem. Soc.* **133,** 7288–7291 (2011).

228. Wu, X. *et al.* Constructing NIR silica-cyanine hybrid nanocomposite for bioimaging in vivo: A breakthrough in photo-stability and bright fluorescence with large Stokes shift. *Chem. Sci.* **4,** 1221–1228 (2013).

229. Jain, P. K., Lee, K. S., El-Sayed, I. H. & El-Sayed, M. A. Calculated absorption and scattering properties of gold nanoparticles of different size, shape, and composition: Applications in biological imaging and biomedicine. *J. Phys. Chem. B* **110,** 7238–7248 (2006).

230. De La Escosura-Muñiz, A., Parolo, C. & Merkoi, A. Immunosensing using nanoparticles. *Mater. Today* **13,** 24–34 (2010).

231. Wei, F. *et al.* Rapid detection of melamine in whole milk mediated by unmodified gold nanoparticles. *Appl. Phys. Lett.* **96,** (2010).

232. Qi, W. J., Wu, D., Ling, J. & Huang, C. Z. Visual and light scattering spectrometric detections of melamine with polythymine-stabilized gold nanoparticles through specific triple hydrogen-bonding recognition. *Chem. Commun.* **46,** 4893–4895 (2010).

233. Mock, J. J., Barbic, M., Smith, D. R., Schultz, D. A. & Schultz, S. Shape effects in plasmon resonance of individual colloidal silver nanoparticles. *J. Chem. Phys.* **116,** 6755–6759 (2002).

234. Cheng, Y., Wang, M., Borghs, G. & Chen, H. Gold nanoparticle dimers for plasmon sensing. *Langmuir* **27,** 7884–7891 (2011).

235. Charrault, E. *et al.* A facile route to homogeneous high density networks of metal nanoparticles. *Langmuir* **25,** 11285–11288 (2009).

236. Xia, Y., Xiong, Y., Lim, B. & Skrabalak, S. E. Shape-controlled synthesis of metal nanocrystals: Simple chemistry meets complex physics? *Angew. Chemie - Int. Ed.* **48,** 60–103 (2009).

237. Taleb, A., Petit, C. & Pileni, M. P. Synthesis of highly monodisperse silver nanoparticles from AOT reverse micelles: A way to 2D and 3D self-organization. *Chem. Mater.* **9,** 950–959 (1997).

238. Matassa, R. *et al.* Two-dimensional networks of Ag nanoparticles bridged by organometallic ligand. *J. Phys. Chem. C* **116,** 15795–15800 (2012).

239. Chang, J. Y., Chang, J. J., Lo, B., Tzing, S. H. & Ling, Y. C. Silver nanoparticles spontaneous organize into nanowires and nanobanners in supercritical water. *Chem. Phys. Lett.* **379,** 261–267 (2003).

240. Oliveira, E., Nuñez, C., Rodríguez-González, B., Capelo, J. L. & Lodeiro, C. Novel small stable gold nanoparticles bearing fluorescent cysteine-coumarin probes as new metal-modulated chemosensors. *Inorg. Chem.* **50,** 8797–8807 (2011).

241. Oliveira, E. *et al*. Bioinspired systems for metal-ion sensing: New emissive peptide probes based on benzo[d]oxazole derivatives and their gold and silica nanoparticles. *Inorg. Chem.* **50,** 8834–8849 (2011).

242. Oliveira, E., Nunes-Miranda, J. D. & Santos, H. M. From colorimetric chemosensors to metal nanoparticles using two new tyrosine Schiff-base ligands for Cu^{2+} detection. *Inorganica Chim. Acta* **380,** 22–30 (2012).

243. Fernández-Lodeiro, J. *et al.* Novel emissive podands based on 8-OH-quinoline: Synthesis, fluorescence materials, DFT and complexation studies. *Inorganica Chim. Acta* **381,** 218–228 (2012).

244. López-Cortés, R. *et al.* Fast human serum profiling through chemical depletion coupled to gold-nanoparticle-assisted protein separation. *Talanta* **100,** 239–245 (2012).

245. Liu, X., Atwater, M., Wang, J. & Huo, Q. Extinction coefficient of gold nanoparticles with different sizes and different capping ligands. *Colloids Surfaces B Biointerfaces* **58,** 3–7 (2007).

246. Sánchez-Iglesias, A. *et al.* Synthesis and optical properties of gold nanodecahedra with size control. *Adv. Mater.* **18,** 2529–2534 (2006).

247. Turkevich, J. A study of the nucleation and growth process in the synthesis of colloidal gold. *Discuss. Faraday Soc.* **55,** 55–75 (1951).

248. Enüstün, B. V. & Turkevich, J. Coagulation of Colloidal Gold. *J. Am. Chem. Soc.* **85,** 3317–3328 (1963).

249. Turkevich, J. Colloidal Gold. Part I. Historical and preparative aspects, morphology and structure. *Gold Bull.* **18,** 86–91 (1985).

250. Turkevich, J. Colloidal Gold Part II: Colour, Coagulation, Adhesion, Alloying and Catalytic Properties. *Gold Bull.* **18,** 125–131 (1985).

251. Zhang, S. *et al.* Nanonecklaces assembled from gold rods, spheres, and bipyramids. *Chem. Commun.* 1816–1818 (2007).

252. Kou, X., Sun, Z., Yang, Z., Chen, H. & Wang, J. Curvature-directed assembly of gold nanocubes, nanobranches, and nanospheres. *Langmuir* **25,** 1692–1698 (2009).

253. Sreeprasad, T. S. & Pradeep, T. Reversible assembly and disassembly of gold nanorods induced by EDTA and its application in SERS tuning. *Langmuir* **27,** 3381–3390 (2011).

254. Moores, A. & Goettmann, F. The plasmon band in noble metal nanoparticles: An introduction to theory and applications. *New J. Chem.* **30,** 1121–1132 (2006).

255. de Dios, A. S. & Díaz-García, M. E. Multifunctional nanoparticles: Analytical prospects. *Anal. Chim. Acta* **666,** 1–22 (2010).

256. Zhang, H., Fung, K. H., Hartmann, J., Chan, C. T. & Wang, D. Controlled chainlike agglomeration of charged gold nanoparticles via a deliberate interaction balance. *J. Phys. Chem. C* **112,** 16830–16839 (2008).

257. Mandal, S., Phadtare, S. & Sastry, M. Interfacing biology with nanoparticles. *Curr. Appl. Phys.* **5,** 118–127 (2005).

258. Chegel, V. *et al.* Gold nanoparticles aggregation: Drastic effect of cooperative functionalities in a single molecular conjugate. *J. Phys. Chem. C* **116,** 2683–2690 (2012).

259. Selvakannan, P. R., Mandal, S., Phadtare, S., Pasricha, R. & Sastry, M. Capping of gold nanoparticles by the amino acid lysine renders them water-dispersible. *Langmuir* **19,** 3545–3549 (2003).

260. Bishop, K. J. M., Wilmer, C. E., Soh, S. & Grzybowski, B. A. Nanoscale forces and their uses in self-assembly. *Small* **5,** 1600–1630 (2009).

261. Gleiter, H., Schimmel, T. & Hahn, H. Nanostructured solids — From nano-glasses to quantum transistors. *Nano Today* **9,** 17–68 (2014).

262. Kelly, K. L., Coronado, E., Zhao, L. L. & Schatz, G. C. The optical properties of metal nanoparticles: The influence of size, shape, and dielectric environment. *J. Phys. Chem. B* **107,** 668–677 (2003).

263. Fernando, A., Weerawardene, K. L. D. M., Karimova, N. V. & Aikens, C. M. Quantum mechanical studies of large metal, metal oxide, and metal chalcogenide nanoparticles and clusters. *Chem. Rev.* **115,** 6112–6216 (2015).

264. Ferrando, R., Jellinek, J. & Johnston, R. L. Nanoalloys: From theory to applications of alloy clusters and nanoparticles. *Chem. Rev.* **108,** 845–910 (2008).

265. Gao, M. R., Xu, Y. F., Jiang, J. & Yu, S.-H. Nanostructured metal chalcogenides: synthesis, modification, and applications in energy conversion and storage devices. *Chem. Soc. Rev.* **42,** 2986–3017 (2013).

266. Wu, S., Du, Y. & Sun, S. Transition metal dichalcogenide based nanomaterials for rechargeable batteries. *Chemical Engineering Journal* **307,** 189–207 (2017).

267. Falkowski, J. M. & Surendranath, Y. Metal chalcogenide nanofilms: Platforms for mechanistic studies of electrocatalysis. *ACS Catal.* **5,** 3411–3416 (2015).

268. Bag, S., Arachchige, U. & Kanatzidis, M. G. Aerogels from metal chalcogenides and their emerging unique properties. *J. Mater. Chem.* **18,** 3628–3632 (2008).

269. Bag, S. & Kanatzidis, M. G. Chalcogels: Porous metal-chalcogenide networks from main-group metal ions. Effect of surface polarizability on selectivity in gas separation. *J. Am. Chem. Soc.* **132,** 14951–14959 (2010).

270. Li, S. L., Tsukagoshi, K., Orgiu, E. & Samorì, P. Charge transport and mobility engineering in two-dimensional transition metal chalcogenide semiconductors. *Chem. Soc. Rev.* **45,** 118–151 (2016).

271. Batabyal, S. K. & Vittal, J. J. Axial-Junction nanowires of Ag_2 Te-Ag as a memory Element. *Chem. Mater* **20,** 5845–5850 (2008).

272. Major, J. D., Treharne, R. E., Phillips, L. J. & Durose, K. A low-cost non-toxic post-growth activation step for CdTe solar cells. *Nature* **511,** 334–337 (2014).

273. Yang, H. *et al.* Composition modulation of Ag_5Te nanowires for tunable electrical and thermal properties. *Nano Lett.* **14,** 5398–5404 (2014).

274. Kuznetsova, N. I. *et al.* Versatile PdTe/C catalyst for liquid-phase oxidations of 1,3-butadiene. *Appl. Catal. A Gen.* **513,** 30–38 (2016).

275. Mal, J., Nancharaiah, Y. V., Van Hullebusch, E. D. & Lens, P. N. L. Metal chalcogenide quantum dots: Biotechnological synthesis and applications. *RSC Adv.* **6,** 41477–41495 (2016).

276. Zhou, W. *et al.* Binary-Phased nanoparticles for enhanced thermoelectric properties. *Adv. Mater.* **21,** 3196–3200 (2009).

277. Pandey, S. *et al.* Tellurium platinate nanowires for photothermal therapy of cancer cells. *J. Mater. Chem. B* **4,** 3713–3720 (2016).

278. Ninad, G., Amey, W., Sandip, D. & Vimal, K. J. Synthesis and characterization of chalcogenolato-bridged allyl Palladium complexes: Versatile precursors for Palladium chalcogenides. *Organometallics* **27,** 6p (2008).

279. Bochmann, M. Metal chalcogenide materials: Chalcogenolato complexes as ‘single-source’ precursors. *Chem. Vap. Depos.* **2,** 85–96 (1996).

280. Barrelet, C. J., Wu, Y., Bell, D. C. & Lieber, C. M. Synthesis of CdS and ZnS nanowires using single-source molecular precursors. *J. Am. Chem. Soc.* **125,** 11498–11499 (2003).

281. Malik, M. A., Revaprasadu, N. & O’Brien, P. Air-stable single-source precursors for the synthesis of chalcogenide semiconductor nanoparticles. *Chem. Mater.* **13,** 913–920 (2001).

282. Maneeprakorn, W., Malik, M. A. & O'Brien, P. The preparation of cobalt phosphide and cobalt chalcogenide (CoX, X = S, Se) nanoparticles from single source precursors. *J. Mater. Chem.* **20,** 2329–2335 (2010).

283. Sun, J. & Buhro, W. E. The use of single-source precursors for the solution-liquid-solid growth of metal sulfide semiconductor nanowires. *Angew. Chemie - Int. Ed.* **47,** 3215–3218 (2008).

284. Jain, V. K. & Chauhan, R. S. New vistas in the chemistry of platinum group metals with tellurium ligands. *Coord. Chem. Rev.* **306,** 270–301 (2016).

285. Oilunkaniemi, R., Laitinen, R. S. & Ahlgrén, M. The X-ray crystallographic study of the reaction of bis(2-thienyl)ditelluride with tetrakis(triphenylphosphine)platinum or -palladium. *J. Organomet. Chem.* **595,** 232–240 (2000).

286. Dey, S. *et al.* Pyridine- and 3-/6-Methylpyridine-2-tellurolate Complexes of Palladium(II) and Platinum (II). *Eur. J. Inorg. Chem.* 744–750 (2003).

287. Chauhan, R. S. *et al.* Tellurium(0) as a Ligand: Synthesis and Characterization of 2-Pyridyltellurolates of Platinum(II) and Structures of $[Pt\{2\text{-}Te\text{-}3\text{-}(R)C_5H_3N\}_2Te(PR'_3)]$ (R = H or Me). *Inorg. Chem.* **49,** 4179–4185 (2010).

288. Chauhan, R. S. *et al.* Reactivity of Dipyridyl Ditellurides with (Diphosphine)Pt^0 and 2-Pyridyltellurolates with (Diphosphine)$PtCl_2$ and Isolation of Different Structural Motifs of Platinum(II) Complexes. *Organom.* **31,** 1743–1750 (2012).

289. Abel, W., Beckett, M. A., Orrel, K. G., Sik, V. & Stephenson, D. Interaction of the Diphenyldichalcogens (E= S, Se and Te), with the tetrameric halogenotrymethylplatinuns. The formation and characterization of $[\{PtX(CH_3)_3\}_2C_6H_5TeTeC_6H_5]$ (X = Br and I) and a dynamic nuclear magnetic resonance study of $[\{PtI(CH_3)_3\}_2C_6H_5]$. *Polyhedron* **7,** 1169–1173 (1988).

290. Fernández-Lodeiro, J. *et al.* Unraveling the Organotellurium Chemistry Applied to the Synthesis of Gold Nanomaterials. *ACS Omega* **1,** 1314–1325 (2016).

291. Petragnani, N. Some developments in organic tellurium chemistry. *Ann. N. Y. Acad. Sci.* **192,** 10–24 (1972).

292. Petragnani, N. & Stefani, H. a. in *Tellurium in Organic Synthesis (Second Edition)* (2007).

293. Sharma, M., Bhasin, K. K., Mehta, S. K., Singh, N. & Kumar, S. An EDXRF study of the photodecomposition of diorganyl ditellurides. *Radiat. Phys. Chem.* **75,** 2029–2038 (2006).

294. Beckmann, J., Bolsinger, J. & Duthie, A. Intramolecularly coordinated telluroxane clusters and polymers. *Chem. - A Eur. J.* **17,** 930–940 (2011).

295. Jiang, N. & Spence, J. C. H. Modeling core-hole effects in electron energy-loss spectroscopy of TeO_2. *Phys. Rev. B - Condens. Matter Mater. Phys.* **70,** 2–7 (2004).

296. Yoshimura, D. *et al.* Adsorption states of dialkyl ditelluride autooxidized monolayers on Au(111). *Langmuir* **21,** 3344–3353 (2005).

297. Li, Y., Silverton, L. C., Haasch, R. & Tong, Y. Y. Alkanetelluroxide-protected gold nanoparticles. *Langmuir* **24,** 7048–7053 (2008).

298. Whiffen, D. Infra-red summation bands of the out-of-plane C-H bending vibrations of substituted

benzene compounds. *Spectrochim. Acta* **7,** 253–263 (2002).

299. Staurt, B. *Infrared Spectroscopy: Fundamentals and Applications*. (Jonh Wiley & Sons, LTD, 2004).

300. Ogawa, A. *et al*. Photo-Induced ditelluration of acetylenes with diphenyl ditelluride. *Tetrahedron* **49,** 1177–1188 (1993).

301. Kunkely, H. & Vogler, A. Excited state properties of dinaphthyl ditelluride. *Inorganica Chim. Acta* **362,** 281–283 (2009).

302. Zangmeister, C. D., Tong, Y. J., Zaluzhna, O., Li, Y. & Allison, T. C. Different mechanisms govern the two-phase Brust–Schiffrin dialkylditelluride syntheses of Ag and Au nanoparticles. *J. Am. Chem. Soc.* **134,** 1990–1992 (2012).

303. Wyckoff, R. W. G. *Crystal Structures*. (New York, Interscience Publisher, 2nd Edition, 1963).

304. Stark, W. J., Stoessel, P. R., Wohlleben, W. & Hafner, A. Industrial applications of nanoparticles. *Chem. Soc. Rev.* **44,** 5793–5805 (2015).

305. Santos, C. S. C. *et al.* Industrial Applications of Nanoparticles - A Prospective Overview. *Mater. Today Proc.* **2,** 456–465 (2015).

306. Heiligtag, F. J. & Niederberger, M. The fascinating world of nanoparticle research. *Mater. Today* **16,** 262–271 (2013).

307. Oliveira, E. *et al.* Revisiting the use of gold and silver functionalised nanoparticles as colorimetric and fluorometric chemosensors for metal ions. *Sensors and Actuators, B: Chemical* **212,** 297–328 (2015).

308. Liu, L. & Corma, A. Metal Catalysts for Heterogeneous Catalysis: From Single Atoms to Nanoclusters and Nanoparticles. *Chem. Rev.* **118,** 4981–5079 (2018).

309. Chinen, A. B. *et al.* Nanoparticle Probes for the Detection of Cancer Biomarkers, Cells, and Tissues by Fluorescence. *Chem. Rev.* **115,** 10530–10574 (2015).

310. Perfézou, M., Turner, A. & Merkoçi, A. Cancer detection using nanoparticle-based sensors. *Chem. Soc. Rev.* **41,** 2606–2622 (2012).

311. Yan, Y., Huang, K., Yang, D., Zhang, H. & Yu, X. Graphene coupled with Pt cubic nanoparticles for high performance, air-stable graphene-silicon solar cells. *Nano Energy* **32,** 225–231 (2016).

312. Kim, J. K., Kim, D. J., Lee, C. S., Cho, H. H. & Kim, J. H. Pt-decorated SnO_2 nanotubes prepared directly on a conducting substrate and their application in solar energy conversion using a solid polymer electrolyte. *Appl. Surf. Sci.* **450,** 9–20 (2018).

313. Zhang, Q. *et al.* Trifolium-like platinum nanoparticle-mediated photothermal therapy inhibits tumor growth and osteolysis in a bone metastasis model. *Small* **11,** 2080–2086 (2015).

314. Pedone, D., Moglianetti, M., De Luca, E., Bardi, G. & Pompa, P. P. Platinum nanoparticles in nanobiomedicine. *Chem. Soc. Rev.* **46,** 4951–4975 (2017).

315. Wang, H. *et al.* Dramatically different kinetics and mechanism at solid/liquid and solid/gas

interfaces for catalytic isopropanol oxidation over size-controlled platinum nanoparticles. *J. Am. Chem. Soc.* **136,** 10515–10520 (2014).

316. Dong, C. *et al.* Size-dependent activity and selectivity of carbon dioxide photocatalytic reduction over platinum nanoparticles. *Nat. Commun.* **9,** 1–11 (2018).

317. Kim, K. S., Demberelnyamba, D. & Lee, H. Size-selective synthesis of gold and platinum nanoparticles using novel thiol-functionalized ionic liquids. *Langmuir* **20,** 556–560 (2004).

318. Onodera, T., Sun, S., Daimon, H., Wang, C. & Koda, T. A general approach to the size- and shape-controlled synthesis of platinum nanoparticles and their catalytic reduction of oxygen. *Angew. Chemie Int. Ed.* **47,** 3588–3591 (2008).

319. Bigall, N. C. *et al.* Monodisperse platinum nanospheres with adjustable diameters from 10 to 100 nm: Synthesis and distinct optical properties. *Nano Lett.* **8,** 4588–4592 (2008).

320. Cao, S., Tao, F. F., Tang, Y., Li, Y. & Yu, J. Size- and shape-dependent catalytic performances of oxidation and reduction reactions on nanocatalysts. *Chem. Soc. Rev.* **45,** 4747–4765 (2016).

321. Narayanan, R. & El-Sayed, M. A. Catalysis with transition metal nanoparticles in colloidal solution: Nanoparticle shape dependence and stability. *J. Phys. Chem. B* **109,** 12663–12676 (2005).

322. Zhang, H., Jin, M., Xiong, Y., Lim, B. & Xia, Y. Shape-controlled synthesis of Pd nanocrystals and their catalytic applications. *Acc. Chem. Res.* **46,** 1783–1794 (2013).

323. Ren, J. & Tilley, R. D. Shape-Controlled growth of platinum nanoparticles. *Small* **3,** 1508–1512 (2007).

324. Strand, M. B. *et al.* Shape-directed platinum nanoparticle synthesis: nanoscale design of novel catalysts. *Appl. Organomet. Chem.* **28,** 1–17 (2013).

325. Huang, X., Zhao, Z., Fan, J., Tan, Y. & Zheng, N. Amine-assisted synthesis of concave polyhedral platinum nanocrystals having {411} high-index facets. *J. Am. Chem. Soc.* **133,** 4718–4721 (2011).

326. Mahmoud, M. A., Tabor, C. E., El-Sayed, M. A., Ding, Y. & Zhong, L. W. A new catalytically active colloidal platinum nanocatalyst: The multiarmed nanostar single crystal. *J. Am. Chem. Soc.* **130,** 4590–4591 (2008).

327. Ma, L. *et al.* Control over the branched structures of platinum nanocrystals for electrocatalytic applications. *ACS Nano* **6,** 9797–9806 (2012).

328. Wang, J. *et al.* One-step and rapid synthesis of 'clean' and monodisperse dendritic Pt nanoparticles and their high performance toward methanol oxidation and p-nitrophenol reduction. *Nanoscale* **4,** 1549–1552 (2012).

329. Yuan, Y. *et al.* Seed-mediated synthesis of dendritic platinum nanostructures with high catalytic activity for aqueous-phase hydrogenation of acetophenone. *J. Energy Chem.* **24,** 660–668 (2015).

330. Gu, H. *et al.* Gaseous NH_3 confers porous Pt nanodendrites assisted by halides. *Sci. Rep.* **6,** 1–11 (2016).

331. Kong, X., Cao, H., Li, C. & Chen, X. One step photochemical synthesis of clean surfaced sponge-

like porous platinum with high catalytic performances. *J. Colloid Interface Sci.* **487,** 60–67 (2017).

332. Rolison, D. R. Catalytic nanoarchitectures - The importance of nothing and the unimportance of periodicity. *Science (80-.).* **299,** 1698–1701 (2003).

333. Shen, Q. *et al.* Three-dimensional dendritic Pt nanostructures: Sonoelectrochemical synthesis and electrochemical applications. *J. Phys. Chem. C* **112,** 16385–16392 (2008).

334. Zuo, Y. *et al.* Platinum dendritic-flowers prepared by tellurium nanowires exhibit high electrocatalytic Activity for glycerol oxidation. *ACS Appl. Mater. Interfaces* **7,** 17725–17730 (2015).

335. Jung, E. G., Shin, Y., Lee, M., Yi, J. & Kang, T. Interfacial synthesis of two-dimensional dendritic platinum nanoparticles using oleic acid-in-water emulsion. *ACS Appl. Mater. Interfaces* **7,** 10666–10670 (2015).

336. Caminade, A.-M. *et al.* Dendritic structures within dendritic structures: dendrimer-induced formation and self-assembly of nanoparticle networks. *Nanoscale* **1,** 233 (2009).

337. Wang, L. & Yamauchi, Y. Facile synthesis of three-dimensional dendritic platinum nanoelectrocatalyst. *Chem. Mater.* **21,** 3562–3569 (2009).

338. Mohanty, A., Garg, N. & Jin, R. A universal approach to the synthesis of noble metal nanodendrites and their catalytic properties. *Angew. Chemie - Int. Ed.* **49,** 4962–4966 (2010).

339. Lee, E. P. *et al.* Facile synthesis of highly faceted multioctahedral Pt nanocrystals through controlled overgrowth. *Nano Lett.* **8,** 4043–4047 (2008).

340. Rizvi, M. A. Complexation modulated redox behavior of transition metal systems (review). *Russ. J. Gen. Chem.* **85,** 959–973 (2015).

341. Rizvi, M. A., Syed, R. M. & Khan, B. Complexation effect on redox potential of Iron(III) - Iron(II) couple: A simple potentiometric experiment. *J. Chem. Educ.* **88,** 220–222 (2011).

342. Zhou, H. T. *et al.* Studies on iron (Fe^{3+}/Fe^{2+}])-complex/bromine (Br_2/Br^-]) redox flow cell in sodium acetate solution. *J. Electrochem. Soc.* **153,** A929 (2006).

343. Schneider, C. A., Rasband, W. S. & Eliceiri, K. W. NIH Image to ImageJ: 25 years of image analysis. *Nat. Methods* **9,** 671–675 (2012).

344. Jones, A. M., Griffin, P. J. & Waite, T. D. Ferrous iron oxidation by molecular oxygen under acidic conditions: The effect of citrate, EDTA and fulvic acid. *Geochim. Cosmochim. Acta* **160,** 117–131 (2015).

345. Ilbert, M. & Bonnefoy, V. Insight into the evolution of the iron oxidation pathways. *Biochimica et Biophysica Acta* **1827**, 161-175 (2013)

346. Song, Y. *et al.* Platinum nanodendrites. *Nanotechnology* **17,** 1300–1308 (2006).

347. Das, R. S., Singh, B., Banerjee, R. & Mukhopadhyay, S. PVP stabilized Pt nano particles

catalyzed de-oxygenation of phenoxazine group by hydrazine in physiological buffer media: Surfactant competes with reactants for the same surface sites. *J. Chem. Soc. Dalt. Trans.* **42,** 4068–4080 (2013).

348. Knecht, M. R. *et al.* Synthesis and characterization of Pt dendrimer-encapsulated nanoparticles: Effect of the template on nanoparticle formation. *Chem. Mater.* **20,** 5218–5228 (2008).

349. Akhter, S., Rahman, M., Ahmed, K., Hossain, M. & Saha, R. Tunable synthesis of platinum nanoparticles by EtOH reduction in presence of poly (vinylpyrrolidone). *Bangladesh J. Sci. Ind. Res.* **50,** 87–92 (2015).

350. Francis, A. J. & Dodge, C. J. Influence of complex structure on the biodegradation of iron-citrate complexes. *Appl. Environ. Microbiol.* **59,** 109–113 (1993).

351. Benítez, L. N. *et al.* Bacterial inactivation with iron citrate complex: A new source of dissolved iron in solar photo-Fenton process at near-neutral and alkaline pH. *Appl. Catal. B Environ.* **180,** 379–390 (2015).

352. Yin, B., Ma, H., Wang, S. & Chen, S. Electrochemical synthesis of silver nanoparticles under protection of Poly(N -vinylpyrrolidone). *J. Phys. Chem. B* **107,** 8898–8904 (2003).

353. Zhou, S., Yang, T. H., Zhao, M. & Xia, Y. Quantitative analysis of the reduction kinetics of a Pt(II) precursor in the context of Pt nanocrystal synthesis. *Chinese J. Chem. Phys.* **31,** 370–374 (2018).

354. McDermott, D. P. Vibrational assignments and normal-coordinate analyses of .gamma.-butyrolactone and 2-pyrrolidinones. *J. Phys. Chem.* **90,** 2569–2574 (1986).

355. Borodko, Y. *et al.* Probing the interaction of poly (vinylpyrrolidone) with platinum nanocrystals by UV-Raman and FTIR. *J. Phys. Chem. B* **110,** 23052–23059 (2006).

356. Du, Y. K., Hua, N. P., Yang, P., Jiang, L. & Mou, Z. G. Thermal decomposition behaviors of PVP coated on platinum nanoparticles. *J. Appl. Polym. Sci.* **99,** 23–26 (2005).

357. Liu, H. *et al.* Hydrothermal synthesis of monodisperse Ag_2Se nanoparticles in the presence of PVP and KI and their application as oligonucleotide labels. *J. Mater. Chem.* **18,** 2573–2580 (2008).

358. Cheong, S., Watt, J., Ingham, B., Toney, M. F. & Tilley, R. D. In situ and ex situ studies of platinum nanocrystals: Growth and evolution in solution. *J. Am. Chem. Soc.* **131,** 14590–14595 (2009).

359. Wang, L., Hu, C., Nemoto, Y., Tateyama, Y. & Yamauchi, Y. On the role of ascorbic acid in the synthesis of single-crystal hyperbranched platinum nanostructures. *Cryst. Growth Des.* **10,** 3454–3460 (2010).

360. Wang, L., Wang, H., Nemoto, Y. & Yamauchi, Y. Rapid and efficient synthesis of platinum nanodendrites with high surface area by chemical reduction with formic acid. *Chem. Mater.* **22,** 2835–2841 (2010).

361. Liu, M., Yan, X., Liu, H. & Yu, W. Investigation of the interaction between polyvinylpyrrolidone and metal cations. *React. Funct. Polym.* **44,** 55–64 (2000).

362. Filice, M., Marciello, M., Morales, M. D. P. & Palomo, J. M. Synthesis of heterogeneous

enzyme-metal nanoparticle biohybrids in aqueous media and their applications in C-C bond formation and tandem catalysis. *Chem. Commun.* **49,** 6876–6878 (2013).

363. Nikoobakht, B. & El-Sayed, M. A. Preparation and growth mechanism of gold nanorods (NRs) using seed-mediated growth method. *Chem. Mater.* **15,** 1957–1962 (2003).

364. Lohse, S. E. & Murphy, C. J. The Quest for Shape Control : A History of Gold Nanorod Synthesis. *Chem. Mater.* **25,** 1250-1261 (2013).

365. Prescott, S. W. & Mulvaney, P. Gold nanorod extinction spectra. *J. Appl. Phys.* **99,** (2006).

366. Chan, W. C. W. *et al.* Quantitative Comparison of Photothermal Heat Generation between Gold Nanospheres and Nanorods. *Sci. Rep.* **6,** 1–13 (2016).

367. Kennedy, L. C. *et al.* A new era for cancer treatment: Gold-nanoparticle-mediated thermal therapies. *Small* **7,** 169–183 (2011).

368. Sari, F., Sarikaya, A. M., Suren, D., Eren, M. & Yilmaz, B. Cancer Cell Imaging and Photothermal Therapy in the Near-Infrared Region by Using Gold Nanorods. *J. Am. Chem. Soc.* **19,** 176–178 (2015).

369. Riley, R. S. & Day, E. S. Gold nanoparticle-mediated photothermal therapy: applications and opportunities for multimodal cancer treatment. *Wiley Interdiscip. Rev. Nanomedicine Nanobiotechnology* **9,** (2017).

370. Elahi, N., Kamali, M. & Baghersad, M. H. Recent biomedical applications of gold nanoparticles: A review. *Talanta* **184,** 537–556 (2018).

371. Alkilany, A. M. & Murphy, C. J. Toxicity and cellular uptake of gold nanoparticles: What we have learned so far? *J. Nanoparticle Res.* **12,** 2313–2333 (2010).

372. Bai, R. *et al.* Surface chemistry of gold nanorods: origin of cell membrane damage and cytotoxicity. *Nanoscale* **5,** 8384 (2013).

373. Allen, J. M. *et al.* Synthesis of less toxic gold nanorods by using dodecylethyldimethylammonium bromide as an alternative growth-directing surfactant. *J. Colloid Interface Sci.* **505,** 1172–1176 (2017).

374. Leonov, A. P. *et al.* Detoxification of Gold Nanorods by Treatment with Polystyrenesulfonate. *ACS Nano* **2,** 2481–2488 (2008).

375. Hauck, T. S., Ghazani, A. A. & Chan, W. C. W. Assessing the effect of surface chemistry on gold nanorod uptake, toxicity, and gene expression in mammalian cells. *Small* **4,** 153–159 (2008).

376. Boca, S. C. & Astilean, S. Detoxification of gold nanorods by conjugation with thiolated poly(ethylene glycol) and their assessment as SERS-active carriers of Raman tags. *Nanotechnology* **21,** (2010).

377. Chen, C.-T. *et al.* Enhanced photoacoustic stability of gold nanorods by silica matrix confinement. *J. Biomed. Opt.* **15,** 016010 (2010).

378. Gorelikov, I. & Matsuura, N. Single-step coating of mesoporous silica on cetyltrimethyl

ammonium bromide-capped nanoparticles. *Nano Lett.* **8,** 369–373 (2008).

379. Detrembleur, C. *et al.* Gold Nanorods Coated with Mesoporous Silica Shell as Drug Delivery System for Remote Near Infrared Light-Activated Release and Potential Phototherapy. *Small* **11,** 2323–2332 (2015).

380. Zhang, Z. *et al.* Mesoporous silica-coated gold nanorods as a light-mediated multifunctional theranostic platform for cancer treatment. *Adv. Mater.* **24,** 1418–1423 (2012).

381. Dias, D. R., Moreira, A. F. & Correia, I. J. The effect of the shape of gold core-mesoporous silica shell nanoparticles on the cellular behavior and tumor spheroid penetration. *J. Mater. Chem. B* **4,** 7630–7640 (2016).

382. Wang, Z., Zong, S., Yang, J., Li, J. & Cui, Y. Dual-mode probe based on mesoporous silica coated gold nanorods for targeting cancer cells. *Biosens. Bioelectron.* **26,** 2883–2889 (2011).

383. Kimbrough, C. W. *et al.* Tumor targeted mesoporous silica-coated gold nanorods facilitate detection of pancreatic tumors using Multispectral optoacoustic tomography. *Nano Res.* **8,** 3864–3877 (2015).

384. Luo, G. F. *et al.* A Triple-Collaborative Strategy for High-Performance Tumor Therapy by Multifunctional Mesoporous Silica-Coated Gold Nanorods. *Adv. Funct. Mater.* **26,** 4339–4350 (2016).

385. Mahmoud, N. N., Alkilany, A. M., Khalil, E. A. & Al-Bakri, A. G. Antibacterial activity of gold nanorods against staphylococcus aureus and propionibacterium acnes: Misinterpretations and artifacts. *Int. J. Nanomedicine* **12,** 7311–7322 (2017).

386. Fouad, S. A., Mohammed, G. M., Elshoky, H. A., Salaheldin, T. A. & Mohamed, M. M. Antibacterial effect of gold nanoparticles against Corynebacterium pseudotuberculosis. *Int. J. Vet. Sci. Med.* **5,** 23–29 (2017).

387. Mahmoud, N. N., Alkilany, A. M., Khalil, E. A. & Al-Bakri, A. G. Nano-Photothermal ablation effect of Hydrophilic and Hydrophobic Functionalized Gold Nanorods on Staphylococcus aureus and Propionibacterium acnes. *Sci. Rep.* **8,** 1–10 (2018).

388. Yang, N., Wang, C., Wang, X. & Li, L. Synthesis of photothermal nanocomposites and their application to antibacterial assays. *Nanotechnology* **29,** (2018).

389. Hu, B., Wang, N., Han, L., Chen, M. L. & Wang, J. H. Core-shell-shell nanorods for controlled release of silver that can serve as a nanoheater for photothermal treatment on bacteria. *Acta Biomater.* **11,** 511–519 (2015).

390. Turcheniuk, K. *et al.* Highly effective photodynamic inactivation of E. coli using gold nanorods/SiO_2 core-shell nanostructures with embedded verteporfin. *Chem. Commun.* **51,** 16365–16368 (2015).

391. Jijie, R. *et al.* Particle-based photodynamic therapy based on indocyanine green modified plasmonic nanostructures for inactivation of a Crohn's disease-associated Escherichia coli strain. *J. Mater. Chem. B* **4,** 2598–2605 (2016).

392. Fonte, P., Reis, S. & Sarmento, B. Facts and evidences on the lyophilization of polymeric

nanoparticles for drug delivery. *J. Control. Release* **225,** 75–86 (2016).

393. Oda, C. M. R. *et al.* Freeze-dried diethylenetriaminepentaacetic acid-functionalized polymeric micelles containing paclitaxel: A kit formulation for theranostic application in cancer. *J. Drug Deliv. Sci. Technol.* **46,** 182–187 (2018).

394. Sangvanich, T. *et al.* Lyophilization and stability of antibody-conjugated mesoporous silica nanoparticle with cationic polymer and PEG for siRNA delivery. *Int. J. Nanomedicine* **13,** 4015–4027 (2018).

395. Alkilany, A. M. *et al.* Colloidal stability of citrate and mercaptoacetic acid capped gold nanoparticles upon lyophilization: Effect of capping ligand attachment and type of cryoprotectants. *Langmuir* **30,** 13799–13808 (2014).

396. Gomez, L. *et al.* Stability and biocompatibility of photothermal gold nanorods after lyophilization and sterilization. *Mater. Res. Bull.* **48,** 4051–4057 (2013).

397. Wu, W. C. & Tracy, J. B. Large-scale silica overcoating of gold nanorods with tunable shell thicknesses. *Chem. Mater.* **27,** 2888–2894 (2015).

398. Nonell, S. *et al.* Comparative effect of photodynamic therapy on separated or mixed cultures of Streptococcus mutans and Streptococcus sanguinis. *Photodiagnosis Photodyn. Ther.* **19,** 98–102 (2017).

399. MacKey, M. A., Ali, M. R. K., Austin, L. A., Near, R. D. & El-Sayed, M. A. The most effective gold nanorod size for plasmonic photothermal therapy: Theory and in vitro experiments. *J. Phys. Chem. B* **118,** 1319–1326 (2014).

400. Zauner, W., Farrow, N. A. & Haines, A. M. R. In vitro uptake of polystyrene microspheres: Effect of particle size, cell line and cell density. *J. Control. Release* **71,** 39–51 (2001).

401. Rowe, L. R., Chapman, B. S. & Tracy, J. B. Understanding and Controlling the Morphology of Silica Shells on Gold Nanorods. *Chem. Mater.* **30,** 6249–6258 (2018).

402. Feng, J. *et al.* Effects of template removal on both morphology of mesoporous silica-coated gold nanorod and its biomedical application. *RSC Adv.* **4,** 28683 (2014).

403. Huang, L., Chen, X. & Li, Q. Synthesis of microporous molecular sieves by surfactant decomposition. *J. Mater. Chem.* **11,** 610–615 (2001).

404. Reinhardt, N., Adumeau, L., Lambert, O., Ravaine, S. & Mornet, S. Quaternary ammonium groups exposed at the surface of silica nanoparticles suitable for DNA complexation in the presence of cationic lipids. *J. Phys. Chem. B* **119,** 6401–6411 (2015).

405. de Barros, H. R. *et al.* Surface interactions of gold nanorods and polysaccharides: From clusters to individual nanoparticles. *Carbohydr. Polym.* **152,** 479–486 (2016).

406. Nithiyanantham, U., Ozaydin, M. F., Tazebay, A. S. & Kundu, S. Low temperature formation of rectangular PbTe nanocrystals and their thermoelectric properties. *New J. Chem.* **40,** 265–277 (2016).

407. Wu, C. & Xu, Q. H. Stable and functionable mesoporous silica-coated gold nanorods as sensitive localized surface plasmon resonance (LSPR) nanosensors. *Langmuir* **25,** 9441–9446 (2009).

408. Alonso, M. J., Fabra, A., Marazuela, A., Janes, K. A. & Fresneau, M. P. Chitosan nanoparticles as delivery systems for doxorubicin. *J. Control. Release* **73,** 255–267 (2002).

409. Wang, Q., Hu, R., Zheng, H., Cao, J. & Davoudi, Z. Synthesis and In Vitro Characterization of Carboxymethyl Chitosan-CBA-Doxorubicin Conjugate Nanoparticles as pH-Sensitive Drug Delivery Systems. *J. Biomed. Nanotechnol.* **13,** 1097–1105 (2017).

410. Hamblin, M. R. Antimicrobial photodynamic inactivation: a bright new technique to kill resistant microbes. *Current Opinion in Microbiology* **33,** 67–73 (2016).

411. Crowe, L. M., Reid, D. S. & Crowe, J. H. Is trehalose special for preserving dry biomaterials? *Biophys. J.* **71,** 2087–2093 (1996).

412. Fonte, P., Reis, S. & Sarmento, B. Facts and evidences on the lyophilization of polymeric nanoparticles for drug delivery. *J. Control. Release* **225,** 75–86 (2016).

413. Abdelwahed, W., Degobert, G., Stainmesse, S. & Fessi, H. Freeze-drying of nanoparticles: Formulation, process and storage considerations. *Adv. Drug Deliv. Rev.* **58,** 1688–1713 (2006).

414. Shenoi, R. A. *Sugar-based systems. Engineering of Biomaterials for Drug Delivery Systems: Beyond Polyethylene Glycol* (Elsevier Ltd, 2018).

415. Silva, A. M. *et al*. Effect of cryoprotectants on the reconstitution of silica nanoparticles produced by sol–gel technology. *J. Therm. Anal. Calorim.* **120,** 1001–1007 (2014).

416. Sameti, M. *et al*. Stabilisation by freeze-drying of cationically modified silica nanoparticles for gene delivery. *Int. J. Pharm.* **266,** 51–60 (2003).

417. Benaroudj, N., Lee, D. H. & Goldberg, A. L. Trehalose Accumulation during Cellular Stress Protects Cells and Cellular Proteins from Damage by Oxygen Radicals. *J. Biol. Chem.* **276,** 24261–24267 (2001).

418. Tang, M., Waring, A. J. & Hong, M. Trehalose-protected lipid membranes for determining membrane protein structure and insertion. *J. Magn. Reson.* **184,** 222–227 (2007).

419. Mandal, S., Debnath, K., Jana, N. R. & Jana, N. R. Trehalose-Functionalized Gold Nanoparticle for Inhibiting Intracellular Protein Aggregation. *Langmuir* **33,** 13996–14003 (2017).

420. Auer, G. K. & Weibel, D. B. Bacterial Cell Mechanics. *Biochemistry* **56,** 3710–3724 (2017).

421. Epand, R. M., Walker, C., Epand, R. F. & Magarvey, N. A. Molecular mechanisms of membrane targeting antibiotics. *Biochim. Biophys. Acta - Biomembr.* **1858,** 980–987 (2016).

422. Li, R. *et al*. Synergistic reaction of silver nitrate, silver nanoparticles, and methylene blue against bacteria. *Proc. Natl. Acad. Sci.* **113,** 13612–13617 (2016).